

For Reference

NOT TO BE TAKEN FROM THIS ROOM

Ex LIBRIS
UNIVERSITATIS
ALBERTAENSIS



Digitized by the Internet Archive
in 2023 with funding from
University of Alberta Library

<https://archive.org/details/Hibbs1977>

THE UNIVERSITY OF ALBERTA

FACULTY OF GRADUATE STUDIES AND RESEARCH
SOURCE EFFECTS IN THE THREE-DIMENSIONAL
ELECTROMAGNETIC INDUCTION PROBLEM WITH EMPHASIS
ON TRANSFER FUNCTION ANALYSIS

The undersigned certify that they have read, and

recommend to the Faculty of Graduate Studies and Research,

by

for acceptance, a thesis entitled SOURCE EFFECTS IN THE

THREE-DIMENSIONAL ELECTROMAGNETIC INDUCTION PROBLEM WITH

EMPHASIS ON TRANSFER FUNCTION ANALYSIS submitted by

ROY D. HIBBS, JR. in partial fulfilment of the

requirements for the degree of Doctor of Philosophy in

Geophysics.

A THESIS

SUBMITTED TO THE FACULTY OF GRADUATE STUDIES AND RESEARCH

IN PARTIAL FULFILMENT OF THE REQUIREMENTS FOR THE DEGREE

OF DOCTOR OF PHILOSOPHY

IN GEOPHYSICS

DEPARTMENT OF PHYSICS

EDMONTON, ALBERTA

SPRING, 1977

Date March 18, 1977

ABSTRACT

The three-dimensional local induction problem is considered for various source configurations. The electromagnetic field solutions for layered conductors are developed and solutions for laterally inhomogeneous conductivity structures are found. A comparison of theoretical and analogue solutions is made. The effect of the source on perturbation and induction arrows is investigated.

DEDICATION

I wish to dedicate this thesis to my Mother and Father for their encouragement and support during my educational career.

The second model consists of an L-shaped highly resistive surface and is excited by a two-dimensional, non-uniform source which approximates an ionospheric electrojet current. A horizontal dipole above a square area is embedded in a poorly conducting rock constitutes the third model. Profiles of the electromagnetic field quantities showing source effects are presented.

A comparison of theoretical calculations with analogue model results is made for uniform two-dimensional non-uniform and a horizontal dipole sources over a three-

ABSTRACT

The three-dimensional local induction problem is considered for various source configurations. The electromagnetic field solutions for layered conductors are developed and solutions for laterally inhomogeneous conductivity structures are found. A comparison of theoretical and analogue solutions is made. The effect of the source on perturbation and induction arrows is investigated.

Three source field and conductivity structure combinations are considered. The first model of a uniform source above a resistive anomaly approximates an island in the deep ocean for Geomagnetic Bay type disturbances. The second model consists of an L-shaped highly resistive sulfide ore body embedded in an average continental conductivity configuration excited by a two-dimensional, non-uniform source which approximates an ionospheric electrojet current. A horizontal dipole above a square ore body embedded in poorly conducting rock constitutes the third model. Profiles of the electromagnetic field quantities showing source effects are presented.

A comparison of theoretical calculations with analogue model results is made for uniform two-dimensional non-uniform and a horizontal dipole sources over a three-

dimensional anomaly. The anomaly on the geophysical scale represents an ore body of lower conductivity embedded in poorly conducting rock. It is found that the theoretical sources used well represent the analogue model sources constructed. In spite of the limitations in the two methods the results indicate a good degree of compatibility between the two methods for studying these problems and they can be used together to learn more about the effects produced by such anomalies. Also, by using two approaches simultaneously, a better understanding of the characteristics of each approach is obtained.

From the theoretical calculations the transfer functions and related perturbation and induction arrows associated with the electromagnetic field solutions are computed. The results show that little source effect is noted on the induction and perturbation arrows for the models chosen. The arrows can be used in the traditional manner to indicate the flow of anomalous currents and point in the direction of conductivity inhomogeneities. The perturbation arrows do not well represent anomalous current vectors. However, by combining the \underline{p} and \underline{q} arrow vectorially the spatial extent of the conductivity anomaly can be outlined. The induction and perturbation arrows are stable for a variety of anomalous and normal field calculations with the perturbation arrow exhibiting the

most stability. For small angular spread in the source field polarization skewing of the induction arrows is produced.

ACKNOWLEDGEMENTS

The author wishes to express his sincere thanks to Dr. F. W. Jones for his supervision and assistance in this research. The author also wishes to express his thanks to Dr. H.W. Dosso for his help and the University of Victoria for the use of its experimental equipment. The author is also grateful to the National Research Council of Canada for financial support in the form of a Postgraduate Scholarship.

TABLE OF CONTENTS

Chapter		Page
1	INTRODUCTION	1
	1.1 General	1
	1.2 Global and Local Problems	2
	1.2.1 Global Problems	2
	1.2.2 Methods for Solving Global Problems	3
	1.2.3 Local Problems	12
	1.2.4 Method for Solving the Local Induction Problem	16
	1.3 Transfer Functions	27
2	SOLUTION OF THE THREE-DIMENSIONAL LOCAL INDUCTION PROBLEM FOR ONE, TWO AND THREE DIMENSIONAL SOURCE FIELDS	30
	2.1 The General Three-Dimensional Local Electromagnetic Induction Problem	30
	2.2 Elementary Solutions of Maxwell's Equations for a Semi-Infinite Conductor with a Plane Boundary	36
	2.2.1 Elementary Solutions of the First Type	38
	2.2.2 Elementary Solutions of the Second Type	41
	2.3 The Two-Dimensional Problem; E and H Polarizations	43
	2.3.1 Determinancy of the Two-Dimensional Problem	45
	2.4 The Uniform Source Two-Dimensional Solution	49

Chapter		Page
2.5	The Two-Dimensional Non-Uniform Source Solution	52
2.6	A Method for Obtaining an Arbitrary Two-Dimensional Source	56
2.6.1	Comparison of Piecewise Continuous Representations and Analytically Integrated Kernel Calculations	58
2.6.2	An Arbitrary Non-Integrable Source Configuration	82
2.7	The Horizontal Magnetic Dipole Source Solution for a Two-Layer Conductor	90
2.8	Three-Dimensional Finite Difference Numerical Technique	98
2.9	Electromagnetic Induction in Three-Dimensional Structures for Various Source Fields	106
2.9.1	One-Dimensional Source Field	107
2.9.2	Two-Dimensional Source Field	115
2.9.3	Three-Dimensional Source Field	121
3	A COMPARISON OF ELECTROMAGNETIC ANALOGUE MODEL MEASUREMENTS AND FINITE-DIFFERENCE NUMERICAL CALCULATIONS FOR THREE DIFFERENT SOURCE FIELDS	130
3.1	Mathematical Analysis	132
3.2	Analogue Model Apparatus	135
3.3	Model Description	139
3.4	Results	147

Chapter		Page
	3.4.1 Uniform Source Results	149
	3.4.2 Two-Dimensional Non-Uniform Source Results	160
	3.4.3 Dipole Source Results	170
	3.5 Summary	180
4	A STUDY OF PERTURBATION AND INDUCTION ARROWS FOR VARIOUS CONDUCTIVITY CONFIGURATIONS AND SOURCE FIELDS	182
	4.1 The Mathematical Formulation of the Induction and Perturbation Arrows	183
	4.2 The Calculation of Perturbation and Induction Arrows for a Uniform Source Over a Three-Dimensional Conductivity Model	187
	4.2.1 Single Source Results	188
	4.2.2 Multiple Source Results	192
	4.3 The Calculation of Perturbation and Induction Arrows for a Three-Dimensional Conductivity Structure and Various Two-Dimensional Source Fields	205
	4.3.1 Single Source Results	208
	4.3.2 Multiple Source Results	212
	4.4 The Calculation of Perturbation and Induction Arrows for a Three-Dimensional Conductivity Model and Dipole Source Fields	221
	4.4.1 Single Source Results	225
	4.4.2 Two-Dipole Source Results	229
	4.5 Summary	243

Chapter	Page
5 CONCLUSIONS AND RECOMMENDATIONS FOR FURTHER RESEARCH	249
BIBLIOGRAPHY	254
APPENDIX A	270

LIST OF TABLES

Table		Page
2.1	Gaussian Representation Comparison Near Origin	59
2.2	Gaussian Representation Comparison at Great Distances	60
2.3	Comparison of Gaussian and Piecewise Continuous Source Near Origin	62
2.4	Comparison of Gaussian and Piecewise Source at Great Distances	63
2.5	Source Intensity Coefficients for the Arbitrary Source	83
3.1	Weighting Coefficients of Rectangular Current Distributions	143

LIST OF FIGURES

Figure		Page
2.1	Coordinate System	37
2.2	Coordinate System	53
2.3	Apparent Resistivity and Phase Curves for Non-Uniform Source in Negative Y Region of First Conductivity Configuration	66
2.4	Apparent Resistivity and Phase Curves for Non-Uniform Source in Positive Y Region of First Conductivity Configuration	68
2.5	Field Profiles for Non-Uniform Source and First Conductivity Configuration	70
2.6	Apparent Resistivity and Phase Curves for Gaussian Source	73
2.7	Field Profiles for Gaussian Source	75
2.8	Apparent Resistivity and Phase Curves for Non-Uniform Source in Negative Y Region of Second Conductivity Configuration	77
2.9	Apparent Resistivity and Phase Curves for Non-Uniform Source in Positive Y Region of Second Conductivity Configuration	79
2.10	Field Profiles for Non-Uniform Source and Second Conductivity Configuration	81
2.11	Apparent Resistivity and Phase Curves for Arbitrary Source in Negative Y Region	85
2.12	Apparent Resistivity and Phase Curves for Arbitrary Source in Positive Y Region	87
2.13	Field Profiles for Arbitrary Source	89

Figure		Page
2.14	Coordinate System	91
2.15	Finite Difference Grid	101
2.16	Anomalous Conductivity Structures	110
2.17	One-Dimensional Source Profiles; Position 1	111
2.18	One-Dimensional Source Profiles; Position 2	113
2.19	One-Dimensional Source Profiles; Position 3	114
2.20	One-Dimensional Source; Three- Dimensional Profiles	116
2.21	Two-Dimensional Source Profiles; Position 1	119
2.22	Two-Dimensional Source Profiles; Position 2	120
2.23	Two-Dimensional Source Profiles; Position 3	122
2.24	Two-Dimensional Source; Three- Dimensional Profiles	123
2.25	Horizontal Dipole Source Profiles; Position 1	125
2.26	Horizontal Dipole Source Profiles; Position 2	127
2.27	Horizontal Dipole Source; Three Dimensional Profiles	128
3.1	Co-ordinate System, Source and Profile Positions	140
3.2	Current Carrying Grid	146
3.3	Uniform Source Profiles; Position 1	151
3.4	Uniform Source Profiles; Position 2	152

Figure		Page
3.5	Uniform Source Profiles; Position 3	153
3.6	Uniform Source; Three-Dimensional Profiles	155
3.7	Non-Uniform Source Profiles; Position 1	162
3.8	Non-Uniform Source Profiles; Position 2	163
3.9	Non-Uniform Source Profiles; Position 3	164
3.10	Non-Uniform Source; Three-Dimensional Profiles	166
3.11	Horizontal Dipole Source Profiles; Position 1	172
3.12	Horizontal Dipole Source Profiles; Position 2	173
3.13	Horizontal Dipole Source Profiles; Position 3	174
3.14	Horizontal Dipole Source; Three-Dimensional Profiles	176
4.1	Perturbation, Current and Induction Arrows for Single Uniform Source at 0.001 Hz	191
4.2	Perturbation, Current and Induction Arrows for Multiple Uniform Source at 0.001 Hz	194
4.3	Perturbation, Current and Induction Arrows for Multiple Uniform Source at 0.0033 Hz	196
4.4	Perturbation, Current, Electric Field and Induction Arrows for Multiple Uniform Sources at 0.001 Hz	199
4.5	Comparison of Induction Arrows for Number and Angular Spread of Current Sources	202
4.6	Perturbation, Current and Induction Arrows for Multiple Uniform Sources at 0.001 Hz with Cochrane and Hyndman (1970) Substitution	204

Figure		Page
4.7	Coordinate System	207
4.8	Perturbation and Induction Arrows for Single Non-Uniform Source at 0.1 Hz	211
4.9	Perturbation and Induction Arrow for Two Non-Uniform Source at 0.1 Hz	214
4.10	Perturbation and Induction Arrow for Two Non-Uniform Source at 0.1 Hz with Cochrane and Hyndman (1970) Substitution	218
4.11	Perturbation and Induction Arrow for Two Non-Uniform Source at 0.1 Hz with Averaged Normal Field	220
4.12	Induction Arrows for Six Distant Sources with Close Angular Spread	223
4.13	Coordinate System	224
4.14	Perturbation and Induction Arrows for Single Horizontal Dipole Source at 0.075 Hz	228
4.15	Perturbation and Induction Arrows for Single Uniform Source at 0.075 Hz	231
4.16	Perturbation and Induction Arrows for Two Horizontal Dipole Sources at 0.075 Hz	234
4.17	Perturbation and Induction Arrows for Two Orthogonal Uniform Sources at 0.075 Hz	237
4.18	Perturbation and Induction Arrows for Two Horizontal Dipole Sources at 0.075 Hz with Cochrane and Hyndman (1970) Substitution	239
4.19	Perturbation and Induction Arrows for Two Horizontal Dipole Sources at 0.075 Hz with Averaged Normal Field	242
4.20	Perturbation and Induction Arrows for Two Horizontal Dipole Sources at 0.075 Hz with Averaged Normal Field and Cochrane and Hyndman (1970) Substitution	245

Figure		Page
A.1	Elemental Gaussian Main Program	272
A.2	Elemental Gaussian Main Program (Continued)	273
A.3	Subroutine Integ	274
A.4	Subroutine Integ (Continued)	275
A.5	Subroutine Const.	276
A.6	Subroutine Const. (Continued)	277
A.7	Program Rectazoid	280
A.8	Program Rectazoid (Continued)	281
A.9	Elemental Gaussian Sample Run	284
A.10	Rectazoid Sample Run	285
A.11	Source Coefficients	286
A.12	Rectazoid Sample Run for Arbitrary Source	287

LIST OF PHOTOGRAPHIC PLATES

Plate		Page
3.1	Analogue Experimental Equipment	136
3.2	Analogue Anomaly and Support Structure	137

CHAPTER 1

INTRODUCTION

1.1 General

External sources which consist of time varying current systems of finite extent flowing in the ionosphere and above produce magnetic fields that induce electric currents in the earth's interior. These currents in turn produce magnetic and electric fields which contribute to the total electromagnetic field at the surface of the earth. The induced currents are perturbed by variations in the conductivity structure of the earth and consequently the associated electromagnetic fields are modified. The analysis of these modifications can yield an estimate of the electrical conductivity distribution of the earth.

In this thesis the global and local problems in electromagnetic induction are discussed and the three dimensional local perturbation problem is considered together with various methods for its solution. The mathematical formulations of the electromagnetic field solutions for uniform, general two-dimensional non-uniform and horizontal dipole sources over a semi-infinite layered earth with a plane boundary are presented. Using these solutions as the boundary conditions for an iterative method the solutions over a laterally non-uniform earth are obtained. A comparison of

theoretically calculated electromagnetic field profiles across a three-dimensional anomaly with the profiles of an equivalent analogue model for a uniform, a two-dimensional, non-uniform and a horizontal dipole source is made. Perturbation and induction arrows are theoretically computed for a variety of source configurations, frequencies and three-dimensional anomalous conductivity structures.

1.2 Global and Local Problems

The mathematical problems encountered in the study of earth currents are of two types. The first type involves inducing fields of global dimensions with averaged conductivities for the earth as a whole; these are known as global problems. The second type may or may not involve inducing fields of global dimensions but the conductivity values are definitely local values; these are known as local problems.

1.2.1 Global Problems

In the first group of problems, since we are interested in large regions having dimensions comparable to those of the earth, spherical polar coordinates are normally used. The electrical conductivity σ is then treated as a smoothed function of the coordinates (r, θ, ϕ) at any point within the earth. This function will not take into account any local variations in conductivity (which may be considerable) but only large scale variations of suitably

defined average σ for any region. For this problem the currents induced in any earth model will depend on the nature and distribution of the inducing field. The first step in solving such a problem is to express the inducing field in terms of spherical harmonics (assumed given). The induction effect of each harmonic is then studied separately and the result obtained from the summation of all the harmonics. The basic theory and method of solution for this type of problem is straightforward, though the calculation may be difficult and laborious.

1.2.2 Methods for Solving Global Problems

One global problem which has been extensively studied is that of the induction, by a varying magnetic field, of electric currents in a spherical conductor in which the conductivity is a function of r , the distance from the center of the earth. Lamb (1883) treated the case for the currents induced in a spherical conductor by variation of an external magnetic potential. Schuster (1889) applied the method of spherical harmonic analysis, as shown possible by Gauss (1839), to the field of the daily magnetic variation and found that the major part is of external origin but that a part is also produced from within the earth. The induced part of the magnetic field was attributed to electric currents in the earth induced by the external magnetic field which he considered to be primary. In cooperation with H.Lamb, Schuster (1889)

concluded that the conductivity of the earth was not uniform but that the earth consists of layers with the inner layers more highly conducting. Chapman (1918) analyzed the average field of magnetic storms and showed that the magnetic field is mainly of external origin with a minor induced part, further confirming the work of Schuster (1889). Chapman (1919) divided the earth into two concentric layers and gave an estimate of the conductivity and size of the uniform inner core and outer poorly conducting layer. The conductivity of the core was determined to be 3.6×10^{-2} mho/m and the thickness of the surrounding non-conducting layer was 250 km. Chapman and Whitehead (1922) showed that the ocean would have an appreciable effect on the induced field. Price (1930, 1931) extended Lamb's solution to aperiodic fields and Chapman and Price (1930) then used this extension to discuss the induced part of the field of magnetic storms. The more general case when σ is any function of r was studied by Lahiri and Price (1939). They developed both formulae and methods of calculation for both periodic and aperiodic fields when dealing with any distribution of conductivity within the sphere $r=a$ that can be expressed in the form:

$$\sigma = \sigma_0(qa/r) \text{ for } r < qa < a \text{ and } \sigma = 0 \text{ for } r > qa \quad (1.1)$$

where σ_0 , q and r are constants.

Lahiri and Price (1939) applied their results using the data of Chapman (1919) to investigate the earth's conductivity structure to a depth of approximately 800 km. Their results showed that the earth's conductivity was uniform and of a value of 10^{-5} to 10^{-4} mho/m down to a depth of 700 km where the conductivity increased to a value of at least 1 mho/m or more.

Using data from the Second Polar Year (1932-1933) Hasagawa and Ota (1948) and Benkova (1940) independently determined that in Chapman's original model the non-conducting layer must be 400 km thick and that the conductivity of the core must be 5×10^{-1} mho/m. Rikitake (1950), using the same data, determined that the earth is composed of a non-conducting layer of thickness 400 km, a conducting mantle of conductivity 5.0×10^{-1} mho/m and a core whose conductivity must be at least an order of magnitude above that of the mantle.

Due to skin depth considerations, the maximum depth of penetration for induced currents is roughly 800-100 km, the conductivity distribution of the mantle, which extends by seismological evidence from a depth of 700 km to 2900 km, is undetermined below a depth of 100 km. Below this depth the longer period geomagnetic secular variation must be used. McDonald (1957) chose a power law for the conductivity distribution of the mantle below 1000 km (conductivities greater than 10 mho/m) and a

compendium of Lahiri and Price (1939) conductivity estimates for depths less than 800 km (conductivities less than 1 mho/m). The intermediate values were smoothed extrapolations from the inner and outer portions of the mantle. Yukutake (1959) also used the secular variation to estimate the conductivity profile of the earth.

Cantwell (1960) gave a more detailed conductivity structure of the upper mantle on the basis of magnetotelluric results. A rapid rise in conductivity near a depth of 80 km to a value in excess of 10^{-2} mho/m was inferred by Cantwell (1960). The Cantwell (1960) and McDonald (1957) curves merge at 800 km in depth.

With the introduction of electronic computers, time-series analysis of large data sets became possible. Eckhardt et al. (1963) studied geomagnetic variations of long period and found strong spectral peaks at periods of six months and harmonics of 27 days. The data fitted the McDonald (1957) profile quite well to depths of approximately 1000 km. Banks (1969) extended this method further so that not only the spectral peaks but also the continuum of the geomagnetic spectrum could be used as well. In the model that was obtained a steep rise in the conductivity took place at 400 km instead of 700 km as in the McDonald (1957) and the Lahiri and Price (1939) models. Further analysis by Banks (1972) found that the depth of the rise of conductivity is much closer to 700 km.

The variation of σ with θ and ϕ within the crust is of importance in both global and local problems. For example, the conductivity of the oceans is several orders of magnitude greater than that of the continents. Since the oceans are a thin surface layer on the earth of relatively high conductivity, the problem can be modelled in terms of electromagnetic induction in thin sheets. Most models consist of thin plane or spherical sheets. The conductivity of the underlying earth represented by a parallel conducting plane or spherical shell of suitable conductivity at a suitable depth. When the effects of the ocean as a whole are considered the plane is infinite or the spherical shell is complete. When coastlines are being studied the plate is finite and in the spherical case a spherical cap is used. If it is desired to model the actual conductivity distribution of the real oceans of the earth numerical methods must be used.

The earliest work on induction in thin sheets was done by Maxwell (1891) for uniform plane and spherical sheets. Lamb (1887a,b) studied non-uniform circular disks. More recently Price (1949) developed a general theory of induction in thin sheets and shells and obtained boundary conditions at the surface of the sheet in terms of the non-uniform distribution of conductivity and the scalar magnetic potentials of the induced and inducing fields. Price also proposed two iterative methods for solving the problem. In the first

Bailey (1970) proved that if the electromagnetic response of the earth is known for all frequencies in a spatial distribution represented by a single spherical harmonic the conductivity distribution of the earth can be uniquely determined assuming spherical symmetry for an exact inversion method. Parker (1970) applied the Backus-Gilbert(1970) inversion method to Banks' 1969 data and obtained significantly greater surface conductivity values than Banks (1969). Parker (1972) obtained bounds on the conductivity in the mantle and tested the observational data for self consistency. Jady (1974) applied an eigenvalue approach to the inversion problem and showed that the top 600 km of mantle is of relatively low conductivity with a rise in conductivity taking place somewhere between 600 and 950 km in depth. Using the data of Malin (1973), Jady (1975) determined that low conductivity is required to a depth of 650 km below the surface.

Apparently there have been no successful attempts to obtain solutions (analytical or numerical) for the induction of currents in a spherical conductor, when the conductivity is not only a function of r but also depends upon θ or ϕ or both. It seems reasonable that, except within the outermost 700 km of the earth, the variation of the conductivity with r is far more important than any dependence upon θ or ϕ .

method self induction and mutual induction are ignored in the starting approximation which is an appropriate approximation for a low frequency inducing field. The second method appropriate to a high frequency inducing field assumes that the vertical component of the induced field is equal and opposite to that of the inducing field in the starting approximation which is equivalent to treating the thin conductor as perfectly conducting initially. Bullard and Parker (1970) used the first method to investigate the 24-hour component of the S_q field in the actual oceans. Difficulties are encountered in the second method when conductivity discontinuities exist (Hobbs, 1971). However a solution in terms of an asymptotic series in inverse powers of the frequency can be obtained in some cases (Price and Ashour, 1974), Hutson, Kendall and Malin (1972) have reformulated the first method of Price (1949) so that high frequency problems can be solved and proved that for axisymmetric problems the solution converges. For non-axisymmetric problems no proof exists, however, the method has been successfully applied by Hewson-Browne (1973). Hewson-Browne et al. (1973) applied a modified version of the method to the problem of induction in a thin strip of finite conductivity and obtained a solution which agrees with Parker (1968). Parkinson (1975) investigated the possibilities of combining the two methods. The first method was used in the ocean

regions and the second method was used over the continents. Although different iteration algorithms were used the convergence rate of the problem was still insufficient to give useful results.

Exact solutions can be obtained for only a few conductivity distributions which include perfectly conducting finite sheets. Smythe (1968) and Lamb (1945) solved the case of an infinite strip of uniform width and a circular disk for a uniform inducing field using elliptic and oblate spheroidal coordinates. For more complex inducing fields, Ashour (1965a) solved the problem exactly with a system of dual integral equations. The solution for spherical caps subjected to symmetric inducing fields has been obtained by Collin (1961) and Ashour (1965a,b). Induction in a highly conducting hemispherical shell was considered by Doss and Ashour (1971) with the purpose of determining the range of frequencies for which an ocean of global dimensions acts as a perfect conductor except near the coast line. The non-symmetric inducing field case can be reduced to a system of integral equations (Ashour, 1965a,b). Weidelt (1971) studied a two-dimensional electromagnetic induction problem for two adjacent half-sheets of different conductivity. The problem was solved by contour integration and showed that the current and tangential magnetic field component are both finite and discontinuous at the boundary of the conductivity discontinuity. A similar

result was obtained by Parker (1968) for induction in an infinite strip by a parallel line current. For sheets in the form of a surface of revolution and when the conductivity and inducing field have axial symmetry, the induction problem can be solved in terms of a Fredholm integral equation (Ashour, 1950). Roden (1964) considered the case of a uniformly conducting strip with an infinitely conducting plane beneath and reduced the problem to a Fredholm equation. A sheet in which the conductivity decreases near the edge to zero represents a more realistic model of the oceans. Ashour (1971a,b) considered a circular disk, an infinite uniform strip and a hemispherical shell with such a conductivity contrast.

Exact solutions for perfectly conducting closed sheets includes the work of Ashour and Price (1948) for induction in a spherical shell for a non-uniform conductivity and inducing field, Price (1949) for induction in a plane sheet with harmonically varying conductivity and Ashour and Ferraro (1964) for applications to the ionosphere for anisotropic conductivity distributions. More recently Hobbs and Price (1970) have derived surface integral formulae for expressing any one field quantity in terms of any other for currents flowing in concentric spherical surfaces. This method is very useful for determining the vertical magnetic field component. Hobbs (1971) successfully applied these formulae to a hemispheric shell representing the Pacific Ocean surrounding a perfectly conducting sphere.

For very slowly varying magnetic fields it is not possible to treat the crust as a thin shell by itself, because of the mutual induction between the crust and conducting mantle below. Cox (1960), first pointed out that the conducting mantle should be taken into account when modelling electromagnetic effects over the ocean. Rikitake (1961) investigated the problem with two-dimensional analog models and a theoretical mathematical model of a conductor covered with a conducting sheet. Bullard and Parker (1970) proposed a model for the conductivity profile of the oceans in which a conducting mantle was overlain by a non-conducting crust-mantle which in turn was covered with a layer of conducting sediments of variable thickness. Cox (1971) assumed that the ocean and its sediments were bounded by perfect insulators which prevented current leakage into the conducting mantle.

1.2.3 Local Problems

In the local problem limited regions of the earth are concerned and variations of conductivity within distances of the order of 100 km are studied. For this the sphericity of the earth can be ignored and the earth treated as either a semi-infinite or thick plate conductor having a non-uniform distribution of conductivity. The inducing field in this problem is often of global dimensions and therefore effectively uniform over the region of interest. However, a knowledge of the inducing

field and surrounding ground conductivity in the immediate vicinity of a particular station are insufficient to define the strength of the induced currents in that region, as pointed out by Price (1965). The induced currents are affected by the distribution of the entire inducing field and by the average properties of the conductor over a region of corresponding dimensions. The entire induced current system will contribute to the field at a particular station, but the largest contribution comes from induced currents in the immediate neighborhood. The important point is that not only the local properties, but the properties of the conductor as a whole determine the strength of the induced currents in the region of interest.

The uniformity of the inducing field for the local problem has sometimes been taken to imply that the actual distribution of the inducing field can be ignored when calculating the induced currents and fields in the region of interest. This assumption is implicit in the theory of the "magnetotelluric method" of conductivity sounding of Cagniard (1953). For models in which the conductivity is a function of depth only, Cagniard defines the "apparent resistivity" as

$$\rho_a = \frac{1}{\mu_0 \omega} \left| \frac{E_x}{H_y} \right|^2 \quad (1.2)$$

in which ω is the angular frequency of the horizontal, orthogonal electromagnetic field components E_x and H_y and μ_0

is the magnetic permeability of free space. The model is assumed to be horizontally stratified in the x - and y -directions extending to infinity. The formula is derived from the skin depth effect for uniform half space conductors excited by alternating currents. As such no source field effects are taken into account. As ω decreases the currents penetrate deeper into the conductor and the manner in which ρ_a varies gives an indication of the conductivity profile. The accuracy of the profile is dependent on the particular geophysical situation being investigated. For moderately uniform terrain and depths the method is convenient and valuable. At greater depth even for horizontally stratified strata it may be necessary to include consideration of the source field as discussed by Wait (1954) and Price (1962).

Price (1964) points out that the variation fields should first be separated into parts of external and internal origin and examined separately in order to objectively interpret local patterns of geomagnetic variations. The anomalous patterns in the fields of the induced currents are produced by non-uniform distributions of conductivity in the earth, since the external inducing field can be assumed to be of a relatively simple form and varies only slightly over the anomalous area except near the equatorial and auroral electrojets. There seems to be no reason to suggest that the ionosphere has anomalous properties over a specific geogra-

phic region, even though a small effect on the (anisotropic) conductivity of the ionosphere might be produced by a strong perturbation of the earth's magnetic field. Even if a considerable disturbance is caused in the ionosphere by such local anomalies it is doubtful that the surface values of the magnetic field would be greatly affected. Also, if the external field is found to reflect to a small extent the anomalous magnetic field distribution, this can be attributed to the general mutual induction between the earth and the ionosphere.

Once the external field and its induced current system is known, the local problem can be reduced to examining the local redistribution of a given average system of induced currents caused by local inhomogeneities of conductivity. However, it is not necessarily a simple problem of redistribution of steady current flow, since the currents are time varying and therefore a skin effect will be encountered. The mathematical problems which must be considered are those relating to the disturbance of skin effect distributions of a current system rather than actual electromagnetic induction problems in which the distribution of the induced currents for a non-uniform conductor is determined directly from a given inducing field. This problem is described by Price (1964) as follows:

"Using cartesian coordinates (x,y,z) with the z axis vertically downwards, a non-uniform conductor occupies the half-space $z > 0$. Near the origin the conductivity is a function (not necessarily continuous) of (x,y,z) , but at great distances from the origin it is a function of z only. A given alternating e.m.f. impels currents near the surface of the conductor. The problem is to determine the distribution and surface field of these currents."

The given e.m.f. is the electric field arising from the varying magnetic field and is controlled by the properties of the conductor at great distances. In essence the problem is formulated in terms of the redistribution of a known current system near a non-uniform conductor in which the distribution of the current system is known at large x and y .

1.2.4 Methods for Solving the Local Induction Problem

In his classic paper, Price (1950) considered electromagnetic induction in a semi-infinite conductor with a plane boundary for any inducing field, which was assumed known. A uniformly layered earth model was considered by Tikhonov (1950). Cagniard (1953), in his derivation of the well known theory of magnetotellurics, assumed a spatially uniform source of infinite extent and sinusoidal time variation, as well as a semi-infinite uniformly stratified earth with a plane boundary. Wait (1954) and Price (1962) discussed Cagniard's results in terms of a source of finite dimensions. However, until the last decade, little attention has been paid to the problem of a vertical fault in the

conductive region which represents the earth. It is well known that there are limited regions in various parts of the earth where temporal changes in the geomagnetic field at relatively near stations show considerable differences in form and amplitude. These differences remain consistent in character for the fluctuations of a given frequency, and form a definite pattern for the area studied. They are associated with lateral variations in conductivity below the earth's surface. Two-dimensional magnetic variometer array studies have well exhibited the consistency of the field configurations and that the differences in form and amplitude are associated with conductivity variations. It is therefore important to understand the manner in which lateral variations affect the surface field in order to interpret such variations.

D'Erceville and Kunetz (1962) obtained a solution for two media of different conductivities in contact along a vertical plane overlaying a horizontal basement that is either infinitely conducting, infinitely resistive or at infinite depth when the magnetic field is everywhere parallel to the strike of the fault, (H-polarization, see Chapter 2). Rankin (1962) applied the method of d'Erceville and Kunetz to the case of a dike of infinite length but finite depth and in which the magnetic field is parallel to the dike.

Weaver (1963) considered a half-space conductor which consisted of two quarter-spaces of different conductivity with a plane vertical fault of infinite depth. He considered both the H-polarization case and the E-polarization case (see Chapter 2) using an analytical technique. His H-polarization case agreed well with that of D'Erceville and Kunetz. However, in order for him to obtain a solution for the E-polarization case he found it necessary to use the approximate boundary condition that the tangential magnetic field is constant along the surface of the conductor. Mann (1970) proposed a perturbation technique to consider the original Weaver (1963) problem, and has shown that Weaver's original solution is just a first approximation to the field inside the conductor for normally incident waves. Weaver and Thomson (1972) have applied this technique and have been able to avoid the approximate boundary condition of the constancy of the horizontal magnetic field along the surface and have obtained approximate solutions. An approximate solution to the field was found for a periodic line current above a non-uniform earth when the height and magnitude of the line current approached infinity in such a way that the inducing field near the earth became uniform and finite. Geyer (1970) has used a similar perturbation technique to investigate the electromagnetic anomalies over several types of subsurface structures, and more recently (Geyer, 1972) has extended this to a dipping

contact. Previous to this, Yukutake (1967) considered induction in a conductor bounded by an inclined interface with a small angle of tilt by a successive approximation method which used repeated reflections of electromagnetic energy between the ground surface and the tilted boundary. Treumann (1970a,b,c) considered induction in non-uniform plates of finite thickness, and has been able to obtain approximate solutions for the field at the surface of the plates when the external inducing field is uniform. Weidelt (1971) has studied induction in two adjacent half sheets with different uniform conductivities. Furthermore, Schumucker (1971a) has used convolution integrals to investigate the induction in a model with a non-uniform surface layer above a layered substratum. Hughes (1973, 1974) presented a semi-analytical linear solution to the two-dimensional E-polarization case problem involving Fourier series representations of the conductivity anomaly. A two-layered earth with a sinusoidally varying overburden was modelled by Hughes and Wait (1975) using the semi-analytical approach of Mann (1964).

Analytical methods generally give solutions for only specialized cases. Anomalous conductivity structures of any shape may occur naturally, and so it is necessary to consider methods to deal with inhomogeneities of arbitrary shape. Several numerical methods have been used to obtain solutions for problems with vertical discontinuities for both

H-polarization and E-polarization cases. Dulaney and Madden (1962) were the first to apply the transmission line analogy over a two-dimensional mesh to such problems as these. The transmission line analogy arises from the similarity in form between Maxwell's equations governing the orthogonal components of E and H and the transmission line equations governing current and voltage on a transmission line. This method has been used by many authors (including Madden and Thompson, 1965; Madden and Swift, 1969; Swift, 1967, 1971; Wright, 1969, 1970; Slankis, 1970; Vozoff, 1971; Ku et al., 1973; and Ku, 1976). The finite element method, which uses the principle that electromagnetic fields behave in such a way as to minimize the energy, has recently been applied to induction problems by Coggon (1971), Ryu (1972), Silvestor and Haslam (1972), and Reddy and Rankin (1973). An anisotropically conducting laterally inhomogeneous medium was modelled by Reddy and Rankin (1975) using the finite element method. Rodi (1976) developed a finite element method which increases the computational accuracy of the field components used in magnetotelluric calculations. Finite difference techniques have been applied by Neves (1957), Latka (1966), Patrick and Bostick (1969) and others. Jones and Price (1969, 1970, 1971a,b) have employed the finite difference technique for studies of various two-dimensional conductivity distributions, and Jones and Pascoe (1971) and Pascoe and Jones (1972) have

given a general computer program for the solution of the local perturbation problem.

The relative merits and disadvantages of the four numerical techniques used to solve the local electromagnetic induction problem can be used to decide which method best fits a particular modelling situation. Both the finite element and transmission line analogy methods use matrix inversion to obtain solutions. For properly chosen grid spacings economical solutions in terms of computer costs can be obtained. However, grids with large numbers of points cannot be accommodated as the computer storage for the matrix inversion becomes prohibitive. Finite difference techniques when properly applied can be used with large grids since matrices are not involved. The computing time used is somewhat longer and the stability of the solution tends to be less than for the finite element method solution. The integral equation method reduces the domain of interest to the anomalous conductivity structure, and the electromagnetic field solutions can be obtained in terms of the scattering currents within it. However large anomalous domains cannot be handled as matrix inversion is involved and large conductivity contrasts ($> 100:1$) cannot be accommodated.

The grid mesh size in all the methods must be chosen properly to obtain a rapid solution. The smaller and more even the mesh size is across conductivity contrasts

the more rapid is the convergence of the solution. If coarser grids are chosen then the convergence of the solution takes substantially longer. However, the total number of grid points is limited and therefore the mesh sizes are chosen so that small uniform steps are taken across conductivity contrasts. Progressively larger grid spacings are used as one approaches the boundary of the mesh so as to keep the anomaly as far away from the boundary as possible.

Jones and Price (1969, 1970) considered the half-space conductor as the limit of a spherical conductor as the radius becomes infinite. They then carefully developed the boundary conditions and were able to obtain solutions for both the H-polarization and E-polarization cases. Jones and Price (1970) studied the field distribution within the whole two-dimensional region of interest, as well as the surface values of the various components, including the Cagniard (1953) apparent resistivity. In more recent work, Jones and Price (1971a,b) and Jones (1971a,b) as well as Hibbs and Jones (1972) have calculated apparent resistivity values along the surface of the conductor. Tatrallyay and Jones (1974a,b) applied a finite difference technique to a cylindrical mesh. Losecke and Muller (1975) investigated a two-dimensional overhanging, high resistivity structure utilizing a finite difference technique. An increase in the rate of convergence of the above problem was obtained by Muller and Losecke (1975).

Williamson, Hewlett and Tammemagi (1974) discovered an error in the Jones and Pascoe (1971) representation of the first derivatives for variable grid spacings. Jones and Thomson (1974) showed that its effect on the calculated results is much reduced when the grid spacings used are not too irregular. Brewitt-Taylor and Weaver (1976) show that for irregular grid spacings across regions of conductivity change the equations for the E-polarization case must be further modified to take into account weighted conductivity averages. The B-polarization equations were found to be incorrect and must be reformulated for all but regions of uniform conductivity. Brewitt-Taylor and Weaver regard conductivity changes as roughly linearly from one value to the next thus reinforcing the Lines and Jones (1973) concept of transition zones.

It should be noted that in all the numerical methods mentioned above the assumption has been made that the inducing field is uniform. A non-uniform source in the form of a line current has been considered by Wait (1962) and Dosso and Jacobs (1968). Schmucker (1971b) has considered non-uniform sources over a laterally inhomogeneous earth in

which the lateral changes in conductivity are confined to a limited depth range. Hermance and Peltier (1970) studied the magnetotelluric field of a line current over a layered subsurface, and later (Peltier and Hermance, 1971) extended their approach to include symmetric current distributions, such as a Gaussian current intensity source. Hutton (1969, 1971) and Hutton and Leggeat (1971) investigated the problem of electromagnetic induction by an equatorial electrojet taking into account the range of periods over which the electrojet effect is exhibited and the relative contributions of the "normal" and "enhanced" part of the inducing field. Hohmann (1971) investigated the two-dimensional line current source problem by deriving a Green's scalar function from Maxwell's equations and expressing the electric field in terms of an integral equation involving volume integrations of the anomalous field vector over only the anomalous domain. The boundary conditions were incorporated in the kernel of the integral equation and were thus automatically satisfied by the solution. The two-dimensional electromagnetic response of a buried cylindrical inhomogeneity excited by a line current source was calculated by Howard (1972) using a similar method. Schmucker (1971b) has considered models with a non-uniform source over a laterally inhomogeneous earth in which the lateral changes in conductivity are confined to a limited depth range. Hibbs and Jones (1973a)

have used the method of Peltier and Hermance (1971) to obtain boundary values for the method of Jones and Price (1970) and Jones and Pascoe (1971) so that perturbations of such fields by embedded inhomogeneities in the E-polarization case may be computed. Hibbs and Jones (1973b) extended this method to consider a non-symmetric, non-uniform source, as well as aperiodic spatially time-varying sources (Hibbs and Jones, 1974). Rikitake (1975) investigated electromagnetic induction in the earth for a modulated inducing field and showed the possibility of appreciable error in electrical conductivity estimation due to the contamination of long period variations in the geomagnetic field by short period variations. The electromagnetic response of a two-dimensional, non-uniform earth to an oscillating magnetic dipole source was solved numerically by Stoyer and Greenfield (1976) using a transmission line analogy. Hibbs and Jones (1976a,b) have given a method for modelling any arbitrary two-dimensional source field.

The use of two-dimensional arrays of magnetic field measuring instruments covering large areas of the earth such as the Western United States and Canada (Porath et al., 1970; Reitzel et al., 1970; Camfield et al., 1971; Porath et al., 1971; Porath and Gough, 1971; Camfield, 1973; Camfield and Gough, 1975; and Alabi et al., 1975), South-eastern Australia (Bennett and Lilley, 1972; Lilley and Bennett, 1972; Gough et al., 1974; Bennett and Lilley, 1973; Bennett and Lilley, 1974; and Lilley, 1976) and

Africa (Gough et al., 1973; and de Beer et al., 1976) and studies related to the interpretation of array data (Lilley and Tammemagi, 1972; Tammemagi and Lilley, 1973; Gough, 1973; Frazer, 1974; Garland, 1975; and Lilley, 1975) have stimulated interest in the three-dimensional induction problem. Treumann (1970d) first showed that the Green's tensor could be used to obtain a solution to the three-dimensional problem. Jones and Pascoe (1972), in an extension of their two-dimensional finite difference method, obtained a solution for a three-dimensional buried conductivity inhomogeneity using a cubic mesh. This work was extended to grids of variable dimensions by Lines and Jones (1973). Hohmann (1975) extended his two-dimensional model theoretical solution to three-dimensions involving a dyadic Green's function. The theoretical solution was obtained in terms of an integral equation which was reduced to a matrix equation numerically soluble for the scattering current in the anomalous body. The electric and magnetic fields outside the body were found by integrating the appropriate half-space dyadic Green's function over the volume of the scattering current. Raiche (1974) and Raiche and Coggon (1975) approached the three-dimensional problem in the same manner. Howard (1975) studied the problem of a buried cylinder excited by a magnetic dipole in three-dimensions. Also, Weidelt (1975) used the Green's tensor method to calculate the electromagnetic induction effects

of a three-dimensional structure. Hibbs and Jones (1976c) have calculated the electromagnetic field response for various three-dimensional conductivity structures for a uniform, two-dimensional non-uniform and a horizontal dipole source.

1.3 Transfer Functions

The use of transfer functions for the detection of anomalous internal currents originated in the work of Parkinson (1959) and was further advanced by Wiese (1962). Parkinson (1959) observed an empirical relationship between the temporal variation of the horizontal ($\Delta X_T, \Delta Y_T$) and vertical (ΔZ_T) magnetic field components. This linear relationship

$$\Delta Z_T = A \Delta X_T + B \Delta Y_T \quad (1.3)$$

where A and B are constants to be determined, has come to be known as the "Parkinson Relationship". Schmucker (1970) extended the original work and provided a formal theoretical approach to the description of the anomalous fields in terms of transfer functions and described both induction (or Parkinson arrows) as well as perturbation arrows. Everett and Hyndman (1967) introduced a unit vector method of transfer function estimation and Cochrane and Hyndman (1970) and Hyndman and Cochrane (1971) simplified the calculation by substituting the observed field components in place of the normal field components in the calculations.

Edwards et al. (1971) presented another approach to the transfer function calculation in which they considered magnetic correlation (M) vectors, and plotted Parkinson arrows for stations in the British Isles. Honkura (1971) compared experimentally computed induction arrows using data from Miyake-jima island with a theoretical model calculation of the arrows. Lilley (1974) analyzed the mathematical formalism of Schmucker (1970) in terms of an "induction tensor", and compared its characteristics for two- and three-dimensional cases. The time variation of induction arrows was studied by Anderson (1975) for the U.L.F. frequency band (1-100 mHz). Serious distortions in the inferred induction arrow directions due to source field variations were shown by Anderson et al. (1976a,b).

Weidelt (1975) calculated induction arrows for a theoretical model of an embedded anomaly using two mutually perpendicular polarizations of the external electromagnetic field to construct his arrows. Hibbs and Jones (1976d,e) have calculated theoretical induction and perturbation arrows for uniform and two-dimensional non-uniform source fields oriented in various directions relative to an embedded three-dimensional anomaly. A similar calculation has been made (Hibbs and Jones, 1976f) for a horizontal dipole source over a highly conducting anomaly for two dipole positions.

The work of this thesis is primarily concerned with finding solutions to the three-dimensional local induction problem for various source configurations and determining the source effect for each source type on the transfer functions which are calculated from these solutions. A comparison of theoretical solutions with an analogue model equivalent for different source field types is also presented.

CHAPTER 2

SOLUTION OF THE THREE-DIMENSIONAL LOCAL INDUCTION PROBLEM FOR ONE, TWO AND THREE DIMENSIONAL SOURCE FIELDS

In this chapter a method of solution for the three-dimensional local electromagnetic induction problem for laterally non-uniform conductivity distributions is given. The general local induction problem as described by Price (1950) is discussed. The solutions for three source configurations (uniform, two dimensional non-uniform and a horizontal dipole) above a uniform layered conductor are presented. In the method, these solutions are used to give boundary conditions for the Lines and Jones (1973) finite difference technique from which the solutions for the electromagnetic fields associated with three-dimensional conductivity inhomogeneities are obtained. The conductivity structures, which differ for each source configuration used, are chosen to represent varying degrees of symmetry and conductivity contrasts. For each combination the source frequency is chosen such that the amplitudes of the electromagnetic field components presented will have large values.

2.1 The General Three-Dimensional Local Electromagnetic Induction Problem

Price (1950) treated the general theory of the induction and of free decay of electric currents in a semi-

infinite conductor with a plane boundary. Two fundamental types of solutions were found and physical explanations for these were presented by him. Methods of calculating induced fields and their current systems corresponding to external inducing magnetic fields were obtained.

The mathematical development here follows closely that given by Price (1950), with the exception that the M.K.S. system of units is used throughout. For a continuous medium the behavior of the electromagnetic fields is described by Maxwell's equations

$$\nabla \times \underline{H} = \underline{J} + \frac{\partial \underline{D}}{\partial t} \quad (2.1)$$

$$\nabla \times \underline{E} = - \frac{\partial \underline{B}}{\partial t} \quad (2.2)$$

Together with the relations

$$\nabla \cdot \underline{B} = 0, \quad \nabla \cdot \underline{J} = - \frac{\partial \rho}{\partial t}, \quad \nabla \cdot \underline{D} = \rho \quad (2.3)$$

where ρ is the volume distribution of charge. In the isotropic and uniform media which are considered throughout this work

$$\underline{B} = \mu \underline{H}, \quad \underline{J} = \sigma \underline{E}, \quad \underline{D} = \epsilon \underline{E} \quad (2.4)$$

where the permeability, μ , the conductivity, σ , and the permittivity, ϵ , are constants.

Operating on both sides of equation (2.1) with the divergence operator and using the appropriate substitution

from (2.4) gives

$$\nabla \cdot \left(\frac{\sigma}{\epsilon} \underline{D} \right) + \nabla \cdot \left(\frac{\partial \underline{D}}{\partial t} \right) = 0 \quad (2.5)$$

and by using (2.3) we have

$$\frac{\sigma}{\epsilon} \rho + \frac{\partial \rho}{\partial t} = 0 \quad (2.6)$$

The solution of equation (2.6) is

$$\rho = \rho_0 e^{-\frac{\sigma}{\epsilon} t}, \quad (2.7)$$

which shows that any initial volume charge distribution (ρ_0) in the conductor disperses at a rate which is not influenced by other field conditions. Therefore, inside a uniform conductor the volume charge can be neglected without loss of generality if the relaxation time constant satisfies the condition

$$\frac{\epsilon}{\sigma} \ll 1 \quad (2.8)$$

We have, then,

$$\nabla \cdot \underline{E} = 0 \quad (2.9)$$

By taking the curl of (2.1) and substituting the expressions obtained for $\nabla \times \underline{E}$ into (2.2) or alternatively by taking the curl of (2.2) and substituting the expression obtained for $\nabla \times \underline{H}$ into (2.1), it can be shown that the electromagnetic field quantities satisfy an equation of the form

$$\nabla^2 G = \mu \left(\sigma \frac{\partial}{\partial t} + \epsilon \frac{\partial^2}{\partial t^2} \right) G \quad (2.10)$$

where G may be either \underline{E} or \underline{H} . In a conductor, when the time changes in the field are not too rapid, $\mu \epsilon \partial G / \partial t$ can be ignored when compared to $\mu \sigma G$. That is, displacement currents are negligible when compared to the conduction currents in the conductor. Garland (1971) discusses the conditions for which displacement currents may be neglected. From equation (2.1), if L and T are taken as the characteristic length and time of the variation of the electromagnetic field, $\partial \underline{D} / \partial t$ is of the order $\epsilon \underline{E} / T$ and $\nabla \times \underline{E}$ is of the order $\underline{E} / L = -\mu \underline{H} / T$. It follows that $\partial \underline{D} / \partial t$ is of the order $\mu \epsilon \underline{H} L / T^2$. Also $\nabla \times \underline{H}$ is of the order \underline{H} / L . For $\partial \underline{D} / \partial t$ to be negligible in comparison with $\nabla \times \underline{H}$

$$\epsilon \mu \underline{H} \frac{L}{T^2} \ll \frac{\underline{H}}{L} \quad (2.11)$$

or
$$T \gg (\mu \epsilon)^{1/2} L \quad (2.12)$$

Hence, the characteristic time must be great compared to the time of travel of the electromagnetic wave across the region. For a characteristic length equal to the diameter of the earth the characteristic time must be much less than 0.03 seconds. In all problems considered in this work the above condition is satisfied. Equation (2.10) then reduces to the diffusion equation

$$\nabla^2 G = \mu \sigma \frac{\partial G}{\partial t} \quad (2.13)$$

in the conducting region.

In a dielectric σ is negligibly small and equation (2.10) becomes

$$\nabla^2 G = \mu \epsilon \frac{\partial^2 G}{\partial t^2} \quad (2.14)$$

where the electromagnetic effects propagate with speed $(\mu \epsilon)^{1/2}$ through the region. Induction fields vary in a relatively slow manner, so that the time of travel across any portion of the dielectric, within the region considered, is negligibly small compared with the time taken for field changes to become effective at the point of interest. Hence, for a dielectric, equation (2.14) reduces to

$$\nabla^2 G = 0 \quad (2.15)$$

The above approximations are equivalent to ignoring the magnetic effects of the displacement current in both the conductor and the dielectric. Although the magnetic effects of $\partial \underline{D} / \partial t$ are negligible, this does not imply that the physical effects of the displacement current can be ignored. Since $\text{curl } \underline{H}$ is zero, \underline{H} can be approximately derived from a scalar potential,

$$\underline{H} = - \nabla \Omega, \quad (2.16)$$

where Ω satisfies Laplace's equation. Equation (2.3) shows that \underline{B} is everywhere solenoidal and hence derivable from a vector potential \underline{A} defined by

$$\underline{B} = \nabla \times \underline{A} \quad (2.17)$$

Substituting this into (2.2) and using the vector identity $\nabla \times (-\nabla\phi) = 0$, gives

$$\underline{E} = - \frac{\partial \underline{A}}{\partial t} - \nabla\phi \quad . \quad (2.18)$$

\underline{A} and ϕ satisfy the fundamental equation (2.10) if they satisfy the relation.

$$\nabla \cdot \underline{A} + \mu\epsilon \frac{\partial \phi}{\partial t} + \mu\sigma\phi = 0 \quad (2.19)$$

Although the electromagnetic field vectors \underline{E} and \underline{B} can be determined when \underline{A} and ϕ are known, the functions \underline{A} and ϕ are not uniquely defined since the electromagnetic fields are invariant under the gauge transformation. However, in a particular problem, any solution of \underline{A} and ϕ can be used to find the unique fields which satisfy the prescribed boundary conditions.

The electromagnetic field quantities must also satisfy certain boundary conditions. The tangential components of \underline{E} and \underline{H} and the normal component of \underline{B} are continuous across the interface between any two media. The normal components of \underline{D} and \underline{J} are not in general continuous and the sum of their components normal to the interface are ρ and $-\frac{\partial \rho}{\partial t}$, respectively.

2.2 Elementary Solutions of Maxwell's Equations for a Semi-Infinite Conductor With a Plane Boundary

The coordinate system is shown in Fig. 2.1. The region $-|h| < z < 0$ is a free space region with conductivity zero. A conductor occupies the half-space $z > 0$ and it is assumed that a current source of some form is located at or above $z = -|h|$.

Since the tangential components of \underline{E} and \underline{H} are continuous at the surface, $z=0$, and the conductivity, σ , and permeability, μ , are not, the elementary solutions of \underline{E} and \underline{H} can be expressed in the form $Z(z,t) \underline{F}(x,y)$. The variable t occurs only in Z because $\frac{\partial}{\partial t}$ is multiplied by $\mu\sigma$ in equation (2.13). Substituting

$$\underline{E} = Z(z,t) \underline{F}(x,y) \quad (2.20)$$

into (2.9), (2.10) and (2.15)

$$Z \left(\frac{\partial^2 \underline{F}}{\partial x^2} + \frac{\partial^2 \underline{F}}{\partial y^2} \right) + \underline{F}_z \frac{\partial Z}{\partial z} = 0 \quad (2.21)$$

$$\frac{\partial^2 \underline{F}}{\partial x^2} + \frac{\partial^2 \underline{F}}{\partial y^2} = \frac{1}{Z} \left(\mu\sigma \frac{\partial Z}{\partial t} - \frac{\partial^2 Z}{\partial z^2} \right) \underline{F} \quad \text{for } z > 0, \quad (2.22)$$

and
$$\frac{\partial^2 \underline{F}}{\partial x^2} + \frac{\partial^2 \underline{F}}{\partial y^2} = -\frac{1}{Z} \frac{\partial^2 Z}{\partial z^2} \underline{F} \quad \text{for } z < 0. \quad (2.23)$$

Since the coefficients of \underline{F} on the right hand of (2.22) and (2.23) are independent of x or y they can be represented by a real constant, $-\lambda^2$, so that

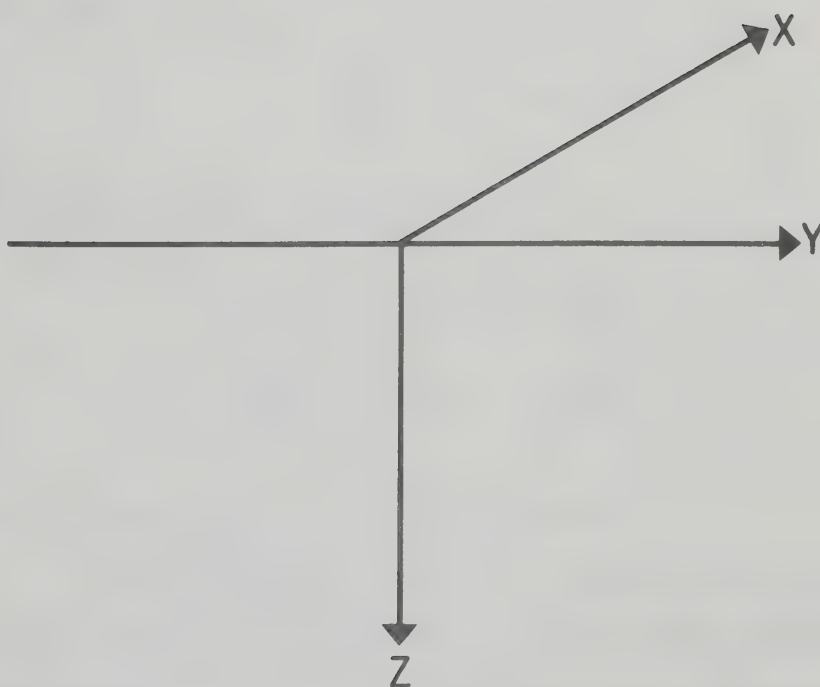


Figure 2.1 The coordinate system. X-Y plane represents the surface of the semi-infinite half-space conductor with a plane boundary.

$$\frac{\partial^2 \underline{F}}{\partial x^2} + \frac{\partial^2 \underline{F}}{\partial y^2} + \lambda^2 \underline{F} = 0 \quad (2.24)$$

It will be seen from equation (2.23) that the constant is necessarily negative.

For the conductor

$$\frac{\partial^2 \underline{Z}}{\partial z^2} - \lambda^2 \underline{Z} - \mu\sigma \frac{\partial \underline{Z}}{\partial t} = 0 \quad (2.25)$$

and for the dielectric

$$\frac{\partial^2 \underline{Z}}{\partial z^2} - \lambda^2 \underline{Z} = 0 \quad (2.26)$$

From (2.21) it follows that either

$$\underline{F}_z = 0 \quad \text{and} \quad \frac{\partial \underline{F}_x}{\partial x} + \frac{\partial \underline{F}_y}{\partial y} = 0 \quad (2.27)$$

$$\text{or} \quad \frac{1}{\underline{F}_z} \left(\frac{\partial \underline{F}_x}{\partial x} + \frac{\partial \underline{F}_y}{\partial y} \right) = - \frac{1}{\underline{Z}} \frac{\partial \underline{Z}}{\partial z} = + \alpha \quad (2.28)$$

where α is any real or complex constant.

The elementary solutions corresponding to (2.27) and (2.28) are of two types: the first type corresponds to current systems in the conductor which have magnetic fields outside and the second type has magnetic fields which are entirely confined within the conductor.

2.2.1 Elementary Solutions of the First Type

From (2.24) it is seen that \underline{F} may be written in the form

$$\underline{E} = \left(\frac{\partial P}{\partial y}, -\frac{\partial P}{\partial x}, 0 \right) \quad (2.29)$$

where P is a function of x and y which from (2.24) must satisfy the relation

$$\frac{\partial^2 P}{\partial x^2} + \frac{\partial^2 P}{\partial y^2} + \lambda^2 P = 0 \quad (2.30)$$

From (2.26) the form of Z in the dielectric must be

$$Z = A(t)e^{-\lambda z} + B(t)e^{+\lambda z}$$

so that

$$\underline{E} = \{A(t)e^{-\lambda z} + B(t)e^{+\lambda z}\} \left(\frac{\partial P}{\partial y}, -\frac{\partial P}{\partial x}, 0 \right) \text{ for } z < 0 \quad (2.31)$$

Since the tangential components of \underline{E} are continuous at the surface, $z=0$, \underline{E} inside the conductor is of the form

$$\underline{E} = Z(z,t) \left(\frac{\partial P}{\partial y}, -\frac{\partial P}{\partial x}, 0 \right) \text{ for } z > 0 \quad (2.32)$$

$$\text{where } Z(+0,t) = A(t) + B(t) \quad (2.33)$$

The magnetic fields inside and outside the conductor can be found by using equation (2.2) which gives

$$-\frac{\partial \underline{B}}{\partial t} = \left(\frac{\partial Z}{\partial z} \frac{\partial P}{\partial x}, \frac{\partial Z}{\partial z} \frac{\partial P}{\partial y}, \lambda^2 Z P \right) \text{ for } z > 0 \quad (2.34)$$

$$\text{and } -\frac{\partial \underline{B}}{\partial t} = \lambda \nabla \{ (A(t)e^{-\lambda z} - B(t)e^{+\lambda z}) P \} \text{ for } z < 0 \quad (2.35)$$

The continuity of the tangential component of \underline{H} leads to the relation

$$\left. \frac{\partial Z}{\partial z} \right|_{z=+0} = -\lambda [A'(t) - B'(t)] \quad (2.36)$$

The field intensity in the conductor must tend to zero as z becomes large, so that

$$Z(z,t) \rightarrow 0 \quad \text{as} \quad z \rightarrow \infty \quad (2.37)$$

In the region $-|h| < z < 0$ the potential of the total magnetic field satisfies Laplace's equation and the elementary solution is of the form

$$\Omega = - \{A'(t)e^{-\lambda z} + B'(t)e^{+\lambda z}\} P(x,y) \quad (2.38)$$

where λ is real and positive (or zero) and P satisfies equation (2.30).

The part of Ω involving $e^{-\lambda z}$ corresponds to the source field over the region $z \leq -|h|$, that is the inducing field. The part involving $e^{+\lambda z}$ corresponds to the field arising from within the conductor, that is the induced field. Therefore $A'(t)$ in (2.38) can be regarded as a known function of the source. Comparing with equation (2.34) gives

$$\lambda A(t) = - \frac{\partial A'(t)}{\partial t} \quad \lambda B(t) = \frac{\partial B'(t)}{\partial t} \quad (2.39)$$

and $A(t)$ can be obtained.

Equations (2.33), (2.36) and (2.37) together with (2.25) determine $B(t)$ and $Z(z,t)$ uniquely in terms of $A'(t)$. The induced field will be completely determined if the initial conditions, $B(-0)$, are known. The induced field is thus expressed entirely in terms of solutions of the first type.

In these solutions the vertical component of \underline{E} and therefore the vertical current is everywhere zero. The induced currents flow parallel to the surface of the conductor.

2.2.2 Elementary Solutions of the Second Type

If equation (2.28) is satisfied then Z must be of the form

$$Z = C(t)e^{-\alpha Z} \quad (2.40)$$

In this case, inside the conductor from (2.25)

$$(\alpha^2 - \lambda^2)C(t) = \mu\sigma \frac{\partial C(t)}{\partial t} \quad (2.41)$$

so that $C(t) = C_0 e^{-\beta t} \quad (2.42)$

where $\beta = \frac{\lambda^2 - \alpha^2}{\mu\sigma} \quad (2.43)$

From (2.28) and (2.24) it can be shown that

$$F_x = -\frac{\alpha}{\lambda^2} \frac{\partial F_z}{\partial x} + \frac{\partial P_1}{\partial y}, \quad F_y = -\frac{\alpha}{\lambda^2} \frac{\partial F_z}{\partial y} - \frac{\partial P_1}{\partial x} \quad (2.44)$$

where P_1 is a function of x and y which satisfies (2.30). The terms involving P_1 lead to solutions of the first type and can be omitted. F_z also satisfies (2.30). Hence, by letting $F_z = \lambda P$ a second type of solution for \underline{E} of the form

$$\underline{E} = C_0 e^{-\beta t - \alpha z} \left(-\frac{\alpha}{\lambda} \frac{\partial P}{\partial x}, -\frac{\alpha}{\lambda} \frac{\partial P}{\partial y}, \lambda P \right) \quad \text{for } z > 0 \quad (2.45)$$

is found.

Outside the conductor Z satisfies (2.26) and comparing with (2.40) it is apparent that $\alpha = \pm \lambda$ for $z < 0$.

\underline{E} is then of the form

$$\underline{E} = \nabla \{ A_1(t) e^{-\lambda z} + B_1(t) e^{+\lambda z} \} P(x, y) \quad \text{for } z < 0. \quad (2.46)$$

The corresponding magnetic field inside the conductor is of the form

$$\frac{\partial \underline{B}}{\partial t} = - c_0 e^{-\beta t - \alpha z} (\lambda - \alpha^2 / \lambda) \left(\frac{\partial P}{\partial y}, - \frac{\partial P}{\partial x}, 0 \right) \quad \text{for } z > 0. \quad (2.47)$$

Since \underline{E} is a vector outside the conductor

$$\frac{\partial \underline{B}}{\partial t} = 0 \quad \text{for } z < 0. \quad (2.48)$$

Therefore, solutions of the second type have no magnetic field outside the conductor and solutions of this type do not enter into the problem of finding currents induced by external magnetic fields. Solutions of this type correspond to the decay of current systems of a special form in the conductor. Freely decaying current systems corresponding to solutions of the first type can also be obtained by setting $A(t)$ to zero in (2.38). The modes of free decay are discussed in detail by Price (1950).

By using solutions of the first type, the local induction problem may be solved for uniform, two-dimensional, non-uniform and horizontal dipole sources over laterally homogeneous conductors. Solutions for the first two of these sources can be formulated in terms of the two-dimensional induction problem. The horizontal dipole source must be dealt with in a more general manner.

2.3 The Two-Dimensional Problem; E and H Polarizations

The coordinate system is as before (Fig. 2.1) with the region $-|h| < z < 0$ a free space region with conductivity equal to zero, and the conductor occupies the half-space $z > 0$. Again, it is assumed that a current source of some form is located at or above $z = -|h|$.

For an oscillating field with time dependence $e^{i\omega t}$ where ω is the angular frequency and the period $2\pi/\omega$ is sufficiently long so that displacement currents may be neglected, Maxwell's equations become:

$$\text{curl } \underline{H} = \sigma \underline{E} \quad (2.49)$$

$$\text{curl } \underline{E} = -i\omega\mu_0 \underline{H} \quad (2.50)$$

where σ is the conductivity appropriate for each region, μ_0 is the magnetic permeability of free space and the time factor $e^{(i\omega t)}$ is understood in all field quantities.

In the two-dimensional problem the fields do not vary in one direction, in this case the x-direction. That is all quantities are independent of x, and Maxwell's equations reduce to

$$\frac{\partial H_z}{\partial y} - \frac{\partial H_y}{\partial z} = \sigma E_x, \quad (2.51)$$

$$\frac{\partial H_x}{\partial z} = \sigma E_y, \quad (2.52)$$

$$-\frac{\partial H_x}{\partial y} = \sigma E_z, \quad (2.53)$$

$$\frac{\partial E_z}{\partial y} - \frac{\partial E_y}{\partial z} = i\omega\mu_0 H_x, \quad (2.54)$$

$$\frac{\partial E_x}{\partial z} = -i\omega\mu_0 H_y, \quad (2.55)$$

$$-\frac{\partial E_x}{\partial y} = -i\omega\mu_0 H_z. \quad (2.56)$$

These equations are such that only E_x , H_y and H_z are involved in (2.51, 2.55 and 2.56) and only H_x , E_y and E_z are involved in (2.52, 2.53 and 2.54). These two separate sets of equations can therefore be solved independently.

Combining (2.51), (2.55) and (2.56) we obtain

$$\frac{\partial^2 E_x}{\partial y^2} + \frac{\partial^2 E_x}{\partial z^2} = i\omega\mu_0 \sigma E_x \quad (2.57)$$

which is the equation to be solved in all regions for the E-polarization case (the case in which the electric field is parallel to any conductivity discontinuities).

Combining (2.52), (2.53) and (2.54) a similar equation is obtained for the H-polarization case (the case in which the magnetic field is parallel to any conductivity discontinuities):

$$\frac{\partial^2 H_x}{\partial y^2} + \frac{\partial^2 H_x}{\partial z^2} = i\omega\mu_0 \sigma H_x. \quad (2.58)$$

With the proper values of σ inserted for each conductive region, and with the proper boundary conditions, these equations can be solved for the two separate cases to obtain the field distributions. For the E-polarization, E_x

is determined from the solution of (2.57), and then (2.55) and (2.56) may be used to calculate the two non-zero magnetic field components associated with this case. Also, for the H-polarization, H_x may be determined from (2.58), and equations (2.52) and (2.53) may be used to obtain the appropriate electric field components.

2.3.1 Determinacy of the Two-Dimensional Problem

Not all two-dimensional problems are determinate. It is important to examine the conditions for determinacy for a periodic inducing field over a semi-infinite uniform conductor with a plane boundary occupying the half-space $z > 0$. Following Price (1950), we let E_x be of the form

$$E_x = Z(z) \cdot Y(y) \cdot e^{i\omega t} \quad (2.59)$$

and substitution of this expression for E_x into equation (2.57) gives:

$$\frac{\partial^2 Y}{\partial y^2} = \frac{1}{Z} \{ i\omega\mu_0 \alpha Z - \frac{\partial^2 Z}{\partial z^2} \} Y \quad (2.60)$$

for $z > 0$, and

$$\begin{aligned} \frac{\partial^2 Y}{\partial y^2} &= - \frac{1}{Z} \frac{\partial^2 Z}{\partial z^2} Y \\ \frac{\partial^2 Y}{\partial y^2} &= - \left(\frac{1}{Z} \right) \cdot \left(\frac{\partial^2 Z}{\partial z^2} \right) \cdot Y \end{aligned} \quad (2.61)$$

for $z < 0$, where the arguments for Y and Z have now been dropped.

Since the coefficients of Y on the right hand side of (2.60) and (2.57) are independent of x and y they must be constants, $-\lambda^2$, where λ is real, positive and non-zero such that

$$\frac{\partial^2 Y}{\partial y^2} = -\lambda^2 Y \quad (2.62)$$

Therefore, in the region $z > 0$

$$\frac{\partial^2 Z}{\partial z^2} - (i\omega\mu_0\sigma + \lambda^2)Z = 0 \quad (2.63)$$

and
$$Z(z) = A e^{-\theta z} + B e^{\theta z} \quad (2.64)$$

where $\theta^2 = i\omega\mu_0\sigma + \lambda^2$ and A and B are constants. In the region $z < 0$,

$$\frac{\partial^2 Z}{\partial z^2} - \lambda^2 Z = 0 \quad (2.65)$$

and
$$Z(z) = a e^{-\lambda z} + b e^{\lambda z}, \quad (2.66)$$

where a and b are constants. The corresponding E field is then

$$E_x = \{A e^{-\theta z} + B e^{\theta z}\}Y \quad (2.67)$$

for $z > 0$, and
$$E_x = \{a e^{-\lambda z} + b e^{\lambda z}\}Y \quad (2.68)$$

for $z < 0$.

As z becomes large, E_x must tend to zero so that B must be zero. At the boundary $z=0$, E_x must be continuous, and so

$$A = a + b \quad (2.69)$$

The corresponding magnetic fields are obtained from (2.55) and (2.56) for $z > 0$:

$$H_y = \frac{i}{\omega\mu_0} \frac{\partial E_x}{\partial z} = - \frac{i\theta A}{\omega\mu_0} e^{-\theta z} \cdot Y \quad (2.70)$$

$$H_z = - \frac{i}{\omega\mu_0} \frac{\partial E_x}{\partial y} = - \frac{iA}{\omega\mu_0} e^{-\theta z} \frac{\partial Y}{\partial y} ; \quad (2.71)$$

and for $z < 0$:

$$H_y = - \frac{i\lambda}{\omega\mu_0} \{a e^{-\lambda z} - b e^{\lambda z}\} Y \quad (2.72)$$

$$H_z = - \frac{i}{\omega\mu_0} \{a e^{-\lambda z} + b e^{\lambda z}\} \frac{\partial Y}{\partial y} \quad (2.73)$$

The tangential component of the magnetic field must be continuous across the boundary $z=0$, which leads to the relation

$$\theta A = \lambda(a - b) \quad . \quad (2.74)$$

The scalar potential Ω of the total magnetic field in the region $-|h| < z < 0$ satisfies Laplace's equation and is of the form

$$\Omega = -\{C e^{-\lambda z} + D e^{\lambda z}\} P(y) \quad (2.75)$$

where $P(y)$ satisfies the equation $\partial^2 P(y) / \partial y^2 = -\lambda^2 P(y)$.

Since the conductivity outside the conductor is zero

$$\nabla \times \underline{H} = 0 \quad (2.76)$$

and H_y and H_z can be found from the relation

$$\underline{H} = - \nabla \Omega \quad (2.77)$$

$$\text{as:} \quad H_y = \{C e^{-\lambda z} + D e^{\lambda z}\} \frac{\partial P(y)}{\partial y} \quad (2.78)$$

$$H_z = - \lambda \{C e^{-\lambda z} - D e^{\lambda z}\} P(y) \quad (2.79)$$

Equating (2.72) and (2.78) gives:

$$- \frac{i \lambda a}{\omega \mu_0} = C \quad \frac{i \lambda b}{\omega \mu_0} = D \quad Y(y) = \frac{\partial P(y)}{\partial y} \quad (2.80)$$

Combining (2.69), (2.74) and (2.80) gives:

$$D = \left\{ \frac{\theta - \lambda}{\theta + \lambda} \right\} C \quad , \quad (2.81)$$

$$a = \frac{i \omega \mu_0}{\lambda} \left\{ \frac{\theta + \lambda}{\theta - \lambda} \right\} D \quad , \quad (2.82)$$

$$b = - \left\{ \frac{\theta - \lambda}{\theta + \lambda} \right\} a \quad , \quad (2.83)$$

$$\text{and} \quad A = - \frac{2 \lambda b}{\theta - \lambda} \quad (2.84)$$

Therefore by specifying C all the other quantities will be determined. This analysis, while confined to uniform subsurfaces, can be extended to multi-layered cases.

The part of Ω in (2.75) which involves $e^{-\lambda z}$ corresponds to the inducing field of the current sources and the part which involves $e^{\lambda z}$ corresponds to the field of the induced currents. It can be assumed that the inducing field potential is specified by the current distribution so that $C e^{-\lambda z} \cdot P(y)$ is known. From the preceding discussion it can be seen that all other fields and potentials are determined

from the inducing field. Therefore the problem is determinate for λ positive and non-zero. The H-polarization case can be shown to be determinate in the same manner. For $\lambda = 0$ the problem becomes indeterminate, that is the induced field cannot in general be specified in terms of the inducing field, as discussed by Price (1950).

2.4 The Uniform Source Two-Dimensional Solution

The form of the total electric or magnetic field for the uniform source for either the E or H polarization case can be found from the solution of equation (2.57) or (2.58). Considering first the H-polarization case, for a uniform conductor $\frac{\partial H_x}{\partial y} = 0$ and (2.58) reduces to

$$\frac{\partial^2 H_x}{\partial z^2} = i\omega\mu_0\sigma H_x \quad \text{for } z > 0 \quad (2.85)$$

This, together with the boundary condition that H_x tends to zero as $z \rightarrow \infty$ leads to the solution

$$H_x = H_0 e^{-1/\sqrt{2}(1+i)(\omega\mu_0\sigma)^{1/2}z} \quad (2.86)$$

inside the conductor.

By virtue of equations (2.52) and (2.53), H_x in the region outside the conductor, where $\sigma=0$, is independent of both y and z and is, therefore, uniform throughout this region. The H field is continuous across the surface boundary, and so H_x is constant everywhere just inside the surface of the conductor. This implies that $\partial H_x / \partial y$ is zero

just inside this surface and therefore from (2.53) that σE_z is zero. This agrees with the fact that normal component of current must be zero at the surface. If (2.58) is solved with the appropriate value of σ and the boundary conditions on H_x , then the required conditions on \underline{E} in the conductor will be satisfied.

In the E polarization case, only the field components E_x , H_y and H_z are involved, and E_x satisfies (2.57). Again, for a uniform conductor, $\frac{\partial E_x}{\partial y} = 0$ and (2.57) reduces to

$$\frac{\partial^2 E_x}{\partial z^2} = i\omega\mu_0\sigma E_x \quad (2.87)$$

Inside the conductor the solution for E_x is of the form

$$E_x = E_0 e^{-1/\sqrt{2}(1+i)(\omega\mu_0\sigma)^{1/2}z} \quad \text{for } z > 0 \quad (2.88)$$

From equation (2.56) it can be seen that H_z is zero. By substituting (2.88) into (2.55) the solution for H_y can be found inside the conductor.

$$i\omega\mu_0 H_y = \frac{1}{\sqrt{2}} (1+i)(\omega\mu_0\sigma)^{1/2} E_0 e^{-1/\sqrt{2}(1+i)(\omega\mu_0\sigma)^{1/2}z} \quad \text{for } z > 0 \quad (2.89)$$

In the non-conducting region $\partial H_y / \partial z$ goes to zero by virtue of equation (2.51). This means that H_y must be constant

(say H_0) with respect to z outside the conductor. Since H_y is continuous across the surface, from (2.89) we have

$$H_0 = \frac{1}{\sqrt{2}} (1 - i) \frac{(\omega\mu_0\sigma)^{1/2}}{\omega} E_0 \quad (2.90)$$

From (2.55) in the non-conductor

$$\frac{\partial E_x}{\partial z} = -i\omega\mu_0 H_0 \quad (2.91)$$

and
$$E_x = E_0 (1 - \frac{1}{\sqrt{2}} (1 + i)(\omega\mu_0\sigma)^{1/2} z) \quad (2.92)$$

Within the conductor all field quantities vanish as $z \rightarrow \infty$. Other boundary conditions are that E_x , H_y and H_z are continuous at $z=0$. As $z \rightarrow -\infty$, $|E|$ goes to infinity. This result is in accordance with an energy source which must exist at or beyond the plane $z = -|h|$. This analysis, while confined to uniform subsurfaces, can be extended to multi-layered cases.

In what follows, the E-polarization case is used throughout for the uniform source boundary conditions. By solving for the electric field in the two-dimensional calculations, these electric field solutions may be used directly in the Lines and Jones (1973) finite differences method to provide boundary and initial conditions for the mesh.

2.5 The Two-Dimensional Non-Uniform Source Solution

In this section a two-dimensional, non-uniform sheet current source with Gaussian current intensity distribution is discussed, and the solution for the electromagnetic field over a layered conductor is derived. In the next section (2.6) a method of using this solution to generate any arbitrary two-dimensional source configuration is given.

The coordinate system used is shown in Fig. 2.2. The layered conductor occupies the half-space $z > 0$ as shown. The sheet current source is assumed to flow parallel to the surface of the earth at a height $z = -|h|$. Following Peltier and Hermance (1971) and from equation (2.53), it can be shown that for a horizontally layered earth and for a symmetric current source the elementary electric field in the n -th layer is of the form

$$E_x^n = \{A_n e^{-\theta_n z} + B_n e^{\theta_n z}\} C(\lambda) \cos(\lambda y) \quad (2.93)$$

where
$$\theta_n^2 = \lambda^2 + i\omega\mu_0 \sigma_n$$

and λ , ω , μ_0 and σ_n are respectively the spatial wave number, the angular frequency, the permeability of free space and the conductivity of the n -th layer. For a sheet current with a Gaussian distribution function

$$C(\lambda) = - \frac{i I_0 \omega \mu_0 \kappa}{\sqrt{2\pi}(\lambda)} e^{(\lambda z_0 - \frac{\lambda^2 \kappa^2}{2})} \quad (2.94)$$

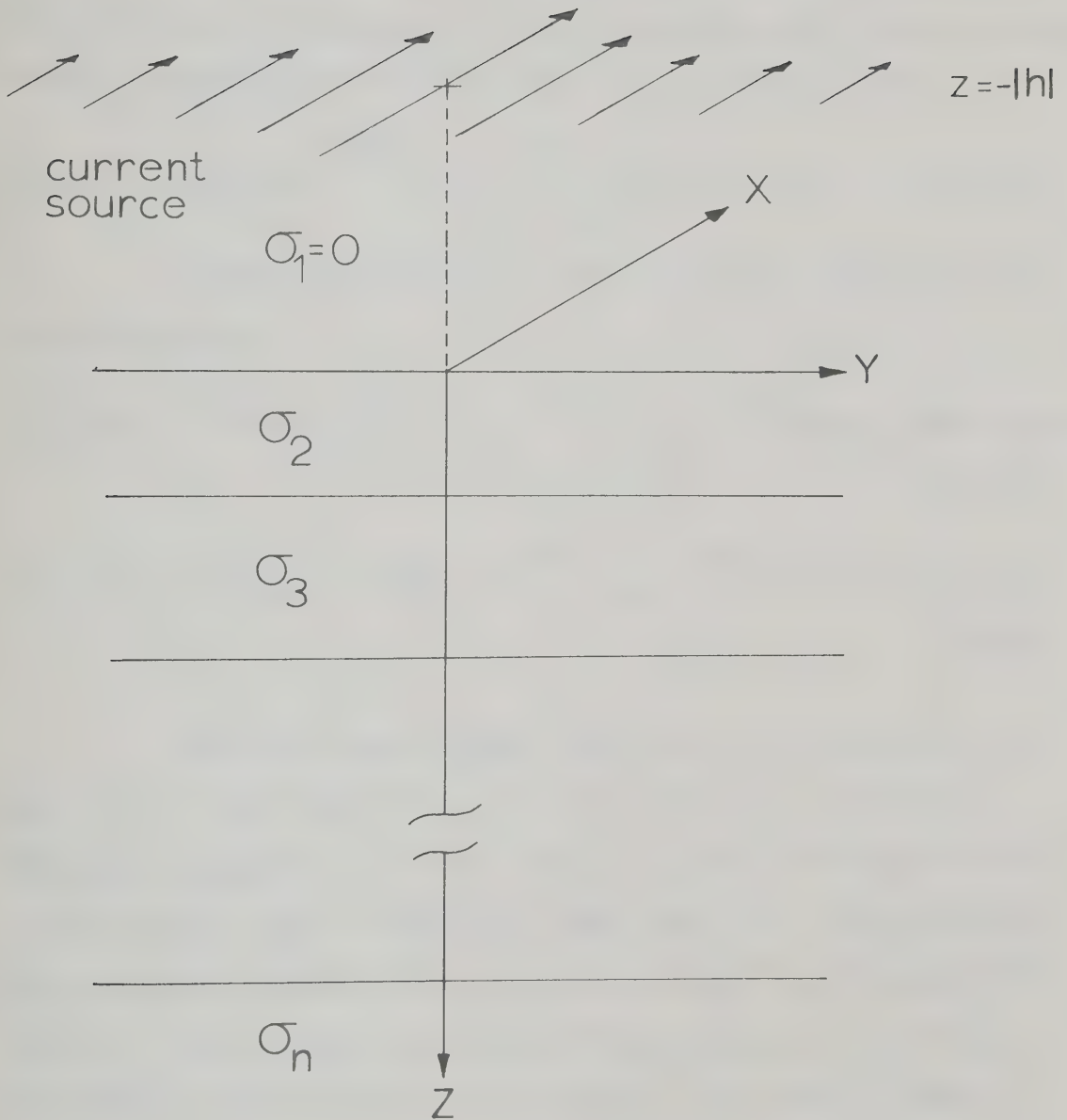


Figure 2.2 The coordinate system, source position and layered model.

where I_0 is the maximum intensity and κ is the standard deviation of the source.

The quantities A_n and B_n are determined by the conductivity configuration and the solution for the electric field is completed by taking the sum of E_x^n over all λ :

$$E_x(y,z) = \int_0^{\infty} \{A_n e^{-\theta_n z} + B_n e^{\theta_n z}\} C(\lambda) \cos(\lambda y) d\lambda \quad (2.95)$$

After calculating E_x , the magnetic components may be determined:

$$H_y(y,z) = - (i/\omega\mu_0) \int_0^{\infty} \{\theta_n [A_n e^{-\theta_n z} - B_n e^{\theta_n z}] C(\lambda)\} \cdot \cos(\lambda y) d\lambda \quad (2.96)$$

$$H_z(y,z) = (i/\omega\mu_0) \int_0^{\infty} \{\lambda [A_n e^{-\theta_n z} + B_n e^{\theta_n z}] C(\lambda)\} \sin(\lambda y) d\lambda \quad (2.97)$$

The half-space above the Earth is considered as the first layer, and if $A_1 = 1$ then $C(\lambda)$ is a frequency dependent parameter of the source. B_1 may be thought of as a reflection coefficient which represents the contribution to the total electric field at the surface by the sub-surface layers. For a three layered conductor $B_4 = 0$ so that E_x^4 will not become infinite with depth. The other A_n and B_n values may be determined since the tangential components of E_x^n and H_y^n must be continuous across layer boundaries. This gives

$$B_1 = \frac{R - 1}{R + 1} \quad (2.98)$$

where

$$R = \frac{\lambda(Q + 1)}{\theta_2(Q - 1)},$$

$$Q = \left[\frac{\theta_2 + \theta_3 + (\theta_2 - \theta_3)Q_1 e^{2\theta_3 d_1}}{\theta_2 - \theta_3 + (\theta_2 + \theta_3)Q_1 e^{2\theta_3 d_1}} \right] e^{2\theta_2 d_1}$$

and

$$Q_1 = \left[\frac{\theta_3 - \theta_4}{\theta_3 + \theta_4} \right] e^{-2\theta_3 d_2},$$

where d_1 and d_2 are the thicknesses of the first and second conducting layers respectively. Also, we have

$$A_2 = \frac{(1 + B_1)Q}{Q + 1},$$

$$B_2 = \frac{1}{Q} A_2, \quad (2.99)$$

$$A_3 = \frac{\{A_2 + B_2 e^{2\theta_2 d_1}\} e^{(\theta_3 - \theta_2)d_1}}{(1 + Q_1) e^{2\theta_3 d_1}},$$

and

$$B_3 = A_3 Q_1$$

$$A_4 = \{A_3 + B_3 e^{2\theta_3 d_2}\} e^{(\theta_4 - \theta_3)d_2}.$$

This general method may be extended to more layers if desired. It should also be pointed out that the convergence of the field integrals is discussed by Hermance and Peltier (1970) and Peltier and Hermance (1971).

The above solutions are limited in that only source configurations for which the source coefficients $C(\lambda)$ as

described by Peltier and Hermance (1971) are obtained analytically could be modelled. It is clear that more general source configurations exist, particularly in high latitude regions (Kisabeth and Rostoker, 1971 ; Kisabeth, 1972).

2.6 A Method for Obtaining an Arbitrary Two-Dimensional Source

A method in which any arbitrary two-dimensional source configuration may be represented is desirable and in this section such a method is given. This method provides field values for a layered earth, and more general problems may be studied by using these values as boundary conditions for a numerical technique. The computer program listing for this method and description of its use are given in Appendix A.

A general source intensity distribution may be constructed from a number of elementary sources by superposition. A Gaussian intensity distribution of small half-width (1 - 10 km) has been chosen here as the elementary source, since $C(\lambda)$ can be obtained analytically for this distribution. A number of these elementary Gaussian sources of equal maximum intensity are then spatially shifted so that a rectangular current intensity distribution may be approximated. The electric and magnetic field values are then obtained by superimposing the spatially shifted fields of the elemental sources.

In this way an arbitrary current intensity distribution may be approximated in a piecewise continuous manner by weighting a number of spatially shifted rectangular current distributions in accordance with the trapezoidal rule where the field components are spatially shifted and superimposed. The solution for a two-dimensional source of arbitrary intensity distribution over a layered Earth may thus be approximated. This is equivalent to convolving the arbitrary current distribution with the Green's Function of the rectangular current distribution.

The arbitrary current source could be approximated by directly shifting and summing the elemental Gaussian field solutions using a criterion such as a least squares process to weight the Gaussians. However, this would increase the number of computations required by a factor equal to the number of Gaussians used to construct the rectangular current source distribution and so is not desirable.

Because of its simplicity, the method is readily applied to modelling problems. The width of the rectangular distribution and therefore the half-width of the elemental Gaussian can be easily estimated by linearly approximating the arbitrary current source to the desired accuracy. As many elemental Gaussians as desired can be used to represent the rectangular distribution and for the examples here 3 and 31 Gaussians have been used.

2.6.1 Comparison of Piecewise Continuous Representations and Analytically Integrated Kernel Calculations

In order to obtain an indication of how well the elemental Gaussian and rectangular representation of a source will approximate the solution for a case in which $C(\lambda)$ may be represented analytically several comparisons are made. It is advantageous to represent the rectangular current distribution using as few elemental Gaussian currents as possible. To determine the number that may be used a comparison of the field values calculated by using 3 elemental Gaussians with those calculated by 31 elemental Gaussians to represent the same rectangular source was made. Calculations of the field values at the surface of a two-layered Earth in which a 50 km layer of 100 ohm-m resistivity overlays a half-space of resistivity 10 ohm-m at three frequencies (1.0 Hz, 0.01 Hz and 0.0001 Hz) were made for Gaussian sheet current intensity distributions with half-widths equal to 0.968 km and 10.0 km. A rectangular current distribution of 30 km width was approximated by 31 of the 0.968 km elemental Gaussian currents spatially shifted one kilometer and compared with a representation of the 30 km rectangular current composed of 3 elemental Gaussian currents of 10 km half-width shifted one half-width. The results are shown in Tables 2.1 and 2.2. The horizontal components are normalized at the origin in both tables, whereas H_z is normalized at 15 km in Table 2.1 and 400 km in Table 2.2.

Comparison of Gaussian representations of rectangular sources near the origin

Frequency: 1 Hz						
Distance from origin (km)	E_x		H_y		H_z	
	3	31	3	31	3	31
0	1.0	1.0	1.0	1.0	0.0	0.1279×10^{-5}
15	0.9813	0.9833	0.9813	0.9833	1.0	1.0
30	0.9353	0.9360	0.9353	0.9359	1.838	1.821
60	0.7823	0.7839	0.7821	0.7837	2.593	2.582
90	0.6140	0.6158	0.6137	0.6156	2.405	2.404
120	0.4713	0.4729	0.4709	0.4726	1.902	1.905
150	0.3624	0.3637	0.3622	0.3635	1.409	1.413

Frequency: 0.01 Hz						
Distance from origin (km)	E_x		H_y		H_z	
	3	31	3	31	3	31
0	1.0	1.0	1.0	1.0	0.0	0.4178×10^{-6}
15	0.9878	0.9891	0.9852	0.9868	1.0	1.0
30	0.9572	0.9575	0.9487	0.9492	1.883	1.870
60	0.8490	0.8498	0.8246	0.8258	2.930	2.919
90	0.7156	0.7168	0.6818	0.6833	3.087	3.083
120	0.5870	0.5882	0.5525	0.5539	2.755	2.756
150	0.4767	0.4778	0.4465	0.4477	2.269	2.273

Frequency: 0.0001 Hz						
Distance from origin (km)	E_x		H_y		H_z	
	3	31	3	31	3	31
0	1.0	1.0	1.0	1.0	0.0	0.1225×10^{-6}
15	0.9931	0.9939	0.9845	0.9861	1.0	1.0
30	0.9759	0.9760	0.9462	0.9467	1.906	1.896
60	0.9127	0.9131	0.8913	0.8207	3.133	3.123
90	0.8295	0.8301	0.6805	0.6821	3.588	3.584
120	0.7420	0.7427	0.5624	0.5639	3.551	3.551
150	0.6588	0.6595	0.4705	0.4718	3.280	3.283

Table 2.1

Comparison of Gaussian representations of rectangular sources at great distances from the origin

Frequency: 1 Hz

Distance from origin (km)	E_x		H_y		H_z	
	3	31	3	31	3	31
0	1.0	1.0	1.0	1.0	0.0	0.8233×10^{-9}
400	0.07232	0.7293	0.07204	0.07265	1.0	1.0
800	0.01829	0.01842	0.01796	0.01809	0.1391	0.1391
1200	0.007588	0.007640	0.007248	0.007297	0.04297	0.04274

Frequency: 0.01 Hz

Distance from origin (km)	E_x		H_y		H_z	
	3	31	3	31	3	31
0	1.0	1.0	1.0	1.0	0.0	0.1222×10^{-9}
400	0.1110	0.1116	0.1052	0.1059	1.0	1.0
800	0.02912	0.02926	0.02742	0.02759	0.1472	0.1470
1200	0.01240	0.01246	0.01143	0.01149	0.04514	0.04504

Frequency: 0.0001 Hz

Distance from origin (km)	E_x		H_y		H_z	
	3	31	3	31	3	31
0	1.0	1.0	1.0	1.0	0.0	0.1133×10^{-6}
400	0.2493	0.2501	0.1707	0.1718	1.0	1.0
800	0.07675	0.07697	0.05785	0.05820	0.2019	0.2018
1200	0.03455	0.03465	0.02609	0.02625	0.06467	0.06463

Table 2.2

From the tables it is clear that the three 10 km elemental Gaussian currents well represent the rectangular current distribution in the calculation of the field values.

Also, in Tables 2.3 and 2.4 the fields associated with a Gaussian sheet current of 240 km half-width calculated in the manner of Peltier and Hermance (1971) and Hibbs and Jones (1973a) are compared with those of a 49 element piecewise continuous source constructed from 30 km rectangular current sources employing the two approximations as used above. The same subsurface and frequencies as in Tables 2.1 and 2.2 were used. E_x and H_y are normalized at the origin in both tables while H_z is normalized at 15 km in Table 2.3 and 400 km in Table 2.4.

Table 2.3 shows that for distances of 150 km or less from the origin the two solutions are nearly identical. Table 2.4 indicates that the two solutions differ as the distance from the origin increases. This is because the piecewise continuous source is terminated at 720 km whereas the Gaussian source continues to infinity. This is particularly evident in the H_z component which one would expect to increase when the current intensity changes rapidly.

A further comparison with previous results was made for a sheet current source of intensity distribution $(y-b) e^{\frac{1}{b}(y-b)}$ $u(y-b)$ where $b = -480$ km and $u(y-b)$ is the unit step function. Using the present method, the source was approximated by forty-nine rectangular sources

Comparison of Gaussian source and Piecewise continuous representations near the origin

Distance from origin (km)		Frequency: 1 Hz					
		E_x	H_y	H_z	H_z	H_z	Gauss
		31	31	3	31	31	
0	1.0	1.0	1.0	1.0	0.8476×10^{-3}	0.2364×10^{-4}	0.0
15	0.9985	0.9986	0.9985	0.9986	1.0	1.0	1.0
30	0.9946	0.9946	0.9946	0.9946	1.992	1.991	1.992
60	0.9785	0.9785	0.9785	0.9785	3.912	3.910	3.912
90	0.9523	0.9523	0.9523	0.9523	5.692	5.689	5.692
120	0.9170	0.9170	0.9169	0.9170	7.273	7.270	7.273
150	0.8737	0.8738	0.8736	0.8737	8.609	7.605	8.607

Distance from origin (km)		Frequency: 0.01 Hz					
		E_x	H_y	H_z	H_z	H_z	Gauss
		31	31	3	31	31	
0	1.0	1.0	1.0	1.0	0.2230×10^{-4}	0.2101×10^{-4}	0.0
15	0.9986	0.9988	0.9986	0.9987	1.0	1.0	1.0
30	0.9950	0.9950	0.9950	0.9950	1.992	1.991	1.992
60	0.9803	0.9803	0.9801	0.9801	3.917	3.915	3.917
90	0.9563	0.9563	0.9559	0.9559	5.710	5.707	5.710
120	0.9239	0.9239	0.9231	0.9231	7.315	7.312	7.314
150	0.8840	0.8840	0.8829	0.8829	8.687	8.684	8.686

Distance from origin (km)		Frequency: 0.0001 Hz					
		E_x	H_y	H_z	H_z	H_z	Gauss
		31	31	3	31	31	
0	1.0	1.0	1.0	1.0	0.9932×10^{-3}	0.1430×10^{-4}	0.0
15	0.9989	0.9990	0.9988	0.9989	1.0	1.0	1.0
30	0.9962	0.9962	0.9957	0.9957	1.994	1.993	1.994
60	0.9848	0.9848	0.9828	0.9828	3.929	3.928	3.929
90	0.9661	0.9661	0.9618	0.9618	5.752	5.750	5.752
120	0.9408	0.9408	0.9334	0.9333	7.414	7.411	7.413
150	0.9094	0.9094	0.8984	0.8984	8.874	8.871	8.872

Table 2.3

Comparison of Gaussian source and piecewise continuous representations at great distances from the origin

Frequency 1 Hz										
Distance from origin (km)	E_x		Gauss		H_y		Gauss		H_z	
	3	31	3	31	3	31	3	31	3	31
0	1.0	1.0	1.0	1.0	1.0	1.0	1.0	1.0	0.1947×10^{-5}	0.2919×10^{-5}
400	0.4041	0.4045	0.4096	0.4096	0.4037	0.4041	0.4097	0.4097	1.0	1.0
800	0.06458	0.06469	0.07317	0.07317	0.06384	0.06395	0.07313	0.07313	0.1510	0.1514
1200	0.02100	0.02102	0.02035	0.02035	0.02020	0.02022	0.02031	0.02031	0.02676	0.02679
Frequency: 0.01 Hz										
Distance from origin (km)	E_x		Gauss		H_y		Gauss		H_z	
	3	31	3	31	3	31	3	31	3	31
0	1.0	1.0	1.0	1.0	1.0	1.0	1.0	1.0	0.2205×10^{-5}	0.9748×10^{-6}
400	0.4397	0.4401	0.4445	0.4445	0.4361	0.4365	0.4416	0.4416	1.0	1.0
800	0.08547	0.08559	0.09277	0.09277	0.08359	0.08371	0.09197	0.09197	0.1862	0.1865
1200	0.02928	0.02931	0.02956	0.02956	0.02812	0.02815	0.02914	0.02914	0.03653	0.03657
Frequency: 0.0001 Hz										
Distance from origin (km)	E_x		Gauss		H_y		Gauss		H_z	
	3	31	3	31	3	31	3	31	3	31
0	1.0	1.0	1.0	1.0	1.0	1.0	1.0	1.0	0.1343×10^{-6}	0.1265×10^{-5}
400	0.5380	0.5383	0.5416	0.5416	0.5012	0.5015	0.5065	0.5065	1.0	1.0
800	0.1610	0.1611	0.1665	0.1665	0.1443	0.1444	0.1526	0.1526	0.3014	0.3017
1200	0.06354	0.06358	0.06584	0.06584	0.05889	0.05893	0.06104	0.06104	0.07950	0.07958

Table 2.4

of 30 km width. Each rectangular source was approximated by three elemental Gaussians of half-width 10 km and spatially shifted one half-width. These calculations were made over a range of periods from 1.0 sec to 10^6 sec for the same subsurface as above. The apparent resistivity (calculated in the manner of Cagniard, 1953) and phase curves for this case are shown in Figs. 2.3 and 2.4. The apparent resistivity curves are calculated for points at intervals of 200 km over the range from -10^3 to 10^3 km. The phase calculations illustrate the difference between the phase of E_x and the phase of H_y for the various frequencies at the different positions on the surface of the Earth beneath the source. The field profiles of E_x , H_y and H_z for 10, 10^3 and 10^5 sec period are shown in Fig. 2.5.

The apparent resistivity curves of Figs. 2.3 and 2.4 illustrate the typical spreading as a function of position at longer periods and compare well with those obtained previously (Hibbs and Jones, 1973b). A comparison of apparent resistivity curves is a good check on the accuracy of the method. Highly accurate field values are required to calculate the apparent resistivity curves since the field values are squared and a ratio taken. If the field values are inaccurate this produces spreading of the apparent resistivity curves at short period as well as incorrect values at long period. Also the field profiles for E_x and H_y of Fig. 2.5 compare favourably with previous

the first part of the paper, we shall consider the case of a single

variable, and then we shall consider the case of several

variables. In the first part of the paper, we shall consider the case of a single

variable, and then we shall consider the case of several

variables. In the first part of the paper, we shall consider the case of a single

variable, and then we shall consider the case of several

variables. In the first part of the paper, we shall consider the case of a single

variable, and then we shall consider the case of several

variables. In the first part of the paper, we shall consider the case of a single

variable, and then we shall consider the case of several

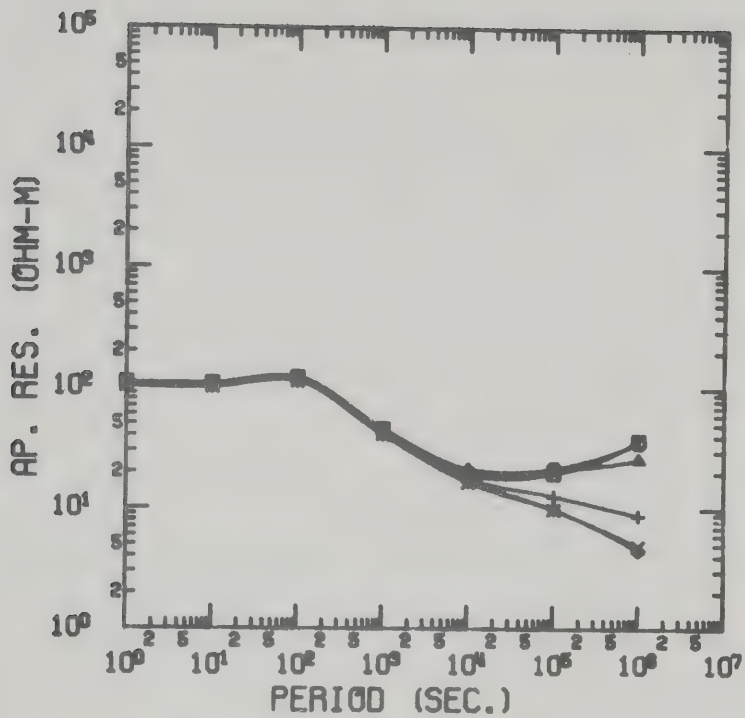
variables.

In the first part of the paper, we shall consider the case of a single

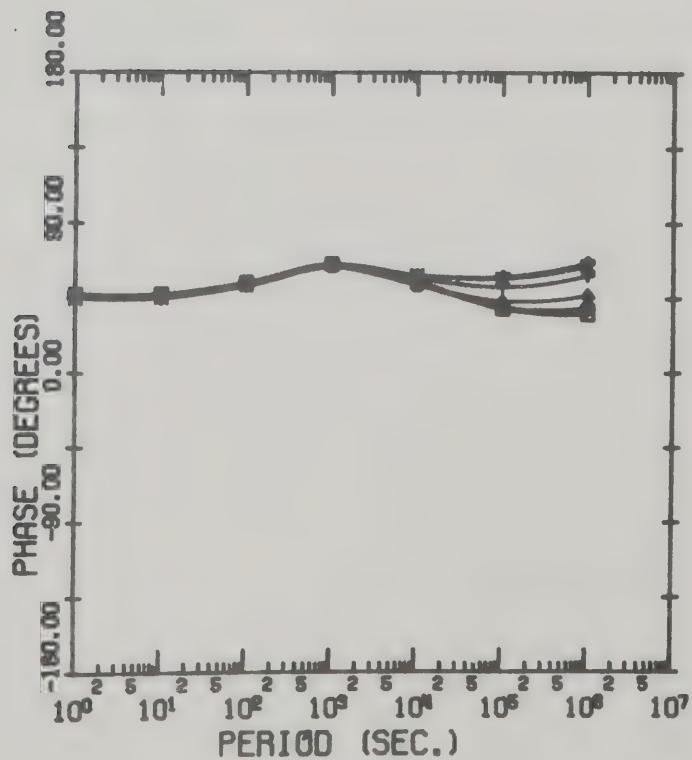
variable, and then we shall consider the case of several

Figure 2.3 Apparent resistivity and phase curves for the $(y-b)\{e^{[\frac{1}{b}(y-b)]}\}u(y-b)$ source over a two-layered conductor with a 50 km thick upper layer of resistivity 100 ohm-m overlying a half-space of resistivity 10 ohm-m. The curves are for the negative y region and are calculated for points along the surface beneath the source.

square	:	-1000 km
circle	:	- 800 km
triangle	:	- 600 km
+	:	- 400 km
X	:	- 200 km
diamond	:	at origin



APPARENT RESISTIVITY CURVES



PHASE CURVES



Figure 1.1.1. A graph of a function $y = f(x)$.



Figure 2.4 As Figure 2.3 but for positive y region.

square : at origin

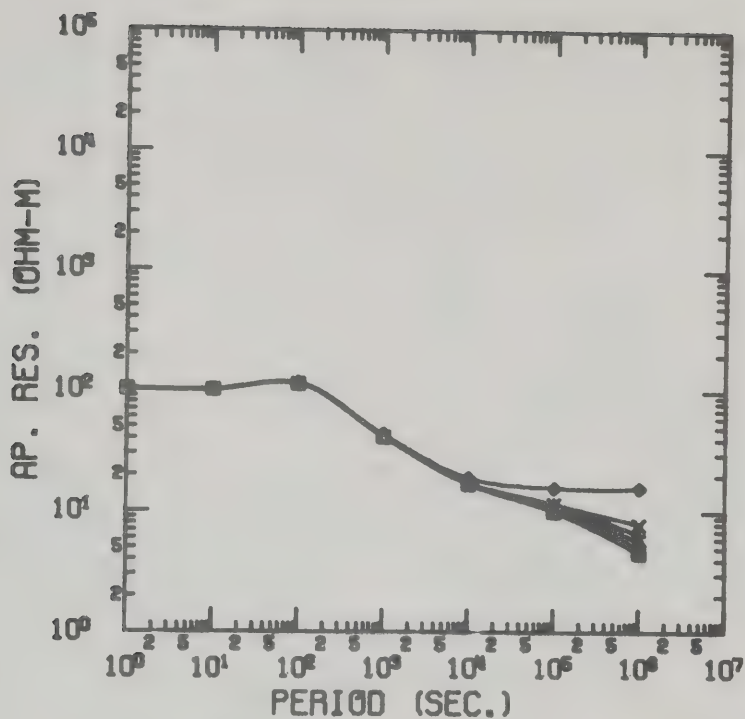
circle : 200 km

triangle : 400 km

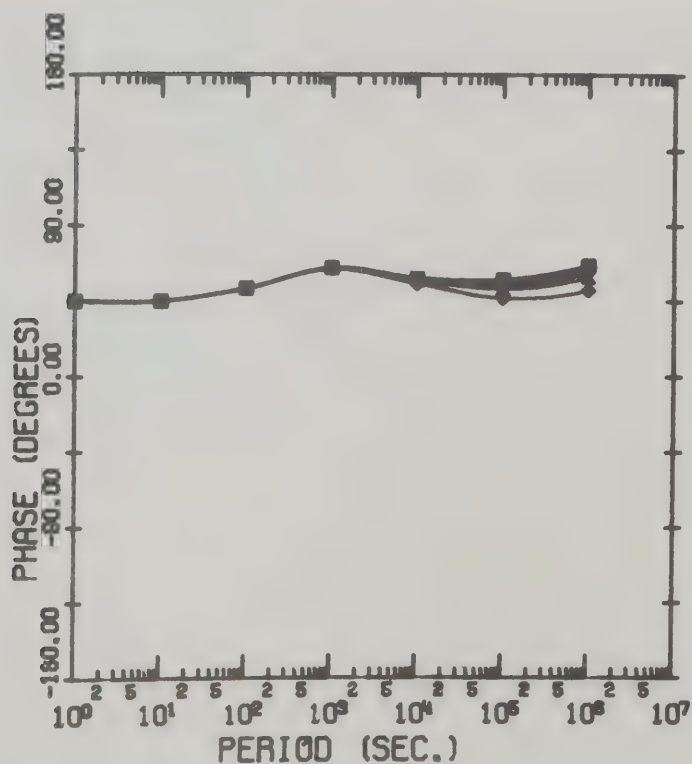
+ : 600 km

X : 800 km

diamond : 1000 km



APPARENT RESISTIVITY CURVES



PHASE CURVES

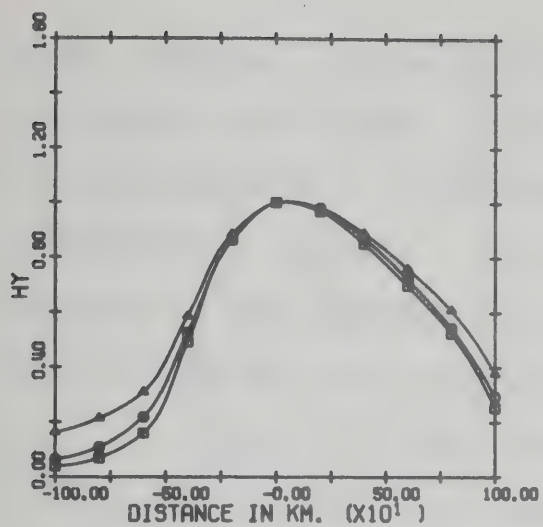
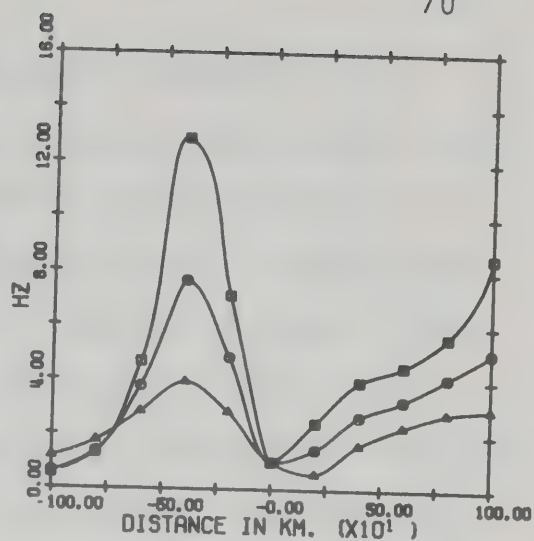
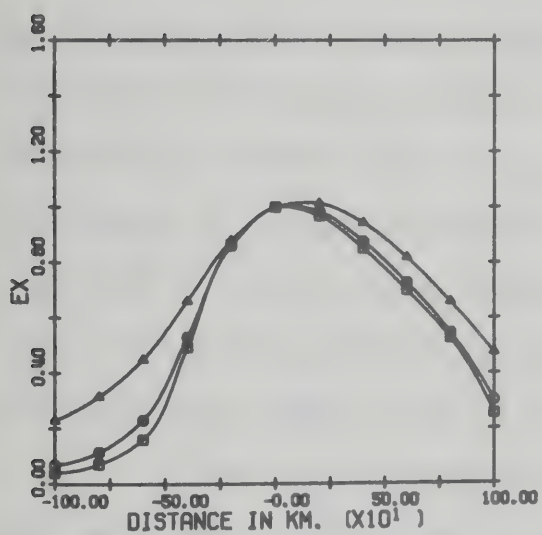


Figure 2.5 Field profiles along the surface of the earth for three periods for model as in Figure 2.3. The field components are normalized with respect to the point at the origin.

square : 10 sec

circle : 10^3 sec

triangle : 10^5 sec

AMPLITUDE OF H_Y VS DISTANCEAMPLITUDE OF H_Z VS DISTANCEAMPLITUDE OF E_X VS DISTANCE

work. However, the vertical magnetic component (H_z) increases near 10^3 km. This is because the current source is terminated at + 1010 km whereas previously the source continued to infinity. The results shown in these plots, as well as the apparent resistivity ones of Figs. 2.3 and 2.4 reflect the non-symmetric character of the source.

Fig. 2.6 gives the apparent resistivity and phase curves for the elemental Gaussian itself. The Gaussian source is symmetric and the results for + y and - y are identical. The spreading of the curves at longer period as a function of position is again evident. At short periods the phase difference between E_x and H_y is 45 degrees at all positions beneath the source. However, as the period increases this phase difference becomes dependent on the position relative to the source. This effect is evident for all the non-uniform source models. The field component profiles are shown in Fig. 2.7.

The second conductivity configuration considered was that of a two-layered Earth with upper layer 4 km thick and resistivity 0.25 ohm-m with an underlying half-space of resistivity 250 ohm-m. The source was constructed in the same manner as in the previous model. The apparent resistivity and phase curves are shown in Figs. 2.8 and 2.9 and the field component profiles in Fig. 2.10. The apparent resistivity curves again compare well with those obtained previously by Hibbs and Jones (1973b).

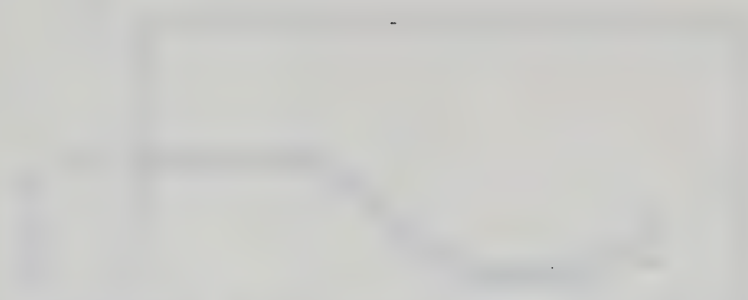


Fig. 1. The dependence of the rate of the reaction on the concentration of the reactants.

where k_1 and k_2 are the rate constants of the reaction.

From (1) we have

$$\frac{dC}{dt} = k_1 C - k_2 C^2 \quad (2)$$

$$C = \frac{k_1}{k_2} \left(1 - e^{-k_2 t} \right) \quad (3)$$

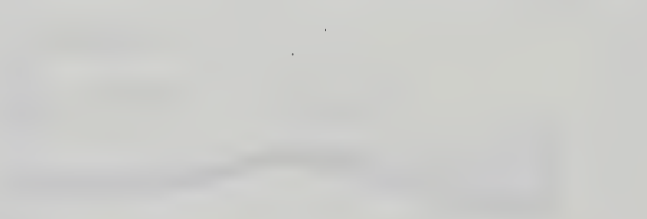
where C is the concentration of the reactants, t is the time, and k_1 and k_2 are the rate constants of the reaction. The dependence of the rate of the reaction on the concentration of the reactants is shown in Fig. 1.

From (3) we can see that the rate of the reaction increases with increasing concentration of the reactants.

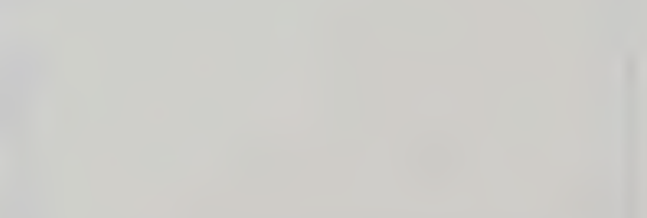
$$C = \frac{k_1}{k_2} \left(1 - e^{-k_2 t} \right) \quad (4)$$

where C is the concentration of the reactants, t is the time, and k_1 and k_2 are the rate constants of the reaction.

The dependence of the rate of the reaction on the concentration of the reactants is shown in Fig. 2.



From (4) we can see that the rate of the reaction increases with increasing concentration of the reactants.



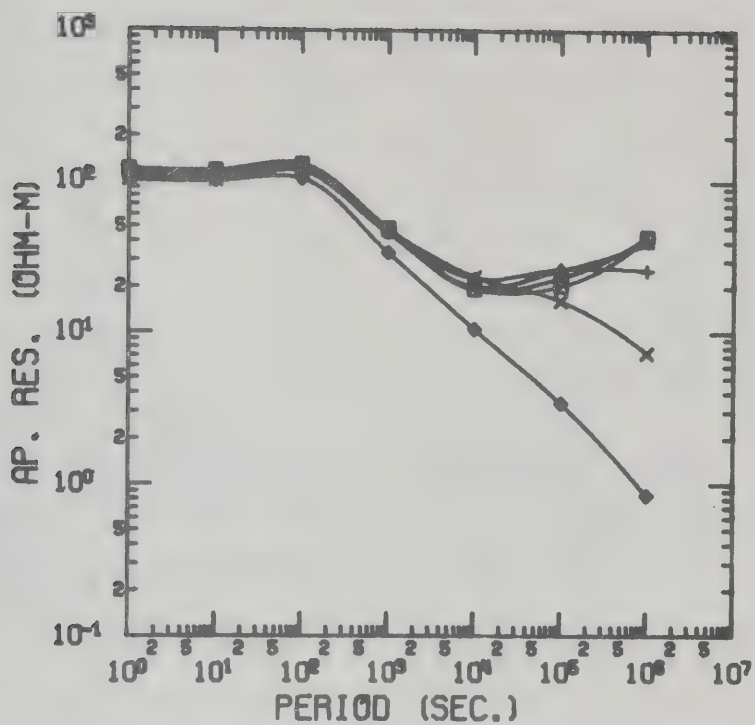
From (4) we can see that the rate of the reaction increases with increasing concentration of the reactants.

The dependence of the rate of the reaction on the concentration of the reactants is shown in Fig. 3.

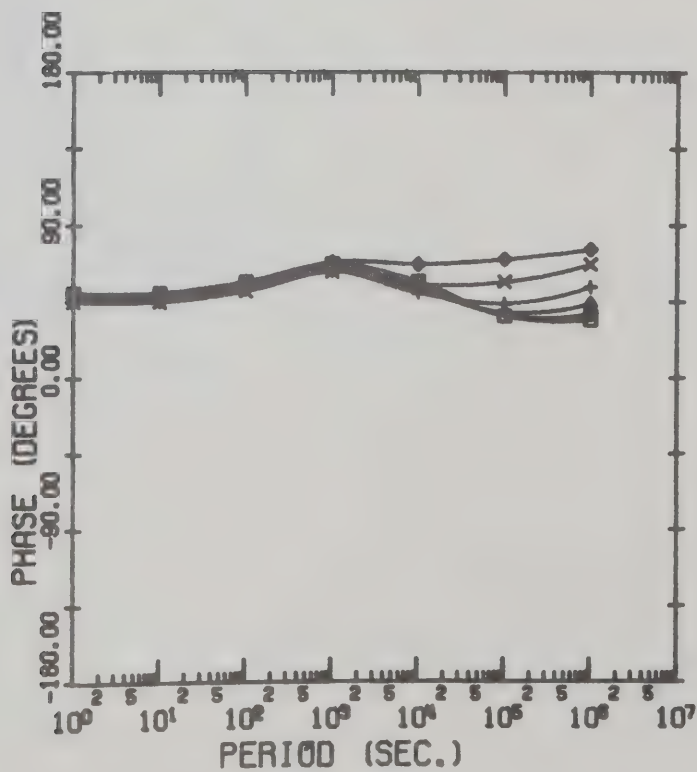
From (4) we can see that the rate of the reaction increases with increasing concentration of the reactants.

Figure 2.6 Apparent resistivity and phase curves for the elemental Gaussian source over a two-layered conductor with 50 km thick upper layer of resistivity 100 ohm-m overlaying a half-space of resistivity 10 ohm-m. The curves are for the positive y region and are calculated for points along the surface beneath the source.

square	:	at origin
circle	:	200 km
triangle	:	400 km
+	:	600 km
X	:	800 km
diamond	:	1000 km



APPARENT RESISTIVITY CURVES



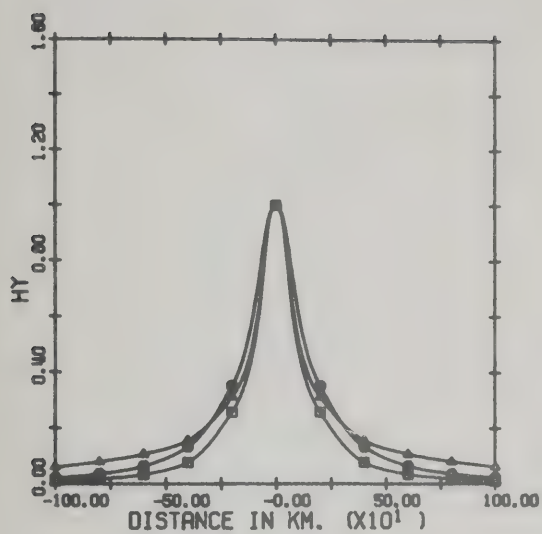
PHASE CURVES

Figure 2.7 Field profiles for model as in Figure 2.6. E_x and H_y are normalized with respect to the origin and H_z with respect to the point at $y = 200$ km.

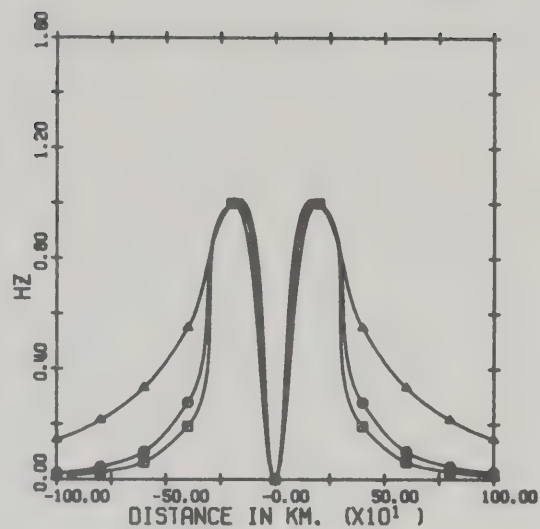
square : 10 sec

circle : 10^3 sec

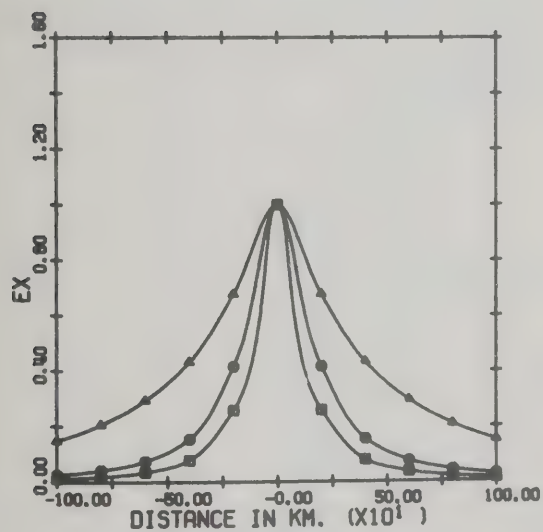
triangle : 10^5 sec



AMPLITUDE OF HY VS DISTANCE



AMPLITUDE OF HZ VS DISTANCE



AMPLITUDE OF EX VS DISTANCE

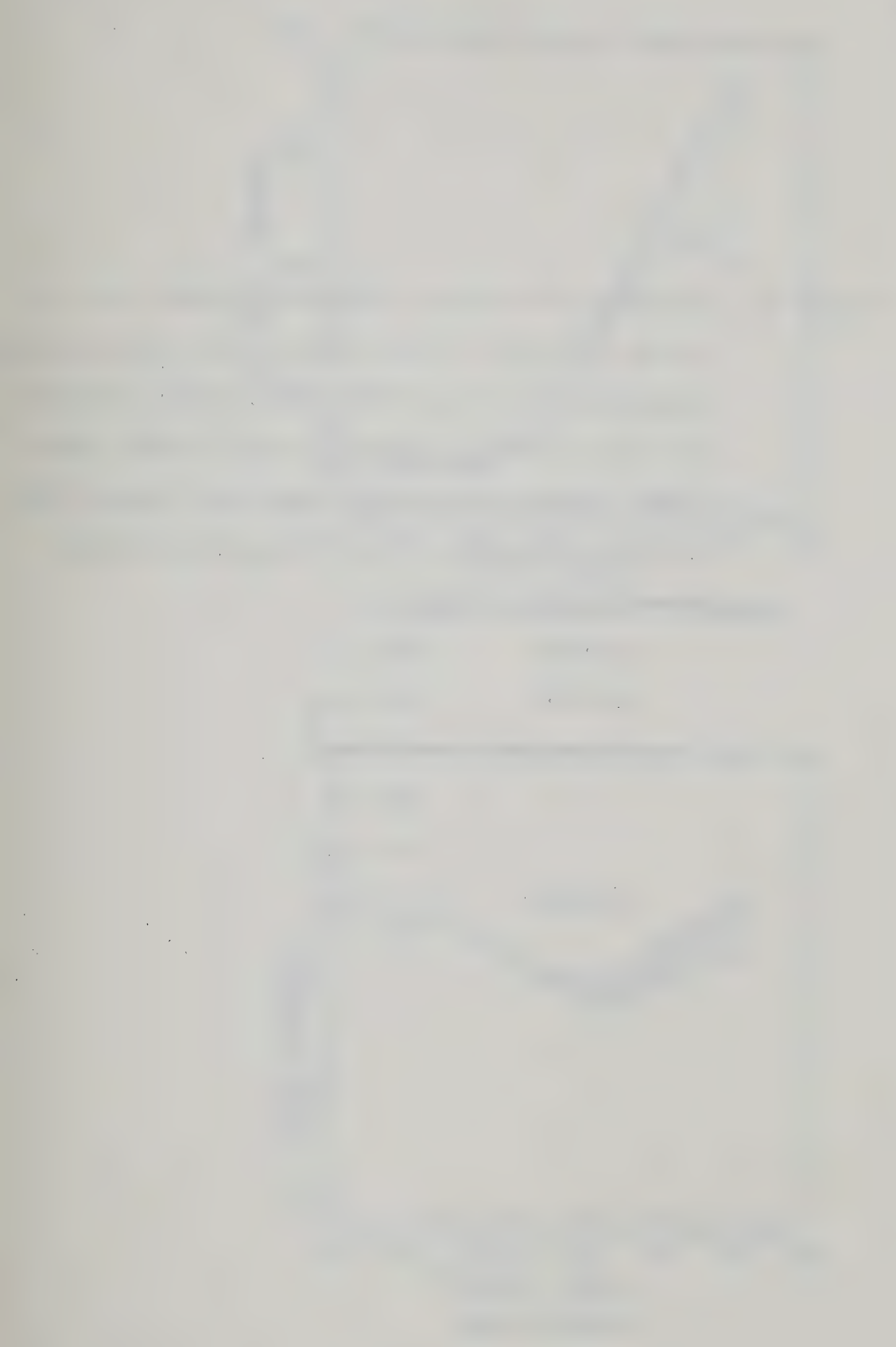
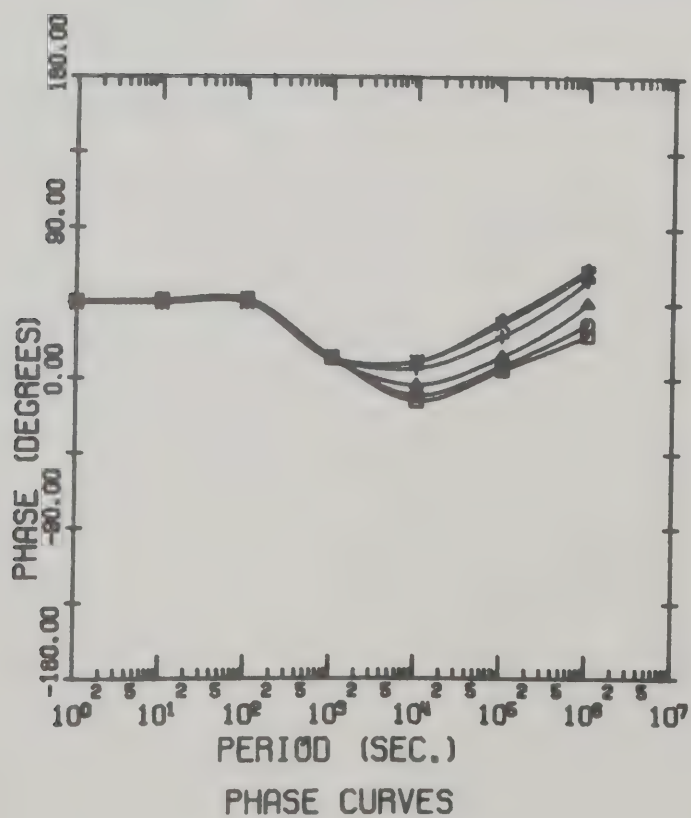
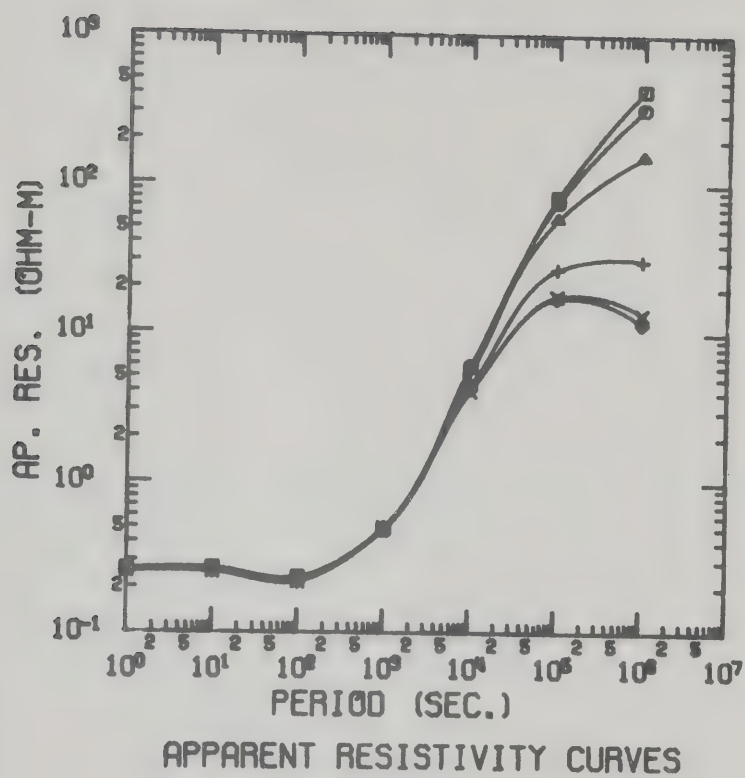


Figure 2.8 Apparent resistivity and phase curves for the $(y-b) e^{\frac{1}{b}(y-b)} u(y-b)$ source over a two layered conductor with 5 km thick upper layer of resistivity 0.25 ohm-m and half-space of 250 ohm-m. These curves are for the negative y region and are calculated for points along the surface beneath the source.

square	:	-1000 km
circle	:	- 800 km
triangle	:	- 600 km
+	:	- 400 km
X	:	- 200 km
diamond	:	at origin



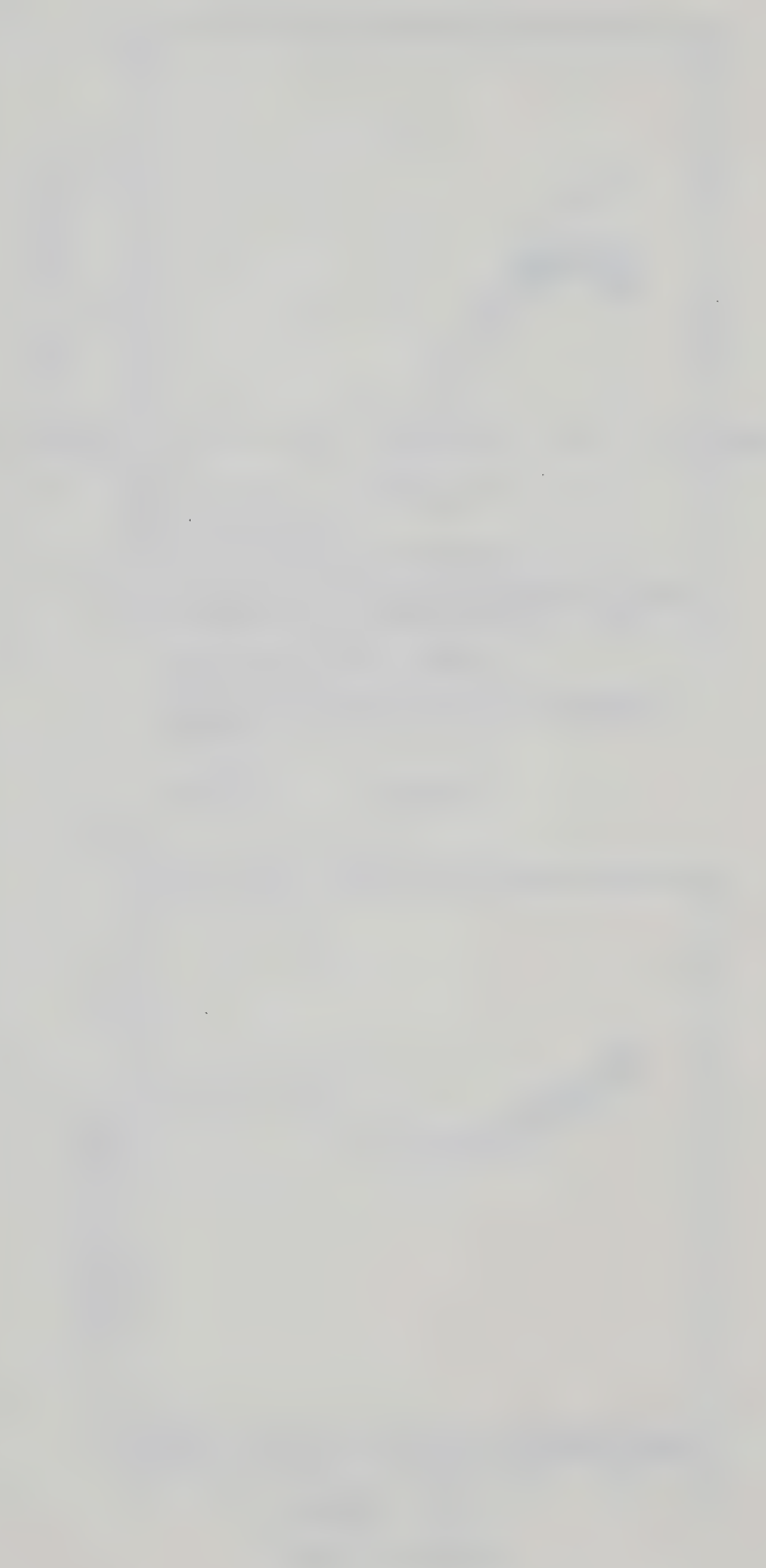
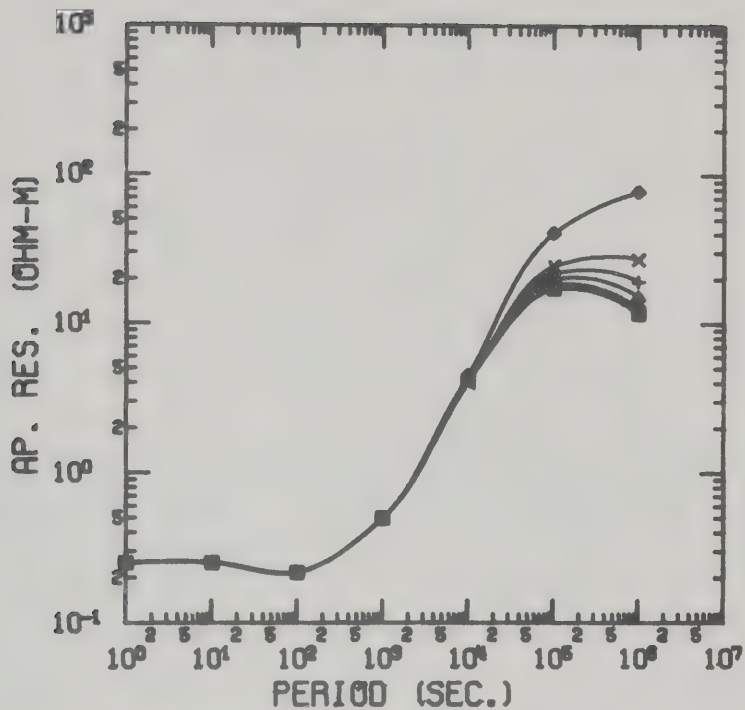
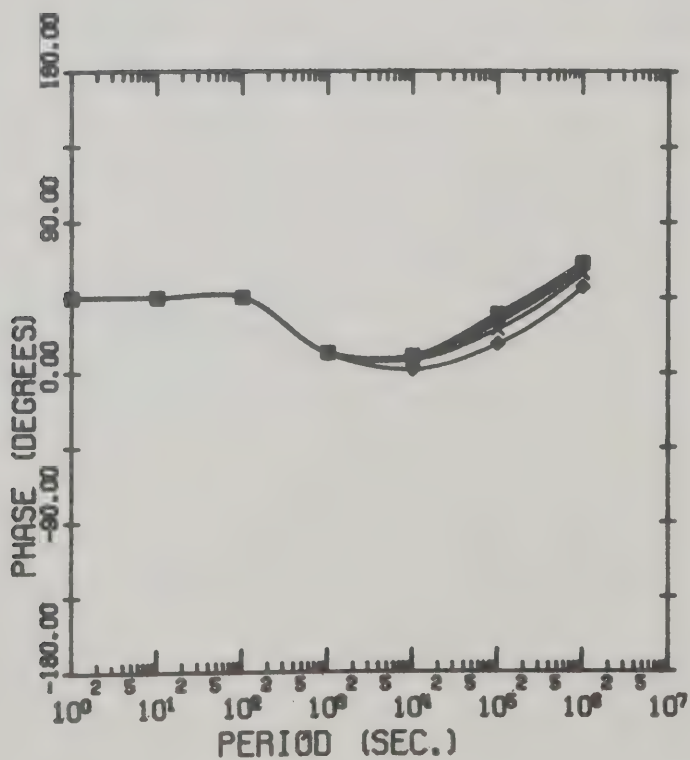


Figure 2.9 As Figure 2.8, but for positive y region.

square	:	at origin
circle	:	200 km
triangle	:	400 km
+	:	600 km
X	:	800 km
diamond	:	1000 km



APPARENT RESISTIVITY CURVES



PHASE CURVES

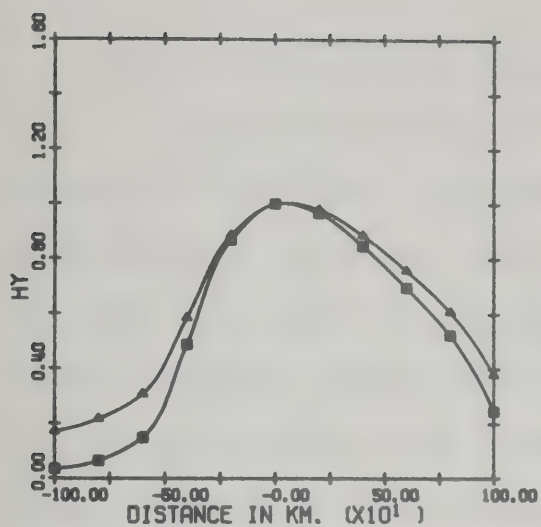
Figure 2.10 Field profiles for model as in Figure 2.8.

All components are normalized with respect to the origin. The results for the 10 sec and the 10^3 sec curves are nearly the same, and these two curves overlap.

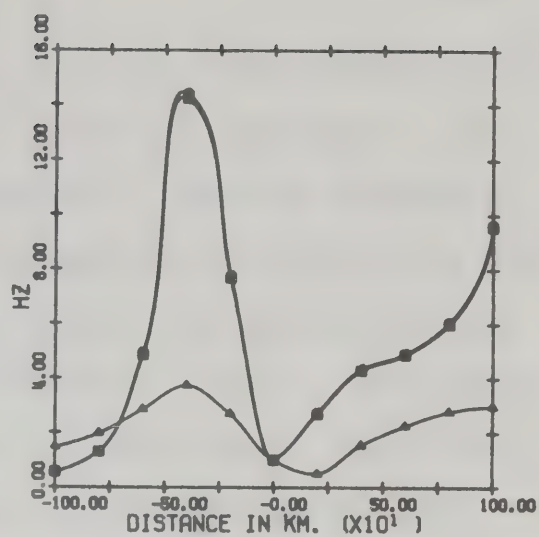
square : 10 sec

circle : 10^3 sec

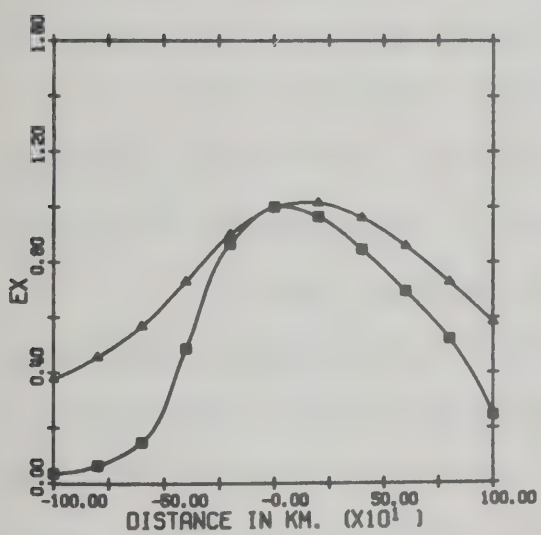
triangle : 10^5 sec



AMPLITUDE OF HY VS DISTANCE



AMPLITUDE OF HZ VS DISTANCE



AMPLITUDE OF EX VS DISTANCE

2.6.2 An Arbitrary Non-Integrable Source Configuration

A third more general model was considered. The source for this model was composed of fourteen rectangles, each 30 km in width and with intensity coefficients as given in Table 2.5. Each of the rectangles was approximated by three elemental Gaussians of 10 km half-width. The conductivity configuration was that of a two-layered Earth with upper layer 50 km deep and resistivity 100 ohm-m. The second layer was a half-space of resistivity 10 ohm-m. The apparent resistivity and phase curves are given in Figs. 2.11 and 2.12 and the field component profiles in Fig. 2.13.

For this third arbitrary model the spreading of the apparent resistivity curves for different positions under the source at long periods is evident as in the other two models.

By superimposing elemental Gaussian solutions to construct rectangular current segments any general source configuration can be approximated. This provides much flexibility in the construction of sources to aid in the removal of source effects from array data and also in the study of source configurations from ground measurements when the conductivity of the earth is considered. This approach may also be used to provide boundary conditions for more general laterally inhomogeneous earth model calculations. A description of the actual program and a discussion of its use is given in Appendix A.

0.200E + 02
0.500E + 02
0.500E + 02
0.500E + 02
0.500E + 02
0.500E + 02
0.300E + 03
0.700E + 03
0.700E + 03
0.700E + 03
0.700E + 03
0. 00
0. 00
0. 00

Table 2.5 Source intensity coefficients for the arbitrary source.



Figure 2.11 Apparent resistivity and phase curves for the arbitrary source over a two-layered conductor with a 50 km thick upper layer of resistivity 100 ohm-m overlaying a half-space of resistivity 10 ohm-m. The curves are for the negative y region and are calculated for points along the surface beneath the source.

square : -1000 km

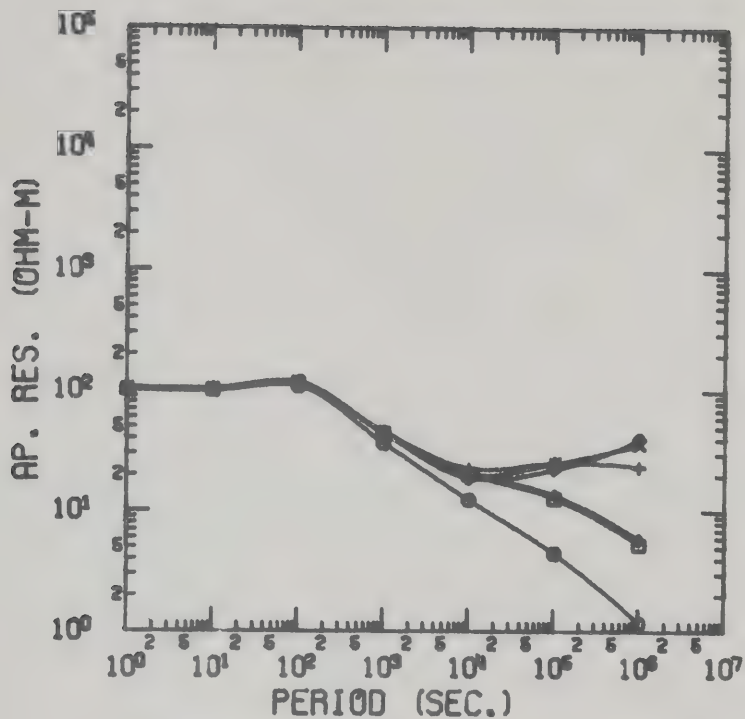
circle : - 800 km

triangle : - 600 km

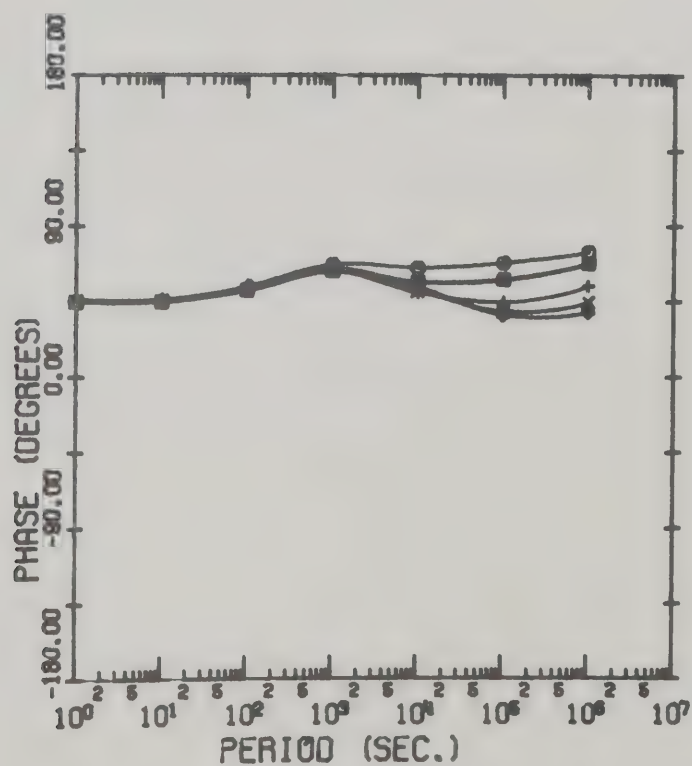
+ : - 400 km

X : - 200 km

diamond : at origin



APPARENT RESISTIVITY CURVES



PHASE CURVES

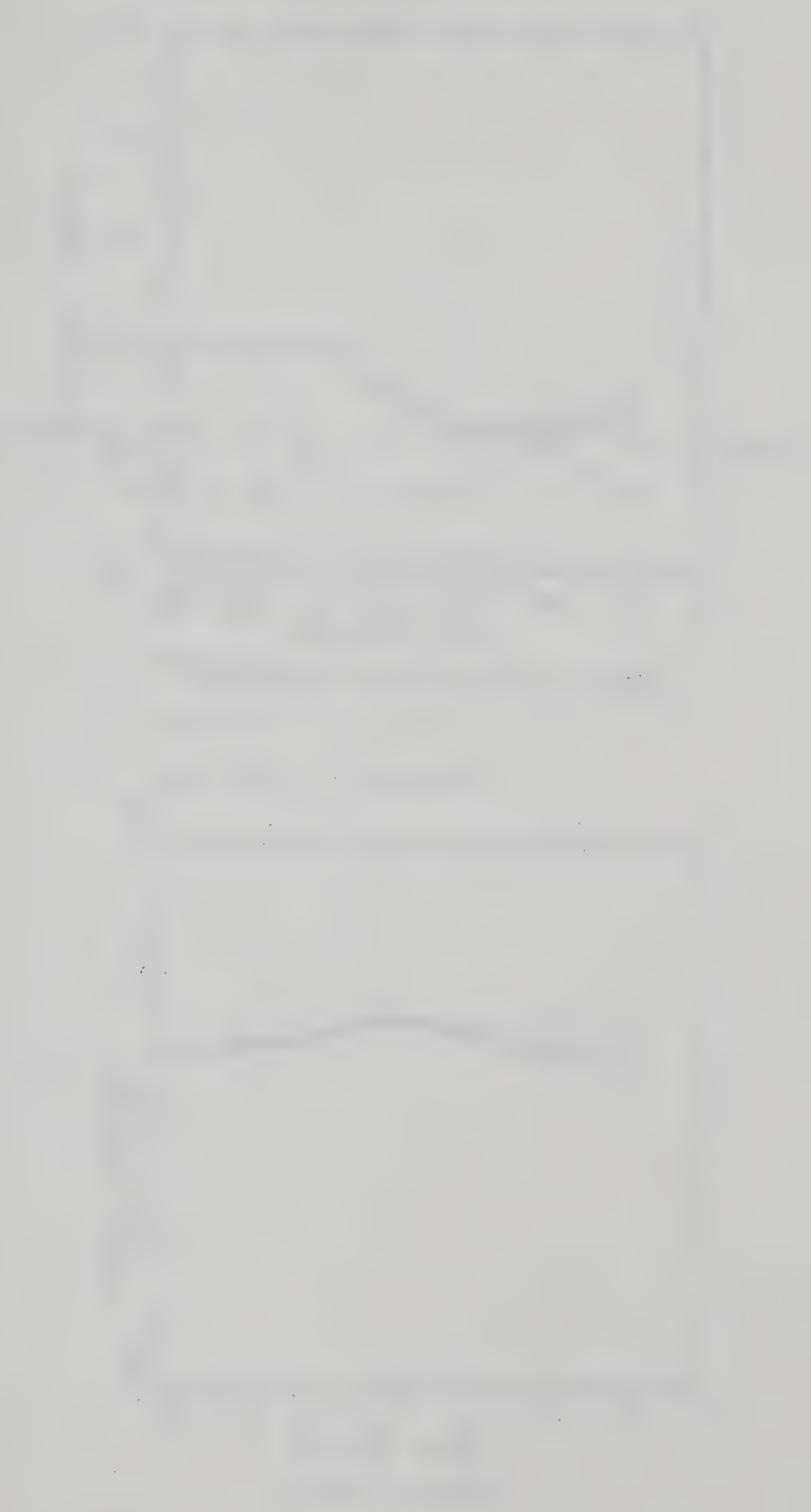


Figure 2.12 As Fig. 2.11, but for the positive y region.

square : at origin

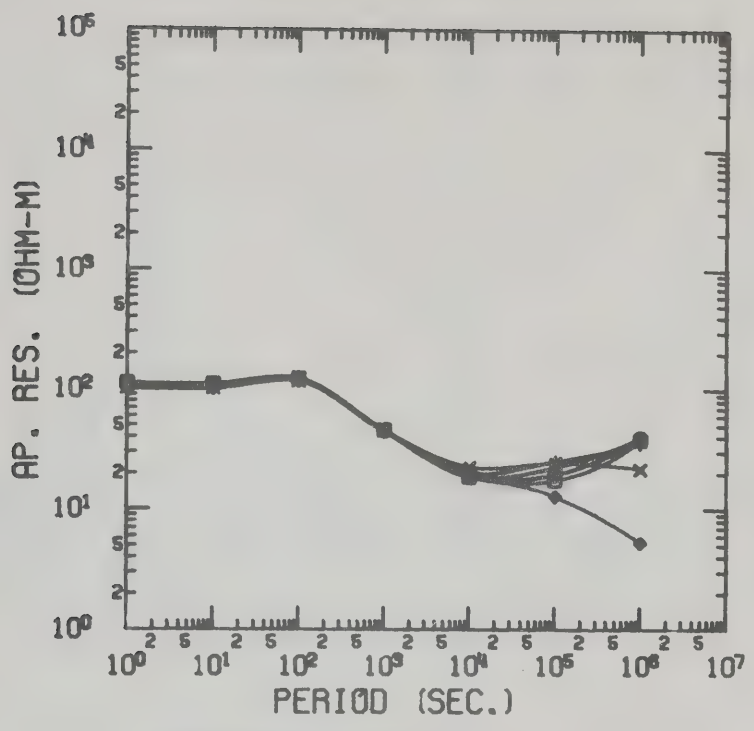
circle : 200 km

triangle : 400 km

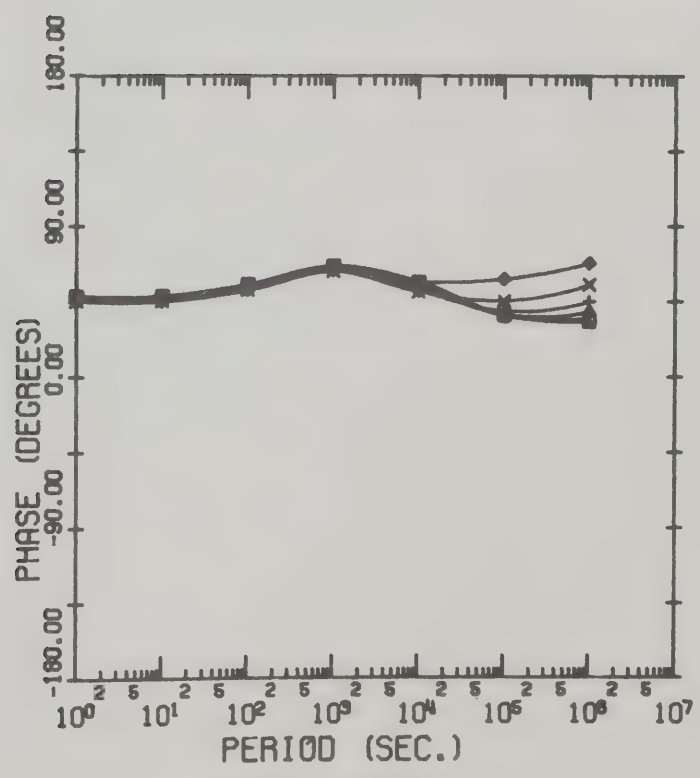
+ : 600 km

x : 800 km

diamond : 1000 km



APPARENT RESISTIVITY CURVES



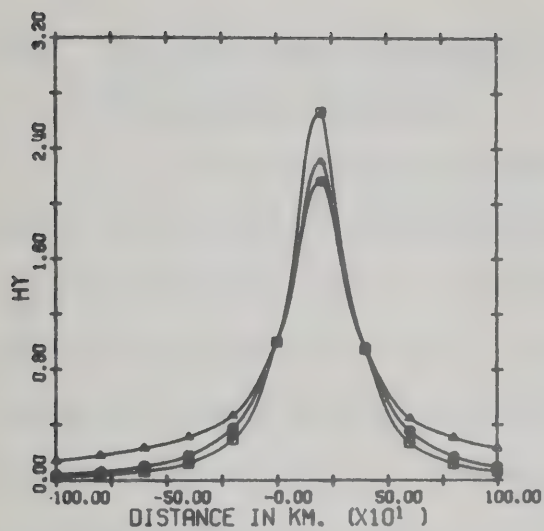
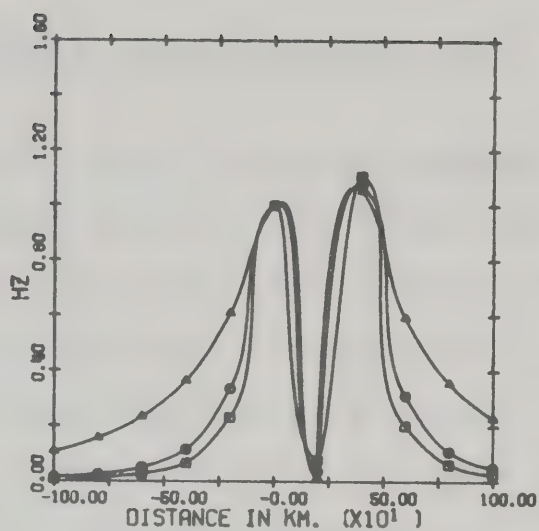
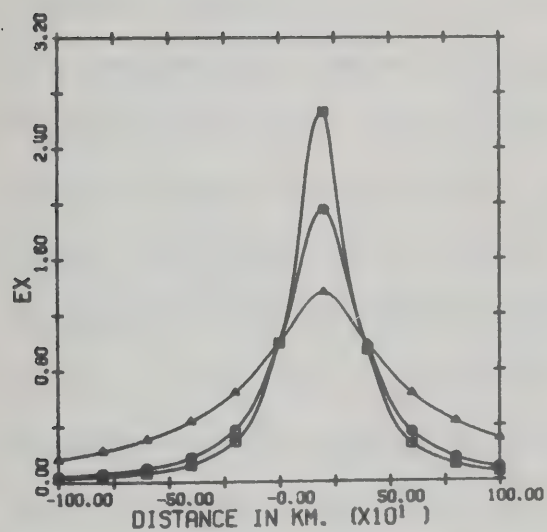
PHASE CURVES

Figure 2.13 Field profiles along the surface of the earth for three periods for model of Fig. 2.11. The field components are normalized with respect to the point at the origin.

square : 10 sec

circle : 10^3 sec

triangle : 10^5 sec

AMPLITUDE OF H_Y VS DISTANCEAMPLITUDE OF H_Z VS DISTANCEAMPLITUDE OF E_X VS DISTANCE

2.7 The Horizontal Magnetic Dipole Source Solution for a Two-Layer Conductor

The horizontal magnetic dipole solution presented here was originally formulated by Grant and West (1965) for a magnetic dipole above a homogeneous earth. The solution for the polar magnetic fields was derived for a monopole and then by simple differentiation the solution for a magnetic dipole was obtained. Ramaswamy (1973) extended this work to include the effect of a two layered conducting earth.

Consider a semi-infinite, three-dimensional, two layered conducting earth occupying the half space $z > 0$ of the rectangular coordinate system shown in Fig. 2.14. The first layer is of conductivity σ_1 and depth d , and the second layer is semi-infinite with conductivity σ_2 . The upper half-space is a free space region. The permeability of both the conductors and the upper half-space is equal to that of free space. From the mathematical model shown in Fig. 2.14, a magnetic pole situated at $(0,0,-h)$ has cylindrical symmetry and cylindrical coordinates (r,θ,z) are used. These are related to the Cartesian coordinates (x,y,z) by

$$x = r \cos \theta \quad \text{and} \quad y = r \sin \theta \quad . \quad (2.100)$$

The vector potential, \underline{A} , for the magnetic pole will have only a θ component due to symmetry which will be a function of r and z , $\pi(r,z)$.

MAGNETIC DIPOLE

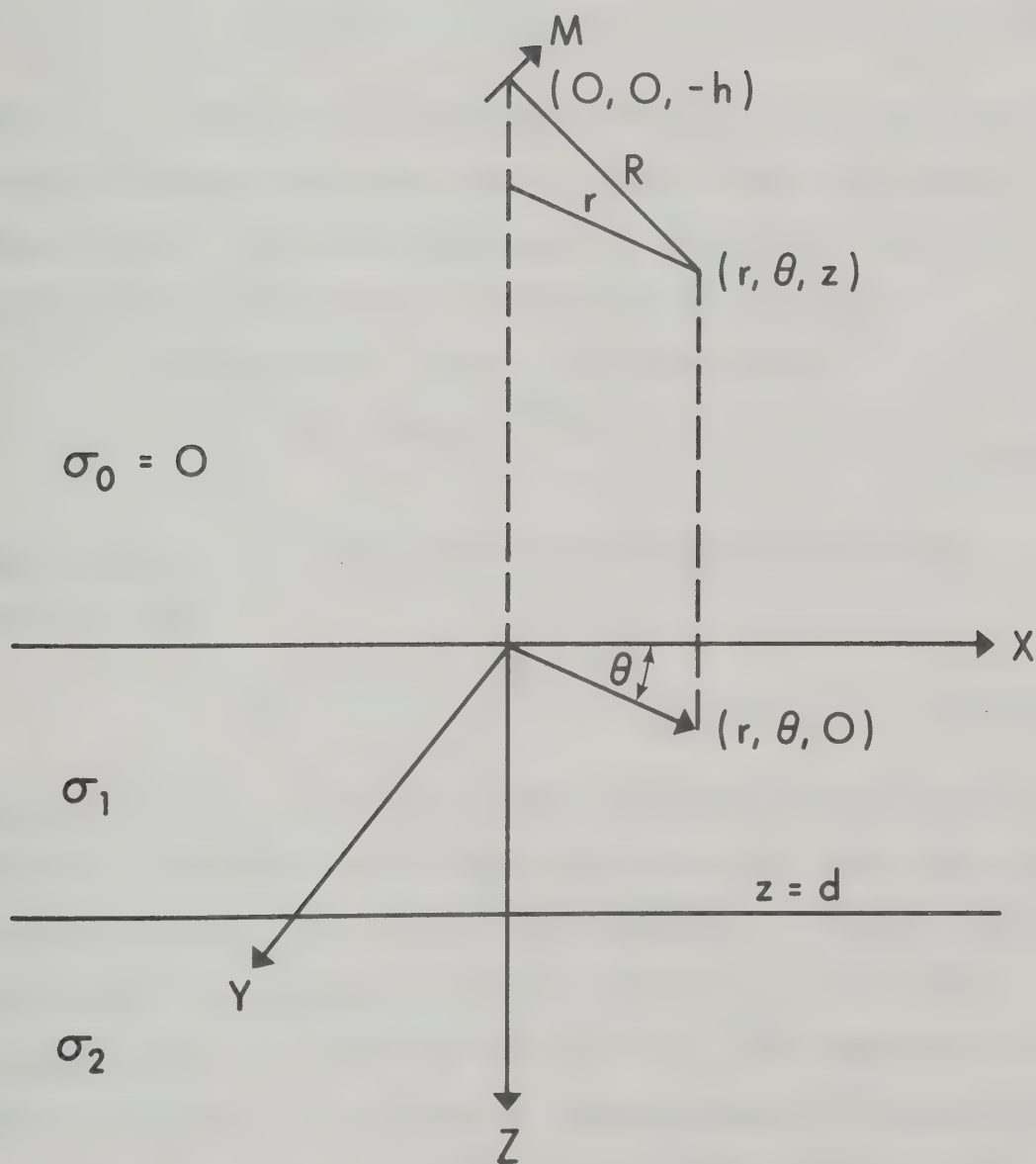


Figure 2.14 The magnetic dipole and the coordinate system.

In the three conductivity regions considered, the source currents are excluded so that equation (2.10) must be satisfied in each region. $\pi(r,z)$ automatically satisfies the relation $\underline{\nabla} \cdot \underline{\pi} = 0$. Therefore,

$$\nabla^2 \pi(r,z) - i\mu_0 \omega \sigma_n \pi(r,z) = 0 \quad (2.101)$$

where μ_0 , ω and σ_n are the permeability of free space, the angular frequency and the conductivity of the n -th layer respectively. The time dependence is sinusoidal and the factor $e^{i\omega t}$ is understood in all field quantities.

Solutions of (2.101) are of the form

$$e^{\left[\pm (\xi^2 + i\mu_0 \omega \sigma_n)^{1/2} z \right]} J_1(r, \xi), \quad (2.102)$$

where $J_1(r, \xi)$ is a Bessel function of the first kind of order 1, and

$$e^{\left[\pm (\xi^2 + i\mu_0 \omega \sigma_n)^{1/2} z \right]} Y_1(r, \xi) \quad (2.103)$$

where $Y_1(r, \xi)$ is the Bessel function of the second kind of order 1. Since the fields must be finite for $r=0$, $z \neq 0$, only solutions of the form (2.102) are permitted. The plus and minus sign in the exponential are chosen so as to reject solutions which are not finite as $z \rightarrow \pm \infty$. The complete solution of (2.101) is obtained by superimposing all possible solutions of the type (2.102). The magnetic field of the pole is obtained from relation (2.17)

$$\underline{\Gamma} = \underline{\nabla} \times \pi(r, z) \hat{\theta} \quad (2.104)$$

where $\hat{\theta}$ is the unit vector in the θ direction.

The horizontal magnetic dipole solution is obtained by considering magnetic poles of strength $(+p)$ and $(-p)$ varying sinusoidally with time which are situated at $(X_1, Y_1, -h)$ and $(X_1, Y_1 + \Delta\ell, -h)$ respectively. The total field at any observational point (x, y, z) is obtained by superimposing the fields of the individual poles. In the limit as $\Delta\ell \rightarrow 0$ the total field will reduce to that of a dipole at $(X_1, Y_1, -h)$ with its dipole moment directed in the negative y -direction, provided that $\Delta\ell$ approaches zero in such a way that p remains constant. That is, if $(\underline{\Gamma})_{Y_1}$ and $(\underline{\Gamma})_{Y_1 + \Delta\ell}$ denote the fields at a point (x, y, z) due to poles $+p$ and $-p$, respectively, then the field at (x, y, z) can be written as

$$\underline{H} = \lim_{\Delta\ell \rightarrow 0} [(\underline{\Gamma})_{Y_1} - (\underline{\Gamma})_{Y_1 + \Delta\ell}] \quad (2.105)$$

expanding $(\underline{H})_{Y_1 + \Delta\ell}$ in a Taylor series about Y_1

$$\underline{H} = \lim_{\Delta\ell \rightarrow 0} [-\Delta\ell \left\{ \frac{\partial \underline{\Gamma}}{\partial Y_1} \right\}_{Y_1} - O(\Delta\ell^2)] \quad (2.106)$$

The dipole moment m is given by the relation

$$\underline{M} = \lim_{\Delta\ell \rightarrow 0} p \Delta\ell \quad (2.107)$$

so that

$$\underline{H} = - \frac{\underline{M}}{p} \frac{\partial \underline{\Gamma}}{\partial Y_1} \quad (2.108)$$

The solution for Γ depends only on the horizontal distance between the pole and the field point, therefore $\frac{\partial \Gamma}{\partial y} = -\frac{\partial \Gamma}{\partial y_1}$.
And

$$H = \frac{M}{p} \frac{\partial \Gamma}{\partial y} \quad (2.109)$$

The field, Γ , is related to the vector potential by (2.17)

$$\underline{\Gamma} = \underline{\nabla} \times \underline{A} \quad (2.110)$$

Using the elementary coordinate transformation

$\Gamma_x = \Gamma_r \cos \theta$ and $\Gamma_y = \Gamma_r \sin \theta$ the x and y components of the dipole field are

$$H_x = \frac{M}{p} \frac{\partial(\Gamma_r \cos \theta)}{\partial y} \quad (2.111)$$

$$H_y = \frac{M}{p} \frac{\partial(\Gamma_r \sin \theta)}{\partial y}$$

$$H_z = \frac{M}{p} \Gamma_z$$

The solution for the electric field is found by taking the curl of \underline{H}

$$\underline{E} = \frac{1}{\sigma} (\nabla \times \underline{H}) \quad (2.112)$$

Following Ramaswamy (1973), the magnetic fields in the first conducting layer are

$$H_r = \frac{M(\mu_0 \omega \sigma_1)^{3/2} \sin \theta}{2\pi} \int_0^\infty \frac{n\xi}{n+\xi} G_-(\xi, z) \left[\xi J_0(r\xi) - \frac{J_1(r\xi)}{r} \right] e^{-\xi h} d\xi \quad (2.113)$$

$$H_{\theta} = \frac{M(\mu_0 \omega \sigma_1)^{3/2} \cos \theta}{2\pi r} \int_0^{\infty} \frac{n\xi}{n+\xi} G_{-}(\xi, z) J_1(r \xi) e^{-\xi h} d\xi \quad (2.114)$$

$$H_z = - \frac{M(\mu_0 \omega \sigma_1)^{3/2} \sin \theta}{2\pi} \int_0^{\infty} \frac{\xi^3}{n+\xi} G_{+}(\xi, z) J_1(r \xi) e^{-\xi h} d\xi \quad (2.115)$$

$$\text{where} \quad n = (\xi^2 + i\mu_0 \omega \sigma_1)^{1/2} \quad (2.116)$$

$$\text{and} \quad G_{\pm} = \frac{e^{-nz} \pm g(\xi) e^{-2nd+nz}}{1 - f(\xi) g(\xi) e^{-2nd}} \quad (2.117)$$

The functions $g(\xi)$ and $f(\xi)$ are defined as

$$f(\xi) = \frac{n-\xi}{n+\xi}, \quad g(\xi) = \frac{n-n_{\sigma}}{n+n_{\sigma}} \quad (2.118)$$

$$\text{where} \quad n_{\sigma} = (\xi^2 + i \frac{\sigma_2}{\sigma_1})^{1/2} \quad (2.119)$$

The corresponding solutions for the electric fields are

$$\begin{aligned} E_r &= \frac{1}{r} \frac{\partial H_z}{\partial \theta} - \frac{\partial H_{\theta}}{\partial z} \\ &= \frac{iM\mu_0^2 \omega^2 \sigma_1 \cos \theta}{2\pi r} \int_0^{\infty} \frac{\xi}{n+\xi} G_{+}(\xi, z) J_1(r \xi) e^{-\xi h} d\xi \end{aligned} \quad (2.120)$$

$$\begin{aligned} E_{\theta} &= - \frac{\partial H_z}{\partial r} + \frac{\partial H_r}{\partial z} \\ &= - \frac{iM\mu_0^2 \omega^2 \sigma_1 \sin \theta}{2\pi} \int_0^{\infty} \frac{\xi}{n+\xi} G_{+}(\xi, z) \left[\xi J_0(r \xi) - \frac{J_1(r \xi)}{r} \right] e^{-\xi h} d\xi \end{aligned} \quad (2.121)$$

$$E_z = \frac{H_{\theta}}{r} + \frac{\partial H_{\theta}}{\partial r} - \frac{1}{r} \frac{\partial H_r}{\partial \theta} = 0 \quad (2.122)$$

The solutions for the magnetic and electric fields in the semi-infinite layer are:

$$H_r = \frac{M(\mu_0 \omega \sigma_1)^{3/2} \sin \theta}{2\pi} \int_0^\infty \frac{n_\sigma \xi}{n+\xi} G_+(\xi, d) \left[\xi J_0(r \xi) - \frac{J_1(r \xi)}{r} \right] e^{-(\xi h + (z-d)n_\sigma)} d\xi \quad (2.123)$$

$$H_\theta = \frac{M(\mu_0 \omega \sigma_1)^{3/2} \cos \theta}{2\pi r} \int_0^\infty \frac{n_\sigma \xi}{n+\xi} G_+(\xi, d) J_1(r \xi) e^{-(\xi h + (z-d)n_\sigma)} d\xi \quad (2.124)$$

$$H_z = - \frac{M(\mu_0 \omega \sigma_1)^{3/2} \sin \theta}{2\pi} \int_0^\infty \frac{\xi^3}{n+\xi} G_+(\xi, d) J_1(r \xi) e^{-(\xi h + (z-d)n_\sigma)} d\xi \quad (2.125)$$

$$E_r = \frac{iM\mu_0^2 \omega \sigma_1 \cos \theta}{2\pi r} \int_0^\infty \frac{\xi}{n+\xi} G_+(\xi, d) J_1(r \xi) e^{-(\xi h + (z-d)n_\sigma)} d\xi \quad (2.126)$$

$$E_\theta = - \frac{iM\mu_0^2 \omega \sigma_1 \sin \theta}{2\pi} \int_0^\infty \frac{\xi}{n+\xi} G_+(\xi, d) \left[\xi J_0(r \xi) - \frac{J_1(r \xi)}{r} \right] e^{-(\xi h - (z-d)n_\sigma)} d\xi \quad (2.127)$$

$$E_z = 0$$

The magnetic field solutions for the free space region are found in the same manner as before.

$$H_r = \frac{M(\mu_0 \omega \sigma_1)^{3/2} \sin \theta}{4\pi} \int_0^\infty \{ e^{-(\xi z)} - \frac{\lambda^*}{\lambda(\xi)} e^{(\xi z)} \} \xi e^{-\xi h} \left[\xi J_0(r \xi) - \frac{J_1(r \xi)}{r} \right] d\xi \quad (2.128)$$

$$H_{\theta} = \frac{M(\mu_0 \omega \sigma_1)^{3/2} \cos \theta}{4\pi r} \int_0^{\infty} \{e^{-(\xi z)} - \ell^*(\xi) e^{(\xi z)}\} \xi J_1(r \xi) e^{-\xi h} d\xi \quad (2.129)$$

$$H_z = - \frac{M(\mu_0 \omega \sigma_1)^{3/2} \sin \theta}{4\pi} \int_0^{\infty} \{e^{-(\xi z)} + \ell^*(\xi) e^{(\xi z)}\} \xi^2 J_1(r \xi) e^{-\xi h} d\xi \quad (2.130)$$

$$\text{where} \quad \ell^*(\xi) = \frac{2\xi}{(n+\xi)} G_+(\xi, d) e^{-(\xi h - d n_{\sigma})} \quad (2.131)$$

In the free space region the electric field cannot be obtained through the use of the curl equation since $\sigma = 0$ there. However, the relation

$$\nabla \times \underline{E} = -i \omega \mu_0 \underline{H} \quad (2.132)$$

must be used in its place.

$$-i \omega \mu_0 H_r = \frac{1}{r} \frac{\partial E_z}{\partial \theta} - \frac{\partial E_{\sigma}}{\partial z} \quad (2.133)$$

$$-i \omega \mu_0 H_{\theta} = \frac{\partial H_r}{\partial z} - \frac{\partial E_z}{\partial r} \quad (2.134)$$

$$-i \omega \mu_0 H_z = \frac{\partial E_{\theta}}{\partial r} + \frac{1}{r} (E_{\theta} - \frac{\partial E_r}{\partial \theta}) \quad (2.135)$$

These equations must be integrated in order to find the electric field. Since E_z vanishes inside the conductor, the conductor acts like a perfect reflector (infinite conductivity) so far as E_z is concerned. Thus geometric imaging of the dipole can be used to find the solution for E_z .

Ramaswamy (1973) shows that

$$E_z = - \frac{iM\mu_0^2 \omega^2 \sigma_1 \cos\theta}{4\pi} \int_0^\infty \xi J_1(r\xi) \{e^{-\xi(h+z)} + e^{-\xi(h-z)}\} d\xi \quad (2.136)$$

Substituting (2.136) into (2.133) and integrating the resulting equation with respect to z gives

$$E_\theta = - \frac{iM\mu_0^2 \omega^2 \sigma_1 \sin\theta}{4\pi} \int_0^\infty \{e^{-\xi z} - e^{+\xi z}\} J_0(\xi r) + \frac{2G_+(\xi, 0)}{n + \xi} e^{\xi z} \{ \xi J_0(\xi r) - \frac{J_1(\xi r)}{r} \} \xi e^{-\xi h} d\xi \quad (2.137)$$

The constant of integration is zero since E_θ in (2.137) must match E_θ given by (2.118) in the region $0 < z < d$ at the boundary $z=0$. Similarly substituting into (2.134) and integrating with respect to z

$$E_r = \frac{iM\mu_0^2 \omega^2 \sigma_1 \cos\theta}{4\pi} \int_0^\infty \{(e^{-\xi z} - e^{\xi z}) J_0(r\xi) + \frac{2G_+(\xi, 0)}{n + \xi} e^{\xi z} \frac{J_1(r\xi)}{r}\} \cdot \xi e^{-\xi h} d\xi \quad (2.138)$$

In this way, the fields associated with a horizontal dipole above a layered conductor may be determined. The foregoing solutions were used for all boundary conditions involving horizontal magnetic dipoles in this work.

2.8 Three-Dimensional Finite Difference Numerical Technique

Many conductivity inhomogeneities of the earth's magnetic variation field can be studied by using two-

dimensional methods. However, some conductivity anomalies such as the Alert, Tucson and Japanese anomalies require a three-dimensional treatment. Also any embedded anomaly with approximately equal spatial dimensions requires a three-dimensional treatment.

Jones and Pascoe(1972) treated the local induction problem in three dimensions for an imbedded cube. Maxwell's equations were solved over a three dimensional uniform grid by the use of finite difference approximations and the Gauss-Seidel iterative method. Lines and Jones (1973) extended the work to a grid with variable dimensions so that more general anomalies could be accommodated and so that the external boundary conditions could be better satisfied. The basic method is described in Lines (1972) and is summarized here.

If the curl of equation (2.2) is taken and substituted into equation (2.1) then the resulting equation for \underline{E} is

$$\nabla^2 \underline{E} - \nabla(\nabla \cdot \underline{E}) = i \omega \mu_0 \sigma \underline{E} \quad (2.139)$$

where the field is assumed to have a time dependence of $e^{(i\omega t)}$ where ω is the angular frequency and the period is sufficiently long so that displacement currents can be neglected. The conductivity σ is that appropriate for the region being considered and μ_0 is the magnetic permeability

of free space. All components of \underline{E} vary with x , y , and z in Cartesian coordinates.

The above vector equation in \underline{E} can be rewritten as three scalar equations

$$\frac{\partial^2 E_x}{\partial y^2} + \frac{\partial^2 E_x}{\partial z^2} - \frac{\partial}{\partial x} \left(\frac{\partial E_y}{\partial y} + \frac{\partial E_z}{\partial z} \right) = i \omega \mu_0 \sigma E_x, \quad (2.140)$$

$$\frac{\partial^2 E_y}{\partial x^2} + \frac{\partial^2 E_y}{\partial z^2} - \frac{\partial}{\partial y} \left(\frac{\partial E_x}{\partial x} + \frac{\partial E_z}{\partial z} \right) = i \omega \mu_0 \sigma E_y, \quad (2.141)$$

$$\frac{\partial^2 E_z}{\partial x^2} + \frac{\partial^2 E_z}{\partial y^2} - \frac{\partial}{\partial z} \left(\frac{\partial E_x}{\partial x} + \frac{\partial E_y}{\partial y} \right) = i \omega \mu_0 \sigma E_z. \quad (2.142)$$

These three equations are solved simultaneously for E_x , E_y and E_z .

In the discussion of the numerical method, only (2.140) will be considered. A similar procedure is used in evaluating (2.141) and (2.142). The three-dimensional finite difference grid is shown in Fig. 2.15. The numerical formulation for point '0' is considered. The distance to adjacent points in the grid are in general unequal. Eight conductivity regions surround the point, '0'. The subscripts of the electric field components refer to the points on the grid of Fig. 2.15 at which the components are evaluated.

In (2.140), the finite difference expressions for $\partial^2 E_x / \partial y^2$ and $\partial^2 E_x / \partial z^2$ at the point '0' are evaluated by using the first three terms of a Taylor series expansion. For $\partial^2 E_x / \partial y^2$

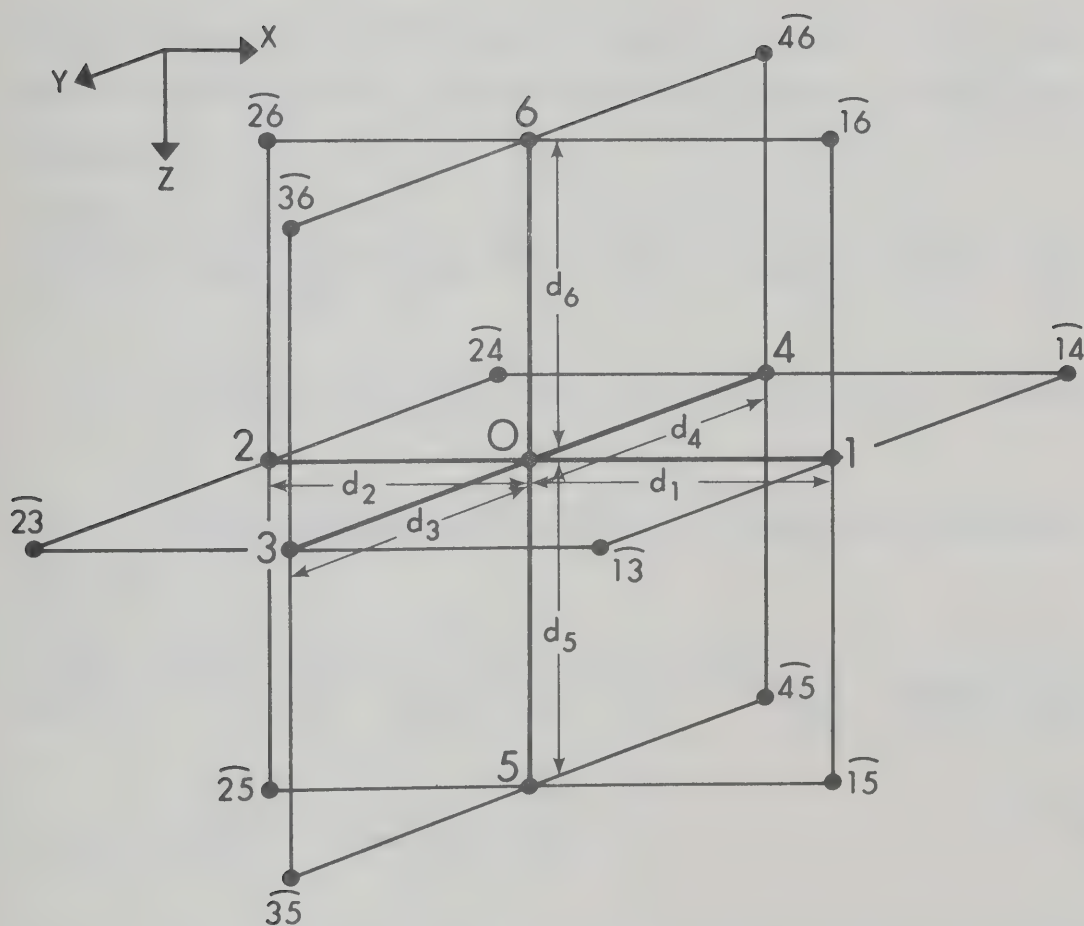


Figure 2.15 Finite difference grid (from Lines, 1972).

$$E_{x3} = E_{x0} + \left(\frac{E_{x3} - E_{x4}}{d_3 + d_4} \right) d_3 + \frac{1}{2} \left(\frac{\partial^2 E_x}{\partial y^2} \right)_0 d_3^2 \quad (2.143)$$

and

$$E_{x4} = E_{x0} - \left(\frac{E_{x3} - E_{x4}}{d_3 + d_4} \right) d_4 + \frac{1}{2} \left(\frac{\partial^2 E_x}{\partial y^2} \right)_0 d_4^2, \quad (2.144)$$

where the central differences have been used for $(\partial E_x / \partial y)$. The value $(\partial^2 E_x / \partial y^2)_0$ is derived by combining (2.143) and (2.144):

$$\begin{aligned} \left(\frac{\partial^2 E_x}{\partial y^2} \right)_0 &= E_{x3} \left(\frac{1}{d_3^2} + \frac{1}{d_3 + d_4} \left(\frac{1}{d_4} - \frac{1}{d_3} \right) \right) + E_{x4} \left(\frac{1}{d_4^2} + \frac{1}{d_3 + d_4} \left(\frac{1}{d_3} - \right. \right. \\ &\quad \left. \left. \frac{1}{d_4} \right) \right) - E_{x0} \left(\frac{1}{d_3^2} + \frac{1}{d_4^2} \right). \end{aligned} \quad (2.145)$$

The value of $(\partial^2 E_x / \partial z^2)_0$ is found in a similar manner:

$$\begin{aligned} \left(\frac{\partial^2 E_x}{\partial z^2} \right)_0 &= E_{x5} \left(\frac{1}{d_5^2} + \frac{1}{d_5 + d_6} \left(\frac{1}{d_6} - \frac{1}{d_5} \right) \right) + E_{x6} \left(\frac{1}{d_6^2} + \frac{1}{d_5 + d_6} \left(\frac{1}{d_5} - \right. \right. \\ &\quad \left. \left. \frac{1}{d_6} \right) \right) - E_{x0} \left(\frac{1}{d_5^2} + \frac{1}{d_6^2} \right). \end{aligned} \quad (2.146)$$

The mixed partial derivatives, $\partial / \partial x (\partial E_y / \partial y)$ and $\partial / \partial x (\partial E_z / \partial z)$, are evaluated through the use of central difference formulae. To find $\partial / \partial x (\partial E_y / \partial y)$ at the point '0', we use central differences, in the x direction, of the central difference expressions for $\partial E_y / \partial y$ nearest the point '0'.

$$\frac{\partial}{\partial x} \left(\frac{\partial E_y}{\partial y} \right)_0 = \frac{1}{d_1+d_2} \left\{ \frac{(E_{y13} - E_{y14})}{d_3+d_4} - \frac{(E_{y23} - E_{y24})}{d_3+d_4} \right\} \quad (2.147)$$

and

$$\frac{\partial}{\partial x} \left(\frac{\partial E_z}{\partial z} \right)_0 = \frac{1}{d_1+d_2} \left\{ \frac{(E_{z15} - E_{z16})}{d_5+d_6} - \frac{(E_{z25} - E_{z26})}{d_5+d_6} \right\} \quad (2.148)$$

Upon substitution of the finite difference expressions for $(\partial^2 E_x / \partial y^2)_0$, $(\partial^2 E_x / \partial z^2)_0$, $\partial / \partial x (\partial E_y / \partial y)_0$ and $\partial / \partial x (\partial E_z / \partial z)_0$ in (2.140) the following finite difference equation is obtained.

$$\begin{aligned} & - E_{x0} \left(\frac{1}{d_3^2} + \frac{1}{d_4^2} + \frac{1}{d_5^2} + \frac{1}{d_6^2} \right) + E_{x3} D_3 + E_{x4} D_4 + E_{x5} D_5 + E_{x6} D_6 \\ & - \frac{1}{d_1+d_2} \left[\frac{1}{d_3+d_4} (E_{y13} - E_{y14} - E_{y23} + E_{y24}) \right. \\ & \left. + \frac{1}{d_5+d_6} (E_{z15} - E_{z16} - E_{z25} + E_{z26}) \right] = i \omega \mu_0 \sigma E_{x0} \end{aligned} \quad (2.149)$$

Similarly for (2.141) and (2.142)

$$\begin{aligned} & - E_{y0} \left(\frac{1}{d_1^2} + \frac{1}{d_2^2} + \frac{1}{d_5^2} + \frac{1}{d_6^2} \right) + E_{y1} D_1 + E_{y2} D_2 + E_{y5} D_5 + E_{y6} D_6 \\ & - \frac{1}{d_3+d_4} \left[\frac{1}{d_1+d_2} (E_{x13} - E_{x23} - E_{x14} + E_{x24}) \right. \\ & \left. + \frac{1}{d_5+d_6} (E_{z35} - E_{z36} - E_{z45} + E_{z46}) \right] = i \omega \mu_0 \sigma E_{y0} \end{aligned} \quad (2.150)$$

and

$$\begin{aligned}
 & - E_{z0} \left(\frac{1}{d_1^2} + \frac{1}{d_2^2} + \frac{1}{d_3^2} + \frac{1}{d_4^2} \right) + E_{z1} D_1 + E_{z2} D_2 + E_{z3} D_3 + E_{z4} D_4 \\
 & - \frac{1}{d_5 + d_6} \left[\frac{1}{d_1 + d_2} (E_{x15} - E_{x25} - E_{x16} + E_{x26}) \right. \\
 & \left. + \frac{1}{d_3 + d_4} (E_{y35} - E_{y45} - E_{y36} + E_{y46}) \right] = i \omega \mu_0 \sigma E_{z0}
 \end{aligned}
 \tag{2.151}$$

where

$$\begin{aligned}
 D_1 &= \frac{1}{d_1^2} + \frac{1}{d_1 + d_2} \left(\frac{1}{d_2} - \frac{1}{d_1} \right) \\
 D_2 &= \frac{1}{d_2^2} + \frac{1}{d_1 + d_2} \left(\frac{1}{d_1} - \frac{1}{d_2} \right) \\
 D_3 &= \frac{1}{d_3^2} + \frac{1}{d_3 + d_4} \left(\frac{1}{d_4} - \frac{1}{d_3} \right) \\
 D_4 &= \frac{1}{d_4^2} + \frac{1}{d_3 + d_4} \left(\frac{1}{d_3} - \frac{1}{d_4} \right) \\
 D_5 &= \frac{1}{d_5^2} + \frac{1}{d_5 + d_6} \left(\frac{1}{d_6} - \frac{1}{d_5} \right) \\
 \text{and } D_6 &= \frac{1}{d_6^2} + \frac{1}{d_5 + d_6} \left(\frac{1}{d_5} - \frac{1}{d_6} \right) .
 \end{aligned}
 \tag{2.152}$$

These equations must be simultaneously satisfied at each interior point of each region. As in the two-dimensional work of Jones and Pascoe (1971), the 'fictitious' values, Smith (1969), must be eliminated by application of

the internal boundary conditions. The condition that the tangential components of \underline{E} and \underline{H} must be continuous eliminate 2/3 of the 'fictitious values'. A problem arises when \underline{E} is normal to a boundary for which σ is discontinuous. \underline{J} must be continuous across the boundary. If σ is discontinuous at a boundary, then \underline{E} must also be discontinuous. However, this cannot be represented by a point value at the boundary. Therefore, the average of \underline{E} on each side of the boundary is used. When expressions of (2.149), (2.150) and (2.151) are summed over all eight regions surrounding the point '0' and the boundary conditions are applied to \underline{E} , the resulting expressions are of the same form as in (2.149), (2.150) and (2.151) with σ being replaced by $\bar{\sigma}$ the average of all the conductivities of the surrounding regions. This implies that discontinuities in conductivity are represented by transition zones between the regions of different conductivity.

The resulting finite difference equations (2.149), (2.150) and (2.151) are solved by using the Gauss-Seidel relaxation technique for simultaneous linear equations.

Initial values are required throughout the interior of the grid to start the iterative process. As shown in the preceding sections of this chapter, these initial values may be determined analytically for a layered half-space. In the next section various source configurations are considered and the boundary conditions for the finite difference mesh

are determined. The solution of the local three-dimensional problem is then obtained for various embedded conductivity anomalies and frequencies.

2.9 Electromagnetic Induction in Three-Dimensional Structures for Various Source Fields

In this section the numerical method is used to calculate the electromagnetic fields associated with three-dimensional conductivity anomalies. Three source field-conductivity structure combinations are considered. A uniform source above an island structure as well as a two-dimensional non-uniform source above an L-shaped embedded structure and a horizontal dipole above an embedded square anomaly are studied. Profiles of selected electromagnetic field quantities and ratios are presented along with the appropriate phases for various positions relative to the anomalous structure. Three dimensional figures of the amplitudes of the electric and magnetic field components are given for each source field-conductivity structure combination. The source field effect is clearly evident in all profiles.

The electromagnetic fields due to one, two, and three-dimensional sources over layered laterally uniform conductors are calculated as discussed previously. For the one-dimensional source the analytical solution for the layered earth as in section 2.4, is used here. For the

two-dimensional source configuration the Fourier series method as described in section 2.6 is used, and for the three-dimensional dipole source the method of Ramaswamy (1973) as described in section 2.7 is used. As pointed out before, the electric field values thus calculated are used to provide boundary and initial conditions for the finite difference mesh of Section 2.8 and from this the electric fields due to three-dimensional embedded conductivity anomalies are determined. The magnetic field quantities are then obtained from the electric field solutions by using the appropriate finite difference equation.

2.9.1 One-Dimensional Source Field

The one-dimensional source field consists of a uniform sheet current flowing above a layered conductor. In the present work, the E-polarization case is considered and the electric field component is polarized in the x -direction with the magnetic field component polarized in the y -direction.

In the model considered, a uniform sheet current flows above a conductivity inhomogeneity embedded in a two-layered semi-infinite conducting region with a plane boundary, which approximates an island in the deep ocean for geomagnetic bay type disturbances. The first layer is 4 km in depth and of conductivity 4 mho/m. The second layer extends to infinity and has conductivity 0.001 mho/m. The embedded anomaly is a 6 km square intrusion

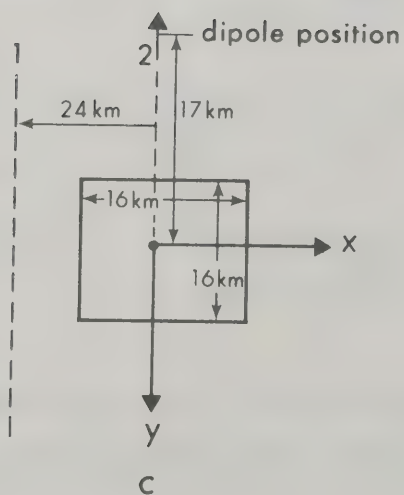
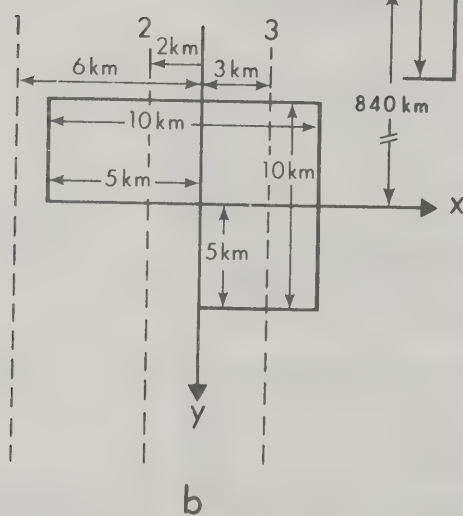
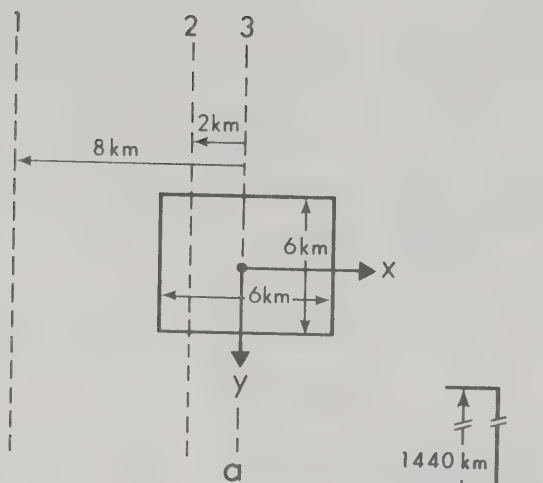
of the lower conductive layer which penetrates the top layer to the surface of the conductor. The calculation was done for a frequency of 0.001 Hz.

From the foregoing solution the profiles of E_x , H_y , H_z , H_z/H_y and the apparent resistivity (calculated in the manner of Cagniard, 1953), as well as their respective phases were calculated for 3 profiles at different positions relative to the anomaly as in Fig. 2.16. The profiles were calculated over the range - 58 km to + 58 km in the y direction. Each field component or ratio with the exception of the apparent resistivity and $|H_z/H_y|$ was normalized with respect to its value at -58 km. All phases are normalized to zero at - 58 km.

The first set of profiles is taken 8 km from the center of the anomaly in the negative x direction and is given in Fig. 2.17. The normalized electric field amplitude E_x , exhibits a slight depression in the field due to the concentration of charge on the boundary of the anomaly. The normalized horizontal magnetic field $|H_y|$ is reasonably constant across this profile and changes by only about 4 percent. Normalized $|H_z|$ and therefore $|H_z/H_y|$ vary in the same manner over the anomaly due to the constant nature of H_y . Since both $|E_x|$ and $|H_y|$ are nearly constant the apparent resistivity (ρ_a) curve is nearly constant at a value of 1 ohm-m. The value differs from the actual resistivity of .25 ohm-m because of the long period used since

Figure 2.16 Anomalous structures with profile positions
(1, 2, 3) indicated,

- (Not to scale)
- a. Anomaly associated with one-dimensional source
 - b. Anomaly associated with two-dimensional source
 - c. Anomaly associated with three-dimensional source



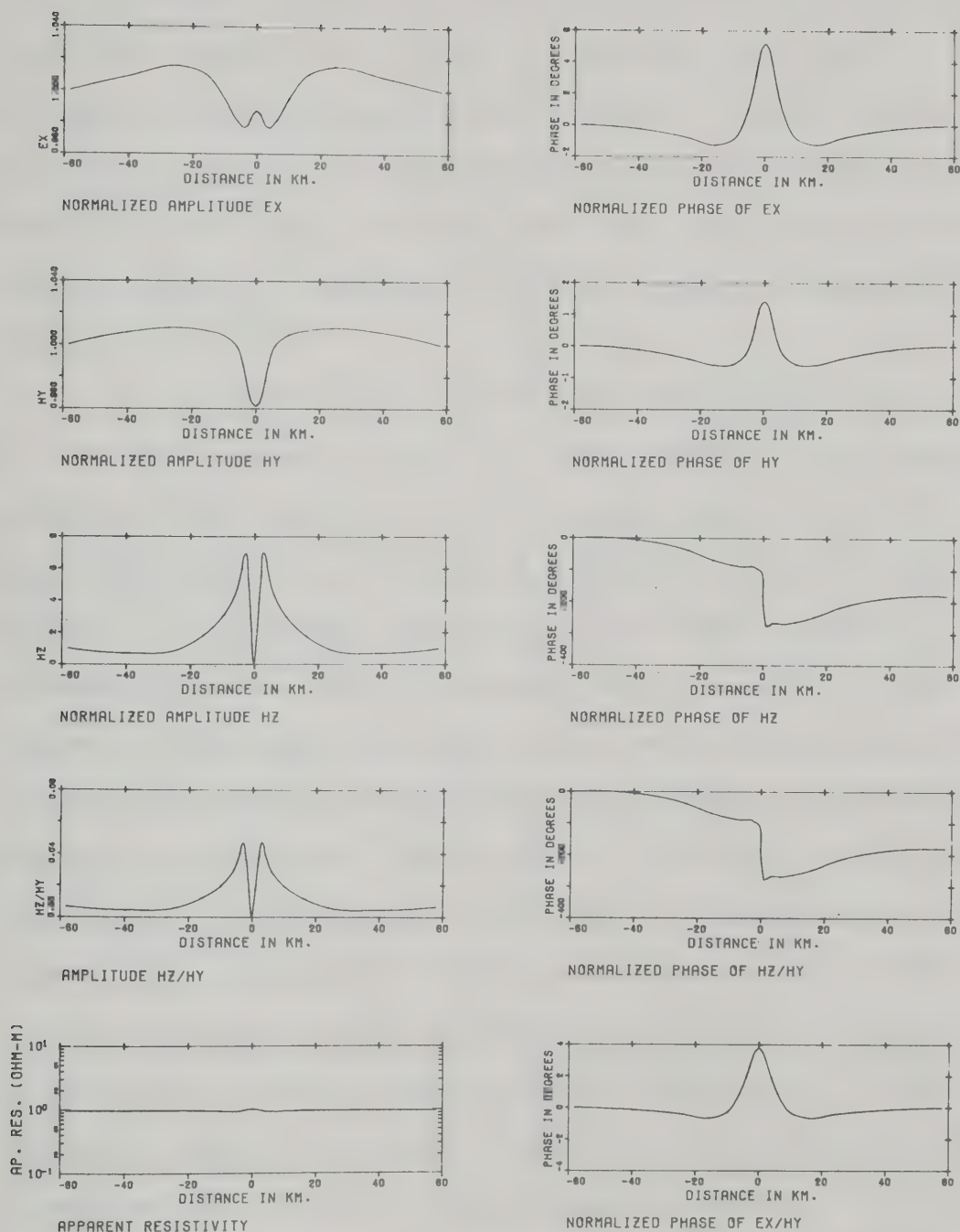


Figure 2.17 Normalized $|E_x|$, $|H_y|$, $|H_z|$, $|H_z/H_y|$ and ρ_a profiles with normalized phases for one-dimensional source field and profile 1.

the calculated apparent resistivity value is influenced by the lower conductivity region. The phases are nearly constant, varying by only a few degrees, for all profiles except H_z and H_z/H_y . As would be expected, the phase of H_z and therefore H_z/H_y shifts by 180° over the center of the anomaly, which is consistent with the change of sign of H_z there.

The second set of profiles, taken along the line $x = -2$ km is given in Fig. 2.18 and clearly illustrates the effects of the anomaly. $|E_x|$ increases over the anomaly and $|H_y|$ decreases. $|H_z|$ and $|H_z/H_y|$ markedly increase over the anomaly. The apparent resistivity now shows a small increase in value over the anomaly and its value is two orders of magnitude below the actual resistivity value. The size of the anomaly is insufficient to cause an appreciable change in the apparent resistivity. The phase of the electric field, E_x , changes by a maximum of 23 degrees over the anomaly when compared to the phase of the electric field at -58 km. The phase of the apparent resistivity is similar to the electric field phase since the phase of H_y is nearly constant. Again the phases of H_z and H_z/H_y change by 180 degrees as the center of the anomaly is crossed.

The third set of profiles, taken across the center of the anomaly is given in Fig. 2.19. This set is almost identical with the second set of profiles except that $|E_x|$ is more sharply peaked as would be expected.

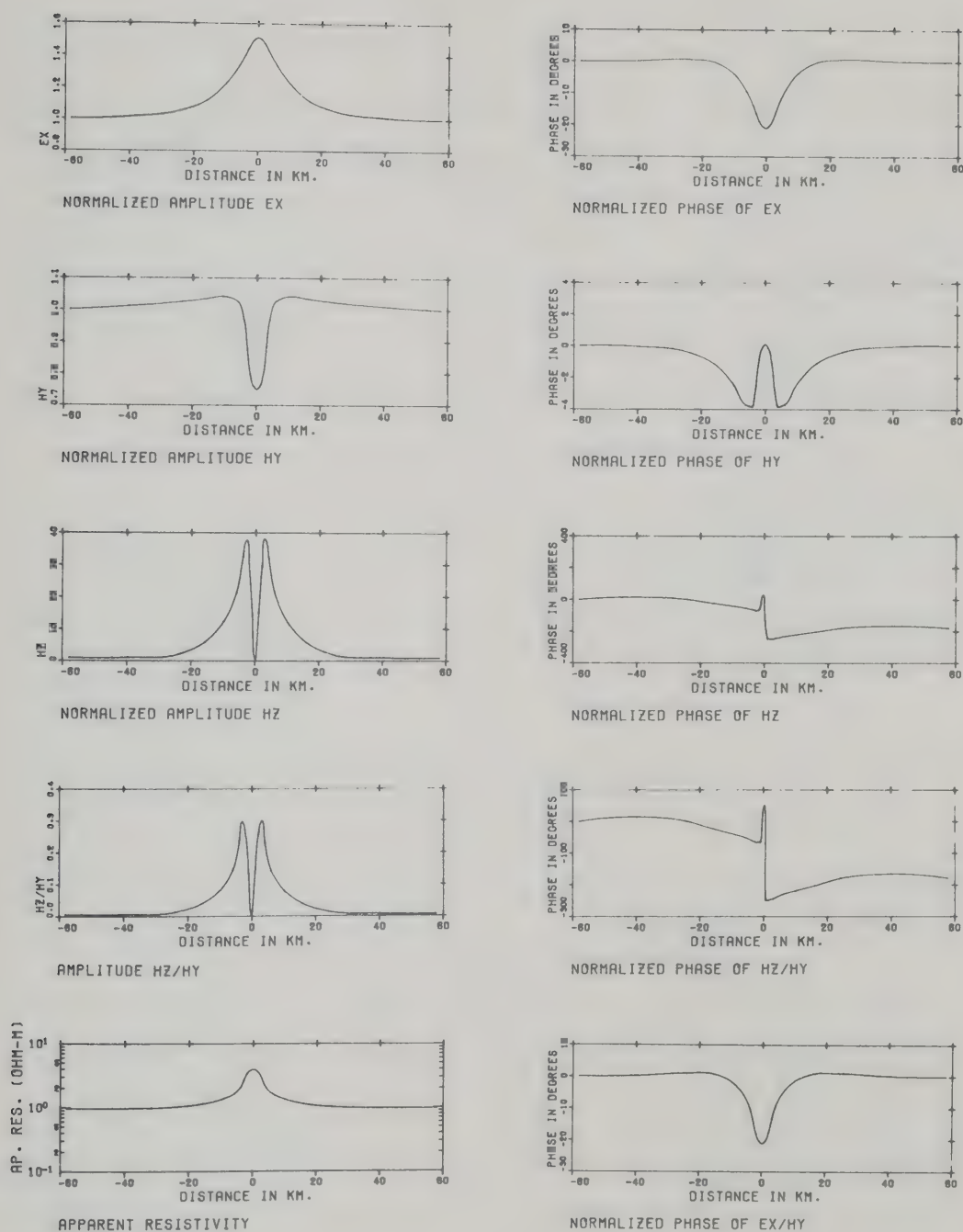


Figure 2.18 As Fig. 2.17, but for profile 2.

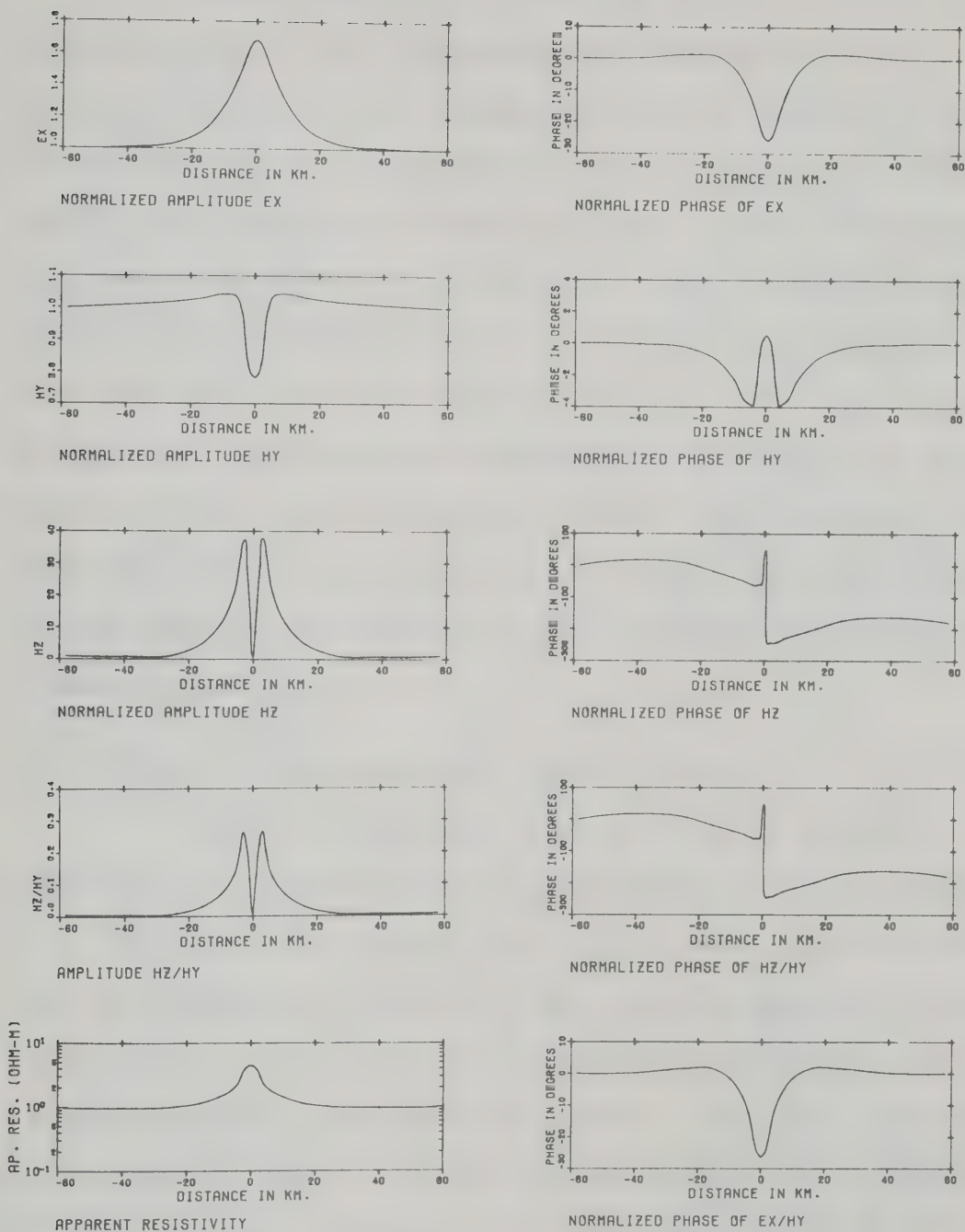


Figure 2.19 As Fig. 2.17, but for profile 3.

Three-dimensional amplitude profiles of the six electromagnetic field components are presented in Fig. 2.20. The decrease in the $|E_x|$ component off the anomaly in the x-direction due to the concentration of charge at the boundary of the anomaly is clearly evident. Over the anomaly $|E_x|$ increases while $|H_y|$ decreases. $|H_z|$ increases over the edges of the anomaly in the + y and - y directions. Near the corners of the anomaly both $|E_y|$ and $|H_x|$ increase as would be expected due to bending of the fields in these regions. The vertical electric field, $|E_z|$, increases on both sides of the anomaly in the + x and - x directions. This is because the current is deflected vertically by the island structure.

2.9.2 Two-Dimensional Source Field

The two-dimensional source field is obtained from a non-uniform sheet current flowing above a layered conductor. Again, in the present work, only the E-polarization case is considered since it is most easily adapted to the formulation of the solution for the electromagnetic fields of a non-uniform sheet current source. For this case both the horizontal magnetic field component, H_y , and the vertical magnetic field component, H_z , will be present in the solution for a layered conducting subsurface.

In this work, a sheet current of rectangular intensity distribution, simulating an ionospheric electrojet, which is 1440 km in width and centered

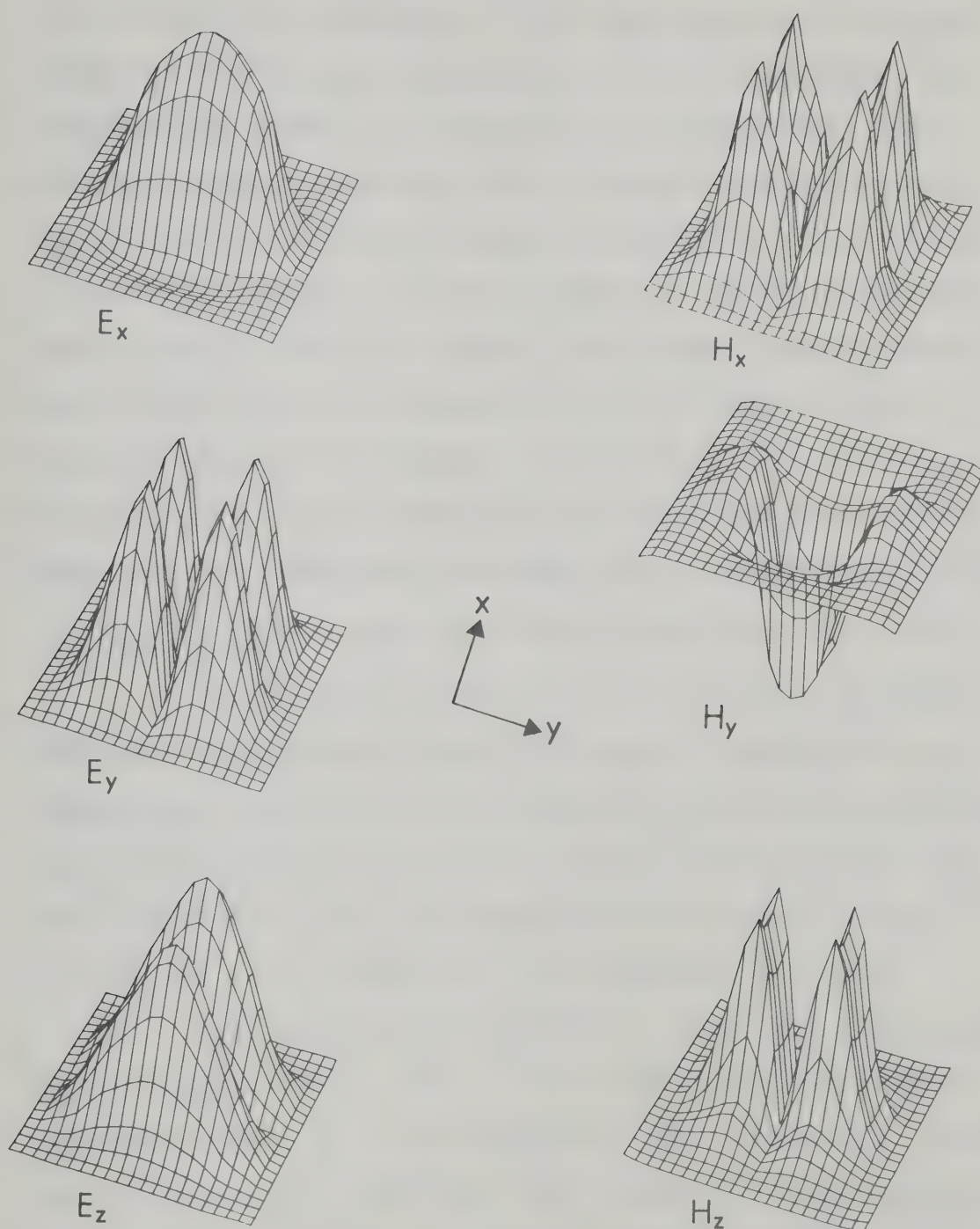


Figure 2.20 Three-dimensional profiles of $|E_x|$, $|E_y|$, $|E_z|$, $|H_x|$, $|H_y|$ and $|H_z|$ for one-dimensional source field.

840 km from the center of the L-shaped embedded anomaly (Fig. 2.16b) is considered. This sheet current flows at a height of 110 km above the surface of the conductor. The conductivity anomaly is embedded in a two-layered, semi-infinite conducting region with a plane boundary which is chosen to represent an average continental vertical conductivity distribution. The first layer is 50 km in thickness and of conductivity 0.01 mho/m. The second layer extends to infinity and has a conductivity of 0.1 mho/m. The embedded anomaly is L-shaped, as in Fig. 2.16b, and has a depth of 3 km. The conductivity of the anomaly is 0.0001 mho/m and the calculation is done for a frequency of 0.1 Hz in order to enhance the magnitude of the anomalous field.

The boundary conditions for the finite difference mesh were determined by using the general method for two-dimensional sheet current distributions over layered conductors as described in section 2.6 above. These values were then substituted into the numerical technique of Section 2.8 and the electromagnetic field solutions obtained.

The three profile positions chosen for this anomaly are shown in Fig. 2.16b. The profiles are calculated over the range - 38 km to + 38 km in the y -direction. Each field component or ratio with the exception of the apparent resistivity and $|H_z/H_y|$ is normalized with respect to its value at - 38 km. All phases are normalized to zero at - 38 km.

The first set of profiles, which is taken 6 km from the center of the anomaly in the x -direction is shown



in Fig. 2.21. The sloping character of the source field is clearly evident in the $|E_x|$, $|H_y|$ and $|H_z|$ profiles. Since the conductivity contrast is only 100 to 1, the effect of the anomaly at this profile position is not evident for $|E_x|$ and $|H_y|$ at this frequency. Also, as will be seen later, the rapid change in the source field tends to screen the effect of the anomaly when the fields are normalized. The effect of the anomaly can be clearly seen in the $|H_z|$ and $|H_z/H_y|$ profiles. The apparent resistivity is constant for this profile and corresponds in value to the conductivity of the upper layer. The phases are sensibly uniform for all quantities for this profile position although the expanded scale of the diagram amplifies any change in phase.

The second set of profiles (Fig. 2.22) is taken 2 km from the center of the anomaly in the x -direction. These show effects due to the anomaly. The anomaly is just evident in the $|E_x|$ profile while in the $|H_y|$ profile the dipping of the profile due to the anomaly is apparent. The $|H_z/H_y|$ profiles clearly show the effect of the anomalous structure. As before, the apparent resistivity profile shows a slight increase due to the anomaly. However, the size of the structure is too small for the apparent resistivity to have a value equal to the resistivity of the anomaly which is 10000. ohm-m. A noticeable change in the phases of both H_z and H_z/H_y is now evident over the anomaly

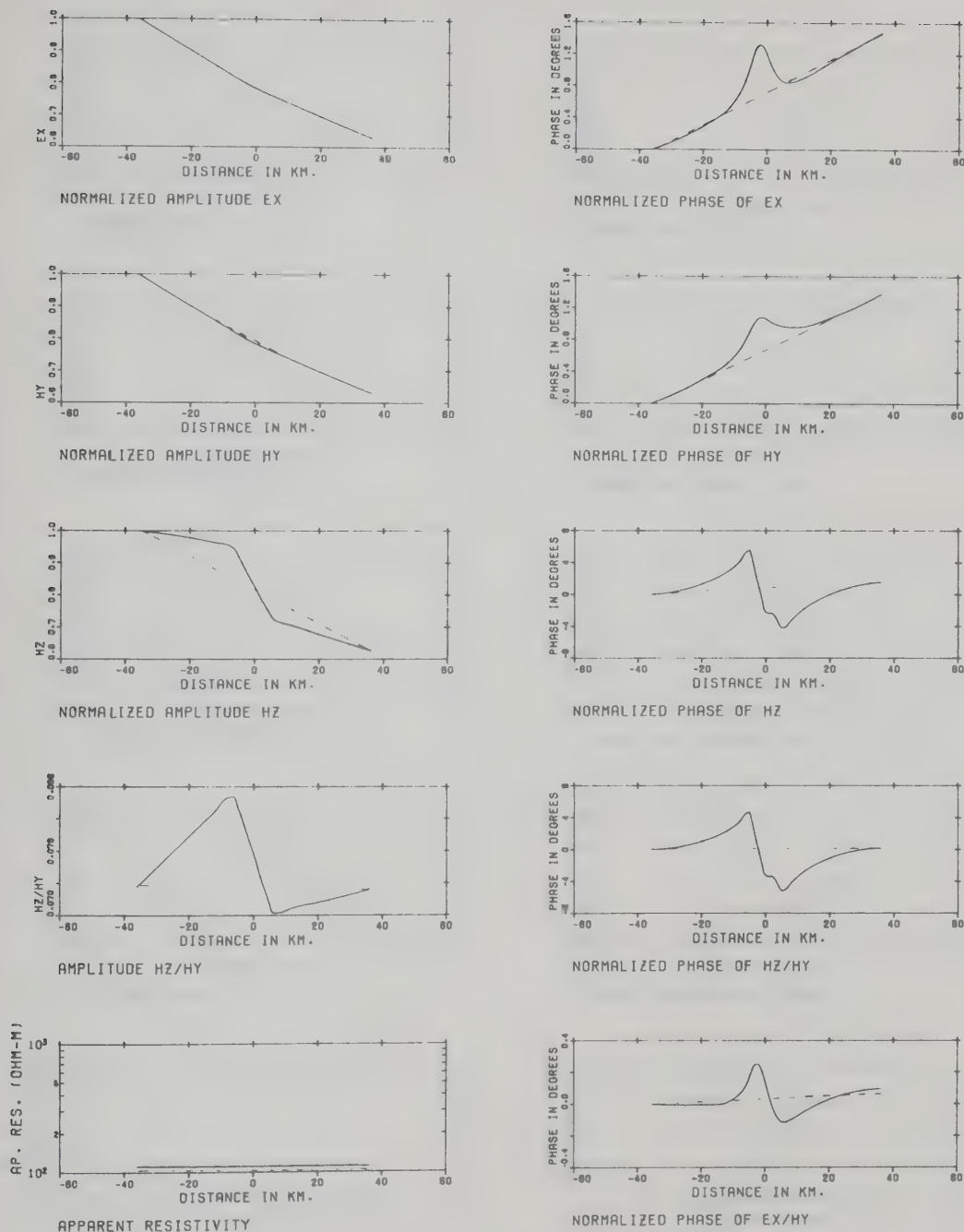


Figure 2.21 Normalized $|E_x|$, $|H_y|$, $|H_z|$, $|H_z/H_y|$ and ρ_a profiles with normalized phases for two-dimensional source field and profile 1.

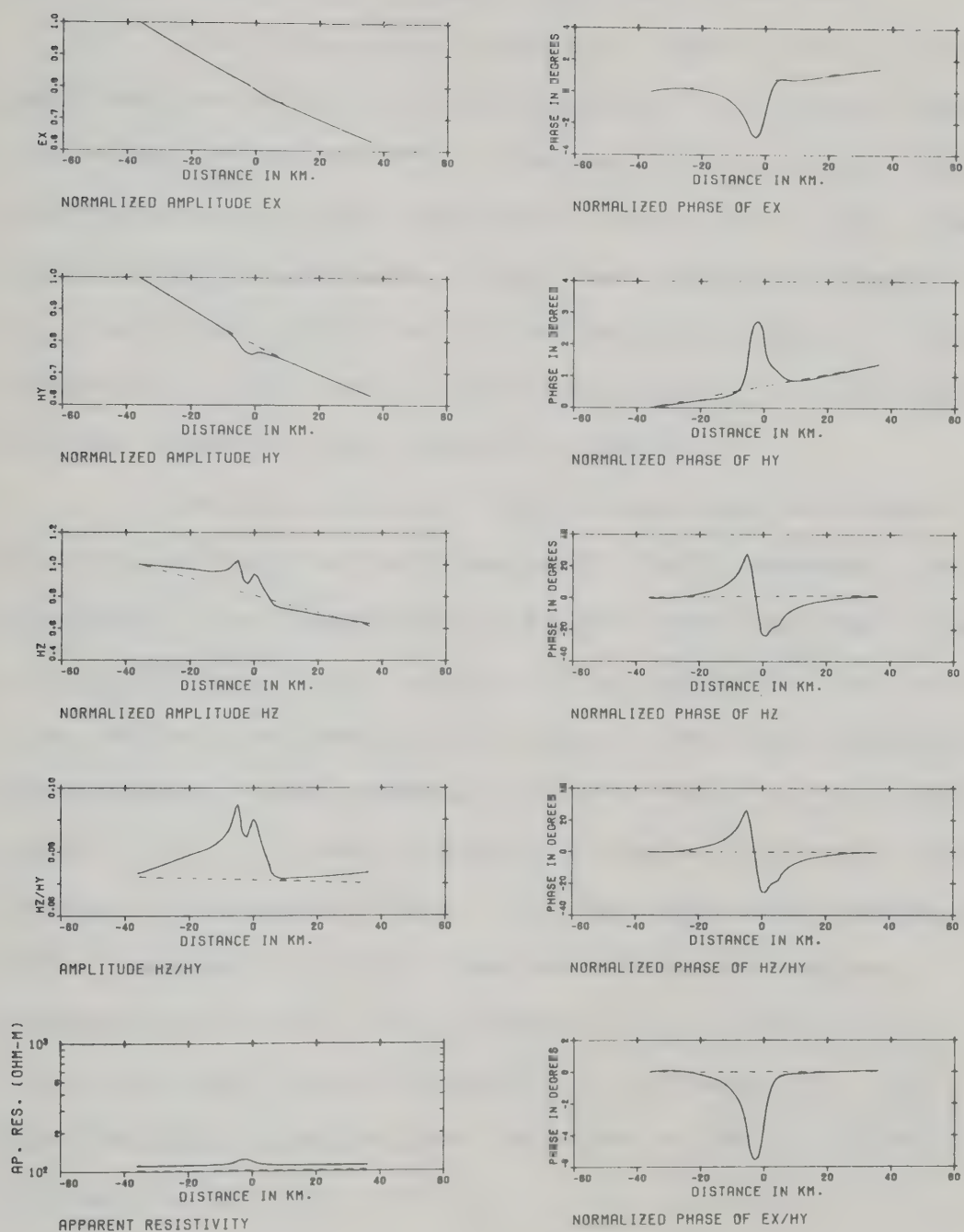


Figure 2.22 As Fig. 2.21, but for profile 2.

while the other phases remain relatively constant.

The third set of profiles, given in Fig. 2.23 is much the same in form as the second set of profiles. However, the effect of the anomaly is apparent over a greater distance than before due to the increase in the width of the anomaly at this profile position. Also, more clearly evident in the $|H_z|$ and $|H_z/H_y|$ profiles is the induction effect of the H_z component of the source field. The peaks in the $|H_z|$ profile are not symmetric and differ in character.

In Fig. 2.24 the three-dimensional amplitude profiles of the six electromagnetic field components are presented. The figures are distorted near the edges since a non-uniform grid was used in calculating the field solutions while a uniform grid is used in the three-dimensional presentation. The anomalous electric field in the x -direction, $|E_x|$, is barely discernible due to the rapid spatial change of the source field. All the other electromagnetic field components clearly show the effects of the non-symmetric structure. The corners of the structures are identified with large increases in $|E_y|$ and $|H_x|$. $|H_y|$ dips over the structure and the edges of the structure are outlined by $|H_z|$ and $|E_z|$.

2.9.3 Three-Dimensional Source Field

A three-dimensional source field can be obtained by using a horizontal magnetic dipole as a source as outlined in section 2.7 above.

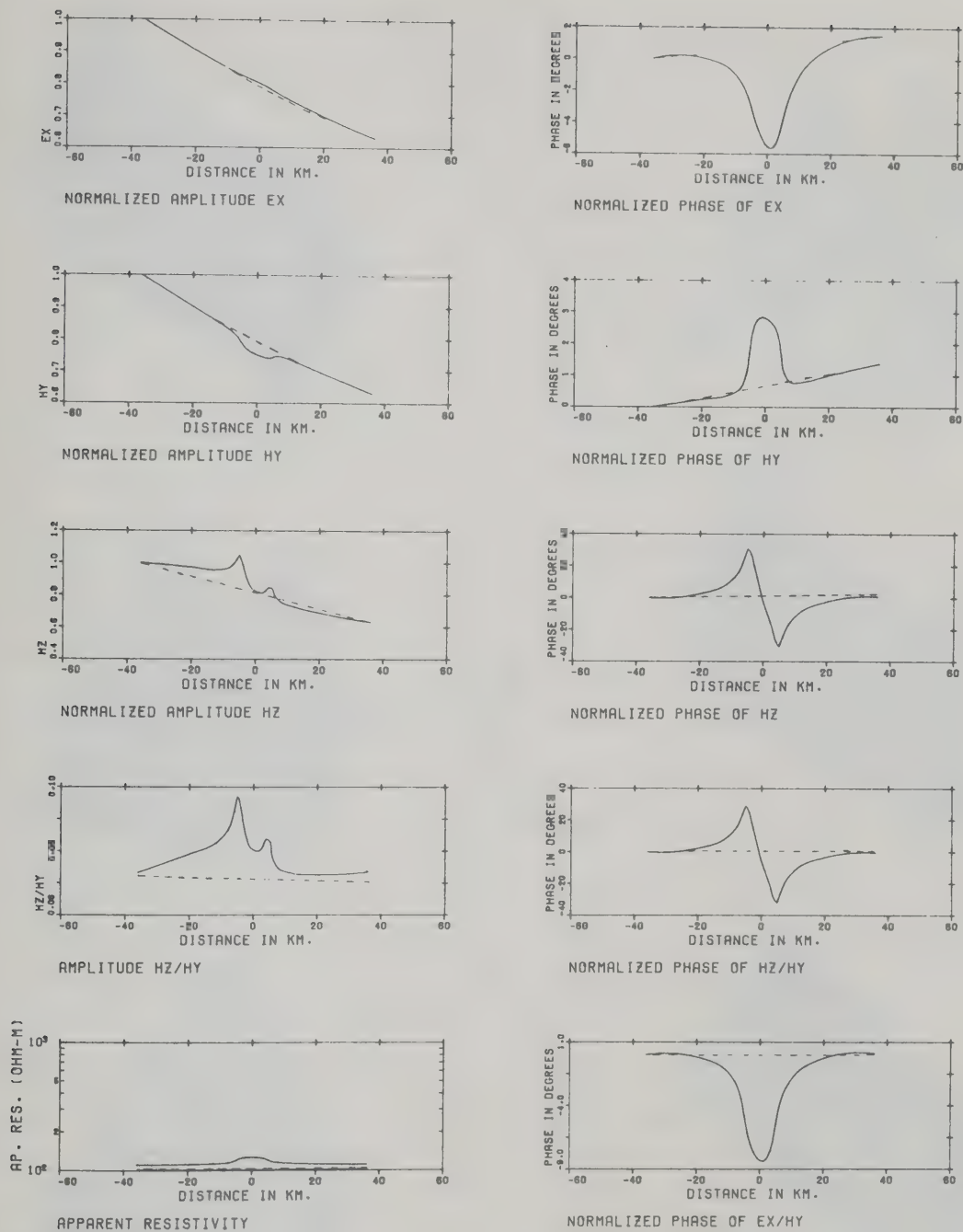


Figure 2.23 As Fig. 2.21, but for profile 3.



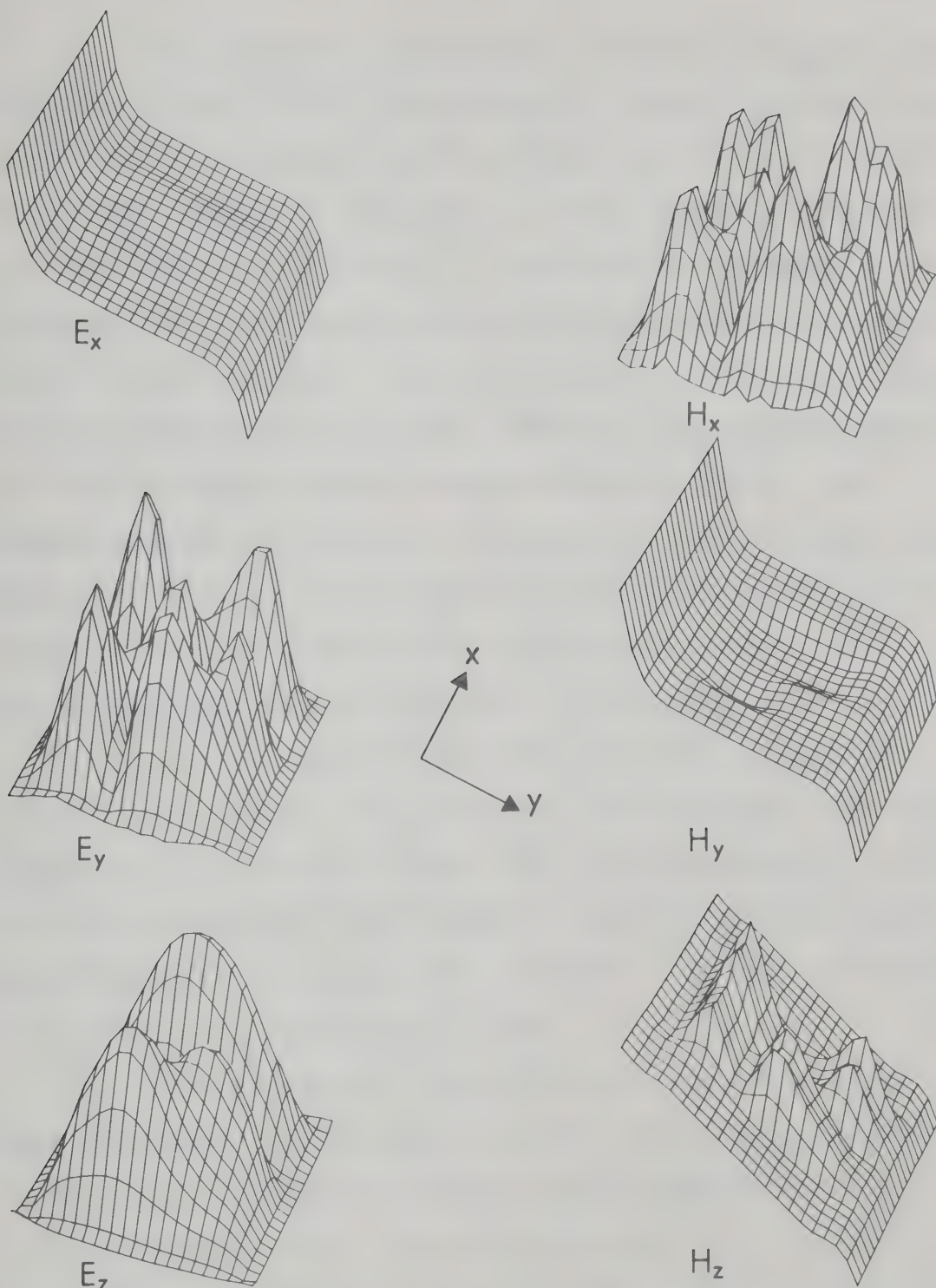


Figure 2.24 Three-dimensional profiles of $|E_x|$, $|E_y|$, $|E_z|$, $|H_x|$, $|H_y|$ and $|H_z|$ for two-dimensional source field.

In the model considered a horizontal magnetic dipole was placed 17 km in the negative y -direction from the center of the anomaly (see Fig. 2.16c) at a height of 150 km above the surface of the anomaly. The dipole is polarized in the negative y -direction. The conductivity anomaly is embedded in a two-layered, semi-infinite conducting region with a plane boundary. The first layer is 128 km in depth and of conductivity 0.21×10^{-3} mho/m. The second layer is of infinite depth and has conductivity 0.8 mho/m. The embedded anomaly (see Fig. 2.16c) is 16 km square and 4 km deep with its top at the surface of the conducting region and has the same conductivity as the lower layer. This calculation was carried out for a frequency of 0.075 Hz.

The two profile positions for this anomaly are shown in Fig. 2.16c. The profiles are calculated over the range $y = -42$ km to $y = +42$ km. Each field component or ratio with the exception of the apparent resistivity and $|H_z/H_y|$ is normalized with respect to its value at -42 km. All phases are normalized to zero at -42 km.

The first set of profiles which is taken 24 km from the center of the anomaly in the x -direction is shown in Fig. 2.25. The non-uniformity of the source field is clearly evident in all the amplitude profiles. For this frequency and conductivity contrast the anomalous structure is evident at this distance away from the anomaly. There is an increase due to the source field

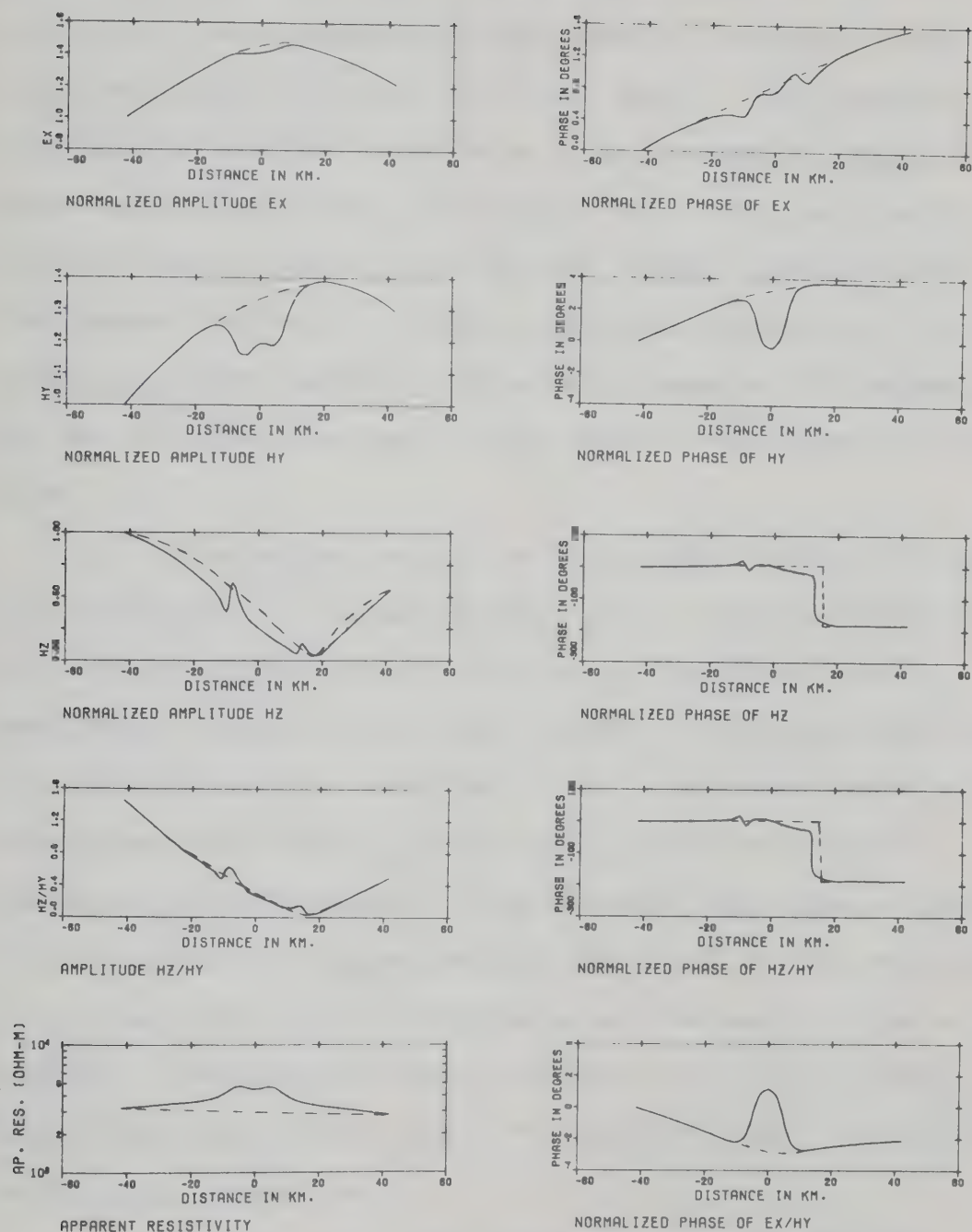


Figure 2.25 Normalized $|E_x|$, $|H_y|$, $|H_z|$, $|H_z/H_y|$ and ρ_a profiles with normalized phases for three-dimensional source field and profile 1.

— Total field due to anomaly
 ---- Normal field without anomaly

in the $|E_x|$ profile and a depression in the $|H_y|$ profile. The boundaries of the anomaly are shown in the $|H_z|$ and $|H_z/H_y|$ profile by slight peaks. The apparent resistivity profile exhibits a slight increase, opposite to what would be expected, because of the increased electric field in that region caused by the charge concentration. The phases are nearly constant with the exception of the H_z and H_z/H_y phases which go through a change of 180 degrees as the vertical component of the source field goes through zero.

The second set of profiles, taken across the center of the anomaly, is shown in Fig. 2.26. In these profiles the effect of the anomaly is clearly displayed in all amplitude components and their phases. A marked depression in the $|E_x|$ profile is evident. $|H_y|$ increases rapidly over the anomaly and the $|H_z|$ and $|H_z/H_y|$ profiles exhibit two peaks over the edges of the anomaly. The apparent resistivity varies from approximately the value of the resistivity of the first layer to the value of the resistivity of the anomaly. Increases in phase are noted for E_x , H_y and ρ_a while the phases of H_z and H_z/H_y change by 180° as the source field goes through zero.

In Fig. 2.27 the three-dimensional amplitude profiles of the six electromagnetic field components are presented for the three-dimensional source field case. A

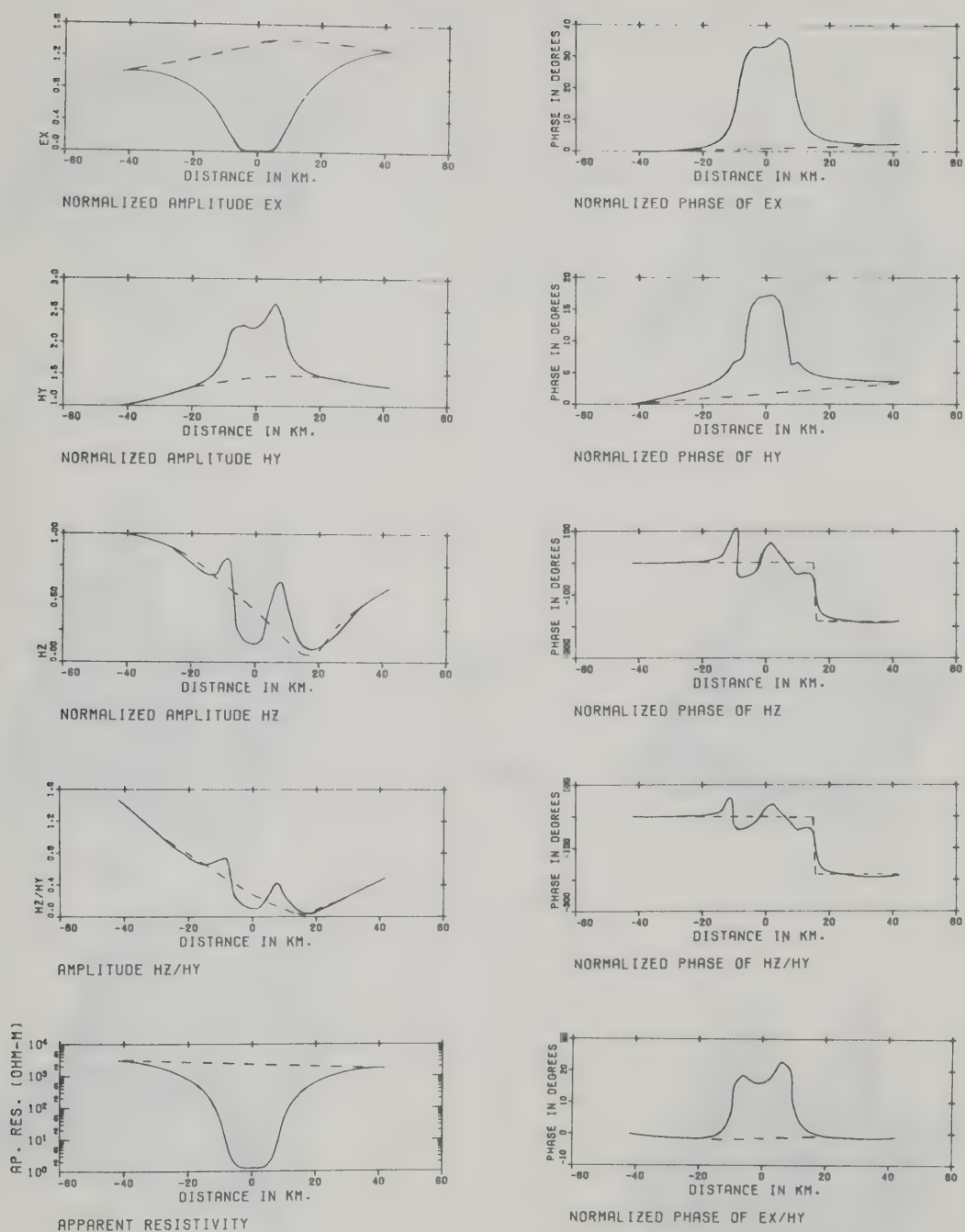


Figure 2.26 As Fig. 2.25, but for profile 2.

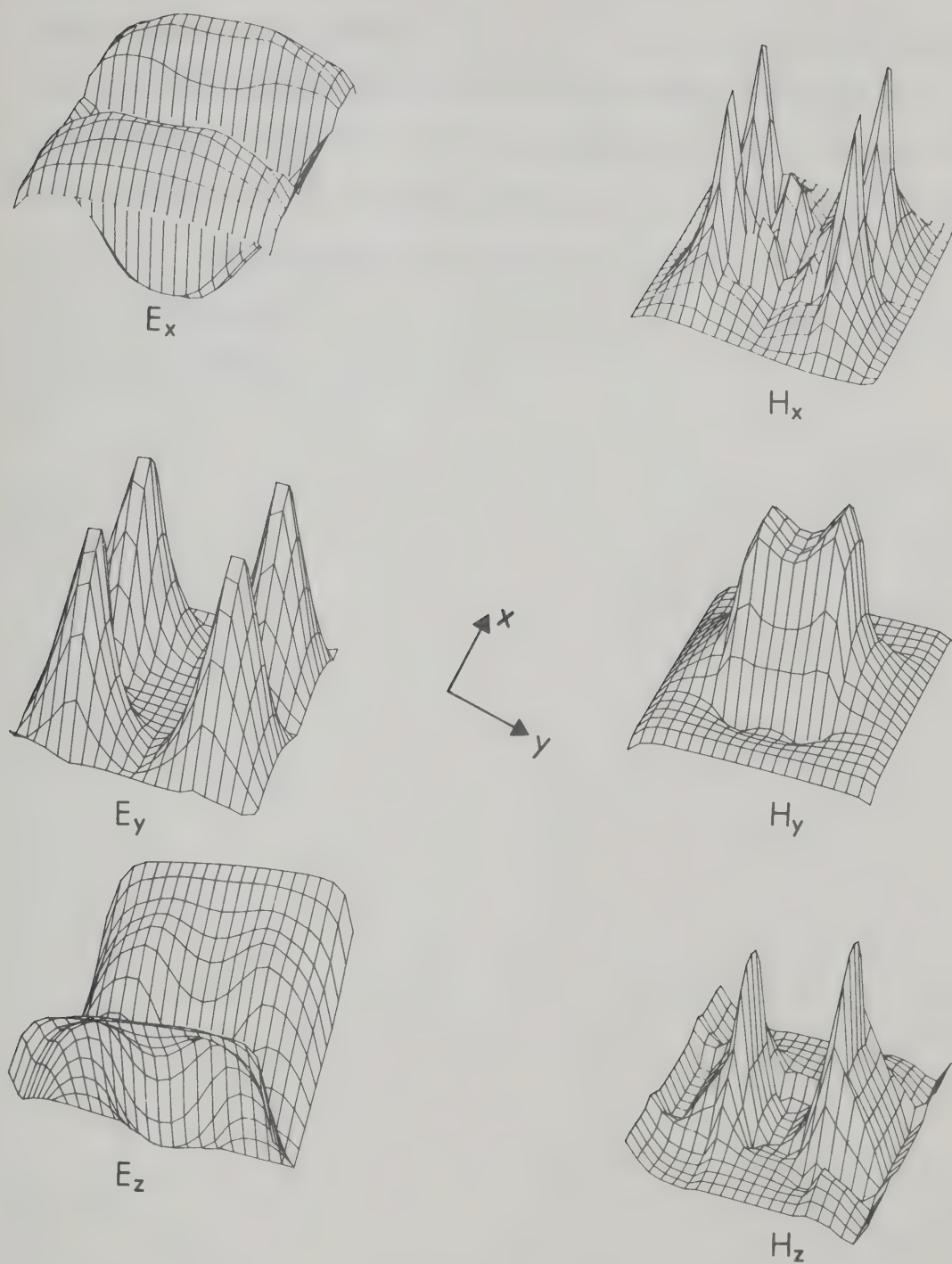


Figure 2.27 Three-dimensional profiles of $|E_x|$, $|E_y|$, $|E_z|$, $|H_x|$, $|H_y|$ and $|H_z|$ for three-dimensional source field. —

large depression in $|E_x|$ is present over the anomaly while just outside the anomaly the field increases slightly due to the varying surface charge on the boundary between the conductivity regions. $|H_y|$ increases over the anomaly and the corners of the anomaly are marked by increases in $|H_x|$ and $|E_y|$. The sides of the anomaly are defined by $|E_z|$ and $|H_z|$. The peaks of $|H_z|$ are not of equal height because of the non-uniform source field.

CHAPTER 3

A COMPARISON OF ELECTROMAGNETIC ANALOGUE MODEL MEASUREMENTS AND FINITE-DIFFERENCE NUMERICAL CALCULATIONS FOR THREE DIFFERENT SOURCE FIELDS

Two methods used to study electromagnetic induction problems are theoretical model calculations and analogue model experiments. Most mathematical methods require highly simplified conductivity distributions and source fields. Models composed of horizontally layered conductors and generalized source fields present no serious mathematical difficulties. Problems in which lateral conductivity contrasts occur are much less tractable analytically and are usually solved by numerical techniques. One such technique which lends itself readily to a wide range of three-dimensional problems is the finite difference method of section 2.8. Various source field configurations can be modelled by supplying the appropriate boundary conditions to the finite difference mesh. In this manner the electromagnetic field solutions for embedded anomalies with the same stratification at all boundaries for various source field configurations can be found. Scaled analogue model methods are appropriate to problems for which no mathematical solution exists or for which numerical

evaluation presents great difficulty. This method is most readily adapted to problems involving high conductivity contrasts (of the order of 10^4) in which suitably shaped graphite bodies simulate highly conducting regions such as ore bodies or oceans, and concentrated salt solutions simulate a poorly conducting host earth. A comparison of results from the two methods is useful in understanding the applicability of both methods as well as gaining an appreciation of the difficulties encountered in them.

One difficulty often encountered in laboratory scale model experiments is the problem of edge effects. Sizeable edge effects can arise in simulating induction problems which involve uniform source fields, since it is often difficult to generate perfectly uniform fields in the laboratory. Another problem in model experiments is that associated with the finite dimensions of the detector probes since a finite-sized detector smoothes out the behaviour of the electromagnetic fields in regions where the fields vary rapidly, i.e., in the neighbourhood of a conductivity discontinuity. There is also a limit to how accurately a finite-sized probe can be positioned. For small sized anomalies the positioning and alignment of the anomaly is a very critical factor in determining the character of anomalous fields. The alignment of the source field also becomes more critical as the dimensions of the

1. The first part of the document discusses the importance of maintaining accurate records of all transactions and activities. It emphasizes the need for transparency and accountability in financial reporting.

2. The second part outlines the various methods used to collect and analyze data. This includes both qualitative and quantitative approaches, as well as the use of statistical tools to interpret the results.

3. The third part focuses on the challenges faced by researchers in this field. These challenges include limited access to data, the complexity of the subject matter, and the need for interdisciplinary collaboration.

4. The fourth part presents the findings of the study. It shows that there is a significant correlation between the variables being studied, and that the results are consistent across different samples and conditions.

5. The fifth part discusses the implications of the findings for practice and policy. It suggests that the results can be used to inform decision-making and to develop more effective interventions.

6. The sixth part provides a conclusion and a summary of the key points. It reiterates the importance of the research and the need for further investigation in this area.

7. The final part includes a list of references and a bibliography. These references provide additional information and resources for those interested in the topic.

current carrying device which produces it decreases.

In numerical modelling techniques a mesh of grid points is superimposed on the conductivity configuration under study so that the conductivity model is represented by a number of cells of uniform conductivity. The accuracy of the numerical method depends on the size of the grid intervals as well as on the uniformity of grid spacings, particularly for points near conductivity discontinuities. The volume of the grid array must be limited due to storage and computing time considerations. This restriction may lead to difficulties in the selection of small and uniform grid spacings or in the satisfaction of the boundary conditions at great distances from the anomaly.

3.1 Mathematical Analysis

A brief mathematical development, following Dosso (1966), of the modelling problem follows. The MKS system of units is used, with the conductivity expressed in mho/m. Consider Maxwell's field equations for a homogeneous conductor

$$\nabla \times \underline{E}' + \mu \frac{\partial \underline{H}'}{\partial t} = 0 \quad (3.1)$$

$$\nabla \times \underline{H}' - \epsilon \frac{\partial \underline{E}'}{\partial t} - \sigma \underline{E}' = 0 \quad (3.2)$$

To write these equations in a dimensionless form, let



$$\underline{E}' = e_0 \underline{E} \quad \underline{H}' = h_0 \underline{H} \quad (3.3)$$

$$\epsilon = \epsilon_0 k_e \quad \mu = \mu_0 k_m \quad (3.4)$$

$$d = d_0 D \quad t = t_0 T \quad \sigma = \sigma_0 S \quad (3.5)$$

where E , H , k_e , k_m , D , T and S are dimensionless numbers, and e_0 , h_0 , ϵ_0 , μ_0 , d_0 , t_0 and σ_0 are the unit quantities of the electric field, magnetic field, dielectric constant, magnetic permeability, length, time and conductivity, respectively. If we substitute (3.3), (3.4) and (3.5) into (3.1) and (3.2), we obtain

$$\nabla^* \times \underline{E} + \alpha \left(\frac{\partial \underline{H}}{\partial T} \right) = 0 \quad (3.6)$$

$$\nabla^* \times \underline{H} - \beta \left(\frac{\partial \underline{E}}{\partial T} \right) - \gamma \underline{E} = 0 \quad (3.7)$$

where ∇^* is the dimensionless curl operator taken with respect to D ,

$$\text{and} \quad \alpha = \frac{d_0 \mu_0 k_m}{t_0} \left(\frac{h_0}{e_0} \right) \quad (3.8)$$

$$\beta = \frac{d_0 \epsilon_0 k_e}{t_0} \left(\frac{e_0}{h_0} \right) \quad (3.9)$$

$$\text{and} \quad \gamma = d_0 \sigma_0 S \left(\frac{e_0}{h_0} \right) \quad (3.10)$$

Equations (3.6) and (3.7) are dimensionless and have the same form as the original field equations. The solutions to these equations are invariant under a change in scale if the dimensionless coefficients α , β and γ are invariant.

Hence, it is possible to design a scaled model of an actual geophysical electromagnetic boundary value problem.

If we confine our attention to problems where ϵ and u have the free-space values and let $S = 1$, and eliminate e_0/h_0 from equations (3.8) to (3.10) then the necessary and sufficient condition that the solutions be invariant under a change of scale is that

$$\frac{d_0}{t_0} = \text{constant} \quad \text{or} \quad d_0 f_0 = \text{constant} \quad (3.11)$$

where f_0 is frequency and

$$d_0 \sigma_0 = \text{constant} \quad . \quad (3.12)$$

If we let primed symbols refer to the geophysical dimensions and unprimed symbols refer to the model dimensions, equations (3.11) and (3.12) can be expressed as

$$df = d'f' \quad (3.13)$$

$$d\sigma = d'\sigma' \quad (3.14)$$

If displacement currents are neglected additional freedom in scaling is obtained. Equation (3.9) can be ignored and by combining (3.8) and (3.10)

$$\sigma f d^2 = \sigma' f' d'^2 \quad (3.15)$$

Equation (3.15) indicates the relationship that must exist between the conductivities, frequencies and lengths involved for the actual problem and its scaled model in order that the ratios of the field components and phase differences are the same for the two problems.

3.2 Analogue Model Apparatus

A photograph of the equipment used is shown in Plate 3.1. The model consists of an overhead oscillating field source (three different ones were used), a large tank (244 cm by 168 cm and 76 cm deep) containing concentrated salt solution (64 cm deep) of conductivity 21.0 mho/m simulating the uniform upper layer of a poorly conducting earth and a graphite block of conductivity 0.8×10^5 mho/m (see Plate 3.2) which served as an anomaly. The graphite anomaly used in the analogue model measurements and a lucite mount designed and constructed by the author to hold it rigidly in the tank are shown in Plate 3.2. To minimize the effects of the concrete floor, the bottom of the tank was lined with a 5 cm thick graphite layer of conductivity 1.2×10^5 mho/m. This layer of graphite acts as a shield for any remaining field at the bottom of the tank. If the tank were much deeper (several skin depths), then the effects of the floor and earth below would present no problem and the graphite

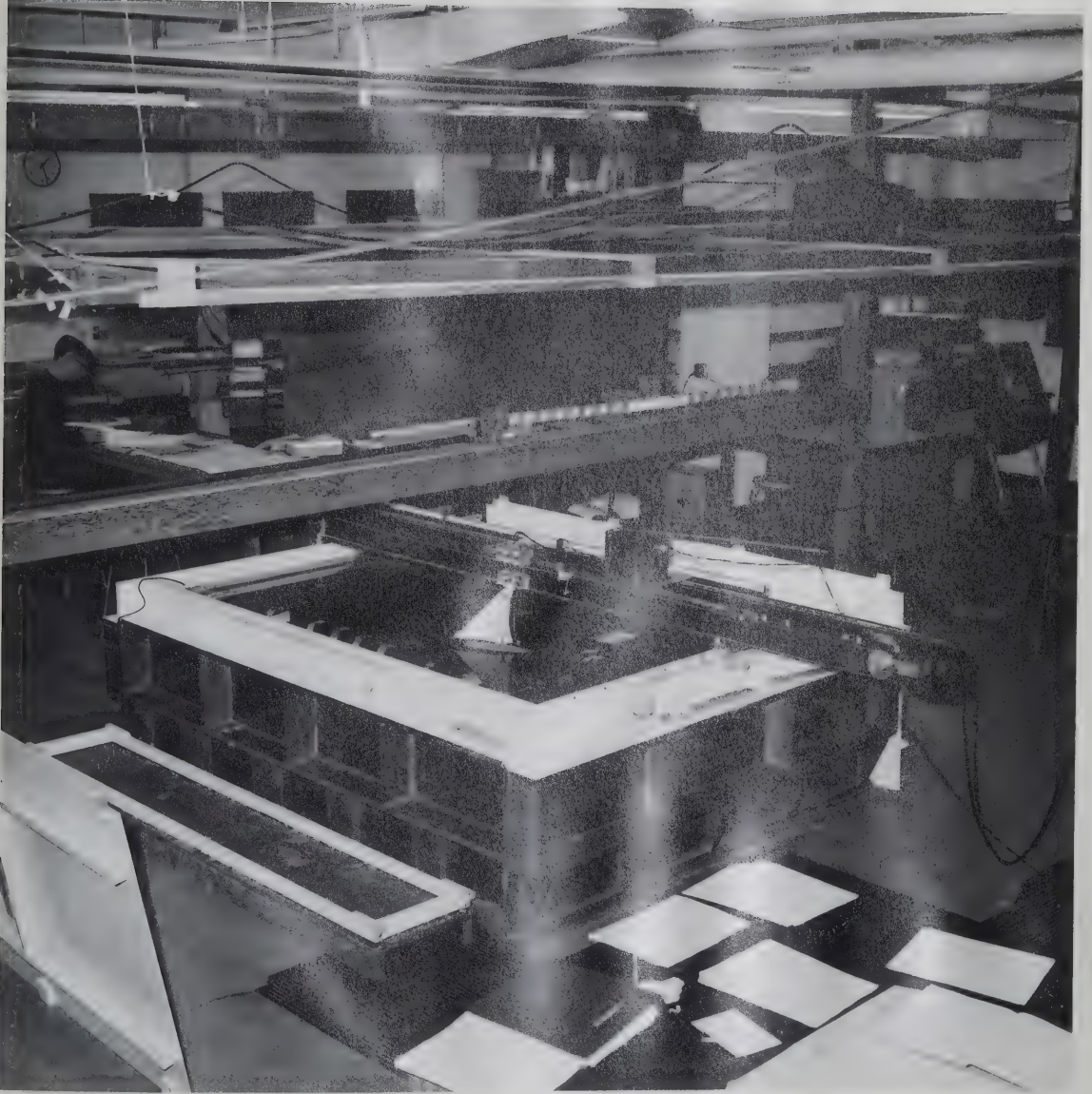


Plate 3.1 Analogue Experimental Equipment

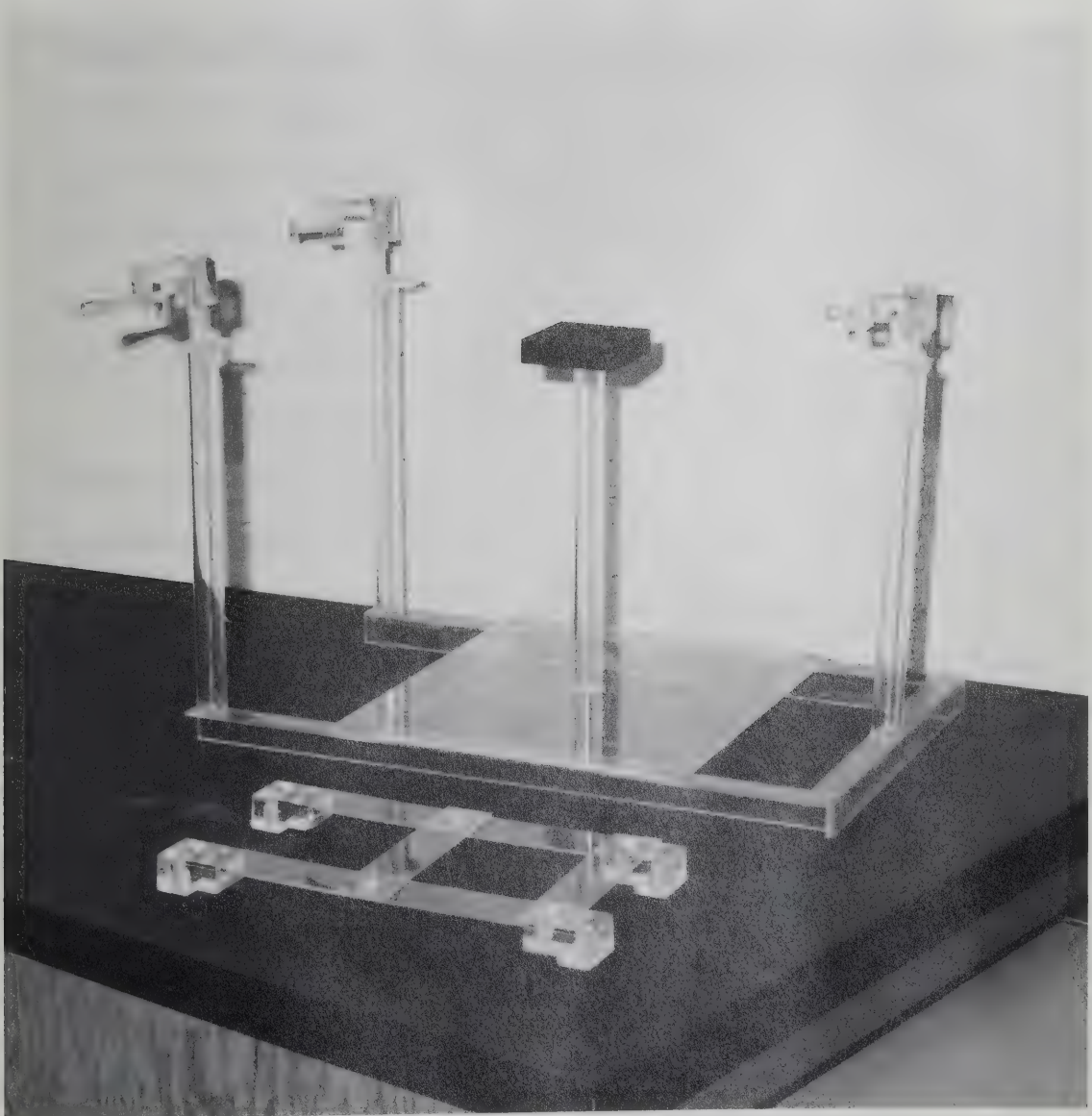


Plate 3.2 Analogue Anomaly and Support Structure

layer would not be necessary. Two stainless-steel sheets lining the tank walls (parallel to the beam which supports the measurement probe) and connected by a copper wire placed outside the tank permitted the currents induced in the salt water to flow parallel to the source current (perpendicular to beam). Without this arrangement the induced currents for two dimensional sources would be constrained to flow perpendicular to the source current near the walls of the tank.

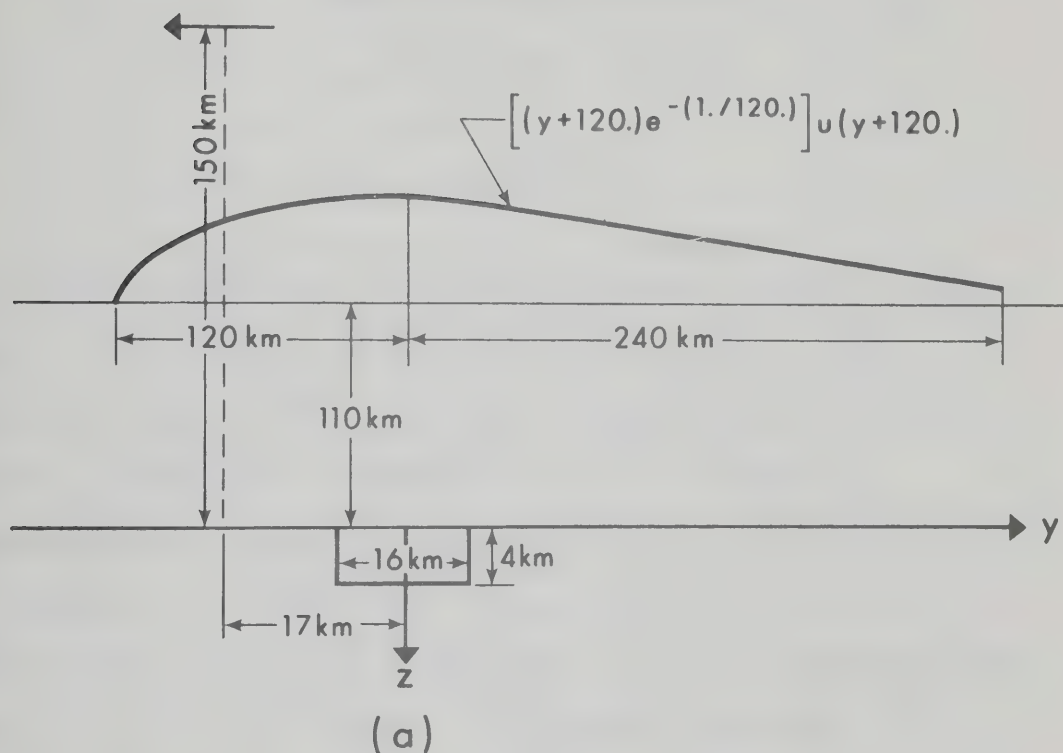
The electric and magnetic field detectors, mounted on the ends of lucite rods, were attached to a moveable lucite plate held on the rigid beam above the tank. The vertical and horizontal magnetic field detectors consisted of twin coils 0.10 cm long and 0.64 cm outer diameter. The coils were designed to have a low inductance in order that the resonant frequency would be well above any frequencies of interest. The signal from the coil was monitored and amplified by a Tektronix 502 oscilloscope. The amplitude of the output of the oscilloscope was measured using a Hewlett-Packard VTVM and the phase angle was measured using a North Atlantic Phase Angle Voltmeter. A reference signal was provided by a small coil situated at a fixed position near the field source. The average field along the surface was determined by measuring the voltage difference between

points 1.48 cm apart. The electric field detector consisted of three probes mounted in a lucite rod with the points just protruding from the end and making contact with the surface of the salt solution. The two outer probes, 1.48 cm apart, were connected by means of a two-core shielded cable to the differential input of the Tektronix 502 oscilloscope. The third probe, situated at the mid point between the end probes, was connected to the cable shield and hence to ground on the oscilloscope. In this way the noise common to both probes was removed. The amplitude and phase angle of the amplified signal were measured in the same way as described for the magnetic field signal.

3.3 Model Description

The geophysical model (see Fig. 3.1b), considered in this work is a highly conducting body of conductivity 0.8 mho/m which is 16 km square and 4 km thick embedded at the surface of a poorly conducting host earth 126.8 km thick and of conductivity 0.21×10^{-3} mho/m. The host earth overlays an infinite half space of conductivity 1.2 mho/m. Three different source field current distributions are used in conjunction with the geophysical model; uniform, ye^{-ay} and a horizontal magnetic dipole. The source frequency in each case is 0.075 Hz.

POSITION OF HORIZONTAL DIPOLE AND $y e^{-ay}$ SOURCE WITH RESPECT TO THE ANOMALY



ANOMALY AND PROFILE POSITIONS

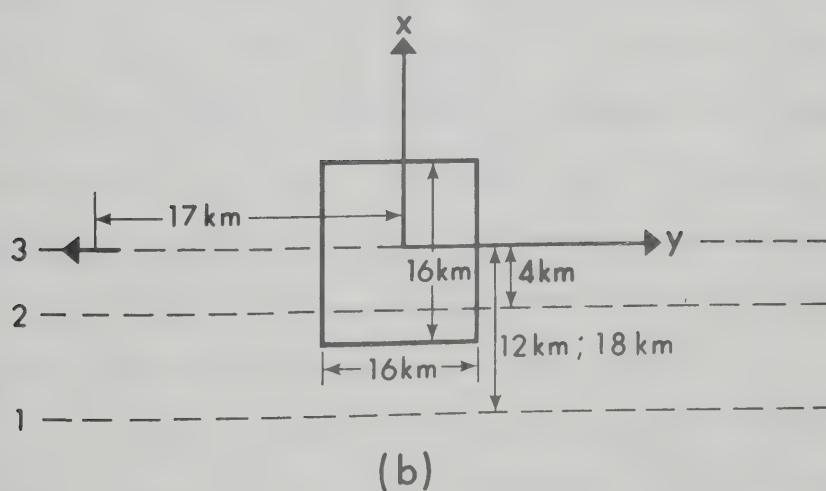


Figure 3.1 Co-ordinate System, Source and Profile Positions

The model scaling factors used here are

$$\frac{\sigma}{\sigma'} = 1 \times 10^5$$

$$\frac{f}{f'} = 4 \times 10^5$$

$$\frac{d}{d'} = .5 \times 10^{-5} \quad .$$

The primed quantities refer to the natural scale in the geophysical problem, while the others refer to the analogue model. Using the above conductivity scaling factor, graphite of conductivity 0.8×10^5 mho/m represents the highly conducting body, of conductivity of 0.8 mho/m, while the concentrated salt solution of conductivity 21.0 mho/m simulates a poorly conducting host earth of 0.21×10^{-3} mho/m. The model frequency of 30 khz simulates a frequency of 0.075 Hz while a scale length of 1 cm in the model represents 2 km in the natural scale. Thus an anomaly 8 cm square and 2 cm thick in the model represents a geophysical anomaly 16 km square and 4 km deep. For this model frequency, the skin depths in graphite and in salt water are 0.84 cm and 63.4 cm, respectively, which correspond to 1.68 km for the sea water and 126.8 km for the land.

The theoretical electromagnetic field solutions for the three sources over laterally uniform conductors can be calculated for the geophysical model by various

methods. For the uniform source the analytical solution, of Jones and Price (1970), for a layered earth is used. The Fourier series method of Hibbs and Jones (1976a,b) is used to obtain the analytic solution for the ye^{-ay} source. This source distribution, where $a = 1./120.$, is theoretically approximated by 37 appropriately weighted rectangular current distributions of width 10 km and these are given in Table 3.1. The rectangular current distribution is approximated by one elemental gaussian of half width 10 km as described in Hibbs and Jones (1976d,e). The current source flows at a height of 110 km (see Fig. 3.1a) in the geophysical model and is positioned such that the maximum value of the current distribution coincides with the center of the anomaly. The analytical solution for the horizontal magnetic dipole is calculated using the method of section 2.7. The magnetic dipole polarized in the negative y direction is placed 17 km from the center of the anomaly, see Fig. 3.1a, at a height of 150 km above the surface.

The electric field values thus calculated are used to provide the boundary and initial conditions for the finite difference mesh of section 2.9 and from this the electric field associated with the three-dimensional embedded conductivity anomaly is determined. The anomalous electromagnetic fields due to the conductivity structure are assumed to be zero at the boundaries of the

Table 3.1
Weighting Coefficients of Rectangular
Current Distributions

0.0
0.208E + 00
0.383E + 00
0.529E + 00
0.649E + 00
0.747E + 00
0.824E + 00
0.885E + 00
0.930E + 00
0.963E + 00
0.984E + 00
0.996E + 00
0.100E + 01
0.997E + 00
0.988E + 00
0.974E + 00
0.955E + 00
0.934E + 00
0.910E + 00
0.884E + 00
0.856E + 00
0.827E + 00
0.797E + 00
0.766E + 00
0.736E + 00
0.705E + 00
0.675E + 00
0.645E + 00
0.615E + 00
0.586E + 00
0.558E + 00
0.530E + 00
0.504E + 00
0.478E + 00
0.453E + 00
0.429E + 00
0.406E + 00

finite difference mesh. A $25 \times 25 \times 25$ mesh of grid points is used in the numerical method. After the electric field is determined, the magnetic field quantities are obtained from the electric field solution by using appropriate finite difference equations. A special technique must be used in the theoretical finite-difference method when both high conductivity contrast ($> 10^3$) and high frequency ($> .01$ Hz) are used in conjunction as in this comparison. In the finite difference method an arithmetic average of the conductivities is normally used and works well in obtaining solutions even for high conductivity contrast as long as the frequency is not too high. However in the high frequency case a transition zone of conductivity must be introduced such that the conductivity contrast is never more than 100. In the model this zone of conductivity 0.21×10^{-1} mho/m surrounds the anomaly just inside the anomaly boundary and is one grid spacing thick. This allows the electric field to vary more rapidly across the anomaly boundary, now diffused, and more accurately represent the actual field there.

This technique would also be helpful along the surface boundary where the E_z caused by the anomaly must be taken into account. Since the conductivity is zero in the region $z < 0$ an infinite number of transition zones would be necessary to allow for a conductivity

contrast of no more than 100 at any one boundary. This is not practical and was therefore not done. However, a layer of host earth ($\sigma = 0.21 \times 10^{-3}$ mho/m) one half kilometer thick was placed over the conductivity configuration to help reduce the effects on E_z . This was also warranted by the fact that the analogue model anomaly requires a layer of salt water (0.1-0.2 cm thick) over the anomaly in order to make the electric field measurements. Since E_z is used in the calculation of H_y an effect can be expected on that component which will be seen in the section 3.4.

In the analogue model the current sources were constructed in the following manner. A reasonably uniform source field was obtained by using two parallel current carrying wires separated by a distance of 2.4 m and situated at a height of 1.2 m above the surface of the salt solution (Ramaswamy et al., 1975). In the model coordinate system, Fig. 3.1b, the current flow in the source field is along the x-direction. The ye^{-ay} source, where $a = 1./60$. (all dimensions in cm), is composed of 37 current carrying wires, see Fig. 3.2, in which only every fifth wire is used. The wires are aligned parallel to the x axis and the current carrying elements are 5 cm apart. Thus each current element approximates a gaussian current distribution of 10 km half width in the geophysical model.

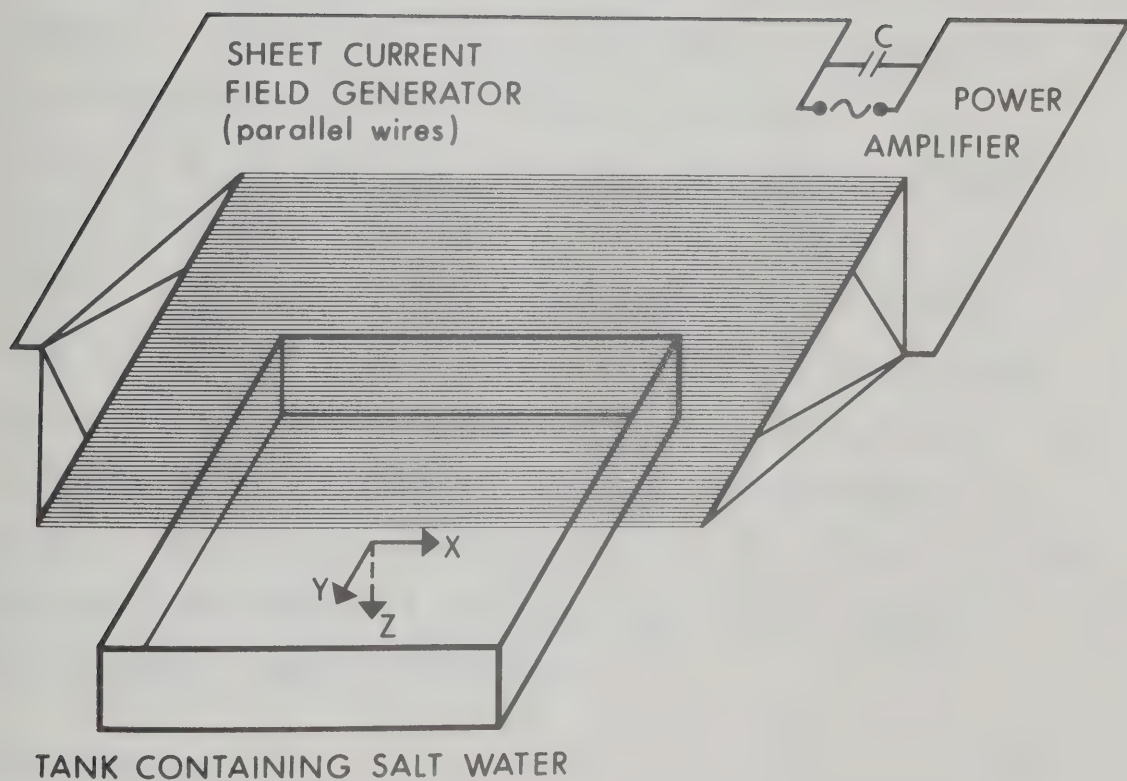


Figure 3.2 Current Carrying Wire Grid for ye^{-ay} Source

The amount of current which flows in any particular current carrying element is controlled by a resistance placed in series with the wire. The values of the resistances vary inversely as the coefficients of the rectangular current distributions in the geophysical source. The thirteenth wire (the element with maximum current) is placed over the center of the anomaly. The grid of wires is situated at a height of 55 cm above the surface of the salt solution. The validity of the analogue model for the overhead magnetic dipole source has been tested earlier (Thomson et al., 1972). The magnetic dipole is modelled by a current loop of radius 6.4 cm placed at a height of 75 cm above the surface of the salt water solution. This height corresponds to a height of 150 km in the geophysical model. The current loop was placed at ($x = 0$ cm, $y = -8.5$ cm) with the moment of the dipole polarized in the y direction as shown in Fig. 3.1b.

3.4 Results

The parameters which are commonly used to describe the effect of conductivity contrasts on the geomagnetic field are the ratio of the amplitude of the vertical magnetic field (H_z) and the component of the horizontal magnetic field (H_y) that is normal to the source current, and the apparent resistivity (ρ_a) which

is defined as

$$\rho_a = \frac{1}{\omega \mu_0} \left| \frac{E_x}{H_y} \right|^2$$

calculated in the manner of Cagniard (1953). Profiles of these quantities and their relevant phases along with the amplitude and phase profiles of the electromagnetic field components from which they are derived are calculated in the theoretical model and measured in the analogue model for 3 positions relative to the anomaly (see Fig. 3.1b) for each source field configuration. The profiles of the theoretical and analogue models are compared over the range -40 km to +40 km in the y direction for the uniform source and +42 km for the other sources. The points for which the calculations are made along the profiles are $y = \pm 0, 2, 4, 6, 7, 8, 9, 10, 12, 16, 24, 40$ km for the uniform source and $y = \pm 0, 2, 4, 6, 8, 10, 12, 14, 18, 26, 42$ km for the other sources. Each field component or ratio with the exception of the apparent resistivity and $|H_z/H_y|$ is normalized with respect to its value at -40 km or -42 km. All phases are normalized to zero at -40 km or -42 km. The positions of the profiles, as shown in Fig. 3.1b, are across the center of the anomaly, $x = 0$ km, four kilometers from the edge of the anomaly, $x = -4$ km, and outside the anomaly four kilometers from the edge for the uniform source, $x = -12$ km, and ten kilometers from the edge, $x = -18$ km, for the other sources. Also three dimensional

figures are given to show the comparison of the electromagnetic field components for the theoretical and analogue model. The range of the profiles in the y direction is the same as previously and the positions of the profiles in the x direction are $x = 0, -2, -4, -6, -7, -8, -9, -10, -12, -16$ km for the uniform source and $x = 0, -2, -4, -6, -8, -10, -12, -14, -18, -26$ km for the other sources. The figures are distorted near the edges since a uniform grid spacing is used in the plotting.

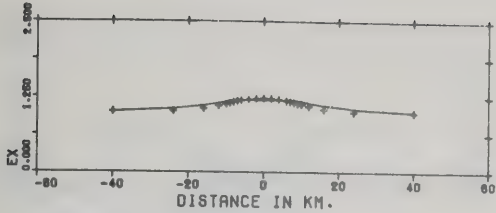
3.4.1 Uniform Source Results

The profiles and three dimensional figures of the results for the uniform source comparison are shown in Figs. 3.3 to 3.6. The first set of profiles given in Fig. 3.3 is taken 12 km from the center of the anomaly in the negative x direction. The normalized electric field amplitude, $|E_x|$, of both the analogue model measurements and the theoretical calculations exhibits an increase in the field due to the concentration of charge on the vertical boundary of the anomaly. The normalized horizontal magnetic field, $|H_y|$, of the analogue model is reasonably constant across this profile as is the theoretical model. The normalized $|H_z|$ curve in the theoretical model exhibits a small anomalous field in comparison to the analogue model which exhibits almost no anomalous field. Since the electric field in the

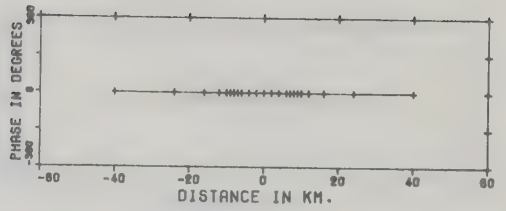
Figure 3.3 $|E_x|$, $|H_y|$, $|H_z|$, $|H_z/H_y|$ and ρ_a profiles
with normalized phases for uniform source
field and profile 1.

- theoretical calculation

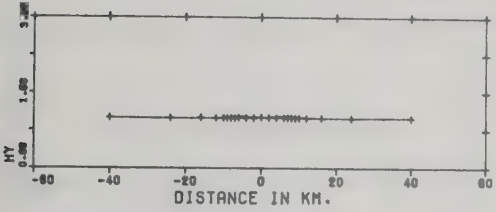
+ analogue model



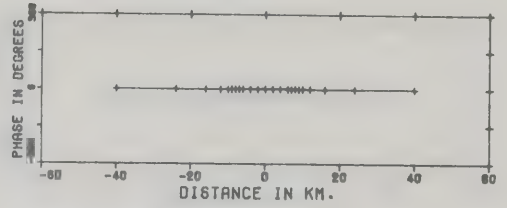
NORMALIZED AMPLITUDE EX



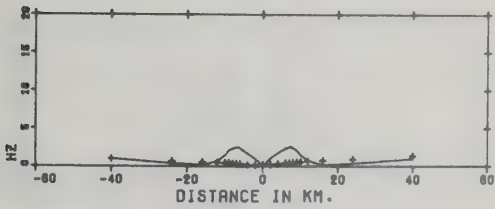
NORMALIZED PHASE OF EX



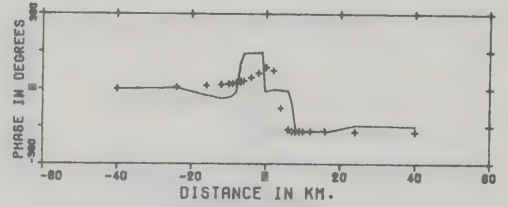
NORMALIZED AMPLITUDE HY



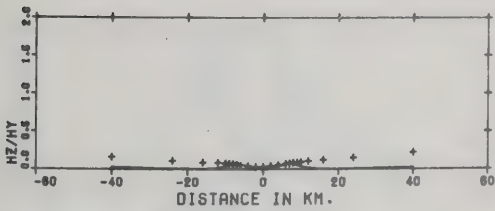
NORMALIZED PHASE OF HY



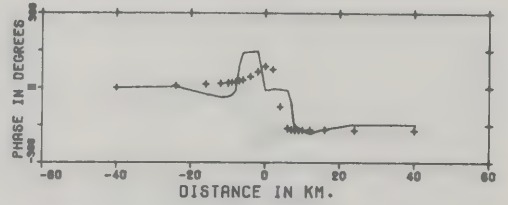
NORMALIZED AMPLITUDE HZ



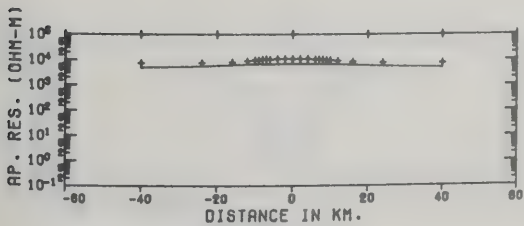
NORMALIZED PHASE OF HZ



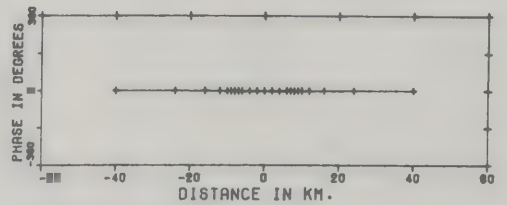
NORMALIZED AMPLITUDE HZ/HY



NORMALIZED PHASE OF HZ/HY



APPARENT RESISTIVITY



NORMALIZED PHASE OF EX/HY

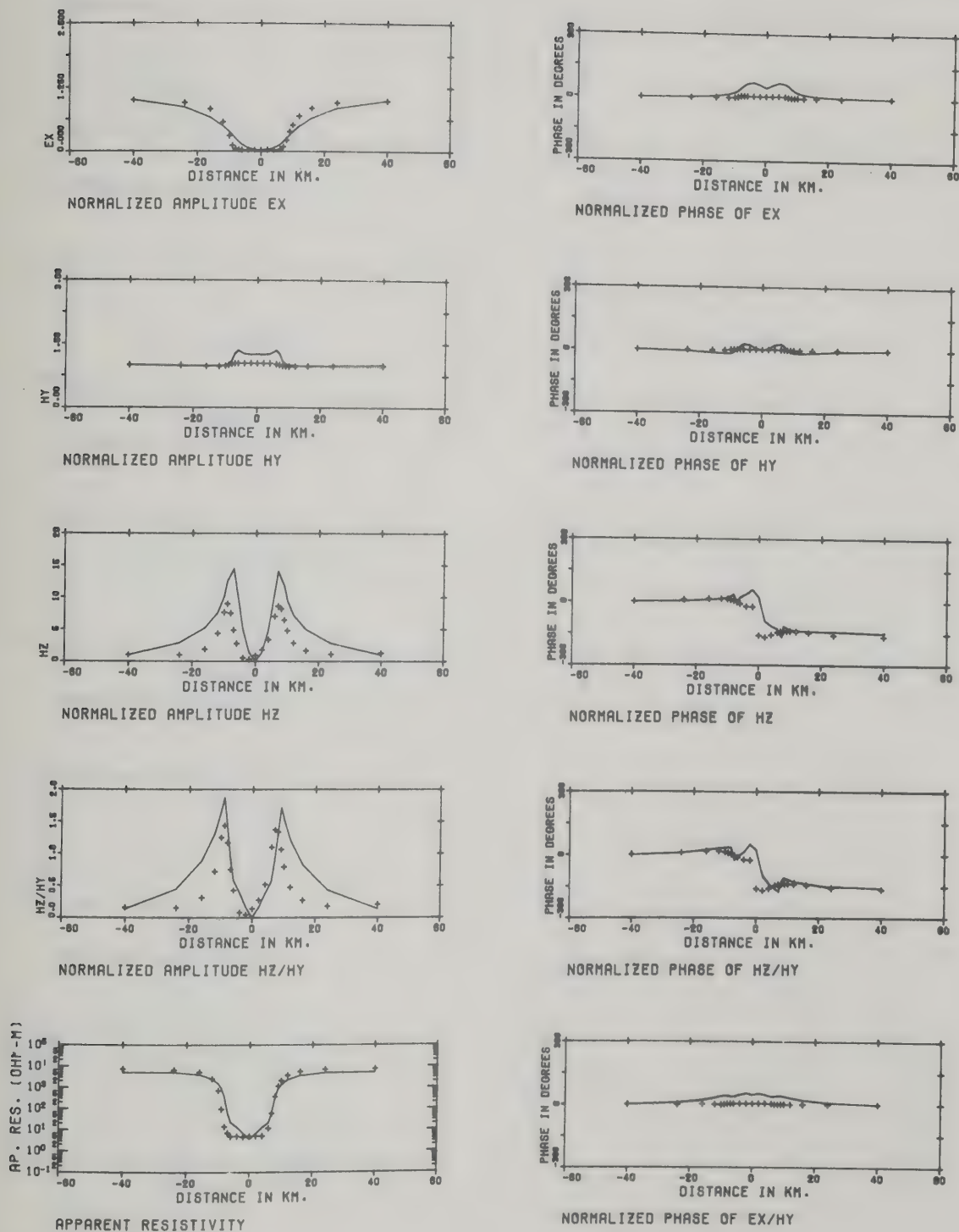


Figure 3.4 As Figure 3.3 but for profile 2.

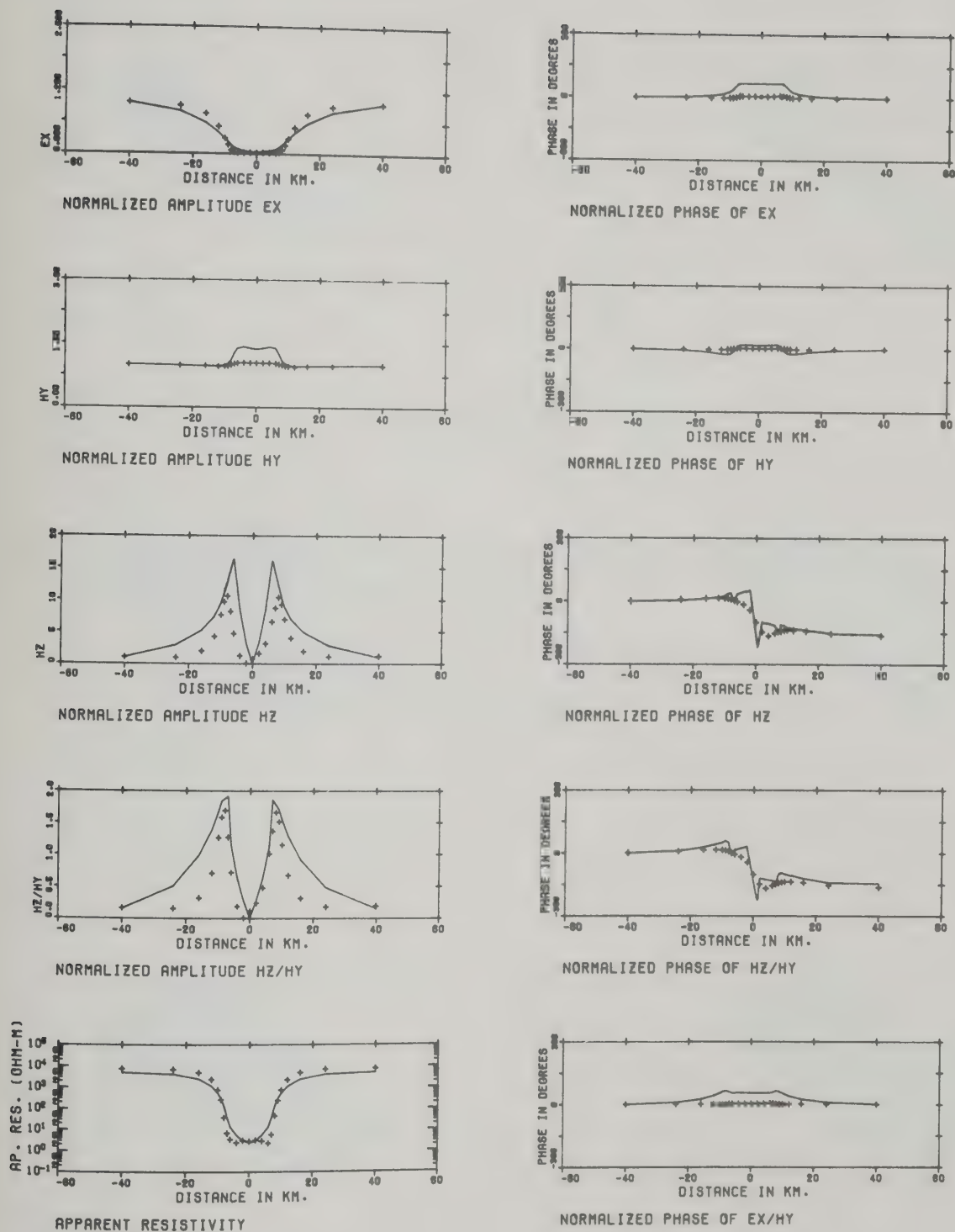
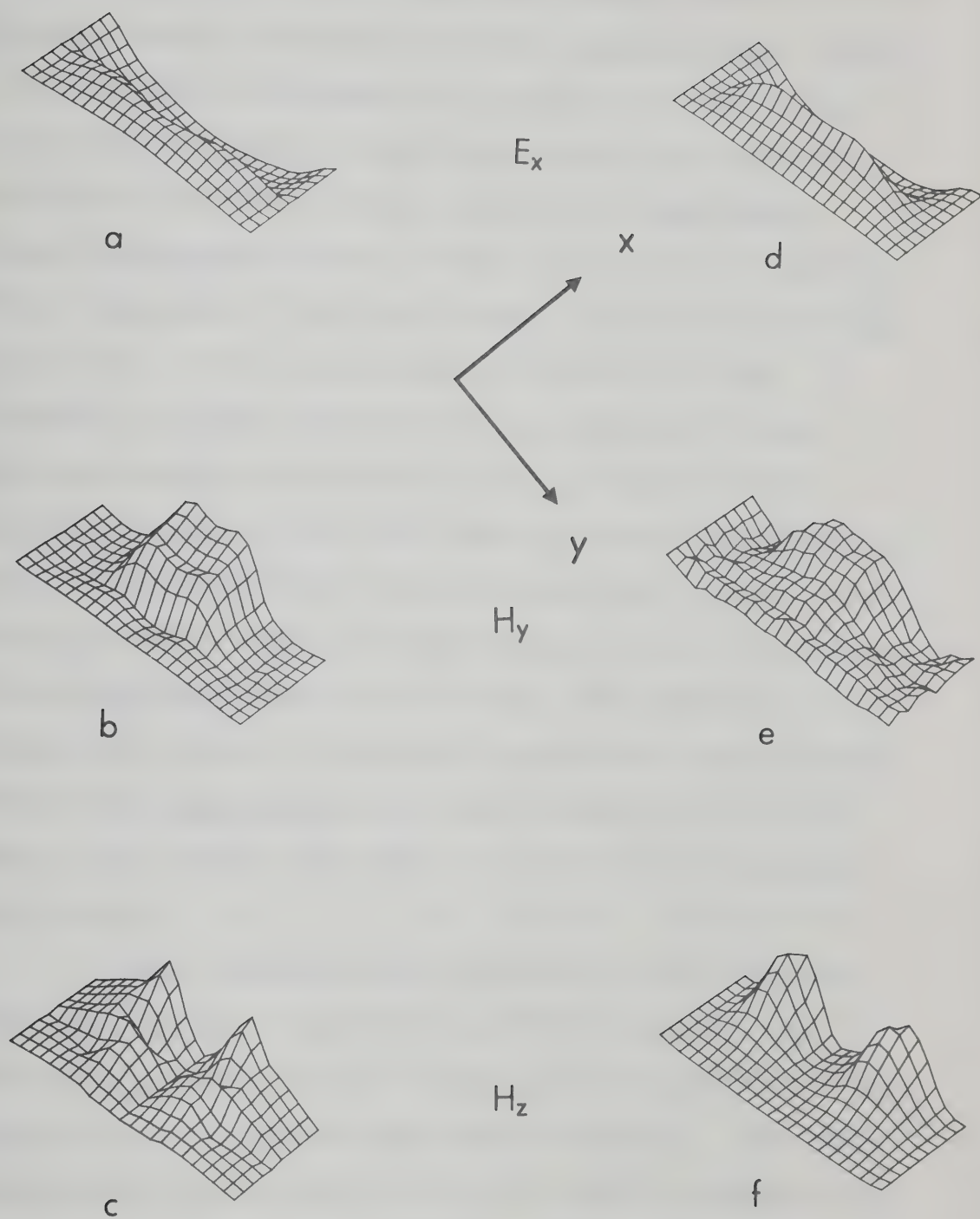


Figure 3.5 As Figure 3.3 but for profile 3.

Figure 3.6 Three-dimensional profiles of $|E_x|$, $|H_y|$ and $|H_z|$ for uniform source field.

Theoretical profiles (a,b,c)

Analogue profiles (d,e,f)



theoretical model varies in a less abrupt manner and over greater spatial distances than the analogue model electric field, it could reasonably be expected that the anomalous magnetic field of the theoretical model will also vary over larger distances than the analogue model anomalous magnetic field. This is the case for the $|H_z|$ field component. Also the magnetic field of the analogue model at $y = \pm 40$ km is greater than that of the theoretical model due to some non-uniformity in the analogue model source field, as can be seen in the $|H_z/H_y|$ profile. This will tend to lessen any anomalous field characteristics in the analogue model curve. The $|H_z/H_y|$ profile shows the small amount of non-uniformity in the analogue model source field. The apparent resistivity curves of both the theoretical and analogue models are approximately the same value of 4.76×10^{-3} ohm/m, the actual resistivity of the poorly conducting host earth.

The analogue curve exhibits a slight increase near the center of the profile, which is due to the increased electric field in that region caused by surface charge concentration on the anomaly boundary. The phase comparisons agree quite well and are nearly constant with the exception of the H_z and H_z/H_y phases which shift through 180° over the center of the anomaly, which is

consistent with the change of sign of H_z there.

The second set of profiles, taken along the line $x = -4$ km is given in Fig. 3.4. The effects of the anomaly are clearly indicated. $|E_x|$ decreases over the anomaly for both the analogue and theoretical model. The theoretical calculation does not vary as rapidly over the edges of the anomaly as do the analogue model results due to the conductivity transition zone which has been introduced at the boundaries of the anomaly of the theoretical model. $|H_y|$ increases over the anomaly for the theoretical and analogue models. The theoretical model exhibits a greater increase which can be attributed to the absence of a transition zone at the surface. The inclusion of a transition zone allows the vertical electric field E_z to vary more rapidly and thus increase the accuracy of the $\frac{\partial E_z}{\partial x}$ term in the calculation of the horizontal magnetic field H_y .

$|H_z|$ and $|H_z/H_y|$ are increased markedly over the boundaries of the anomaly for both the theoretical and analogue model as would be expected. A spreading of the peaks of the theoretical curve is noted for both profiles. This is attributable to the slower variation of the electric field components in the theoretical model. The apparent shifts in the minima of the $|H_z|$ and $|H_z/H_y|$ curves are due to the difficulty in positioning the

anomalous structure in the analogue model. The comparison of the apparent resistivities shows the effect of the anomaly. The theoretical and analogue calculations vary from the value of the poorly conducting host earth, 4.76×10^3 ohm/m, to approximately the value of the highly conducting anomaly, 0.8 ohm/m. The shape of the theoretical curve near the anomaly resembles the shape of the $|E_x|$ curve. The phases of E_x and H_y increase over the boundaries of the anomaly which can be attributed to the transition zone while the phase of ρ_a shows a small general increase over the whole anomaly. Again the phases of H_z and H_z/H_y change by 180° as the center of the anomaly is crossed. The phase comparisons for this profile agree reasonably well. Near the boundaries of the anomaly small discrepancies are noted.

The third set of profiles, taken across the center of the anomaly, $x = 0$ km, is given in Fig. 3.5. The shapes of the amplitude curves in this profile are much the same as in the second profile. However, the $|E_x|$, ρ_a and $|H_z/H_y|$ comparison curves agree more closely in this profile. The phase comparisons are similar to the last profile with the H_z and H_z/H_y phases slightly more accentuated.

The three dimensional amplitude profiles of the comparison of the three electromagnetic field components is shown in Fig. 3.6. The $|E_x|$, $|H_y|$ and $|H_z|$ three

dimensional profiles for the theoretical model are shown in Figs. 3.6a,b,c and for the analogue model in Figs. 3.6d,e,f. Each figure is scaled individually. The increase in $|E_x|$ just outside the anomaly due to charge on the boundary is clearly evident in the analogue model Fig. 3.6d along with the decrease in the field over the anomaly. In Fig. 3.6a the smoothing effect of the finite difference calculation can be seen. In Fig. 3.6b and 3.6e an increase in $|H_y|$ can be seen for both models. The erratic behaviour of Fig. 3.6e is due to the small variation in the $|H_y|$ field over the anomaly which when combined with the scaling of the three dimensional figure shows the slight errors in manual digitization of the analogue model records. The value of $|H_y|$ over the boundary of the anomaly parallel to the y axis in Fig. 3.6b is higher than would be expected and can be attributed to the transition zone. A comparison of Fig. 3.6c and Fig. 3.6f shows that $|H_z|$ increases over the edges of the anomaly for both models. However, the theoretical model shows an increase over the boundary of the anomaly parallel to the y axis, again due to the transition zone there.

The discrepancies noted in the magnetic field components between the analogue and theoretical models occur mainly near the transition zone at the edge of the anomaly. In the analogue model rapid spatial variations due to surface charge distributions are noted in the

electric field for profiles just outside the boundaries of the anomaly. Such large variations do not occur in the theoretical model since the fields vary slowly through the transition zone which represents the boundary and the charge distributions there are more diffuse and the electric fields associated with them are less. Since the theoretical electric fields show less effect due to the charge in the transition zone, the magnetic field solutions are consequently affected and higher values of magnetic field are thus generated in the theoretical model near the transition zone. The smoothing introduced by the transition zone is greater than that of the finite size of the sensor in the analogue model since the width of the transition zone is twice the probe spacing in the sensor.

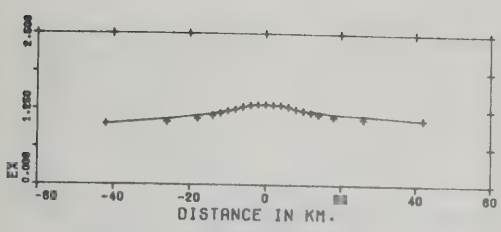
3.4.2 Two-Dimensional Non-Uniform Source Results

The profiles and three dimensional figures of the results for the ye^{-ay} source comparison are shown in Figs. 3.7 to 3.10. The first set of profiles (Fig. 3.7) is taken 18 km from the center of the anomaly in the negative x direction. The $|E_x|$, $|H_y|$ and ρ_a comparison curves agree well and are similar in shape to the uniform source curves for the profile except for a slight tilting due to the non-uniform source field. The $|H_z|$ and $|H_z/H_y|$ comparison curves show a more definite source effect in the form of a general decrease in the amplitude across the region of interest. The theoretical and analogue models agree well at the $y = \pm 42$ km points thereby verifying the theoretical boundary value calculations of

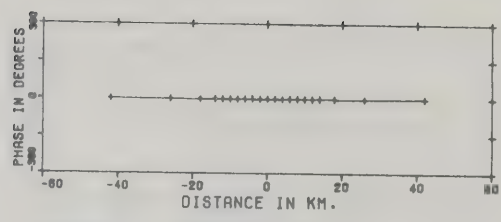
Figure 3.7 $|E_x|$, $|H_y|$, $|H_z|$, $|H_z/H_y|$ and ρ_a profiles
with normalized phases for a two-dimensional
source field and profile 1.

- theoretical calculations

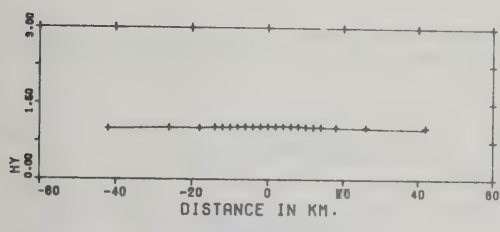
+ analogue model



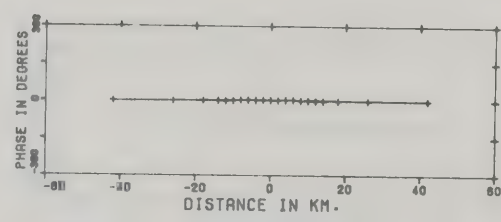
NORMALIZED AMPLITUDE EX



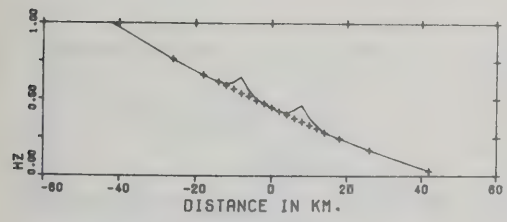
NORMALIZED PHASE OF EX



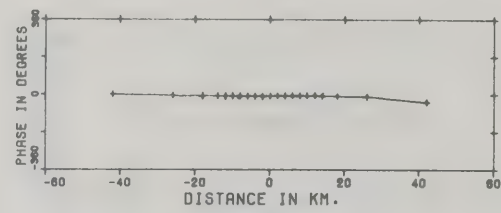
NORMALIZED AMPLITUDE HY



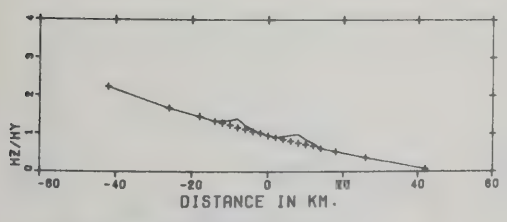
NORMALIZED PHASE OF HY



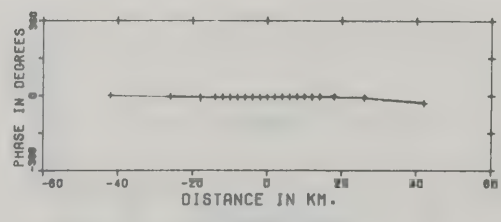
NORMALIZED AMPLITUDE HZ



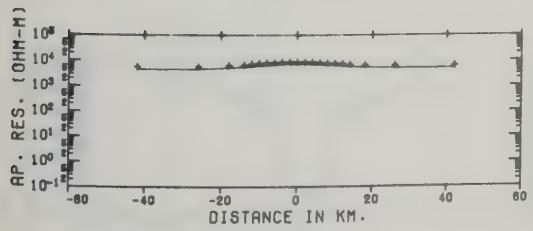
NORMALIZED PHASE OF HZ



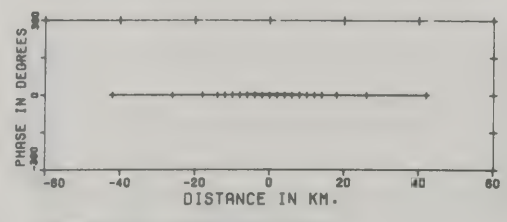
NORMALIZED AMPLITUDE HZ/HY



NORMALIZED PHASE OF HZ/HY



APPARENT RESISTIVITY



NORMALIZED PHASE OF EX/HY

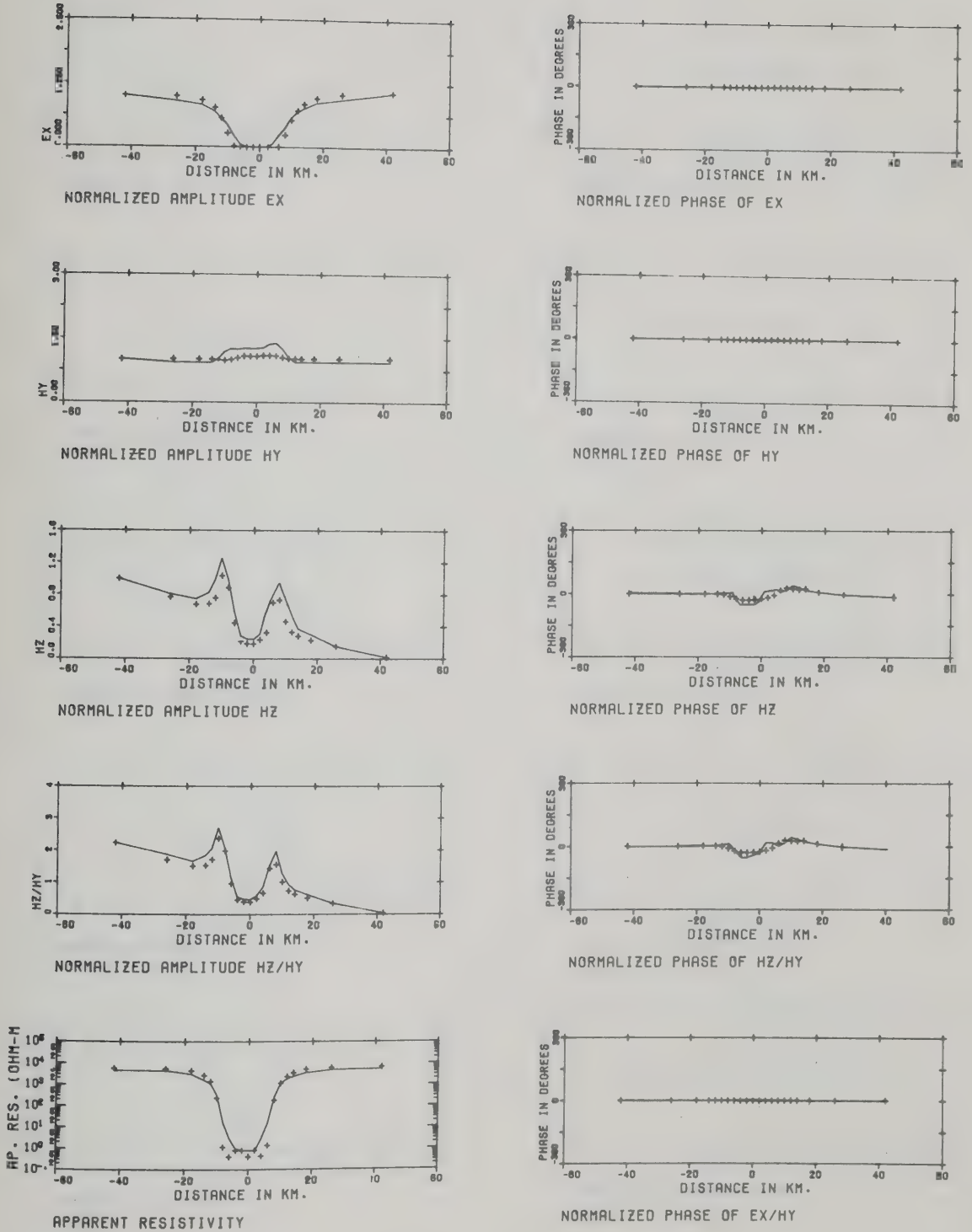


Figure 3.8 As Figure 3.7 but for profile 2.

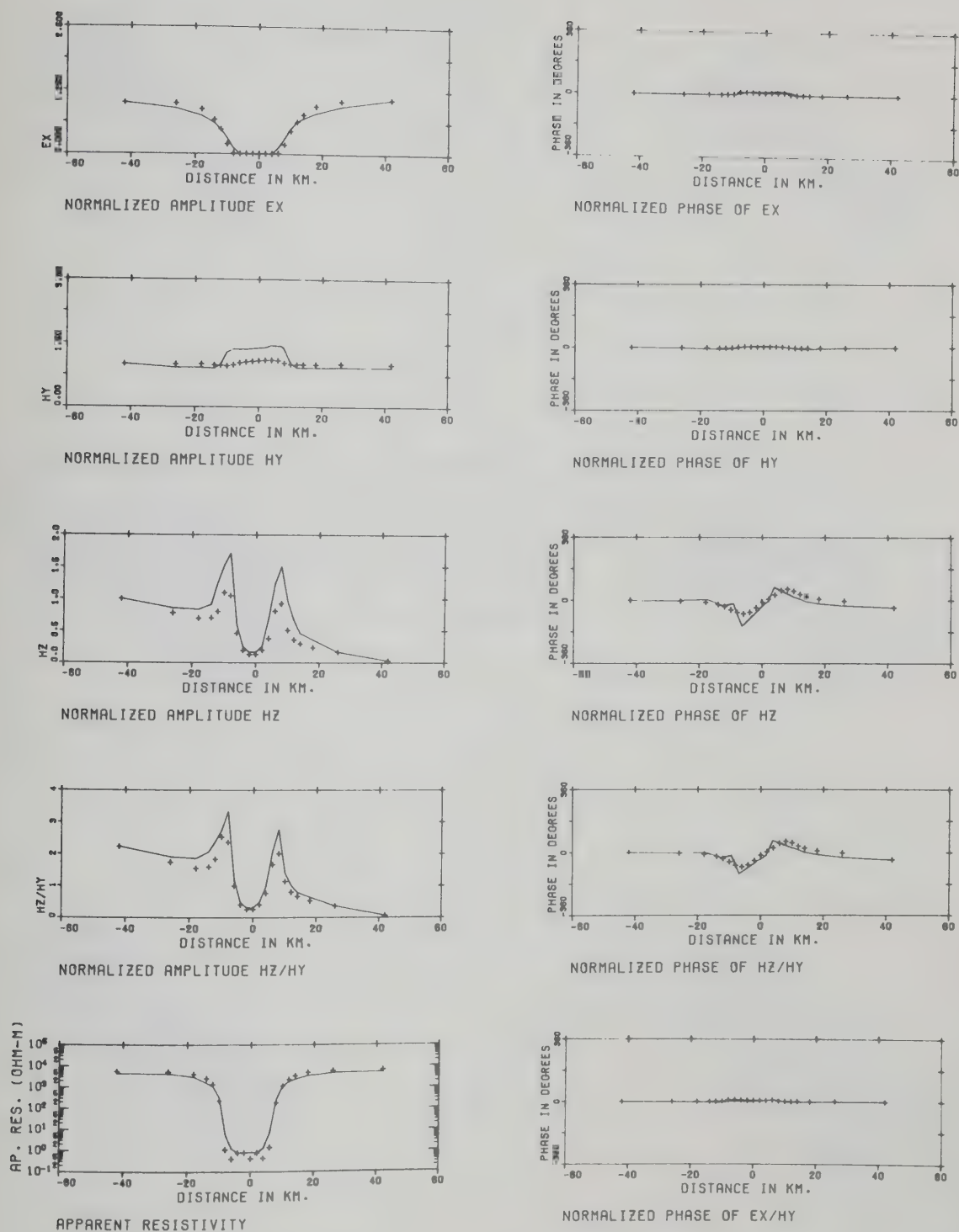
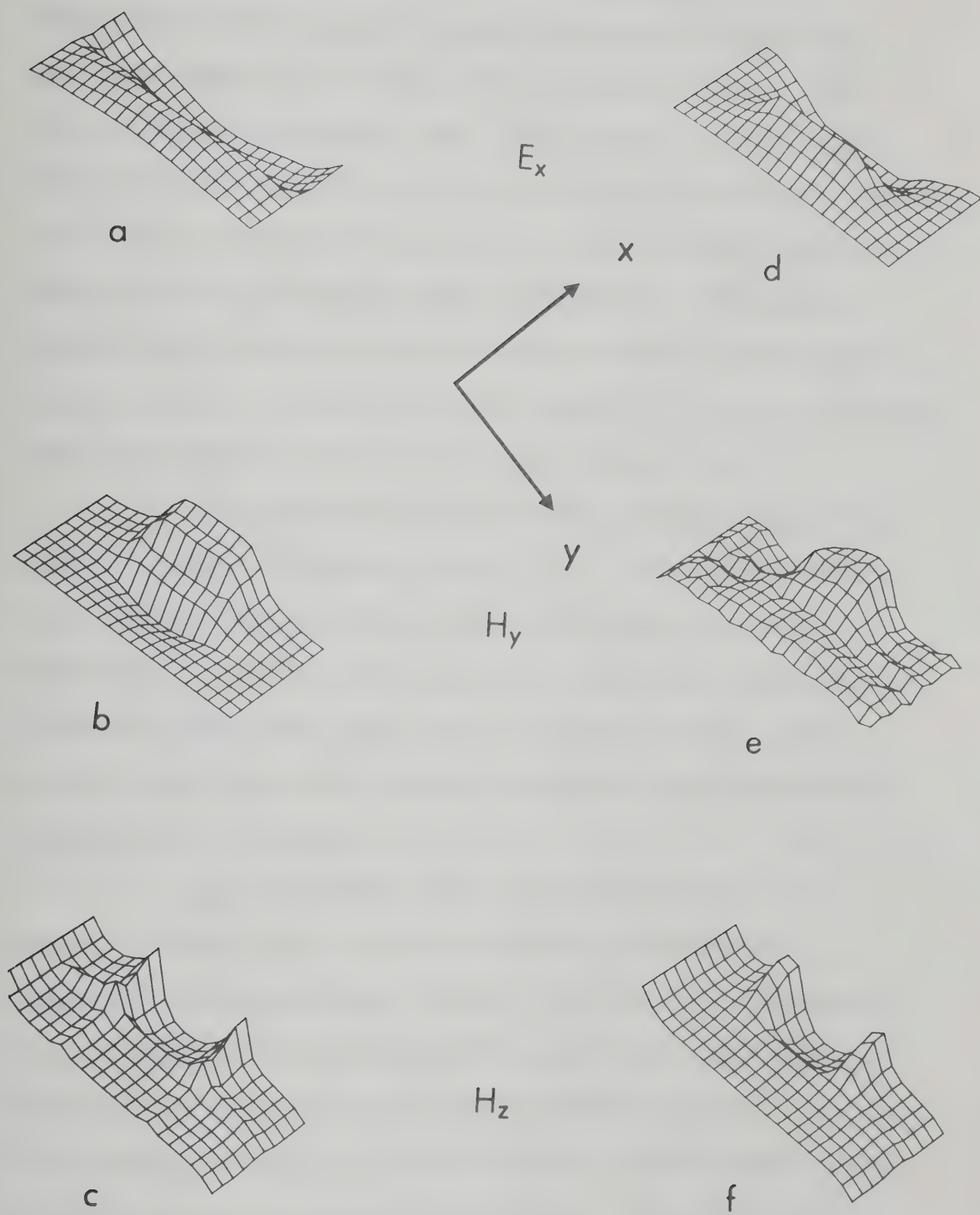


Figure 3.9 As Figure 3.7 but for profile 3.

Figure 3.10 Three-dimensional profiles of $|E_x|$, $|H_y|$ and $|H_z|$ for the ye^{-ay} source field.

Theoretical profiles (a,b,c)

Analogue profiles (d,e,f)



Hibbs and Jones (1976d,e). Over the anomaly the theoretical curve shows a small anomalous field for the same reason as in the uniform source case, while the analogue curve does not. The effect of the source field is greatest on the $|H_z|$ and $|H_z/H_y|$ profiles for this source field configuration. Only a slight source effect was noted in the other profiles. The phase comparisons agree quite well and are nearly constant for E_x , H_y and ρ_a . The phases of H_z and H_z/H_y vary slightly over the anomaly for the analogue model.

The second set of profiles, taken along the line $x = -4$ km is given in Fig. 3.8. The effects of both the anomaly and the source field are clearly indicated. The $|E_x|$ curves agree quite well with the effect of the transition zone clearly evident. The source field for both models increases from the negative to positive y regions.

$|H_y|$ increases over the anomaly and tilts upward slightly due to source effect in both the theoretical and analogue models. The larger increase in $|H_y|$ for the theoretical model occurs for the same reason as given earlier for the uniform source. The small peaks in the $|H_y|$ profile at $y = \pm 8$ km are due to the transition zones at those points. $|H_z|$ and $|H_z/H_y|$ increase over the edges of the anomaly for both

theoretical and analogue models though less in the case of the analogue model. The peaks are now non-symmetric. Both analogue and theoretical curves exhibit the same behaviour. The comparison of the apparent resistivities shows the effect of the anomaly but no spatial variation of apparent resistivity due to the non-uniform source is evident. The phases of E_x and ρ_a increase slightly over the boundaries of the anomaly for the theoretical calculation. The phase of H_y remains constant in both analogue and theoretical model. The phase of H_z and H_z/H_y dips to -60° at $y = -8$ km and increases to $+60^\circ$ at $y = +8$ km over the boundaries of the anomaly for the analogue model. At $y = +42$ km the phase of the analogue model begins to decrease as a consequence of the 180° phase change which takes place outside the range of interest, due to the non-uniform source. The phase curves of the theoretical model exhibit approximately the same behaviour as the analogue model but due to the transition zones the curves do not coincide.

The third set of profiles taken across the center of the anomaly, $x = 0$ km, is given in Fig. 3.9. The shapes of the amplitude curves in this profile are much the same as in Fig. 3.8 with the exception that the $|E_x|$ and ρ_a comparison curves agree more closely in this profile. The $|H_y|$ comparison curves show a greater increase over the anomaly than in the previous profile.

Both the analogue and theoretical $|H_z|$, $|H_z/H_y|$ comparison curves are more peaked over the boundaries of the anomaly than in the preceeding profile. The phases of E_x , H_y and E_x/H_y are constant for both models. The phases of H_z and H_z/H_y are of the same character as the previous profiles with an analogue model phase decrease to -90° at $y = -8$ km and increase to $+90^\circ$ at $y = +8$ km.

The three dimensional amplitude profiles of the comparison of the three electromagnetic field components are shown in Fig. 3.10. The $|E_x|$, $|H_y|$ and $|H_z|$ three-dimensional profiles for the theoretical model are shown in Fig. 3.10a,b,c and for the analogue model in Fig. 3.10d,e,f. Each figure is scaled individually. As before the increase in $|E_x|$ just outside the anomaly due to the charge on the boundary is evident in the analogue model, Fig. 3.10d, along with the decrease in the field over the anomaly. In Fig. 3.10a the smoothing effect of the transition zone can be seen. In Fig. 3.10b and Fig. 3.10e an increase in $|H_y|$ can be seen for both models. When compared with the three-dimensional figures for the uniform source the effect of the ye^{-ay} source is evident in the tilting of the $|H_y|$ profiles. The value of $|H_y|$ over the boundary of the anomaly parallel to the y axis is higher than would be expected due to the

transition zone as in the uniform source case. A comparison of Fig. 3.10c and Fig. 3.10f shows that $|H_z|$ increases over the edges of the anomaly in both profiles. The source field causes non-symmetry in the peak values. As before an increase in the theoretical $|H_z|$ figure is noted over the boundary of the anomaly parallel to the y axis.

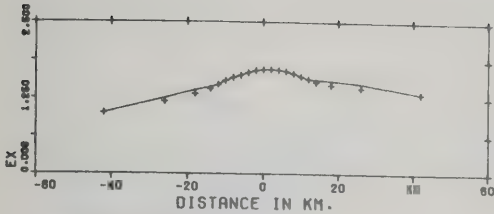
3.4.3 The Horizontal Dipole Source Results

The profiles and three dimensional figures of the results for the horizontal dipole source comparison are shown in Fig. 3.11 to Fig. 3.14. The first set of profiles, Fig. 3.11, is taken 18 km from the center of the anomaly in the negative x direction. The concentration of charge on the boundary of the anomaly is clearly evident in the analogue model electric field $|E_x|$ profile. Also the non-uniform source field and its effect on the anomalous electric field is apparent. The theoretical curve agrees well with the analogue curve confirming the theoretical boundary value calculation of Ramaswamy (1973) used here. The magnetic field, ($|H_y|$), profile of the analogue model shows the source field variation but little effect from the anomaly. The theoretical field curve increases from negative to positive y but by an insufficient amount to exactly match the analogue curve. This misalignment of the curve is

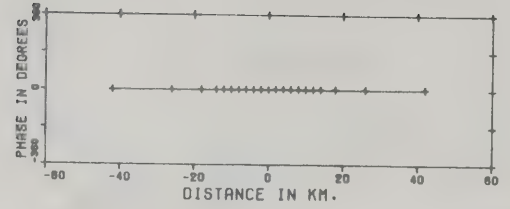
Figure 3.11 $|E_x|$, $|H_y|$, $|H_z|$, $|H_z/H_y|$ and ρ_a profiles
with normalized phases for the horizontal
dipole source field and profile 1.

- theoretical calculation

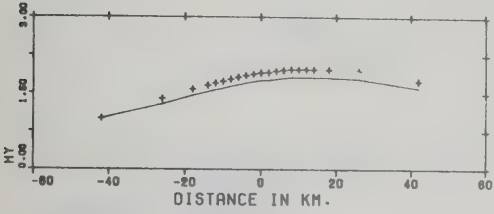
+ analogue model



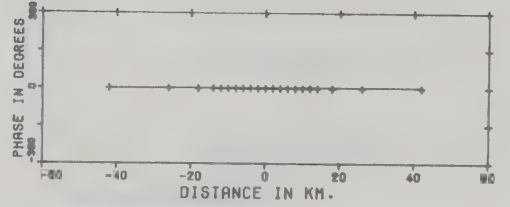
NORMALIZED AMPLITUDE EX



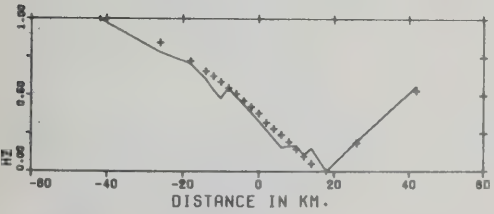
NORMALIZED PHASE OF EX



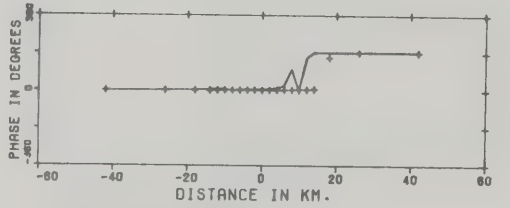
NORMALIZED AMPLITUDE HY



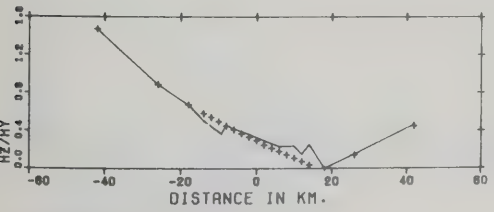
NORMALIZED PHASE OF HY



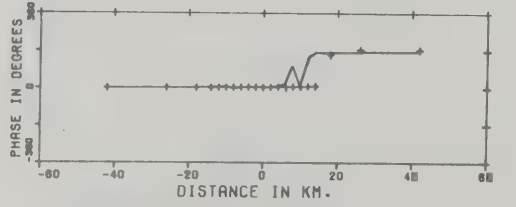
NORMALIZED AMPLITUDE HZ



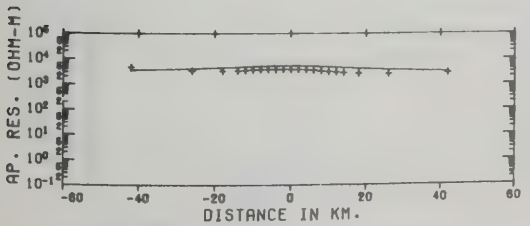
NORMALIZED PHASE OF HZ



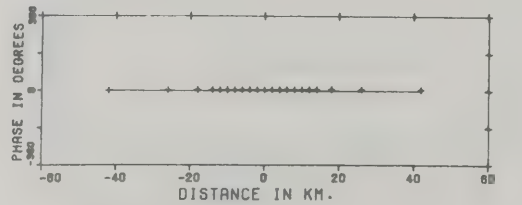
NORMALIZED AMPLITUDE HZ/HY



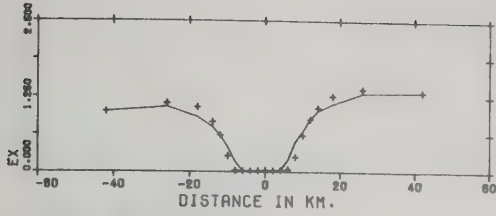
NORMALIZED PHASE OF HZ/HY



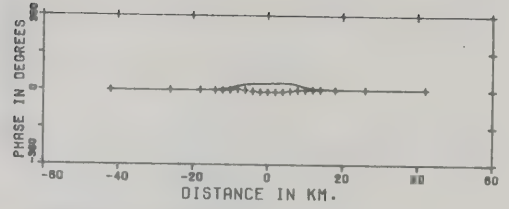
APPARENT RESISTIVITY



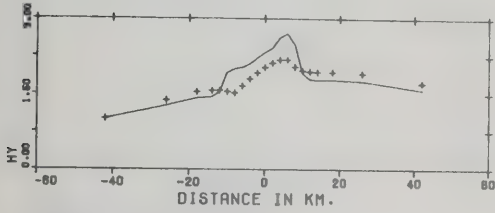
NORMALIZED PHASE OF EX/HY



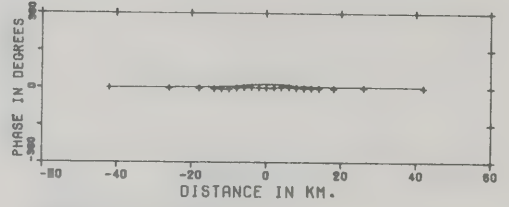
NORMALIZED AMPLITUDE EX



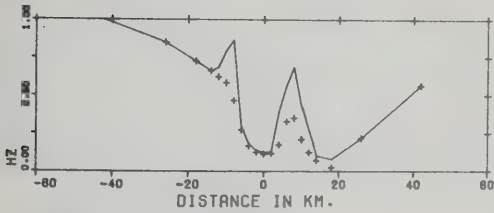
NORMALIZED PHASE OF EX



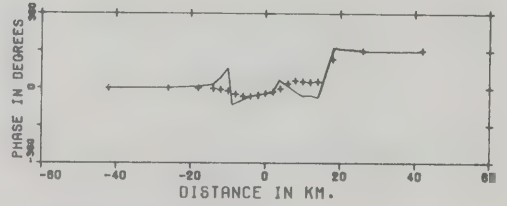
NORMALIZED AMPLITUDE HY



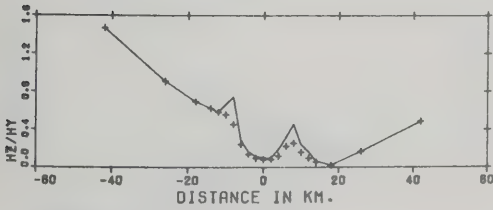
NORMALIZED PHASE OF HY



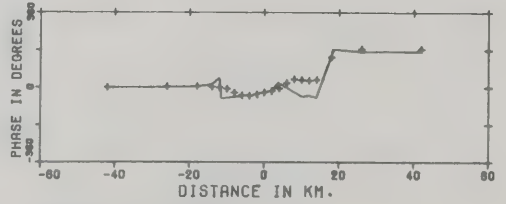
NORMALIZED AMPLITUDE HZ



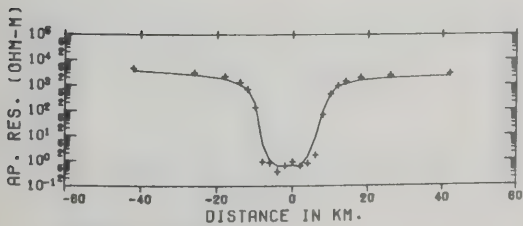
NORMALIZED PHASE OF HZ



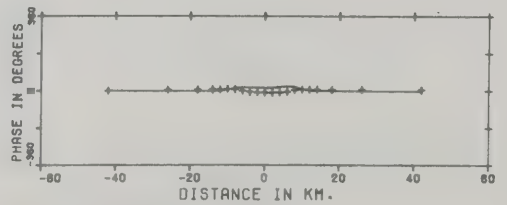
NORMALIZED AMPLITUDE HZ/HY



NORMALIZED PHASE OF HZ/HY



APPARENT RESISTIVITY



NORMALIZED PHASE OF EX/HY

Figure 3.12 As Figure 3.11 but for profile 2.

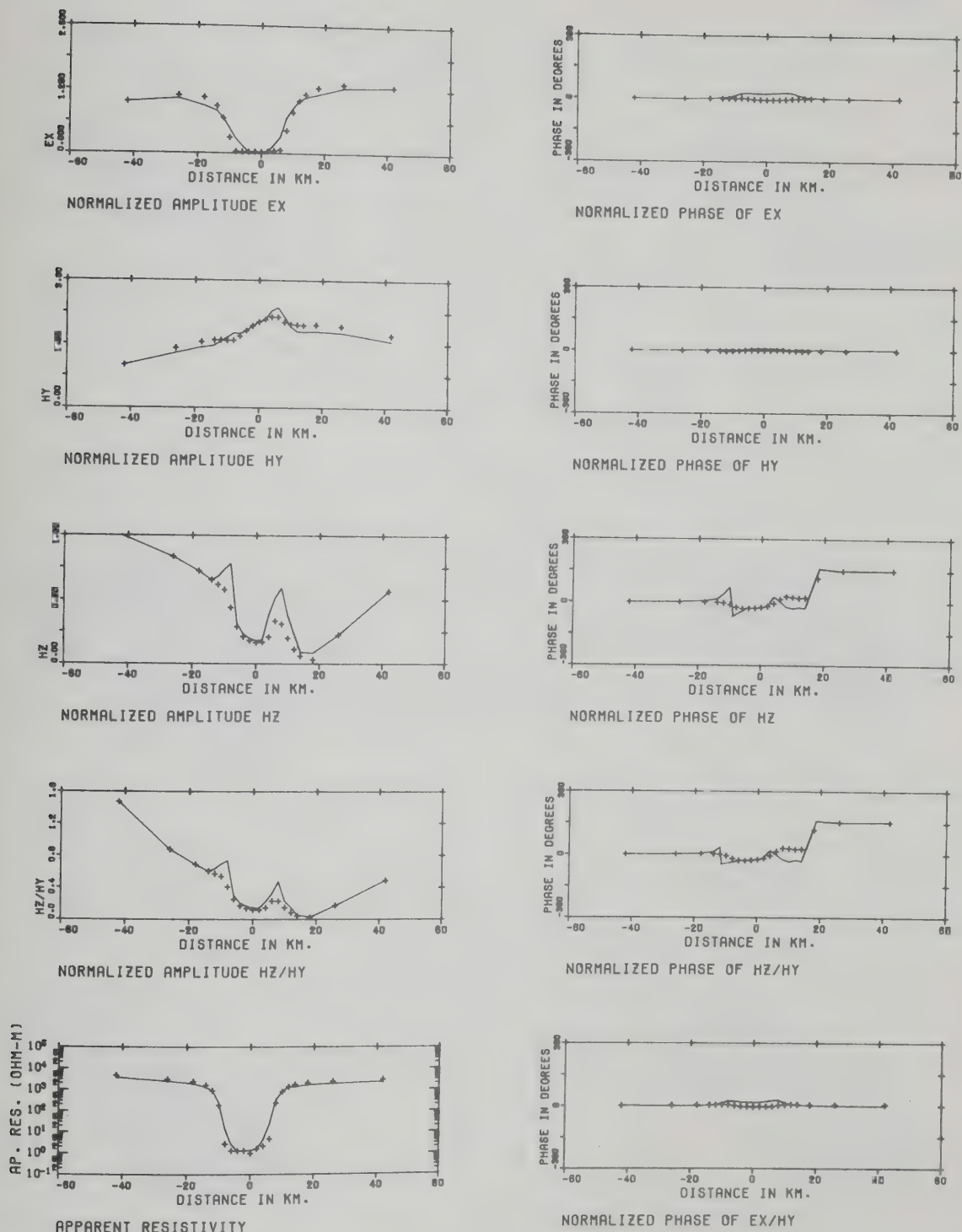
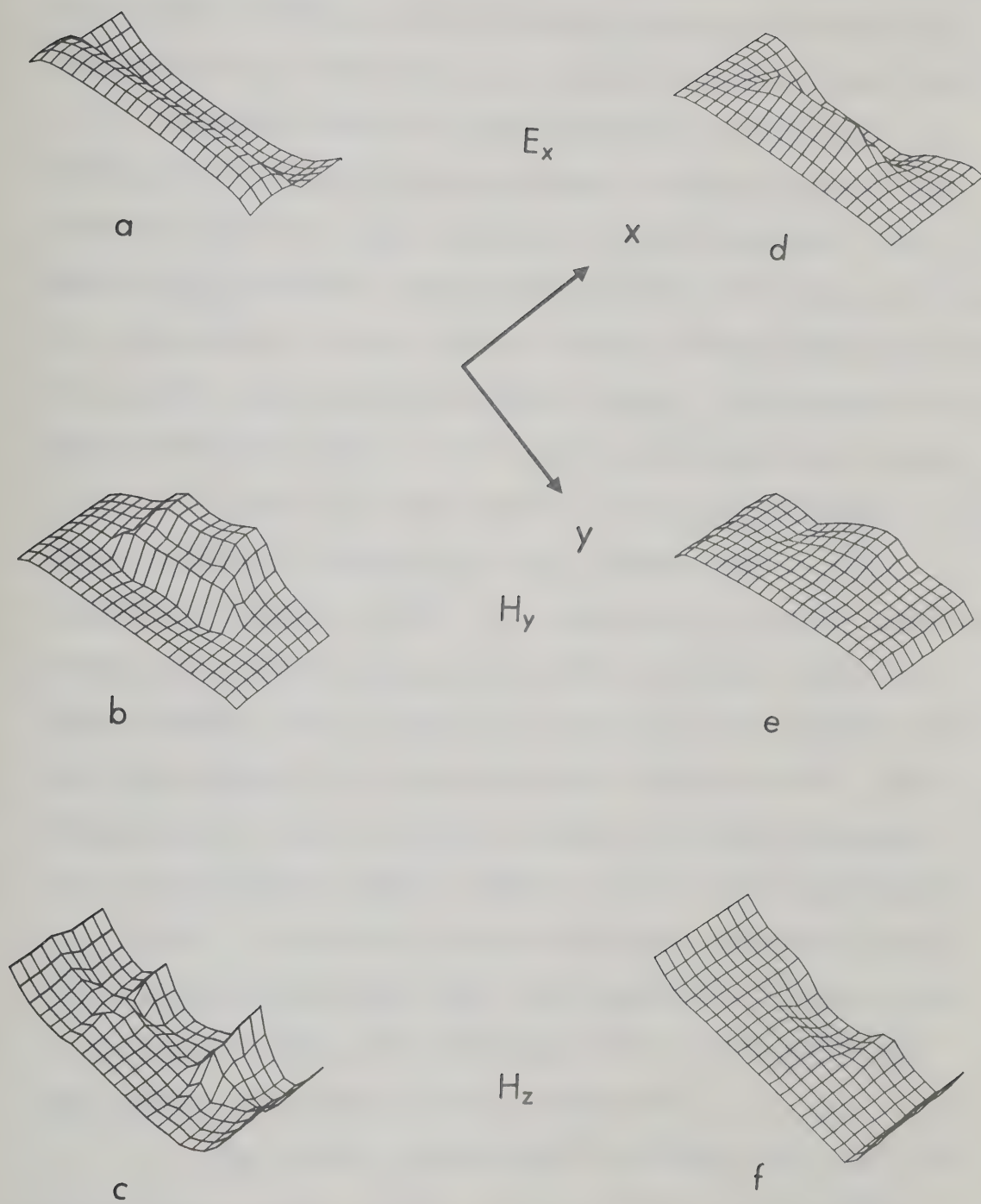


Figure 3.13 As Figure 3.11 but for profile 3.

Figure 3.14 Three-dimensional profiles of $|E_x|$, $|H_y|$ and $|H_z|$ for the horizontal dipole source field.

Theoretical profiles (a,b,c)

Analogue profiles (d,e,f)



explained by the fact that the value of the magnetic field at $y = -42$ km used to normalize the curve is slightly less accurate due to the wider grid spacing used at that point. This, combined with the larger spatial variation of the source field, serves to accentuate the misalignment when compared with the $|H_y|$ profiles of other sources. The $|H_z|$ and $|H_z/H_y|$ profiles compare quite well with this profile. The theoretical curves show a slightly more anomalous field as was the case for the uniform source. The apparent resistivity has the value of the poorly conducting host earth, 4.76×10^3 ohm/m, for both models. The analogue model curve shows a slight increase over the anomaly due to the increased electric field. This increase is not as large as noted for previous sources for this profile. This is a source effect due to the fact that $|H_y|$ has a larger value over the anomaly for the horizontal dipole source. The theoretical curve is slightly higher than the analogue curve due to the slightly lower value of the theoretical $|H_y|$ curve. The phase comparisons agree reasonably well and are nearly constant with the exception of the H_z and H_z/H_y phases which shift through 180° at the minima of the amplitude curves of these quantities.

The second set of profiles taken along the line $x = -4$ km is given in Fig. 3.12. As before the effects of the anomaly are clearly evident in this profile. Both the analogue and theoretical $|E_x|$ curves decrease over the

anomaly by approximately the same amount and exhibit the same source field with the exception of the effect of the transition zone.

Near $y = \pm 42$ km both the theoretical and analogue $|H_y|$ curves assume the same relationship as in the previous profile, however, over the anomaly both curves now increase. The theoretical curve tilts upward in the positive y direction over the anomaly with the two small peaks at $y = \pm 8$ km. The analogue curve exhibits a decrease over the edge of the anomaly at $y = -8$ km and an increase over the edge at $y = +8$ km.

The $|H_z|$ and $|H_z/H_y|$ curves for the theoretical and analogue models exhibit two non-symmetric peaks over the edges of the anomaly along with the profile of the source field. The theoretical curve peaks are slightly higher and wider as was the case for the uniform source. The theoretical and analogue apparent resistivity curves vary from approximately the poorly conducting value of the host earth, 4.76×10^3 ohm/m, to the value of the highly conducting anomaly, 0.8 ohm/m. The phases of E_x and ρ_a increase slightly over the boundaries of the anomaly for the theoretical calculation which can be attributed to the transition zone at the boundaries. The phase of H_y remains constant in both the analogue and theoretical models. The phase of H_z and H_z/H_y dips to -60° at

$y = -8$ km and increases to $+60^\circ$ at $y = +8$ km over the boundaries of the anomaly for the analogue model. A 180° phase shift is noted at $y = +18$ km due to the source field in the analogue model. The phase curves of the theoretical model exhibit first an increase and then a decrease at $y = \pm 8$ km due to the transition zone. The theoretical curve then remains constant until the 180° phase shift at $y = +18$ km.

The third set of profiles taken across the center of the anomaly, $x = 0$ km, is given in Fig. 3.13. As was the case for the previous sources these profiles have much the same shapes for the amplitude curves as the previous profiles of Fig. 3.12. The $|E_x|$ and ρ_a comparison curves more closely agree in these profiles. The trends of the $|H_y|$, $|H_z|$ and $|H_y/H_z|$ curves seen in the previous profiles for the analogue model are fully defined in this profile. The increase of the theoretical $|H_y|$ curve is more pronounced. The phase profiles are much the same as in the previous profile.

The three dimensional amplitude profiles of the comparison of the three electromagnetic field components is shown in Fig. 3.14. The $|E_x|$, $|H_y|$ and $|H_z|$ three-dimensional profiles for the theoretical model are shown in Fig. 3.14a,b,c and for the analogue model in Fig. 3.14 d,e,f and each figure is scaled individually as before.

As with the other sources the increase in $|E_x|$ just outside the anomaly due to the charge on the boundary is evident in the analogue model, Fig. 3.14d, along with the decrease in the field over the anomaly. In Fig. 3.14a the smoothing effect of the transition zone can be seen. The source effect is clearly evident in the $|H_y|$ and $|H_z|$ profiles for the analogue model, Figs. 3.14c,f. The values of the theoretical $|H_y|$ and $|H_z|$ curves, Fig. 3.14b,c, over the boundary of the anomaly parallel to the y axis are higher than would be expected due to the transition zone. A comparison of Fig. 3.14c and Fig. 3.14f shows that $|H_z|$ increases over the edges of the anomaly for both the theoretical model and analogue model. However, the analogue model variation of $|H_z|$ is less accentuated.

3.5 Summary

The two very different methods for studying electromagnetic perturbation problems show general agreement. The condition of a gradually changing electric field through transition zones in the theoretical calculations leads to differences in the results near the boundary of the anomaly especially for the magnetic field. This effect, however, has been lessened by the inclusion of the transition zone. This effect is both a function of the frequency, the conductivity contrast and

to a lesser extent the grid spacing. The solution over the anomaly and at large distances agrees well with the analogue model thereby confirming the boundary condition calculations of Hibbs and Jones (1976d,e) and Ramaswamy (1975). The frequency, .075 Hz, together with the high conductivity contrast tests the limits of the approximations in the methods. It is seen that a transition zone must be introduced in the numerical method to allow the fields to vary more rapidly. For longer periods or lower conductivity contrasts the fields vary less rapidly and are better approximated particularly in the numerical calculations. It has thus been instructive to examine the possible limits on the approximations applied to the iterative process due to the complexity of the process and the large number of configurations which can be modelled.

CHAPTER 4

A STUDY OF PERTURBATION AND INDUCTION ARROWS FOR VARIOUS CONDUCTIVITY CONFIGURATIONS AND SOURCE FIELDS

The numerical methods of Chapter 2 are used to calculate the electromagnetic fields associated with three dimensional conductivity anomalies. The calculations were done for three source fields and three conductivity configurations. A uniform field oriented in various directions relative to the anomaly is considered first. The transfer functions and related perturbation and induction arrows associated with the fields are calculated. The results show that the perturbation arrows do not well describe the anomalous currents for the three-dimensional model considered, but can give a method of outlining the spatial extent of the anomaly. The induction arrows may be used in the traditional way to indicate the flow of anomalous currents and point toward conductivity inhomogeneities. Two methods of calculating the induction arrows are compared.

The second type of source field considered is due to a number of two-dimensional sheet current sources with different current intensity distributions, variously positioned and orientated with respect to the conductivity anomaly. The transfer functions and related perturbation

and induction arrows associated with the fields are calculated as before. In addition, approximate normal and perturbation fields are used in the transfer function calculations and comparisons are made.

The third source field considered is due to horizontal magnetic dipoles placed at two different positions with respect to the conductivity anomaly. The transfer functions and related perturbation and induction arrows associated with the fields are calculated and compared with the arrows obtained from a uniform source calculation. Again, the results show the source effect on the induction arrows and indicate that the perturbation arrows provide a method of outlining the spatial extent of the anomaly. The transfer function calculations are made for both exact and approximate normal fields. In the transfer function calculation the anomalous fields are correlated with a normal field as suggested by Schmucker (1970) and Cochrane and Hyndman (1970).

4.1 The Mathematical Formulation of the Induction and Perturbation Arrows

In studies of geomagnetic variations, it is common to seek empirical relationships between different magnetic field components which are independent of time. The electromagnetic induction phenomena encountered in geomagnetic studies obey Maxwell's equations. These

equations are linear, and thus linear induction matrices can be defined. The determination of the elements of these matrices and from them the conductivity structure of the earth is the goal of transfer function analysis. Schmucker (1970) defined two sets of arrows, the induction and perturbation arrows, in terms of the elements of his induction matrix.

In his approach, Schmucker (1970) assumed that a linear relationship exists between the Fourier transforms of the anomalous internal field components and the normal field components for a single frequency and this is expressed as:

$$\begin{vmatrix} C_{x_a} \\ C_{y_a} \\ C_{z_a} \end{vmatrix} = \begin{vmatrix} h_x & h_y & h_z \\ d_x & d_y & d_z \\ z_x & z_y & z_z \end{vmatrix} \begin{vmatrix} C_{x_n} \\ C_{y_n} \\ C_{z_n} \end{vmatrix} + \begin{vmatrix} C_{\Delta x} \\ C_{\Delta y} \\ C_{\Delta z} \end{vmatrix} \quad (4.1)$$

The quantities C_{x_a} , C_{y_a} and C_{z_a} are Fourier transforms of the anomalous parts of the x, y and z components of the magnetic field respectively; C_{x_n} , C_{y_n} and C_{z_n} are the Fourier transforms of the normal parts of the x, y and z magnetic field components respectively; and $C_{\Delta x}$, $C_{\Delta y}$ and $C_{\Delta z}$ are the Fourier transforms of the uncorrelated portions of the x, y and z components, where

the Fourier transform for a function $R(t)$ is defined as

$$C_R(f) = \int_{-\infty}^{+\infty} R(t) e^{-i\omega t} dt \quad (4.2)$$

The transfer functions h , d and z are in general complex and their real parts are referred to as the in-phase transfer functions while their imaginary parts are the quadrature-phase transfer functions. Then for the anomalous part of Z_a

$$C_{Z_a} = Z_x C_{x_n} + Z_y C_{y_n} + Z_z C_{z_n} + C_{\Delta z} \quad (4.3)$$

The autocorrelation power spectrum of C_{Z_a} is defined as

$$S_{Z_a Z_a} = C_{Z_a} \cdot C_{Z_a}^* / T_0 \quad (4.4)$$

where T_0 is the period chosen, $S_{Z_a Z_a}$ is the limiting value as $T_0 \rightarrow \infty$ and $C_{Z_a}^*$ denotes the complex conjugate of C_{Z_a} .

In a similar manner the cross correlation power spectrum between C_{Z_a} and C_{x_n} for example is defined as

$$S_{Z_a x_n} = S_{x_n Z_a}^* = (C_{Z_a} \cdot C_{x_n}) / T_0 \quad (4.5)$$

Using the crosscorrelation and autocorrelation power spectra of the anomalous and normal field components along with the condition that the crosscorrelation power spectra between the residual and normal field components

be zero, Schmucker (1970) obtained a linear matrix involving the transfer functions and power spectra. For the z transfer functions:

$$\begin{aligned} z_x S_{x_n x_n} + z_y S_{y_n x_n} + z_z S_{z_n x_n} &= S_{z_a x_n} \\ z_x S_{x_n y_n} + z_y S_{y_n y_n} + z_z S_{z_n y_n} &= S_{z_a y_n} \\ z_x S_{x_n z_n} + z_y S_{y_n z_n} + z_z S_{z_n z_n} &= S_{z_a z_n} \end{aligned} \quad (4.6)$$

Similar matrices can be obtained for the h and d transfer functions.

Schmucker (1970) represented the transfer functions as two sets of arrows. If we let \underline{i} and \underline{j} be Cartesian unit vectors in the x and y directions respectively, the induction arrows are defined for a particular frequency as:

$$\underline{c}_{\text{real}} = -z_{x_{\text{real}}} \underline{i} - z_{y_{\text{real}}} \underline{j} \quad (\text{in-phase arrow}) \quad (4.7)$$

$$\underline{c}_{\text{imaginary}} = z_{x_{\text{imaginary}}} \underline{i} + z_{y_{\text{imaginary}}} \underline{j} \quad (\text{quadrature-phase arrow})$$

in accordance with the orientation of the Parkinson (1959) arrow. The in-phase arrows, as defined here, point toward current concentrations and thus toward regions of higher conductivity than the surroundings.

The second set of arrows, called perturbation arrows, is defined as:

$$\begin{aligned}\underline{p} &= h_x \underline{i} + d_x \underline{j} \\ \underline{q} &= h_y \underline{i} + d_y \underline{j}\end{aligned}\tag{4.8}$$

for both in-phase and quadrature-phase arrows. Schmucker (1970) points out that when these arrows are rotated 90° counter-clockwise they indicate the strength and direction of the anomalous internal current field which is superimposed on the unperturbed normal current flow. The \underline{p} arrow represents the anomalous current in the - y direction and the \underline{q} arrow that in the x direction.

In the present work the in-phase induction arrows are made negative with respect to the definition by Schmucker (1970) and consequently point away from high conductivity areas toward areas of low conductivity. The perturbation arrows are rotated 90° counter-clockwise in the manner suggested by Schmucker (1970).

4.2 The Calculation of Perturbation and Induction Arrows for a Uniform Source Over a Three-Dimensional Conductivity Model

The calculations are carried out for uniform sources linearly polarized at various directions over a conductivity inhomogeneity embedded in a two-layered semi-infinite conducting region with a plane boundary. The

first layer is 4 km in depth and of conductivity 4 mho/m. The second layer is of infinite depth and has conductivity 0.001 mho/m. The embedded anomaly is a 6 km square intrusion of the lower conductive layer which penetrates the top layer to the surface of the conductor.

This conductivity configuration was chosen because of its symmetry since all the electric field solutions for the source polarization angles presented could be derived from three independent solutions (0° , 23° , 45°).

The numerical technique of Section 2.8 is used to obtain the electric field solution from which the magnetic fields and transfer functions are calculated. The calculations have been made for two frequencies: 0.001 Hz and 0.0033 Hz.

4.2.1 Single Source Results

For linear polarization and a single orientation of the source field in which the normal magnetic field is in the y direction the transfer function matrix reduces to a single equation. For the z transfer function matrix this equation is:

$$z_y = \frac{S_{z_a y_n}}{S_{y_n y_n}} \quad (4.9)$$

Similar equations can be obtained from the h and d transfer function matrices.

The transfer functions obtained in this manner for the model considered are shown in the arrow representation in Figure 4.1 for 0.001 Hz. Since the normal current is polarized in the x direction, the \underline{p} perturbation arrow is undefined. The \underline{q} perturbation arrow should then describe the magnitude and direction of the anomalous current. The \underline{q} arrow together with the arrows associated with the calculated anomalous current (from the known electric perturbation field and the conductivity structure) and the induction arrows are shown in Figure 4.1.

Away from the anomaly the perturbation arrows (Figure 4.1A) qualitatively resemble the anomalous current arrows (Figure 4.1B). Nearer the anomaly the in-phase perturbation arrows differ markedly from the in-phase anomalous current arrows. Over the anomaly the in-phase perturbation arrows greatly increase in magnitude. Since the conductivity of the anomaly decreases by a factor of 4×10^3 , the current flowing in the anomaly is small relative to that flowing in the surrounding material and therefore only small anomalous current arrows appear over the anomaly. In the method of Section 2.8 the conductivity associated with a particular node is the average of the conductivities of the surrounding regions, and the boundary between the anomaly and the surrounding region is not abrupt as indicated in the figure but consists of a transition zone between the conductive regions.

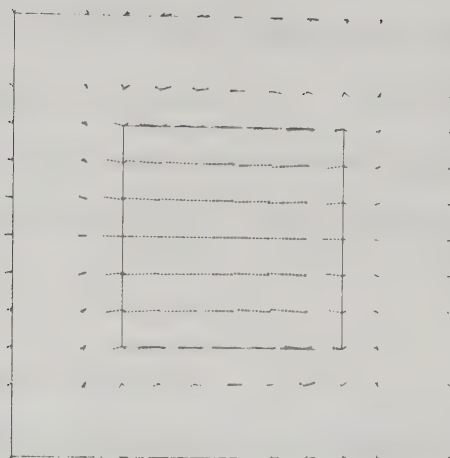
Figure 4.1 Single source with the normal current field in the X direction for 0.001 Hz. The dashed arrows are the in-phase arrows and the solid arrows are the quadrature-phase arrows.

(A) g perturbation arrows,

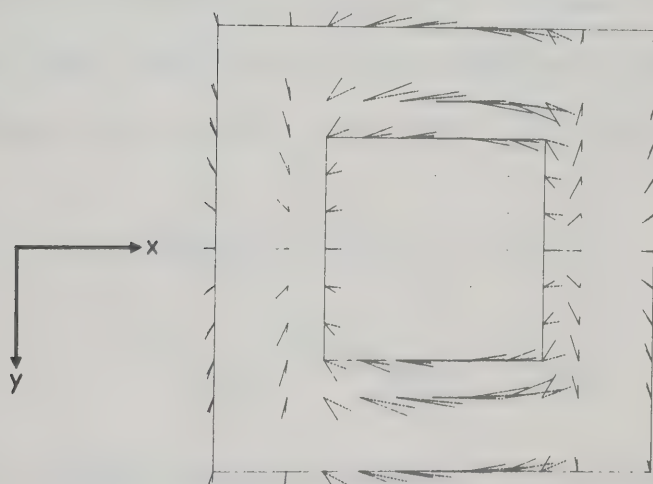
(B) anomalous current arrows,

(C) induction arrows.

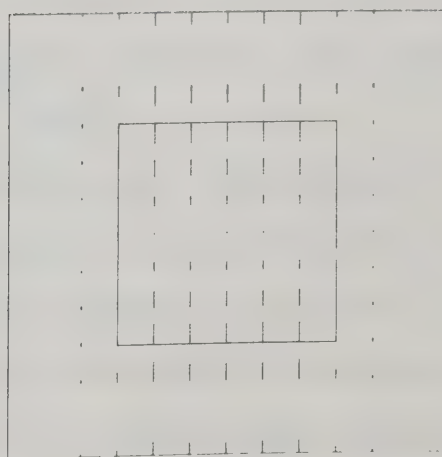
The surface of the conducting region near the anomaly is shown and the inner square region represents the anomalous structure.



A



B



C

Figure 4.1C gives the induction arrows associated with this simple source orientation. The arrows are polarized in the direction of the normal magnetic field. They vary in magnitude over the grid and point toward the conductivity anomaly.

4.2.2 Multiple Source Results

For a number of sources with the inducing field linearly polarized and oriented in various different directions the transfer function matrix is represented by a two-dimensional matrix. For the z transfer functions

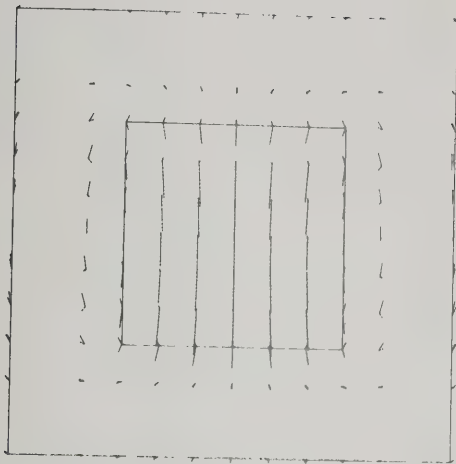
$$\begin{aligned} z_x S_{x_n x_n} + z_y S_{y_n x_n} &= S_{z_a x_n} \\ z_x S_{x_n y_n} + z_y S_{y_n y_n} &= S_{z_a y_n} \end{aligned} \quad (4.10)$$

The cross correlation and autocorrelation power spectra are calculated for each source polarization and these are averaged and the transfer functions are determined in the manner of Schmucker (1970).

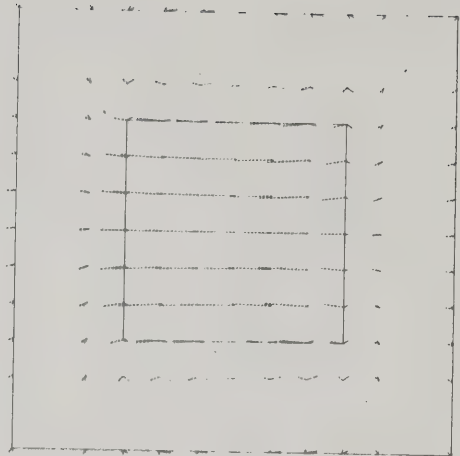
The results from the calculation of transfer functions for six sources for periods of 0.001 Hz and 0.0033 Hz are shown in Figures 4.2 and 4.3. For the case of multiple sources at different orientations both \underline{p} and \underline{q} arrows are defined. By adding these two arrows vectorially ($\underline{p} + \underline{q}$) an arrow to represent the total anomalous

Figure 4.2 Perturbation, current and induction arrows calculated from six source orientations: 23° , 45° , 90° , 135° , 248° and 315° as measured counter-clockwise from the x-axis for 0.001 Hz. The dashed arrows are the in-phase arrows and the solid arrows are the quadrature-phase arrows.

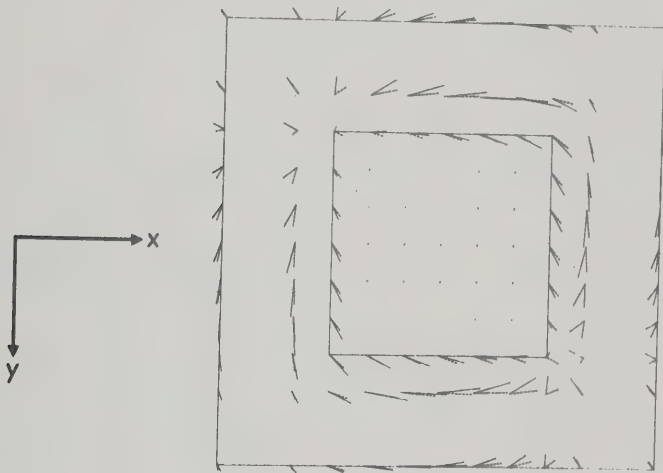
- (A) \underline{p} perturbation arrows,
- (B) \underline{q} perturbation arrows,
- (C) anomalous current arrows,
- (D) $\underline{p} + \underline{q}$ perturbation arrows,
- (E) induction arrows.



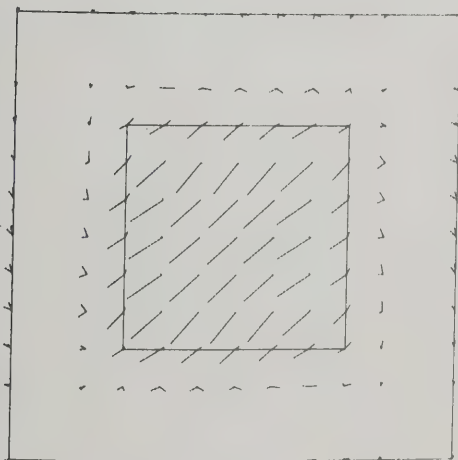
A



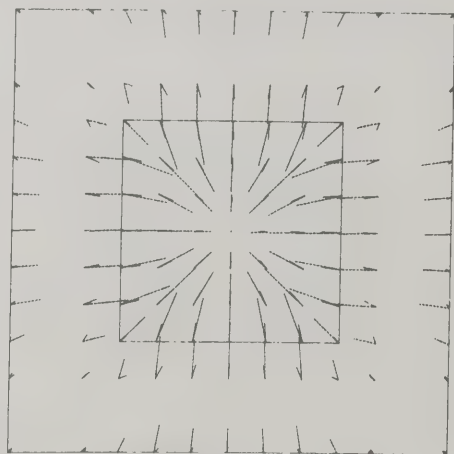
B



C

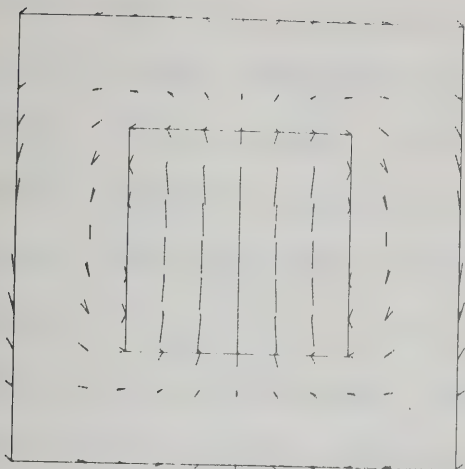


D

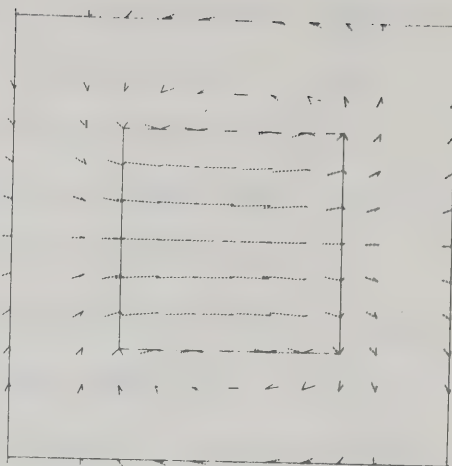


E

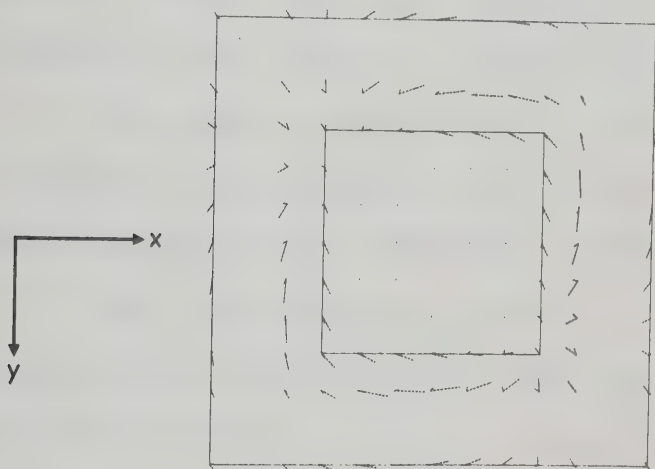
Figure 4.3 As Figure 4.2 but for 0.0033 Hz.



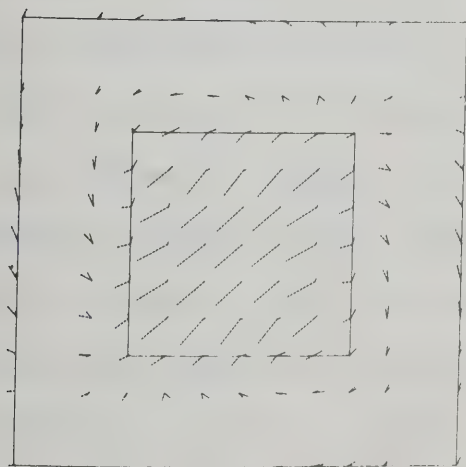
A



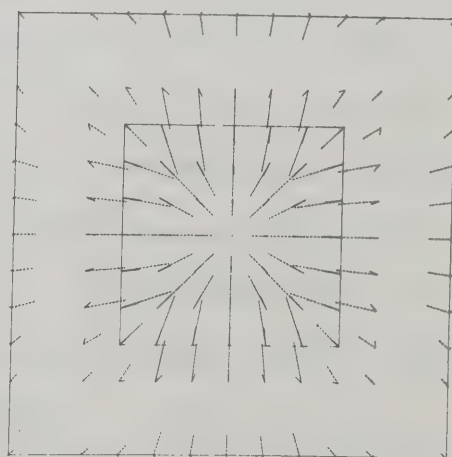
B



C



D



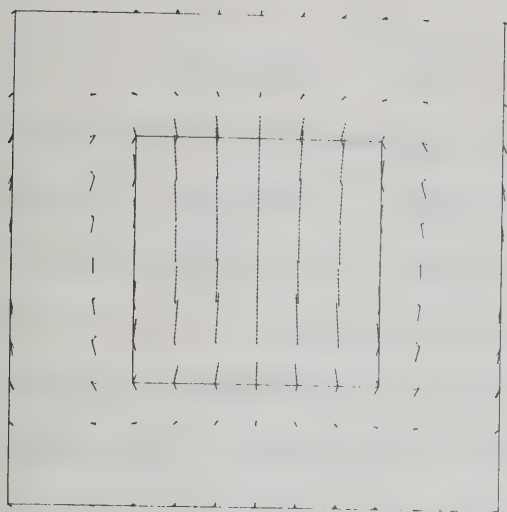
E

current should be obtained. The \underline{p} and \underline{q} arrows together with the arrows representing $\underline{p} + \underline{q}$ are given in these figures. Also, vectors which describe the calculated anomalous electric currents determined from the anomalous electric field and known conductivities are shown in Figures 4.2C and 4.3C. It is apparent that the $(\underline{p} + \underline{q})$ arrows do not compare well with the anomalous current arrows for this three-dimensional model. From Figures 4.2E and 4.3E, we see that the induction arrows are no longer polarized, but now point toward the center of the anomaly over the whole surface region. The stability of the perturbation and induction arrows with frequency for this model is apparent by comparison of Figures 4.2 and 4.3.

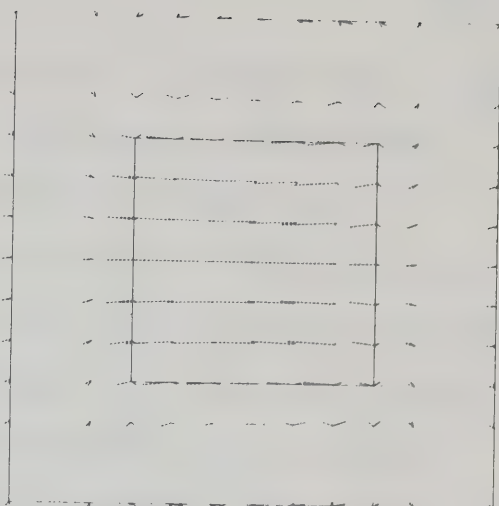
If the \underline{p} perturbation arrow is made negative with respect to the definition by Schmucker (that is, it now defines the anomalous internal current superimposed on the normal currents flowing in the $+y$ direction) as in Figure 4.4A and then added to the \underline{q} perturbation arrow to give a new $(\underline{p} + \underline{q})$ arrow as in Figure 4.4E, this new $(\underline{p} + \underline{q})$ arrow now agrees qualitatively with the calculated anomalous current arrows (Figure 4.4D) for regions away from the anomaly. As the anomaly is approached both the in-phase and quadrature-phase $(\underline{p} + \underline{q})$ arrows differ from the anomalous current arrows. However, both sets of arrows exhibit the same general trend. Over the edge of the anomaly the $(\underline{p} + \underline{q})$ perturbation arrows point approximately opposite in direction to the anomalous current arrows.

Figure 4.4 Perturbation, electric field, current and induction arrows calculated from six source orientations: 23° , 45° , 90° , 135° , 248° and 315° at 0.001 Hz. The dashed arrows are the in-phase arrows and the solid arrows are the quadrature-phase arrows.

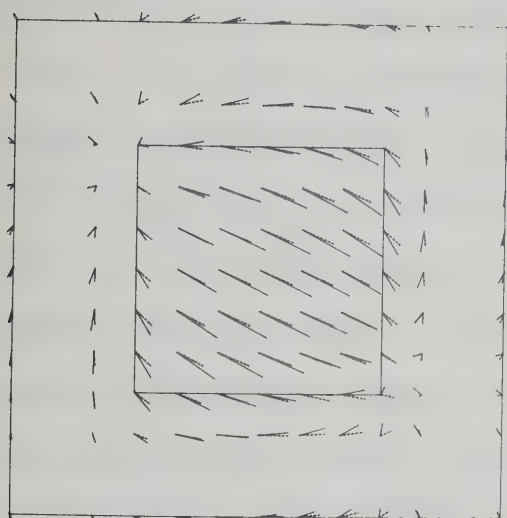
- (A) p perturbation arrows,
- (B) q perturbation arrows,
- (C) anomalous electric field arrows,
- (D) anomalous current arrows,
- (E) $p + q$ perturbation arrows,
- (F) induction arrows.



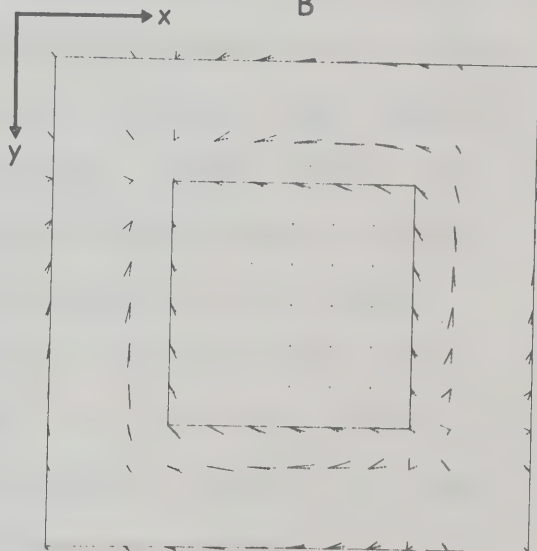
A



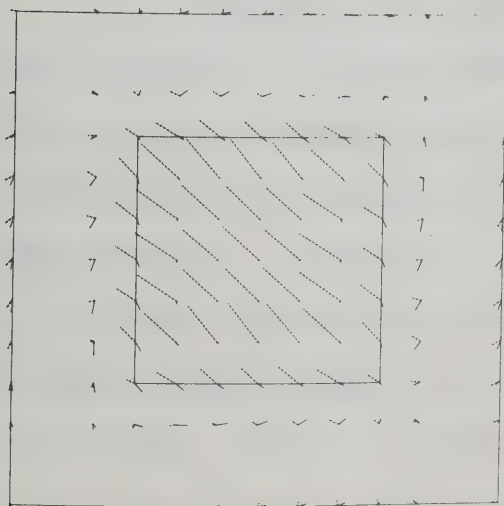
B



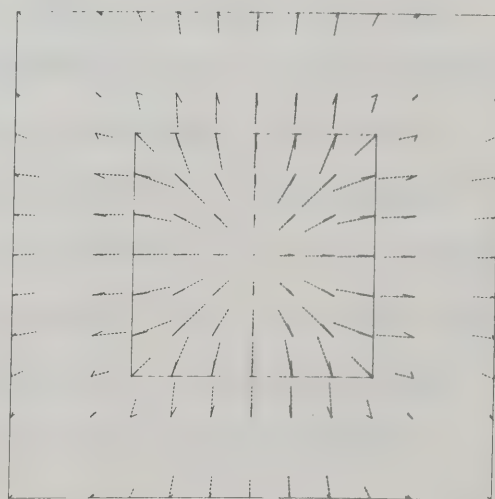
C



D



E



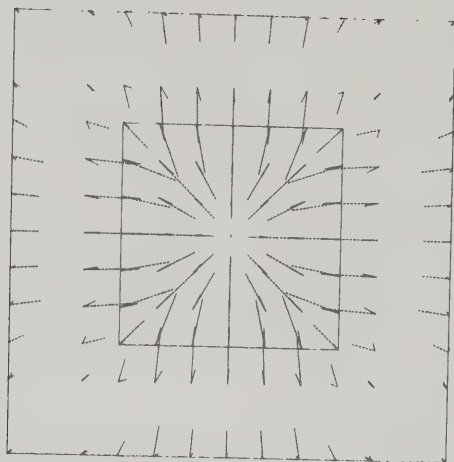
F

Schmucker (1970) stated that at least five random source field orientations are required to assure stable transfer functions. Figure 4.5 gives a comparison of induction arrows for three sets of polarization angles at 0.001 Hz. In Figure 4.5A two source orientations which are mutually perpendicular are used and the induction arrows compare well with those of Weidelt (1975) calculated by superposition for a somewhat similar model. In Figure 4.5B three source field orientations spread over a range of 45° are used to construct the arrows and some skewing of the induction arrows is evident. Figure 4.5C is for six source field orientations which are spread throughout the full 360° range and in this there is very little skewing of the arrows. It appears that less than six source orientations may be used, but if this is done the direction of the source fields must be chosen with care and should be quite different from one another.

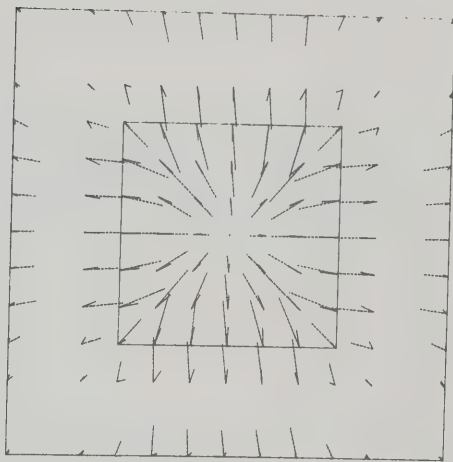
Cochrane and Hyndman (1970) proposed that the total magnetic field be substituted for the normal magnetic field in the transfer function calculations since this would be easier to apply in the analysis of experimental observations. Figure 4.6 is a recalculation of the arrows as in Figure 4.2 but with this change, and it is seen that no appreciable change in the configuration of the arrows is produced. This is expected because the horizontal

Figure 4.5 Comparison of number and angular spread of current sources. The dashed arrows are the in-phase arrows and the solid arrows are the quadrature-phase arrows.

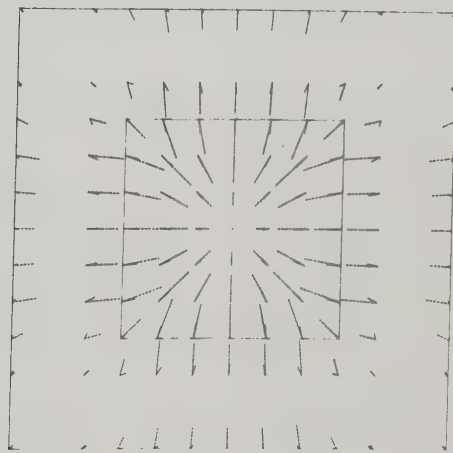
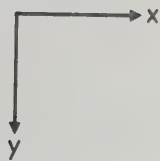
- (A) induction arrows for source polarization angles of 0° and 90° ,
- (B) induction arrows for source polarization angles of 0° , 23° and 45° ,
- (C) induction arrows for source polarization angles of 23° , 45° , 90° , 135° , 248° and 315° .



A

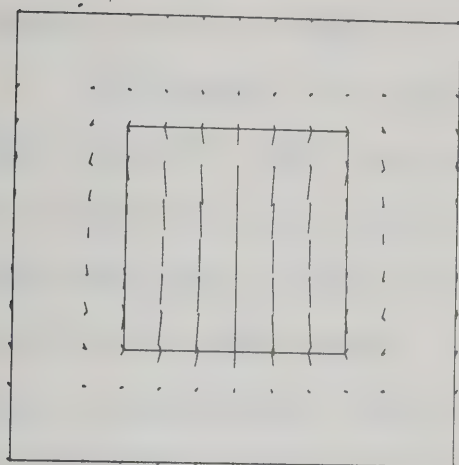


B

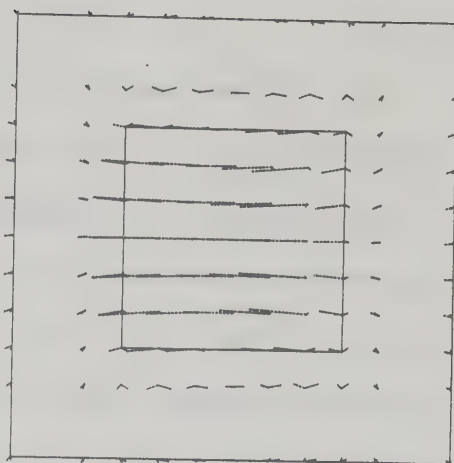


C

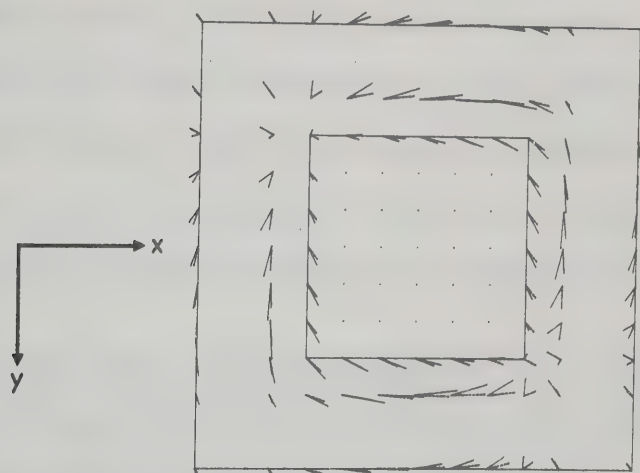
Figure 4.6 Perturbation, current and induction arrows calculated as in Figure 4.2, but with the substitution as suggested by Cochrane and Hyndman (1970). A, B, C, D and E parts as in Figure 4.2.



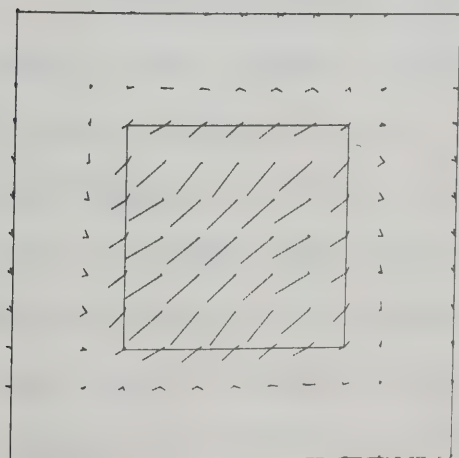
A



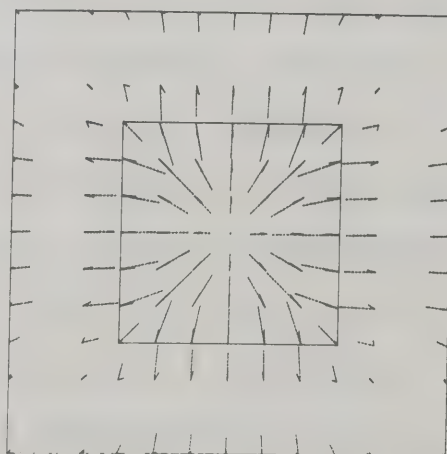
B



C



D



E

magnetic field decreases by only about 25 percent over the anomaly for this model.

In Figures 4.4C and 4.4E a comparison of the anomalous electric field and the new ($\underline{p} + \underline{q}$) perturbation arrows is made for six source orientations at 0.001 Hz. Both the anomalous electric field and perturbation arrows are sensitive to the anomaly. The electric field is more sensitive to anomalous structure than the magnetic field. It may therefore be desirable, since in most experimental work of this nature the magnetic fields are measured, to obtain electric field information from quantities calculated from the observed magnetic fields. In this respect, the ($\underline{p} + \underline{q}$) perturbation arrow should be useful in accurately outlining regions of anomalous conductivity.

4.3 The Calculation of Perturbation and Induction Arrows for a Three-Dimensional Conductivity Structure and Various Two-Dimensional Source Fields

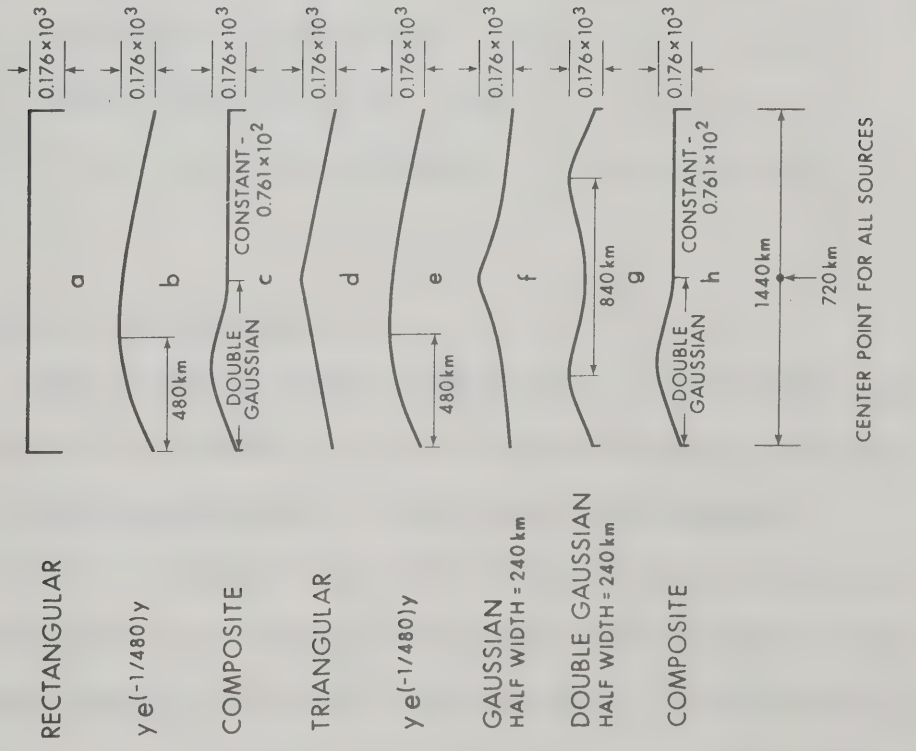
The calculations were carried out for eight two-dimensional sheet current sources with spatial intensity as in Figure 4.7 oscillating with a circular frequency of $2\pi/\omega$ and flowing at a height of 110 km above a two-layered semi-infinite conducting region with a plane boundary and an embedded conductivity anomaly. The first layer is 50 km in depth and of conductivity 0.01 mho/m. The second layer extends to infinity and has a conductivity of 0.1

Figure 4.7 Coordinate system, sources and anomaly
(not to scale).

SOURCE SHEET CURRENT DISTRIBUTION

ANGLE OF SOURCE
POLARIZATION

DISTANCE
FROM CENTER POINT OF
SOURCE TO CENTER POINT
OF ANOMALY, y DIRECTION
IN km



CENTER POINT FOR ALL SOURCES

mho/m. The embedded anomaly is L-shaped, as in Figure 4.7 and has a depth of 3 km. The conductivity of the anomaly is 0.0001 mho/m, and the calculation is done for a frequency of 0.1 Hz.

The boundary conditions for the finite difference mesh were determined by using the general method for two dimensional sheet current distributions over layered conductors as described in Section 2.6. Each source was approximated in a piecewise linear manner by 49 suitably weighted rectangular current distributions of 30 km width. The rectangular current distributions were approximated by three elemental gaussians of 10 km half-width each spatially shifted one half-width. These field values were then substituted into the numerical technique of Section 2.8 and the electromagnetic field solutions obtained.

4.3.1 Single Source Results

The normal magnetic field for a non-uniform sheet current source polarized in the x direction will contain magnetic field components in the y and z direction. However, the z component is small in comparison with the y component over the anomaly and surrounding region. For this reason the 3x3 transfer function matrix (equation 4.6) is ill-conditioned and must be reduced to a one-dimensional relationship. For the z transfer function matrix this

equation is:

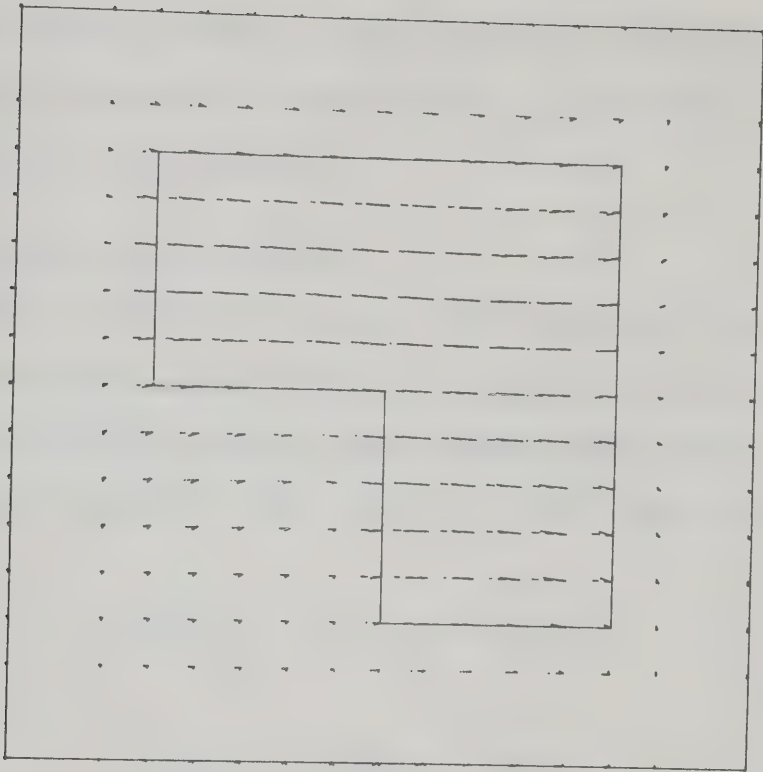
$$z_y = \frac{S_{z_a y_n}}{S_{y_n y_n}} \quad (4.11)$$

Similar equations are obtained from the h and d transfer function matrices upon reduction to the one-dimensional case.

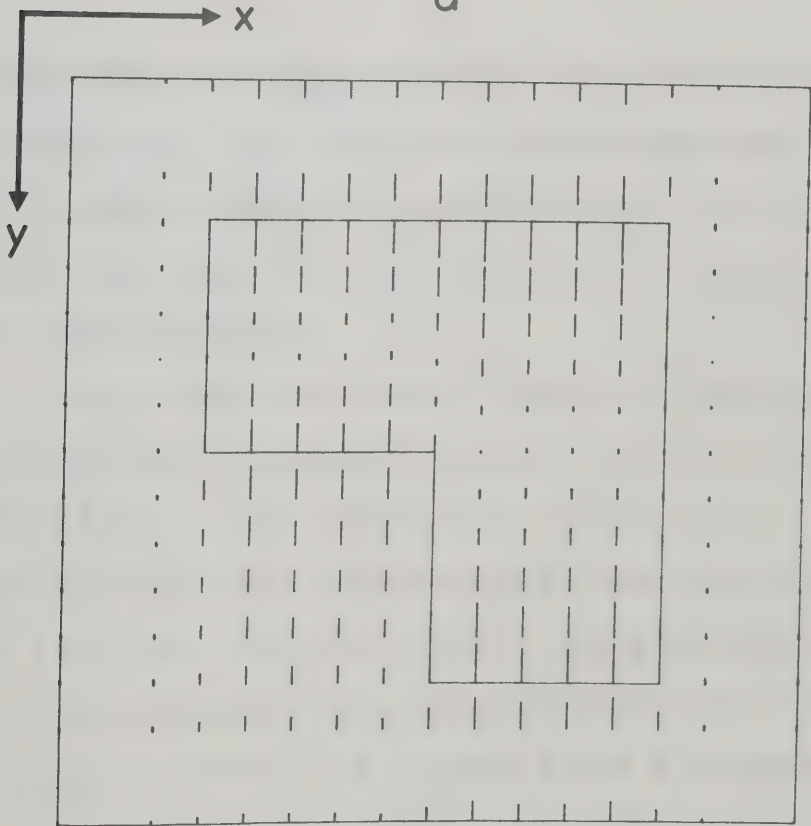
The non-uniform sheet current source with the electric field polarized in the x direction used in this model is shown in Figure 4.7A. The transfer functions obtained in this manner for the model considered are shown in the arrow representation in Figure 4.8. Since only h_y , d_y , and z_y are defined for this source, the \underline{p} perturbation arrow is undefined. The \underline{q} perturbation arrows (Figure 4.8A) should then describe the magnitude and direction of the anomalous current. At some distance from the anomaly as was found in Section 4.2, the \underline{q} perturbation arrows qualitatively resemble the anomalous current arrows. However, over the anomaly the perturbation arrows increase in magnitude and are not representative of the anomalous currents. This is to be expected since the anomalous magnetic field is most intense over the anomaly. Also, for this source, the induction arrows, Figure 4.8B, are polarized in the y direction. The induction arrows vary in magnitude over the grid and point toward the anomaly. As would be expected the null of the induction arrows

Figure 4.8 Single source with normal current field in the x direction for 0.1 Hz. The dashed arrows are the in-phase arrows, the solid arrows are the quadrature-phase arrows.

(A) q perturbation arrows,
(B) induction arrows.



a



b

inside the anomaly shifts in the positive y direction as the anomaly is crossed in the positive x direction due to the broadening of the anomaly.

4.3.2 Multiple Source Results

For a number of sources with inducing fields linearly polarized and orientated in various directions the transfer function matrix must now be represented by a two-dimensional matrix. For the z transfer functions:

$$\begin{aligned} z_x S_{x_n x_n} + z_y S_{y_n x_n} &= S_{z_a x_n} \\ z_x S_{x_n y_n} + z_y S_{y_n y_n} &= S_{z_a y_n} \end{aligned} \quad (4.12)$$

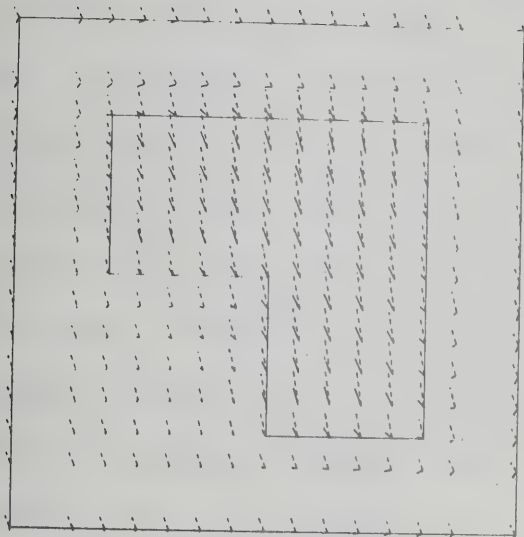
Similar equations are obtained from the h and d transfer function matrices. The cross correlation and auto-correlation power spectra are calculated for each source polarization and these are averaged and the transfer functions are determined.

The two sources used to represent a multiple source orientation are shown in Figure 4.7B,C. An approximate separation of 70° in the orientation of the source polarizations allows the calculation of the transfer functions with less than six source field polarizations.

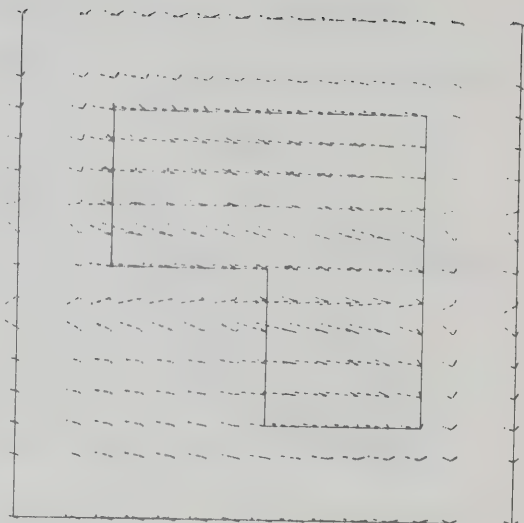
The results of this calculation for the frequency used are shown in Figure 4.9. Since h and d transfer

Figure 4.9 Two sources with polarizations separated by 70° situated near anomaly for 0.1 Hz. The dashed arrows are the in-phase arrows and the solid arrows are the quadrature-phase arrows.

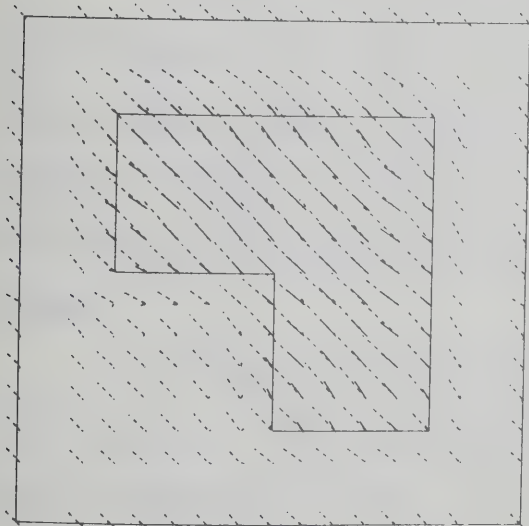
- (a) \underline{p} perturbation arrows,
- (b) \underline{q} perturbation arrows,
- (c) $\underline{p} + \underline{q}$ perturbation arrows,
- (d) induction arrows.



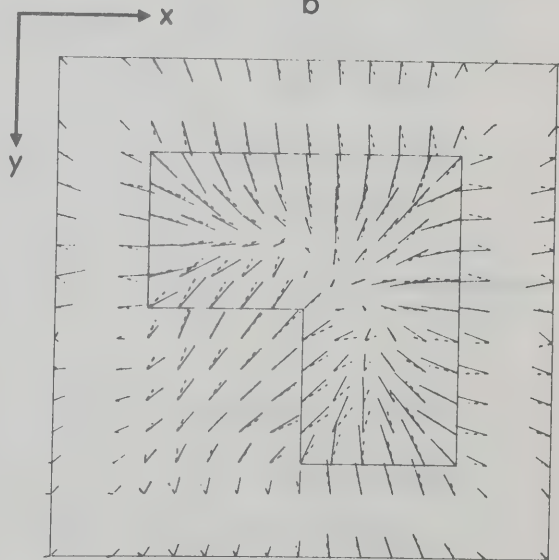
a



b



c



d

function matrices are two-dimensional in x and y both the \underline{p} (Figure 4.9a) and \underline{q} (Figure 4.9b) arrows are defined. The \underline{p} perturbation arrows have been made negative with respect to the definition of Schmucker (1970) (that is, they now define the anomalous internal current superimposed on the normal currents flowing in the $+y$ direction. If these two arrows are added vectorially ($\underline{p} + \underline{q}$) as in Figure 4.9c, the spatial extent of the anomaly is outlined by arrows polarized at an angle of approximately 135° counter-clockwise to the positive x axis. The ($\underline{p} + \underline{q}$) arrows are approximately 50% larger than the surrounding arrows over the anomaly.

In this case the induction arrows (Figure 4.9d) are no longer polarized in the y direction. The arrows tend to point radially toward the central moment of the anomaly. However, some source effect due to the non-uniformity of the source field can be noted in the in-phase arrows.

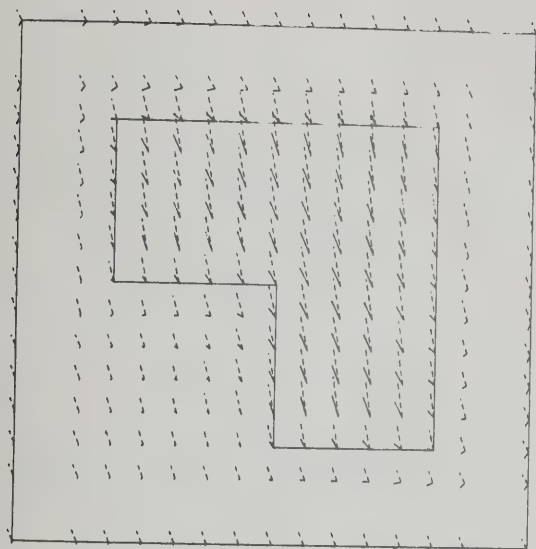
As pointed out by Cochran and Hyndman (1970), the problem of defining the normal field for the calculation of induction arrows can be partially overcome by substituting the total field as the normal field in the transfer function calculations, since this is easier to apply in the analysis of experimental observations. In their calculations Cochran and Hyndman (1970) assumed that the magnetic field component in the z direction was

totally anomalous which thus allows a calculation of the induction arrows. This assumption cannot be made when calculating the anomalous field for the horizontal components of the magnetic field. Figure 4.10 is a recalculation of the arrows in Figure 4.9 using the Cochrane and Hyndman (1970) suggestion. As can be seen in Figure 4.10, little change is noted in the perturbation and induction arrows, which depend on the horizontal magnetic field components. However, the anomalous field used to calculate the perturbation and induction arrows in Figure 4.10 is exact.

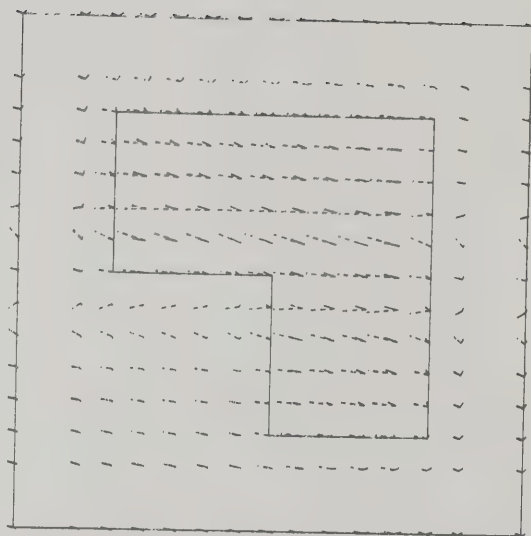
It is important to determine the effect on the calculations if the anomalous and normal fields are approximate. In Figure 4.11 the perturbation and induction arrows are given for a calculation in which the normal field is assumed to be constant and the anomalous field is the result of subtracting the normal field from the total magnetic field. The value for the normal field was obtained by averaging the field values along the boundary of the finite difference mesh. The boundary forms a square with a perpendicular distance of 58 km from the center of the anomaly. Figure 4.11 gives an indication of the relative stability of the Schmucker method.

Schmucker (1970) stated that at least five random source field orientations are required to assure

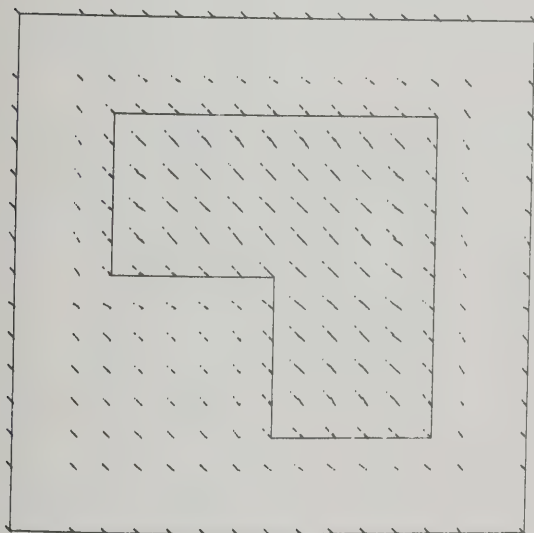
Figure 4.10 As Figure 4.9 but with substitution as suggested by Cochrane and Hyndman (1970).



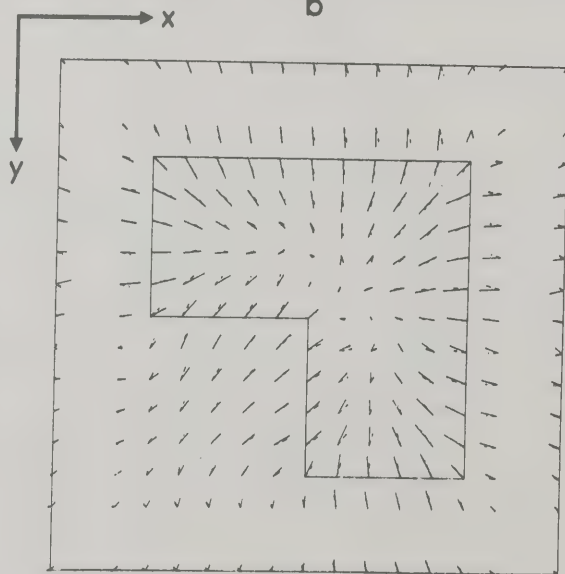
a



b

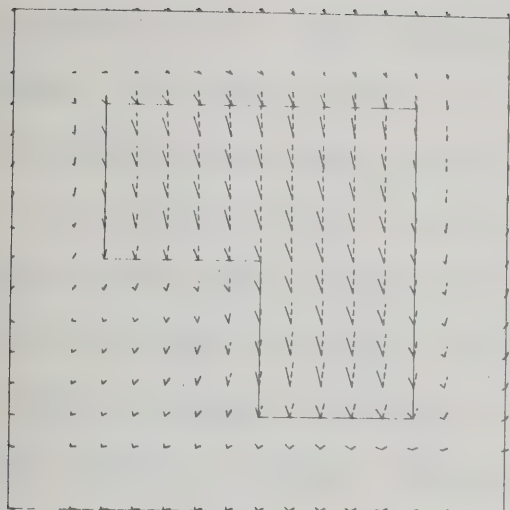


c

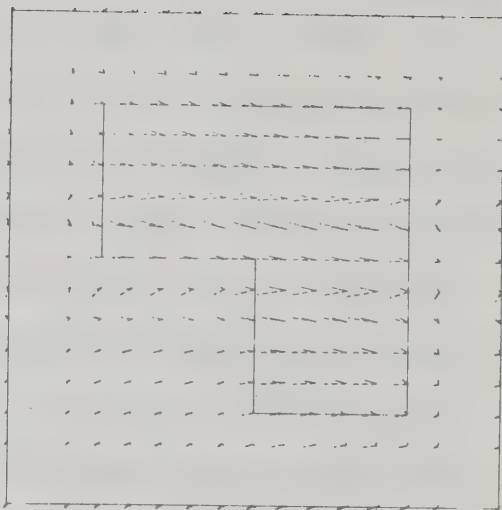


d

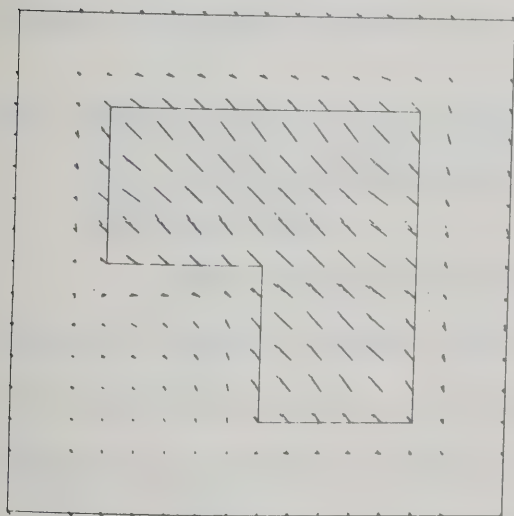
Figure 4.11 As Figure 4.9 but for averaged normal field.



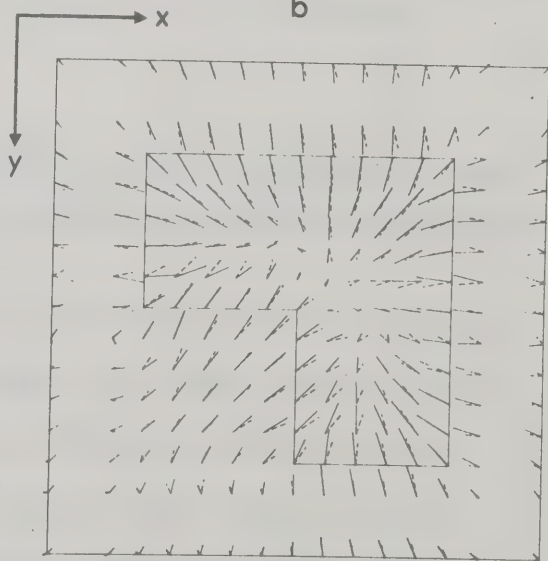
a



b



c



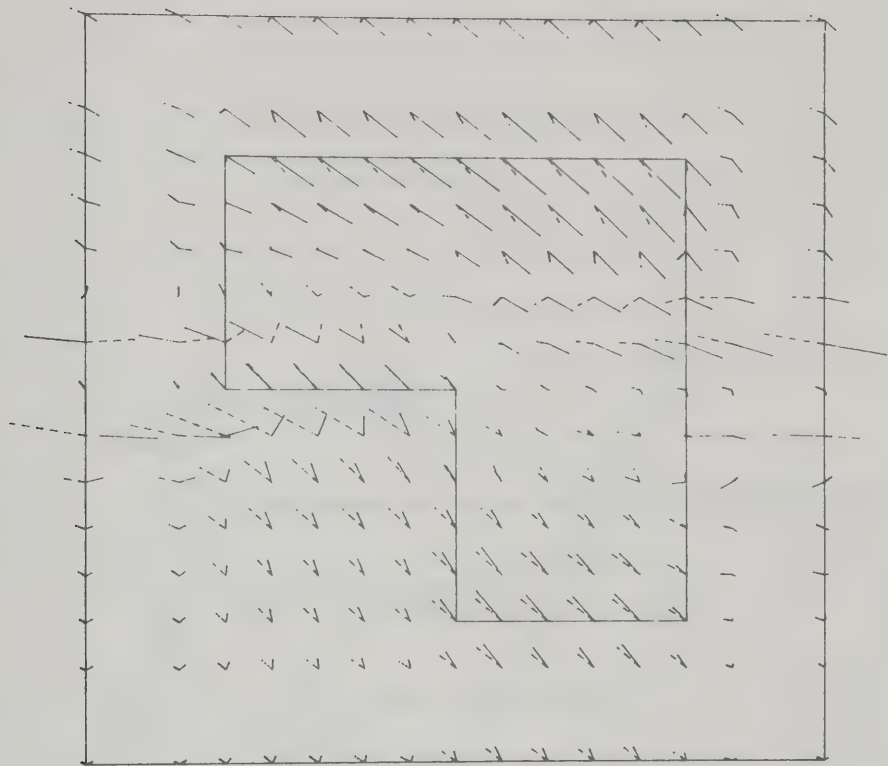
d

stable transfer functions. Figure 4.12 shows the result of calculating the induction arrows for six sources centered a large distance from the anomaly with an angular spread of 63° . The sources used in this calculation are shown in Figure 4.7a, d, e, f, g, h. In Figure 4.12a the calculation was done in the manner of Schmucker (1970) and it is apparent that severe skewing of the induction arrows is evident when compared to Figure 4.9d. The calculation of the induction arrows according to Cochrane and Hyndman (1970) is shown in Figure 4.12. Again severe skewing of the arrows is noted. However, the appearance of the two diagrams differs much more than was the case between Figure 4.9d and Figure 4.10d.

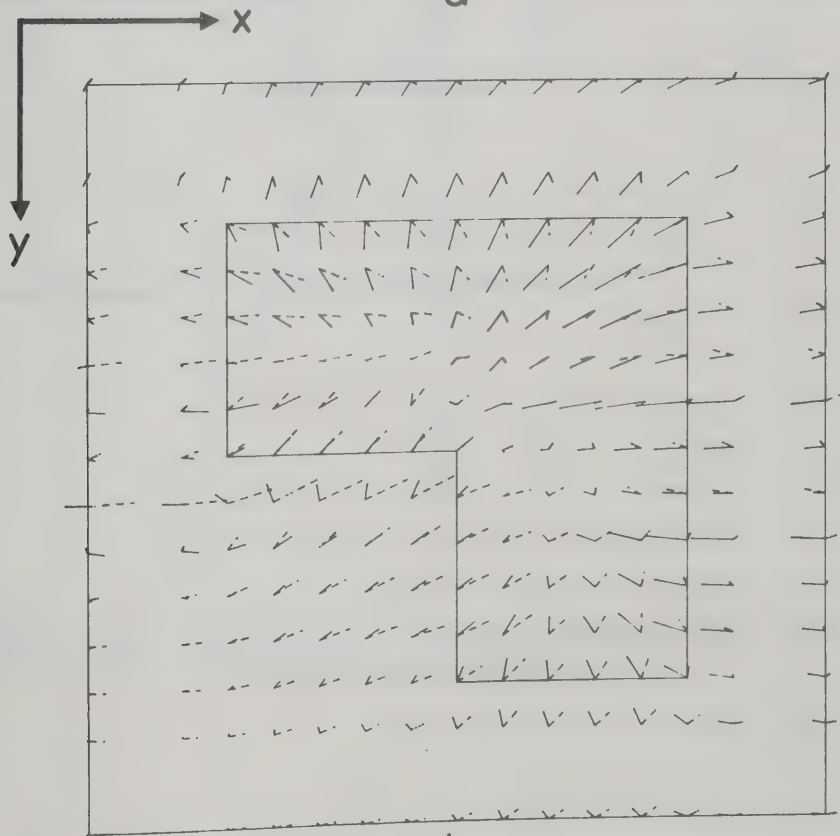
4.4 The Calculation of Perturbation and Induction Arrows for a Three-Dimensional Conductivity Model and Dipole Source Fields

The calculations were carried out for horizontal magnetic dipole sources indicated by 1 and 2 as in Figure 4.13 oscillating with a circular frequency of $2\pi/\omega$ and placed at a height of 150 km above a two-layered semi-infinite conducting region with a plane boundary and an embedded conductivity anomaly. The first layer is 128 km in depth and of conductivity 0.21×10^{-3} mho/m. The second layer is of infinite depth and has conductivity 0.8 mho/m. The embedded anomaly (indicated by the inner

Figure 4.12 Induction arrows for six distant sources
with close angular spread (68°).
(a) calculation according to Schmucker (1970),
(b) calculation according to Hyndman (1970).



a



b

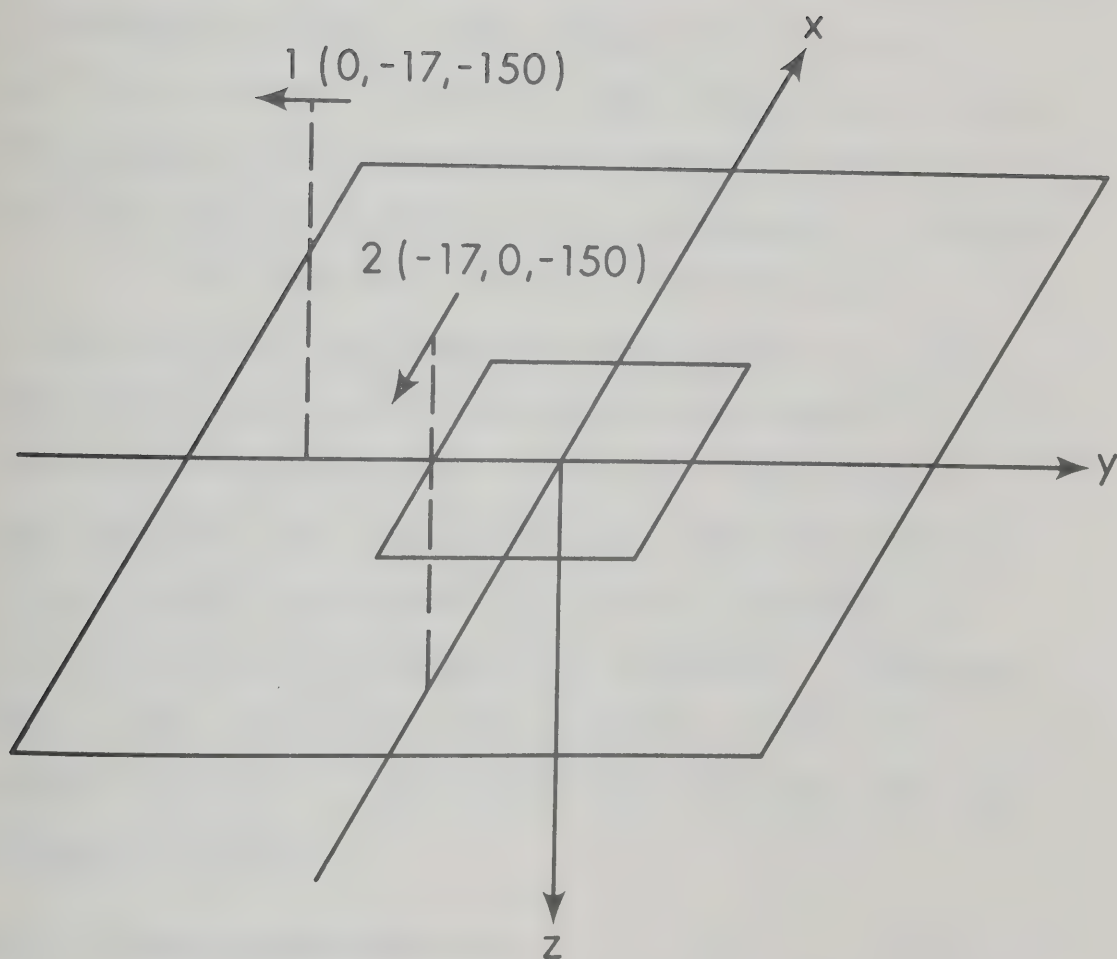


Figure 4.13 Coordinate system, anomaly and two dipole sources (not to scale).

square of Figure 4.13) is 16 km square and 4 km deep with its top at the surface of the conducting region and has the same conductivity as the lower layer. With the origin of the coordinate system at the center of the anomaly, the position (in Cartesian coordinates) of the first dipole is ($x=0$ km, $y=-17$ km, $z=-150$ km) and of the second is ($x=-17$ km, $y=0$ km, $z=-150$ km). The dipole moment of the first dipole is polarized in the negative y direction and the second dipole is polarized in the negative x direction.

The numerical technique of Section 2.8 is used to obtain the electric field solution for the three-dimensional model and from this the magnetic fields and transfer functions are calculated. The boundary conditions for the finite difference mesh are obtained for the dipole source above the layered conductor by means of a program supplied by V. Ramaswamy, (Ramaswamy, 1973). Near the boundary the anomalous fields are assumed to be zero. The calculations were made for the frequency 0.075 Hz.

4.4.1 Single Source Results

For a single magnetic dipole at position 1 the theoretically calculated normal magnetic fields contain all three field components. However, the x and z components are small in comparison to the y component over the anomaly and surrounding region due to the

position of the dipole at $x=0$ km, $y=-17$ km and $z=-150$ km. For this reason the 3×3 transfer function (equation 4.6) is ill-conditioned and must be reduced to a one-dimensional relationship. For the z transfer function matrix this equation is:

$$z_y = \frac{S_{z_a y_n}}{S_{y_n y_n}} \quad (4.13)$$

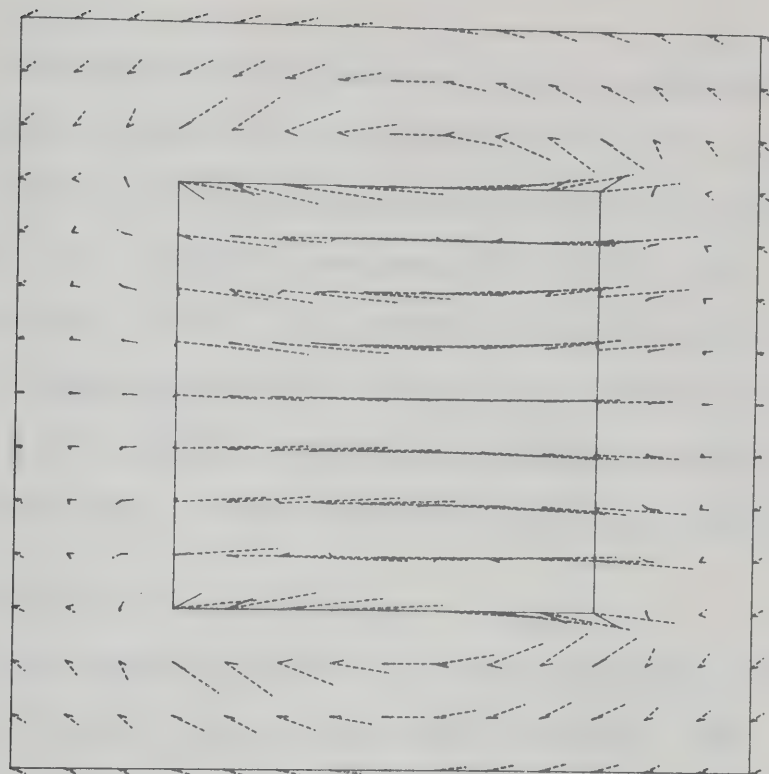
Similar equations are obtained from the h and d transfer function matrices upon reduction to the one-dimensional case.

The transfer functions obtained in this manner for the model considered are shown in the arrow representation in Figure 4.14. Since only h_y , d_y and z_y are defined for this source, the p perturbation arrow is undefined. The q perturbation arrows (Figure 4.14A) should then describe the magnitude and direction of the anomalous current. At some distance from the anomaly as was found previously, the q perturbation arrows qualitatively resemble the anomalous current arrows. However, over the anomaly the perturbation arrows increase in magnitude and are not representative of the anomalous currents. Also, for this source, the induction arrows, Figure 4.14B, are polarized in the y direction. The induction arrows vary in magnitude over the grid and point away from the anomaly.

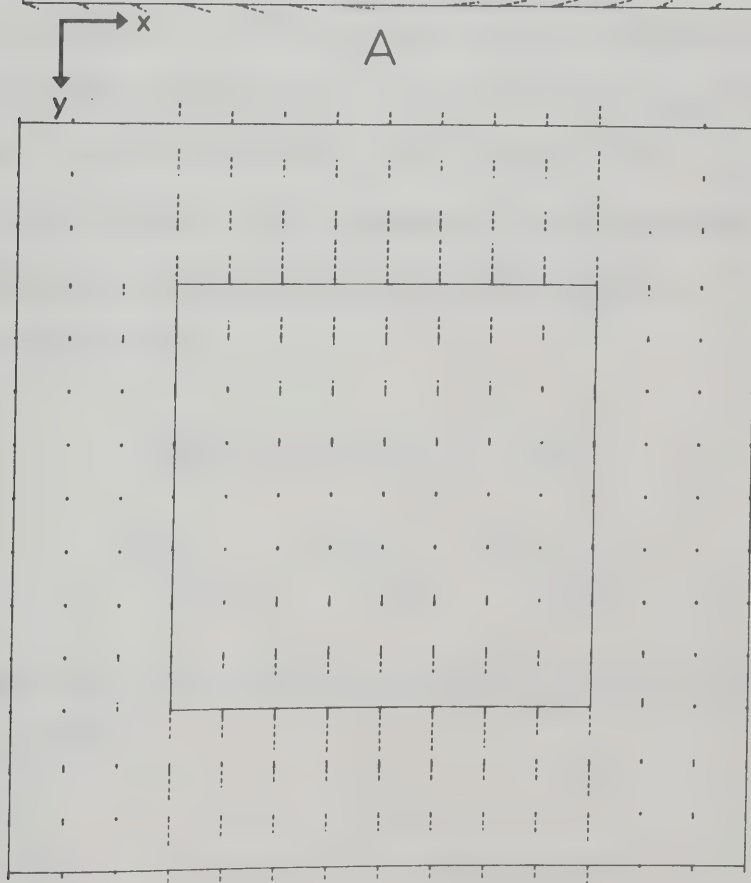
Figure 4.14 Single horizontal dipole source with moment polarized in y direction positioned at $x=0$ km, $y=17$ km and $z=150$ km. The dashed arrows are the in-phase arrows and the solid arrows are the quadrature-phase arrows.

(A) q perturbation arrows,
(B) induction arrows.

The surface of the conducting region near the anomaly is shown and the inner square region represents the anomalous structure.



A



B

For purposes of comparison the q perturbation and induction arrows for a uniform source with a normal magnetic field polarized in the $+y$ direction are given in Figure 4.15. In the q perturbation arrows the quadrature-phase arrows are greater in magnitude compared with the in-phase arrows for the uniform field source. Also, the q perturbation arrows are more perturbed in the uniform field case. The induction arrows are very similar.

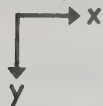
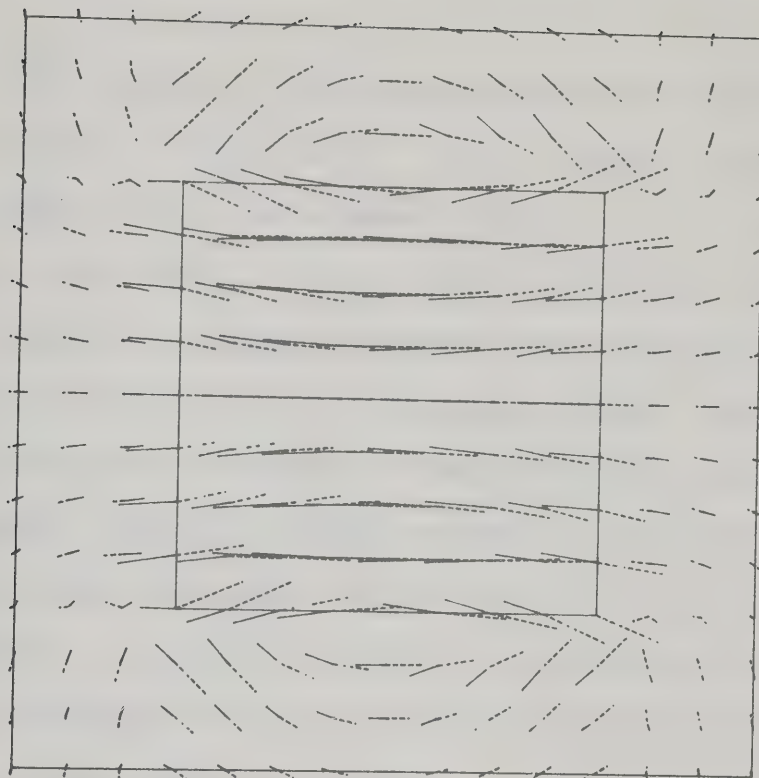
4.4.2 Two-Dipole Source Results

For the two-dipole source the magnetic field solution of dipole 1 was rotated 90° to obtain the solution for dipole 2. The cross correlation and auto-correlation power spectra are calculated for each individual dipole source and these are averaged and the transfer functions determined. The transfer function matrix must now be represented by a two-dimensional matrix. For the z transfer functions:

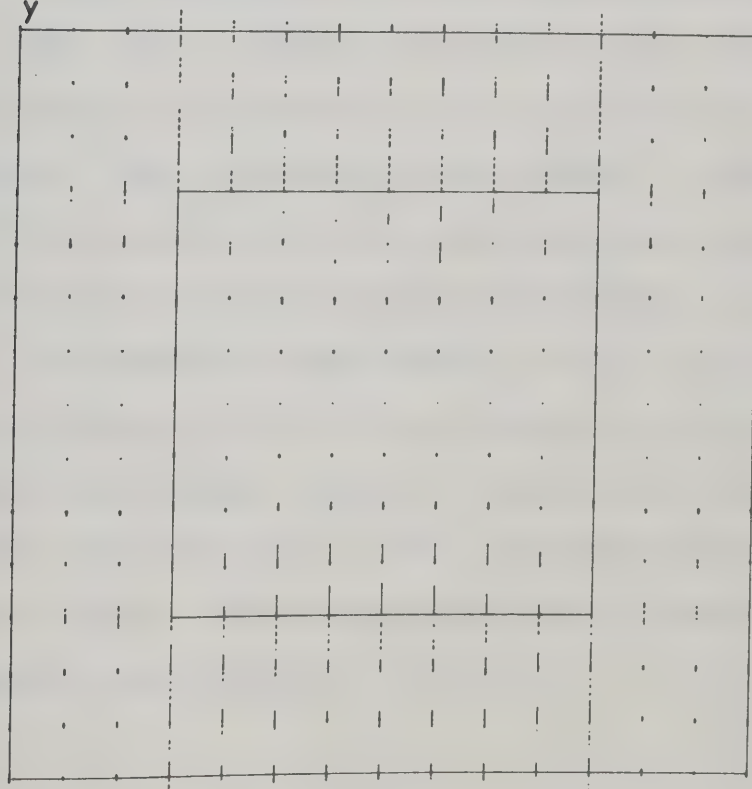
$$\begin{aligned} z_x S_{x_n x_n} + z_y S_{y_n x_n} &= S_{z_a x_n} \\ z_x S_{x_n y_n} + z_y S_{y_n y_n} &= S_{z_a y_n} \end{aligned} \quad (4.14)$$

Similar equations are obtained from the h and d transfer function matrices.

Figure 4.15 As Figure 4.14 but for a uniform source with a normal magnetic field polarized in the y direction.



A



B

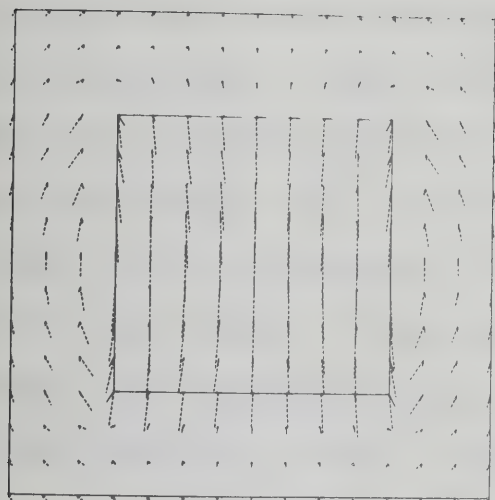
The results of this calculation for the frequency used are shown in Figure 4.16. Since h and d transfer function matrices are two-dimensional in x and y , both the \underline{p} (Figure 4.16A) and \underline{q} (Figure 4.16B) arrows are defined. The \underline{p} perturbation arrows have been made negative with respect to the definition of Schmucker (1970) (that is, they now define the anomalous internal current superimposed on the normal currents flowing in the $+y$ direction. If these two arrows are added vectorially ($\underline{p} + \underline{q}$) as in Figure 4.16C, the spatial extent of the anomaly is outlined by arrows polarized at an angle of approximately 45° clockwise to the positive x axis.

In the two-dipole case the induction arrows (Figure 4.16D) are no longer polarized in the y direction. Over the anomaly the induction arrows tend to point radially away from the center of the anomaly. However, away from the anomaly the arrows are polarized approximately perpendicularly to the boundary and decrease in magnitude near the corners of the anomaly. This is due to the high concentration of circulating anomalous current within the conductivity anomaly since the conductivity there is greater by a factor of $3.81 \times 10^{+3}$ compared with the surrounding region. Also, the small size of the anomaly contributes to the skewing of the arrows.

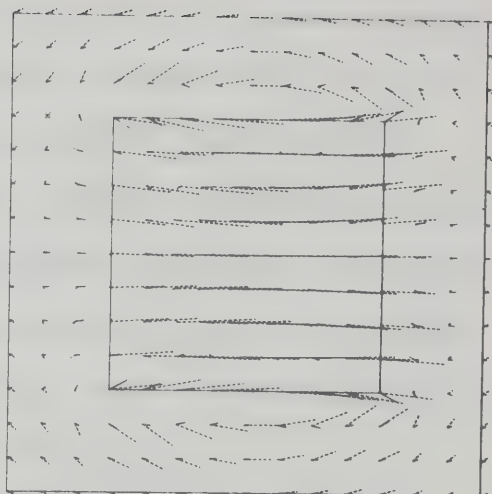
Figure 4.16 Horizontal two-dipole source with moment polarized in the y direction for dipole (1) and in the x direction for the dipole (2). The dashed arrows are the in-phase arrows and the solid arrows are the quadrature-phase arrows.

- (A) p perturbation arrows,
- (B) q perturbation arrows,
- (C) $p + q$ perturbation arrows,
- (D) induction arrows.

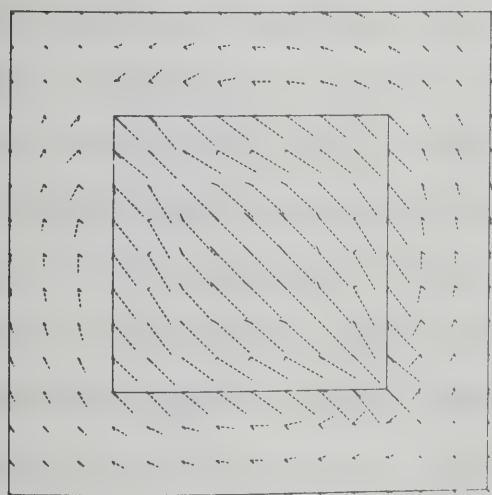
The surface of the conducting region near the anomaly is shown and the inner square region represents the anomalous structure.



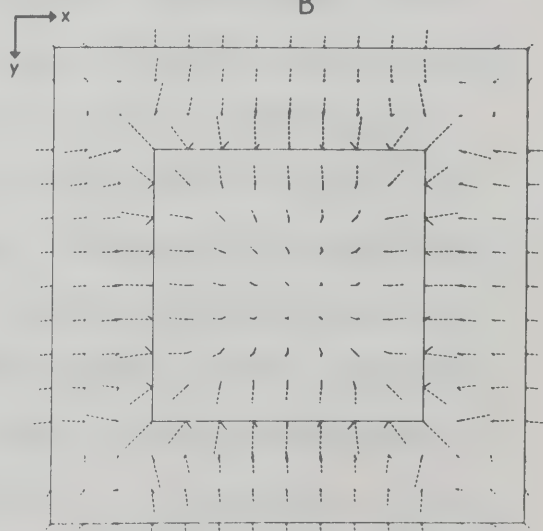
A



B



C

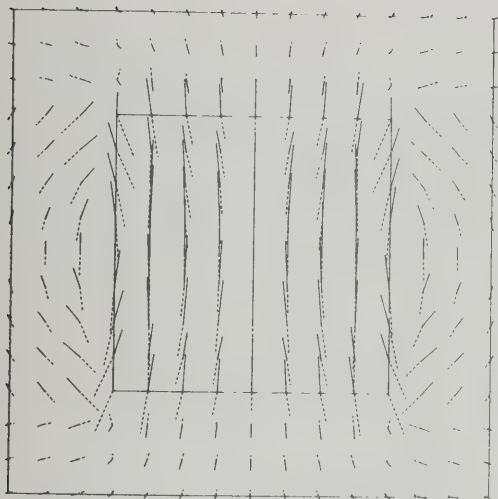


D

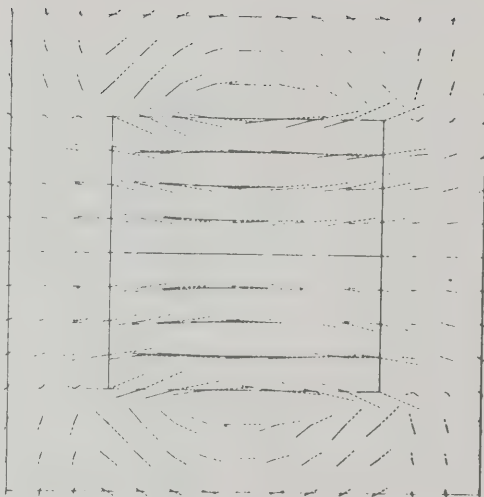
For comparison the perturbation and induction arrows of two orthogonal uniform sources polarized in the x and y directions are presented in Figure 4.17. As found in the single dipole case, the \underline{p} , \underline{q} and $\underline{p} + \underline{q}$ perturbation quadrature-phase arrows are greater in magnitude compared with the in-phase arrows for the uniform field source. Also, as before, the perturbation arrows are more perturbed in the uniform field case. The quadrature-phase induction arrows are greater in magnitude compared with the in-phase arrows for the uniform source field case. The orientation of the induction arrows is very similar.

As pointed out by Cochrane and Hyndman (1970), the problem of defining the normal field for the calculation of induction arrows can be partially overcome by substituting the total field as the normal field in the transfer function calculations, since this is easier to apply in the analysis of experimental observations. In their calculations Cochrane and Hyndman (1970) assumed that the magnetic field component in the z direction was totally anomalous which thus allows a calculation of the induction arrows. This assumption cannot be made when calculating the anomalous field for the horizontal components of the magnetic field. Figure 4.18 is a recalculation of the arrows in Figure 4.16 using the Cochrane and Hyndman (1970) suggestion. As can be seen

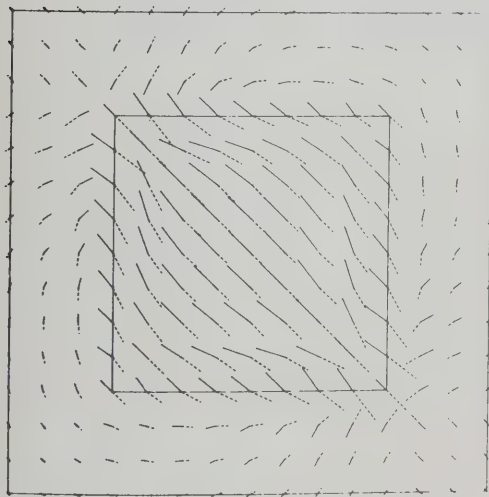
Figure 4.17 As Figure 4.16 but for two orthogonal uniform sources with the normal magnetic field polarized in the x and y directions.



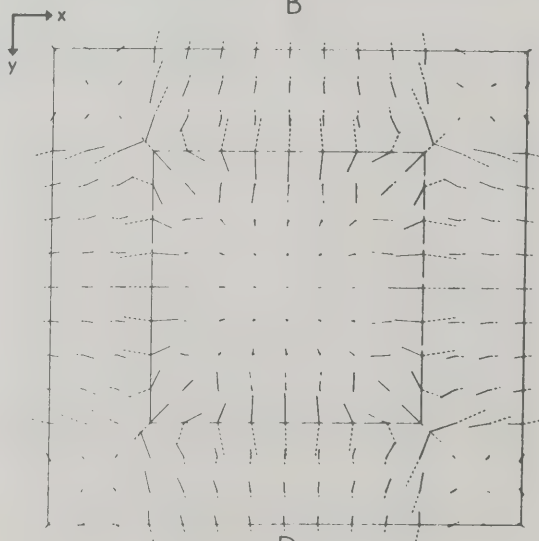
A



B



C

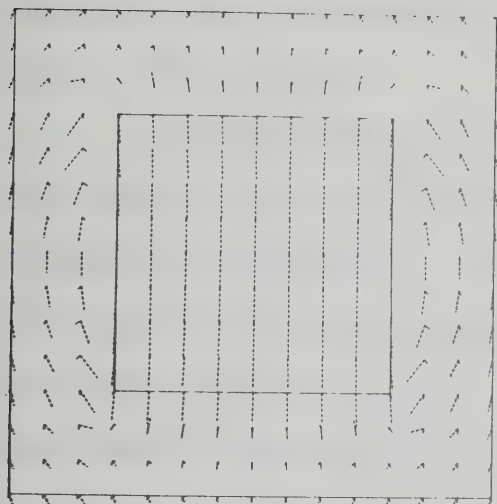


D

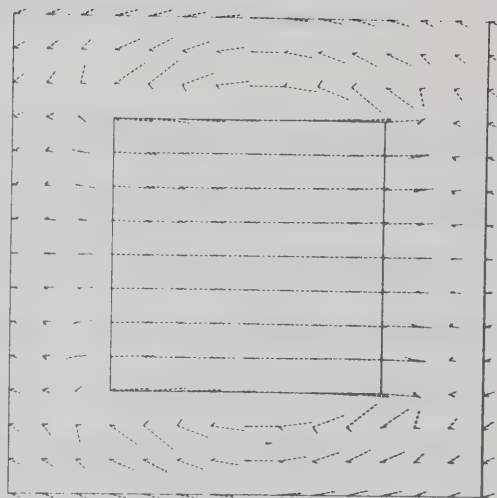
Figure 4.18 Horizontal two-dipole source with moment polarized in the y direction for dipole (1) and in the x direction for dipole (2). The transfer functions are calculated as suggested by Cochrane and Hyndman (1970). The dashed arrows are the in-phase arrows and the solid arrows are the quadrature-phase arrows.

- (A) \underline{p} perturbation arrows,
- (B) \underline{q} perturbation arrows,
- (C) $\underline{p} + \underline{q}$ perturbation arrows,
- (D) induction arrows.

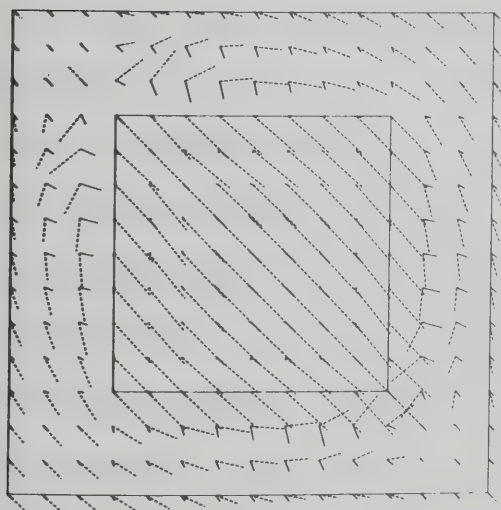
The surface of the conducting region near the anomaly is shown and the inner square region represents the anomalous structure.



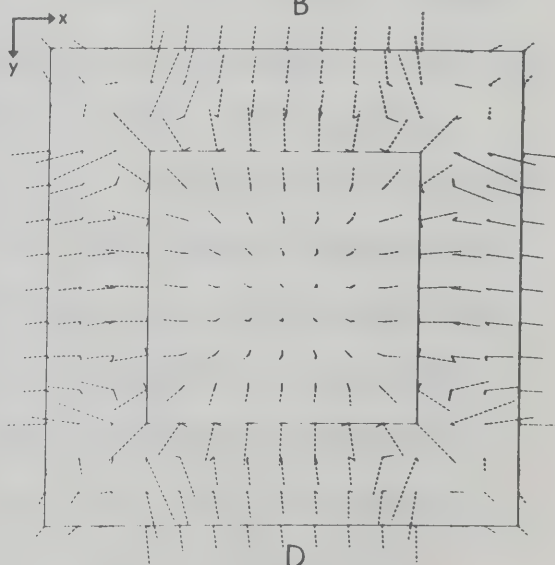
A



B



C

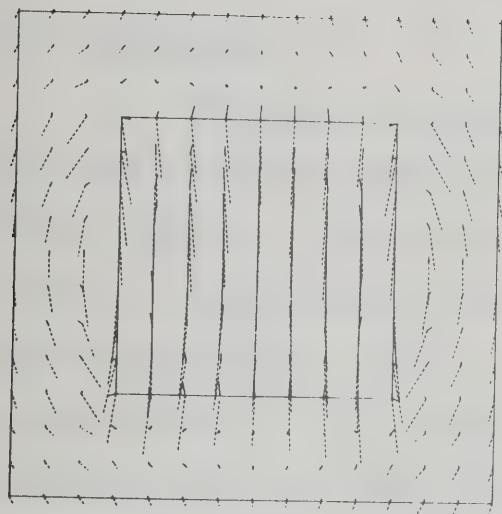


D

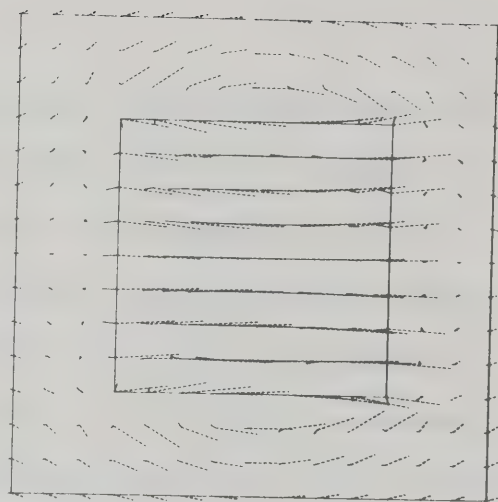
in Figure 4.18, little change is noted in the perturbation arrows, which are dependent on the horizontal magnetic field components. However, the anomalous field used to calculate the perturbation and induction arrows in Figure 4.18 is exact.

In this respect, it is of interest to determine the effect on the calculations if the anomalous and normal fields are approximate. In Figure 4.19 the perturbation and induction arrows are given for a calculation in which the normal field is assumed to be constant and the anomalous field is the result of subtracting the normal field from the total magnetic field. The value for the normal field was obtained by averaging the field values along the boundary of the finite difference mesh. The boundary forms a square with a perpendicular distance of 60 km from the center of the anomaly. This will give a reasonable approximation to the normal field since the dipoles are located near the anomaly and some symmetry is expected. Also the field is reasonably uniform over the region of the anomaly. For dipoles placed far from the anomaly a better approximation would be a linear interpolation across the grid and this latter approximation may also be useful for large anomalies. In Figure 4.19 a slight skewing of the arrows is noted but no appreciable change in their configuration is apparent.

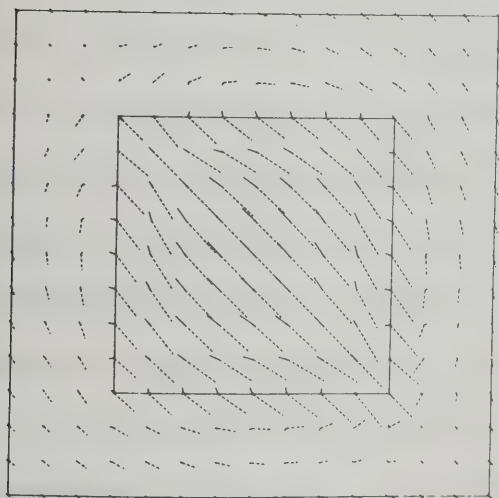
Figure 4.19 As Figure 4.18 but for averaged normal field values.



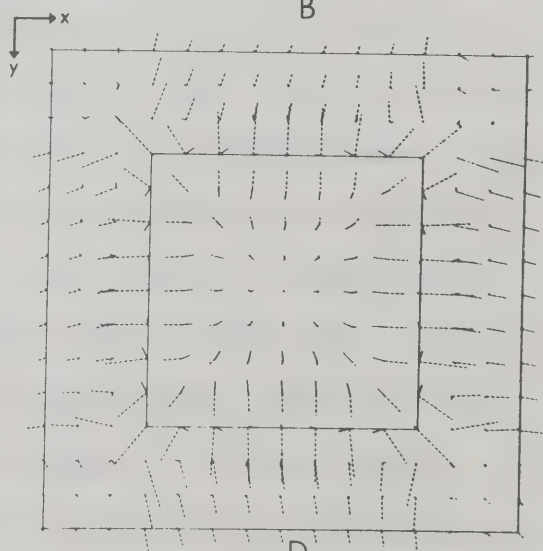
A



B



C



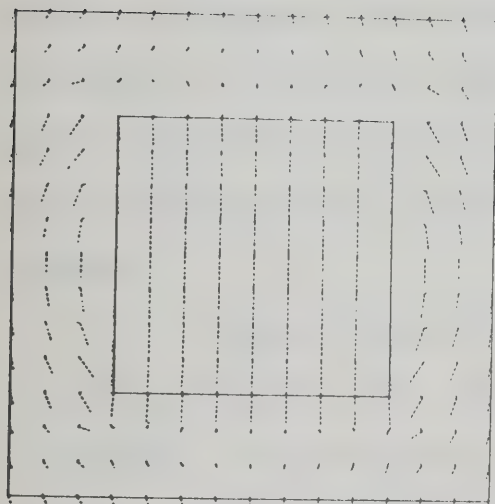
D

In Figure 4.20 the calculation is done as in Figure 4.19 but the total field is substituted for the constant normal field.

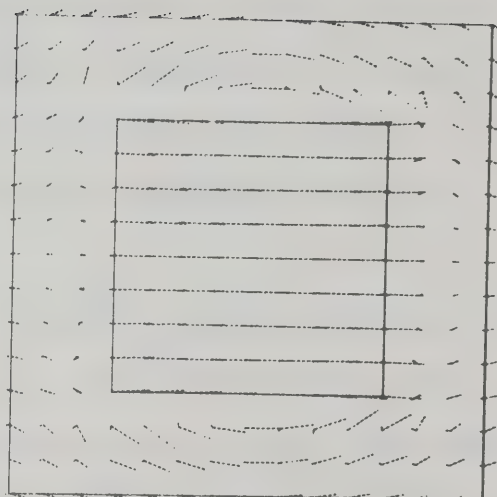
4.5 Conclusions

The transfer functions and related perturbation and induction arrows associated with the electromagnetic fields induced in various conductivity anomalies by uniform, two-dimensional non-uniform and horizontal dipole sources oriented in various directions have been studied in this chapter. For single sources the induction arrows are polarized in a single direction, which, for the uniform and two-dimensional non-uniform sources, is in the direction perpendicular to source current flow. This is due to the polarization of the normal field in the uniform source case and the polarization of the horizontal normal field component and the smallness of the vertical normal field component in the two-dimensional non-uniform case. For the horizontal dipole the induction arrows are polarized in the direction of the dipole moment. In the region immediately beneath a horizontal dipole source the normal magnetic field component, which is in the direction of the dipole moment; is much greater in magnitude than either the vertical or perpendicular normal magnetic field component, hence the polarization of the induction arrows.

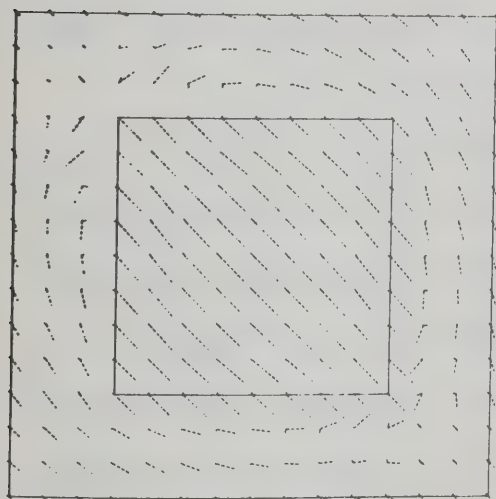
Figure 4.20 As Figure 4.18 but for averaged normal field values with substitution as suggested by Cochrane and Hyndman (1970).



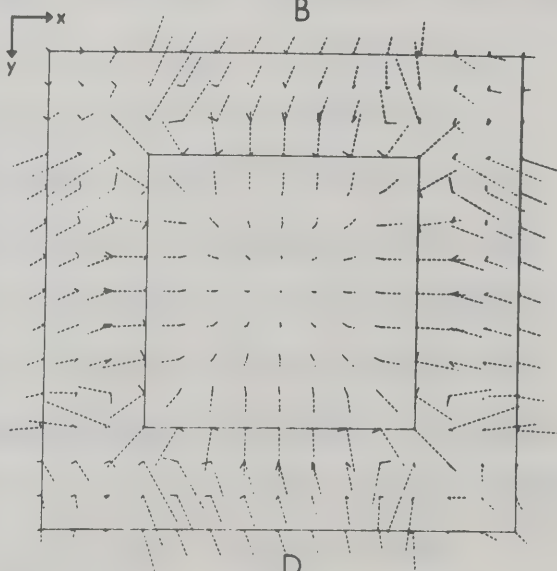
A



B



C



D

The perturbations arrows for the single sources for which only the \underline{q} arrow is defined qualitatively resemble the anomalous current outside the anomaly. However, near and over the anomaly, the in-phase induction arrows increase markedly in magnitude regardless of whether the anomaly is more conductive or resistive than the surrounding material which would not be expected of the anomalous current vectors.

Various methods were used to calculate the transfer functions for the multiple source orientation models presented. The induction arrows are no longer polarized and now point toward (or away from) the conductivity anomaly. Both \underline{p} and \underline{q} perturbations are defined for these cases.

In the uniform source case the concept of a normal field following Schmucker (1970) is used in the transfer function calculations and is compared with the Cochrane and Hyndman (1970) transfer function calculations. It is found that perturbation and induction arrows are stable with frequency for the range considered. For this source the introduction of the Cochrane and Hyndman (1970) substitution produces no appreciable change in the configurations of the perturbation and induction arrows. It is found that the perturbation arrows when summed vectorially do not compare well with the anomalous current vectors calculated, nor do they compare with the calculated

electric field vectors. However, this new $(p + q)$ perturbation arrow is very sensitive to changes in conductivity and can be used to outline the spatial extent of the anomaly much in the same way as one would use electric field information if it could be accurately obtained. The degree of randomness of the source orientations was also investigated. Less than five source field polarizations can be used if the sources are at least 90° spatially apart. Small angular spreads of source field polarization produce skewing of the induction arrows.

Similar calculations were done for the two-dimensional non-uniform sources and the horizontal dipole sources. In addition to the Schmucker (1970) and Cochrane and Hyndman (1970) formulation of the transfer functions, the effect of both an approximate anomalous and normal field was considered. By using an averaged field value for the normal field, the anomalous field is determined by subtracting the averaged normal field from the total field. The induction arrows are skewed slightly for the Cochrane and Hyndman (1970) calculation due to the source effect for both source types with the horizontal dipole induction arrows showing slightly more deflection due to the increased source effect. The averaged normal field calculation shows increased skewing for both source types.

In general, though, it can be concluded that the induction arrows are stable for a variety of anomalous and normal field calculations. The perturbation arrows were more stable than the induction arrows for these changes and could again be used to outline the spatial extent of the anomaly. In the two-dimensional non-uniform source calculations the effect of a small angular spread in source field polarizations showed the severe skewing that can result.

CHAPTER 5

CONCLUSIONS AND RECOMMENDATIONS FOR FURTHER RESEARCH

A study of the three-dimensional local induction problem has been presented in this work. Solutions for the electromagnetic fields were obtained for various sources and laterally non-uniform conductivity distributions. These calculations were used to compare with analogue model measurements for three different source configurations. Transfer functions and their related perturbation and induction arrows were also calculated for the three source types and various embedded conductivity anomalies.

The local induction problem for embedded three-dimensional conductivity inhomogeneities for various sources was solved through the use of the finite difference technique of Lines and Jones (1973). Solutions for the three source configurations (uniform, two-dimensional, non-uniform and horizontal dipole) above a uniform layered conductor were obtained and used as boundary conditions for the finite difference mesh. In the case of the two-dimensional non-uniform source a computer program was developed to calculate the electromagnetic fields associated with any arbitrary two-dimensional source intensity current distribution

over a layered earth. Utilizing the calculated boundary conditions, three source field conductivity structure combinations were considered. 1. A uniform current source above an island structure in the deep ocean; 2. A latitudinally confined ionospheric electrojet (across which current is uniformly distributed) above L-shaped sulfide ore body embedded in material with an average continental conductivity; 3. A horizontal dipole above an ore body of relatively low conductivity which is embedded in poorly conducting rock. The profiles of selected electromagnetic field quantities and appropriate phases for various positions relative to the anomalous structures were presented as well as three-dimensional amplitude figures of the electric and magnetic field components. The effect of the source was clearly apparent in all profiles except that of the apparent resistivity. The effect of charge concentration at the boundary of the anomaly is evident in the $|E_x|$ and ρ_a component profiles furthest from the anomaly. The ρ_a curve exhibits a slight anomaly in the opposite sense to the change which would be expected. This effect is due to the charge on the boundary and affects the ρ_a calculation for this profile. The three-dimensional amplitude figures of the six electromagnetic field components also exhibits strong source effects. The corners of the anomalies could easily be identified by amplitude maxima in $|H_x|$. The sides of the anomaly were

marked by increases in the amplitude of $|H_z|$.

A comparison of theoretical calculations with analogue model measurements was made for three source field configurations over an ore body of relatively low conductivity embedded in poorly conducting rock. Calculations and measurements were made for uniform, two-dimensional non-uniform and horizontal dipole sources. Selected electromagnetic field quantities and their phases were presented in profiles for various positions relative to the conductivity structure. It was found that in the finite difference method used a transition zone must be introduced in the conductivity configuration if both high frequency and high conductivity contrast are used. Even with the refinement differences were noted in the three-dimensional electromagnetic field profiles for the theoretical and analogue models over the transition zone. In spite of these limitations a good degree of compatibility was demonstrated for the two methods and their simultaneous use in studying the effects of conductivity anomalies is indicated. In addition it was found that the theoretical source calculations well represented the analogue model sources.

Transfer functions and related perturbation and induction arrows associated with the theoretical electromagnetic field calculations were computed. The uniform, two-dimensional non-uniform and horizontal

dipole sources oriented in various directions and positioned variously with respect to the conductivity structure were used. A number of methods (i.e., Schmucker (1970); Cochrane and Hyndman (1970)) were used to calculate the transfer functions. Depending on the method used and the approximations made for the normal and anomalous fields a slight amount of skewing in the arrows was noted. In this respect the greatest skewing noted was due to the use of averaged normal and approximate anomalous fields. However, in general, the induction arrows were stable for the variety of anomalous and normal field calculations used. The perturbation arrows were even more stable in this respect. Little source effect was noted for either induction or perturbation arrows. Only if a very small angular spread in source field polarizations was used would severe skewing be noted. This was most evident for the two-dimensional non-uniform sources far from the anomaly. As would possibly be the case for measurements made at mid-latitudes due to auroral electrojets. The results showed that the induction arrows could still be used to indicate the flow of anomalous currents and point in the direction of conductivity anomalies. The perturbation arrows when added vectorially ($\underline{p} + \underline{q}$) were not found to compare well with either the anomalous current or the anomalous

electric field vectors. However, this new arrow was found to be very sensitive to conductivity changes in much the same manner as the electric field and could be used to outline the spatial extent of the anomaly.

The difficulty of defining a normal field in the perturbation and induction arrow transfer function analysis emphasizes the desirability of defining the transfer functions in terms of the observed surface field components. A correlation between the spatial derivatives of the horizontal and vertical magnetic field components exists. Arrows could be defined from the calculated transfer functions such that the boundaries of the anomalous conductivity region could be defined.

BIBLIOGRAPHY

- Alabi, A.O., Camfield, P.A., and Gough, D.I., 1975. The North American central plains conductivity anomaly, *Geophys. J.R.A.S.*, 43, 815-833.
- Anderson, C.W., 1975. Analysis of earth induction effects on ground-based observations of ULF pulsations near $L=4$, *J. Geomag. Geoelectr.*, 27, 217.
- Anderson, C.W., Lanzerotti, L.J., and MacLennan, C.G., 1976a. Local time variation of induction vectors as indicators of internal and external current systems, *Geophys. Res. Letters*, 3, 495-498.
- Anderson, C.W., Lanzerotti, L.J., and MacLennan, C.G., 1976b. Local time variation of induction vectors: Implications for deducing internal and external current systems, *Geophys. J.R.A.S.*, (submitted).
- Ashour, A.A., 1950. The induction of electric currents in a uniform circular disk, *Quart. J. Mech. Appl. Math.*, 3, 119-127.
- Ashour, A.A., 1965a. Electromagnetic induction in finite thin sheets, *Quart. J. Mech. Appl. Math.*, 18, 73-86.
- Ashour, A.A., 1965b. On a transformation of coordinates by inversion and its application to electromagnetic induction in a thin perfectly conducting hemispherical shell, *Proc. Lond. Math. Soc.*, 15(3), 557-576.
- Ashour, A.A., 1971a. Electromagnetic induction in thin finite sheets having conductivity decreasing to zero at the edge, with geomagnetic applications-I, *Geophys. J.R.A.S.*, 22, 417-443.
- Ashour, A.A., 1971b. Electromagnetic induction in thin finite sheets having conductivity decreasing to zero at the edge, with geomagnetic applications-II, *Geophys. J.R.A.S.*, 25, 447-467.
- Ashour, A.A., and Ferraro, V.C.A., 1964. The induction of electric currents in an anisotropic ionosphere with a belt of high conductivity running along the equator, *J. Atmos. Terr. Phys.*, 26, 509-523.

- Ashour, A.A., and Price, A.T., 1948. The induction of electric currents in a non-uniform ionosphere, *Proc. R. Soc. Lond., Ser. A.*, 195, 198-224.
- Backus, G., and Gilbert, E., 1970. Uniqueness in the inversion of inaccurate gross earth data, *Phil. Trans. Soc.*, A266, 123-192.
- Bailey, R.C., 1970. Inversion of the geomagnetic induction problem, *Proc. R. Soc. Lond., Ser. A.*, 315, 185-194.
- Banks, R.J., 1969. Geomagnetic variations and the electrical conductivity of the upper mantle, *Geophys. J.R.A.S.*, 17, 457-487.
- Banks, R.J., 1972. The overall conductivity distribution of the earth, *J. Geomag. Geoelectr.*, 24, 337-351.
- Benkova, N.P., 1940. Spherical harmonic analysis of the Sq variations, May-August, 1933, *Terr. Mag.*, 425-432.
- Bennett, D.J., and Lilley, F.E.M., 1972. Horizontal polarizations in array studies of anomalous geomagnetic variations, *Nature (London), Phys. Sci.*, 237, 8-9.
- Bennett, D.J., and Lilley, F.E.M., 1973. An array study of daily magnetic variations in southeast Australia, *J. Geomag. Geoelectr.*, 25, 39-62.
- Bennett, D.J., and Lilley, F.E.M., 1974. Electrical conductivity structure in the south-east Australia region, *Geophys. J.R.A.S.*, 37, 191-206.
- Brewitt-Taylor, C.R., and Weaver, J.T., 1976. On the finite difference solution of two dimensional induction problems, *Geophys. J.R.A.S.*, 47, 375-396.
- Bullard, E.C., and Parker, R.L., 1970. Electromagnetic induction in the oceans, *The Sea, Vol. IV*, Chap. 18.
- Cagniard, L., 1953. Basic theory of the magneto-telluric method of geophysical prospecting, *Geophysics*, 18, 605-635.
- Camfield, P.A., 1973. Studies with a two-dimensional magnetometer array in northwestern United States and southwestern Canada, Ph. D. Thesis, University of Alberta, Edmonton, Alberta (unpublished).
- Camfield, P.A., and Gough, D.I., 1975. Anomalies in daily variation magnetic fields and structure under North-western United States and Southwestern Canada, *Geophys. J.R.A.S.*, 41, 193-218.

- Camfield, P.A., Gough, D.I., and Porath, H., 1971. Magnetometer array studies in the North-western United States and South-western Canada, *Geophys. J.R.A.S.*, 22, 201-221.
- Cantwell, T., 1960. Detection and analysis of low frequency magnetotelluric signals, Thesis, Mass. Inst. Tech., Cambridge, Massachusetts.
- Chapman, S., 1918. An outline of a theory of magnetic storms, *Proc. Roy. Soc., A*, 95, 61-83.
- Chapman, S., 1919. The solar and lunar diurnal variations of terrestrial magnetism, *Phil. Trans. Roy. Soc. London, A*, 218, 1-118.
- Chapman, S., and Price, A.T., 1930. The electric and magnetic state of the interior of the earth as inferred from terrestrial magnetic variations, *Phil. Trans. Roy. Soc. London, A*, 229, 427-460.
- Chapman, S., and Whitehead, T.T., 1922. The influence of electrically conducting material within the earth on various phenomena of terrestrial magnetism, *Trans. Phil. Soc. Cambridge*, 22, 463-482.
- Cochrane, N.A., and Hyndman, R.D., 1970. A new analysis of geomagnetic depth-sounding data from western Canada, *Can. J. Earth Sci.*, 7, 1208-1218.
- Coggon, J.H., 1971. Electromagnetic and electrical modeling by the finite element method, *Geophysics*, 36, 132-155.
- Collin, W.D., 1961. On some dual series equations and their application to electrostatic problems for spheroidal caps, *Proc. Cam. Philos. Soc.*, 57, 367-384.
- Cox, C.S., 1960. Magnetic induction at oceanic margins, (Unpublished).
- Cox, C.S., 1971. In: J. Heacock (Editor), *Geophysical Monograph*, 14, A.G.U., Washington, D.C., p. 227.
- de Beer, J.H., van Zijl, J.S.V., Huyssen, R.M.J., Hugo, P.L.V., Joubert, S.J., and Meyer, R., 1976. A magnetometer array study in South-west Africa, Botswana and Rhodesia, *Geophys. J.R.A.S.*, 45, 1-17.

- D'Erceville, I., and Kunetz, G., 1962. The effect of a fault on the earth's natural electromagnetic field, *Geophysics*, 27, 651-665.
- Doss, S.S., and Ashour, A.A., 1971. Some results on the magnetic field of electric currents induced in a thin hemispherical shell of finite conductivity, with geomagnetic applications, *Geophys. J.R.A.S.*, 22, 385-400.
- Dosso, H.W., 1966. A plane wave analogue model for studying electromagnetic variations, *Can. J. Phys.*, 44, 67-80.
- Dosso, H.W., and Jacobs, J.A., 1968. Analogue model measurements of electromagnetic variations in the near field of an oscillating line current, *Can. J. Earth Sci.*, 5, 23-29.
- Dulaney, E.N., and Madden, T.R., 1962. Analogue relaxation net calculation of two-dimensional magnetotelluric response curves, *S.E.G. Yearbook*, p. 265 (Abstract).
- Eckhardt, D., Larner, K., and Madden, T., 1963. Long-period magnetic fluctuations and mantle electrical conductivity estimates, *J. Geophys. Res.*, 68, 6279-6286.
- Edwards, R.N., Law, L.K., and White, A., 1971. Geomagnetic variations in the British Isles and their relation to electrical currents in the ocean and shallow seas, *Phil. Trans. Roy. Soc. London, A*, 270, 289-323.
- Erdelyi, A., Magnus, W., Oberhettinger, F., and Tricomi, F., 1954. *Tables of integral transforms*, 1, McGraw-Hill Book Co. Inc., New York.
- Everett, J.E., and Hyndman, R.D., 1967. Geomagnetic variations and electrical conductivity structure in south-western Australia, *Phys. Earth Planet. Int.*, 1, 24-34.
- Frazer, M.C., 1974. Geomagnetic deep sounding arrays of magnetometers, *Rev. Geophys. Space Phys.*, 12, 401-420.

- Garland, G.D., 1971. Introduction to Geophysics Mantle Core and Crust, Saunders Book Company, Philadelphia.
- Garland, G.D., 1975. Correlation between electrical conductivity and other geophysical parameters, Phys. Earth Planet. Int., 10, 220-230.
- Gauss, 1839. Allgemeine Theorie der Erdmagnetismus, p. 13.
- Geyer, R.G., 1970. The effect of subsurface geologic structure in electromagnetic induction prospecting, Thesis, Colorado School of Mines, Golden, Colorado.
- Geyer, R.G., 1972. The effect of a dipping contact on the behavior of the electromagnetic field, Geophysics, 37, 337-350.
- Gough, D.I., 1973. The interpretation of magnetometer array studies, Geophys. J.R.A.S., 35, 83-98.
- Gough, D.I., de Beer, J.H., and van Zijl, J.S.V., 1973. A magnetometer array study in southern Africa, Geophys. J.R.A.S., 34, 421-433.
- Gough, D.I., McElhinny, M.W., and Lilley, F.E.M., 1974. A magnetometer array study in southern Australia, Geophys. J.R.A.S., 36, 345-362.
- Grant, F.S., and West, G.F., 1965. Interpretation Theory in Applied Geophysics, McGraw-Hill Book Co. Inc., New York.
- Hasagawa, M., and Ota, M., 1948. On the magnetic field of Sq in the middle and lower latitudes during the II Polar Year, Trans. of 1948 Oslo Meeting IATME, IATME Bull., 13, 426-430.
- Hermance, J.F., and Peltier, W.R., 1970. Magnetotelluric fields of a line current, J. Geophys. Res., 75, 3351-3356.
- Hewson-Browne, R.C., 1973. Magnetic effects of ocean tides, Phys. Earth Planet. Int., 7, 161-166.
- Hewson-Browne, R.C., Hutson, V.C.L., Kendall, P.C., and Malin, S.R.C., 1973. New iterative methods of solution of oceanic induction problems, Phys. Earth Planet. Int., 7, 431-436.

- Hibbs, R.D., and Jones, F.W., 1972. Apparent resistivity calculations for laterally inhomogeneous structures, *Phys. Earth Planet. Int.*, 5, 184-189.
- Hibbs, R.D., and Jones, F.W., 1973a. Electromagnetic induction in the earth by a symmetric non-uniform source, *Geophys. J.R.A.S.*, 32, 269-277.
- Hibbs, R.D., and Jones, F.W., 1973b. Electromagnetic induction in the earth by a non-symmetric non-uniform source, *J. Geomag. Geoelectr.*, 25, 75-86.
- Hibbs, R.D., and Jones, F.W., 1974. Electromagnetic induction in the earth by an aperiodic non-uniform current source, *J. Geomag. Geoelectr.*, 26, 39-53.
- Hibbs, R.D., and Jones, F.W., 1976a. The calculation of the electromagnetic fields of a sheet current with arbitrary spatial intensity distribution over a layered half-space, I. The general method and results, *Geophys. J.R.A.S.*, 46, 433-452.
- Hibbs, R.D., and Jones, F.W., 1976b. The calculation of the electromagnetic fields of a sheet current with arbitrary spatial intensity distribution over a layered half-space, II. The computer program and its application, *Geophys. J.R.A.S.*, 46, 453-465.
- Hibbs, R.D., and Jones, F.W., 1976c. Electromagnetic induction in three-dimensional structures for various source fields, (submitted).
- Hibbs, R.D., and Jones, F.W., 1976d. The calculation of perturbation and induction arrows for a three-dimensional conductivity model, *J. Geomag. Geoelectr.*, (in press).
- Hibbs, R.D., and Jones, F.W., 1976e. The calculation of perturbation and induction arrows for a three-dimensional conductivity model and various two-dimensional source fields, (submitted).
- Hibbs, R.D., and Jones, F.W., 1976f. The calculation of perturbation and induction arrows for a three-dimensional conductivity model and dipole source fields, *Pure and Appl. Geophys.*, (in press).

- Hobbs, B.A., 1971. The calculation of geophysical induction effects using surface integrals, *Geophys. J.R.A.S.*, 25, 481-509.
- Hobbs, B.A., and Price, A.T., 1970. Surface integral formulae for geomagnetic studies, *Geophys. J.R.A.S.*, 20, 49-63.
- Hohmann, G.W., 1971. Electromagnetic scattering by conductors in the earth near a line source of current, *Geophysics*, 36, 101-131.
- Hohmann, G.W., 1975. Three-dimensional induced polarization and electromagnetic modelling, *Geophysics*, 40, 309-324.
- Honkura, Y., 1971. Geomagnetic variation anomaly on Miyake-jima Island, *J. Geomag. Geoelectr.*, 23, 307-333.
- Howard, A.Q., 1972. The electromagnetic fields of a subterranean cylindrical inhomogeneity excited by a line current source, *Geophysics*, 37, 975-984.
- Howard, A.Q., 1975. A canonical solution to the three-dimensional electromagnetic prospecting problem, *Radio Science*, 10, 4, 461-471.
- Hughes, W.J., 1973. The effect of two periodic conductivity anomalies on geomagnetic micropulsation measurements, *Geophys. J.R.A.S.*, 31, 407-431.
- Hughes, W.J., 1974. The polarization of micropulsations and geo-electric structure, *Geophys. J.R.A.S.*, 38, 95-117.
- Hughes, W.J., and Wait, J.R., 1975. Electromagnetic induction over a two-layer Earth with a sinusoidal overburden, *Pageoph.*, 113, 591-599.
- Hutson, V.C.L., Kendall, P.C., and Malin, S.R.C., 1972. Computations of the solution of geomagnetic induction problems: A general method, with applications, *Geophys. J.R.A.S.*, 28, 489-498.
- Hutton, R., 1969. Electromagnetic induction in the earth by the equatorial electrojet, *Nature*, 222, 363-364.

- Hutton, R., 1971. Some problems of electromagnetic induction in the equatorial electrojet region-I. Magneto-telluric relations, *Geophys. J.R.A.S.*, 28, 267-284.
- Hutton, R., and Leggeat, A., 1971. Some problems of electromagnetic induction in the equatorial electrojet region-II. The analysis of magnetic and telluric variations at Zaria, Nigeria, *Geophys. J.R.A.S.*, 28, 411-424.
- Hyndman, R.D., and Cochrane, N.A., 1971. Electrical conductivity structure by geomagnetic induction at the continental margin of Atlantic Canada, *Geophys. J.R.A.S.*, 25, 425-466.
- Jady, R.J., 1974. Conductivity of earth models, *Geophys. J.R.A.S.*, 36, 399-410.
- Jady, R.J., 1975. Upper-mantle conductivity determined by the geomagnetic lunar daily variation, *Phys. Earth Planet. Int.*, 10, 377-381.
- Jones, F.W., 1971a. Electromagnetic induction in a non-horizontally stratified two-layered conductor, *Geophys. J.R.A.S.*, 22, 17-28.
- Jones, F.W., 1971b. Electromagnetic induction in a two-dimensional model of an asymmetric two-layered conductor, *Phys. Earth Planet. Int.*, 4, 417-424.
- Jones, F.W., and Pascoe, L.J., 1971. A general computer program to determine the perturbation of alternating electric currents in a two-dimensional model of a region of uniform conductivity with an embedded inhomogeneity, *Geophys. J.R.A.S.*, 24, 3-30.
- Jones, F.W., and Pascoe, L.J., 1972. The perturbation of alternating geomagnetic fields by three-dimensional conductivity inhomogeneities, *Geophys. J.R.A.S.*, 27, 479-485.
- Jones, F.W., and Price, A.T., 1969. The perturbation of an alternating field by a conductivity anomaly, *I.A.G.A. Bulletin 26 (Abstract III-106)*, p. 196.
- Jones, F.W., and Price, A.T., 1970. The perturbations of alternating geomagnetic fields by conductivity anomalies, *Geophys. J.R.A.S.*, 20, 317-334.

- Jones, F.W., and Price, A.T., 1971a. The geomagnetic effects of two-dimensional conductivity inhomogeneities at different depths, *Geophys. J.R.A.S.*, 22, 333-345.
- Jones, F.W., and Price, A.T., 1971b. Geomagnetic effects of sloping and shelving discontinuities of earth conductivity, *Geophysics*, 36, 58-66.
- Jones, F.W., and Thomson, D.J., 1974. A discussion of the finite difference method in computer modelling of electrical conductivity structures, *Geophys. J.R.A.S.*, 37, 537-543.
- Kisabeth, J.L., 1972. The dynamical development of the polar electrojets, Ph.D. Thesis, Univ. of Alberta.
- Kisabeth, J.L., and Rostoker, G., 1971. Development of the polar electrojet during polar magnetic substorms, *J. Geophys. Res.*, 76, 6815-6828.
- Ku, C.C., 1976. Numerical inverse magnetotelluric problems, *Geophysics*, 41, 276-286.
- Ku, C.C., Hsieh, M.S., and Lim, S.H., 1973. The topographic effect in electromagnetic field, *Can. J. Earth Sci.*, 10, 645-656.
- Lahiri, B.N., and Price, A.T., 1939. Electromagnetic induction in non-uniform conductors, and the determination of the conductivity of the earth from terrestrial magnetic variations, *Phil. Trans. Roy. Soc. London*, A, 237, 509-540.
- Lamb, H., 1883. On electrical motions in a spherical conductor, *Phil. Trans. Roy. Soc. London*, A, 174, 519-549.
- Lamb, H., 1887a. On ellipsoidal current sheets, *Phil. Trans. Roy. Soc. London*, 178, 131-159.
- Lamb, H., 1887b. On the principle electric time-constant of a circular disk, *Proc. Roy. Soc. Lond.*, Ser. A, 42, 289-296.
- Lamb, H., 1945. *Hydrodynamics*, Cambridge Univ. Press, London.
- Latka, R., 1966. Modellrechnungen zur Induktion im elektrisch leitfähigen untergrund, *Zeitschrift für Geophysik*, 32, 512-517.

- Lilley, F.E.M., 1974. Analysis of the geomagnetic induction tensor, *Phys. Earth Planet. Int.*, 8, 301-316.
- Lilley, F.E.M., 1975. Magnetometer array studies: A review of the interpretation of observed fields, *Phys. Earth Planet. Int.*, 10, 231-240.
- Lilley, F.E.M., 1976. A magnetometer array study across southern Victoria and the Bass Strait area, Australia, *Geophys. J.R.A.S.*, 46, 165-184.
- Lilley, F.E.M., and Bennett, D.J., 1972. An array experiment with magnetic variometers near the coasts of south-east Australia, *Geophys. J.R.A.S.*, 29, 49-64.
- Lilley, F.E.M., and Tammemagi, H.Y., 1972. Magnetotelluric and depth sounding methods compared (in southern Australia), *Nature (London), Phys. Sci.*, 240, 184-187.
- Lines, L.R., 1972. A numerical study of the perturbation of alternating geomagnetic fields near island and coastline structures, M.Sc. Thesis, Univ. of Alberta.
- Lines, L.R., and Jones, F.W., 1973. The perturbation of alternating geomagnetic fields by three-dimensional island structures, *Geophys. J.R.A.S.*, 32, 133-154.
- Losecke, W., and Muller, W., 1975. Two-dimensional magnetotelluric model calculations for overhanging, high-resistivity structures, *J. Geophys.*, 41, 311-319.
- Madden, T.R., and Swift, C.M., 1969. Magnetotelluric studies of the electrical conductivity structure of the crust and upper mantle, in: *The Earth's Crust and Upper Mantle*, edited by P.J. Hart, pp. 469-479, A.G.U. Monograph 13.
- Madden, T., and Thompson, W., 1965. Low frequency electromagnetic oscillations of the earth-ionosphere cavity, *Rev. Geophys.*, 3, 211-254.
- Malin, S.R.C., 1973. Worldwide distribution of geomagnetic tides, *Phil. Trans. Roy. Soc. London, Ser. A*, 274, 551-594.

- Mann, J.E., 1964. Magnetotelluric theory of the sinusoidal interface, *J. Geophys. Res.*, 69, 3517-3524.
- Mann, J.E., 1970. A perturbation technique for solving boundary value problems arising in the electrodynamics of conducting bodies, *Appl. Sci. Res.*, 22, 113-126.
- Maxwell, J., 1891. *Electricity and Magnetism*, Oxford 3rd edition.
- McDonald, K.L., 1957. Penetration of the geomagnetic secular variation through a mantle with variable conductivity, *J. Geophys. Res.*, 62, 117-141.
- Muller, W., and Losecke, W., 1975. Accelerating convergence techniques and grid spacing problems in two-dimensional magnetotelluric modelling, *Geophys. J.R.A.S.*, 41, 185-191.
- Neves, A., 1957. The generalized magneto-telluric method, Ph.D. Thesis, Dept. of Geol. and Geophys., M.I.T.
- Pascoe, L.J., and Jones, F.W., 1972. Boundary conditions and calculation of surface values for the general two-dimensional electromagnetic induction problem, *Geophys. J.R.A.S.*, 27, 179-193.
- Parker, R.L., 1968. Electromagnetic induction in a thin strip, *Geophys. J.R.A.S.*, 14, 487-495.
- Parker, R.L., 1970. The inverse problem of electrical conductivity in the mantle, *Geophys. J.R.A.S.*, 22, 121-138.
- Parker, R.L., 1972. Inverse theory with grossly inadequate data, *Geophys. J.R.A.S.*, 29, 123-138.
- Parkinson, W.D., 1959. Directions of rapid geomagnetic fluctuations, *Geophys. J.R.A.S.*, 2, 1-14.
- Parkinson, W.D., 1975. The computation of electric currents induced in the oceans, *J. Geomag. Geoelectr.*, 27, 33-46.
- Patrick, F.W., and Bostick, F.X., 1969. Magnetotelluric modelling techniques, Tech. Rept. 59, Electronics Research Center, Univ. of Texas, Austin.

- Peltier, W.R., and Hermance, J.F., 1971. Magnetotelluric fields of a Gaussian electrojet, *Can. J. Earth Sci.*, 8, 338-346.
- Porath, H., and Gough, D.I., 1971. Mantle conductive structures in the western United States from magnetometer array studies, *Geophys. J.R.A.S.*, 22, 261-275.
- Porath, H., Gough, D.I., and Camfield, P.A., 1971. Conductive structures in the northwestern United States and southwestern Canada, *Geophys. J.R.A.S.*, 23, 387-398.
- Porath, H., Oldenburg, D.W., and Gough, D.I., 1970. Separation of magnetic variation fields and conductive structures in the western United States, *Geophys. J.R.A.S.*, 19, 237-260.
- Price, A.T., 1930. Electromagnetic induction in a conducting sphere, *Proc. London Math. Soc.*, (2), 31, 217-224.
- Price, A.T., 1931. Electromagnetic induction in a permeable conducting sphere, *Proc. London Math. Soc.*, (2), 33, 233-245.
- Price, A.T., 1949. The induction of electric currents in non-uniform thin sheets and shells, *Quart. J. Mech. Appl. Math.*, 2, 283-310.
- Price, A.T., 1950. Electromagnetic induction in a semi-infinite conductor with a plane boundary, *Quart. J. Mech. Appl. Math.*, 3, 385-410.
- Price, A.T., 1962. The theory of magnetotelluric fields when the source field is considered, *J. Geophys. Res.*, 67, 1907-1918.
- Price, A.T., 1964. A note on the interpretation of magnetic variations and magnetotelluric data, *J. Geomag. Geoelectr.*, 15, 241-248.
- Price, A.T., 1965. Effects of induced earth currents on low-frequency electromagnetic oscillations, *Radio Science J. Res. NBS/USNC-URSI* 69D (8), 1161-1168.
- Price, A.T., and Ashour, A.A., 1974. Electromagnetic induction in thin conductors, *Geophys. J.R.A.S.*, 37, 263-270.

- Raiche, A.P., 1974. An integral equation approach to three-dimensional modelling, *Geophys. J.R.A.S.*, 36, 363-376.
- Raiche, A.P., and Coggan, J.H., 1975. Analytic green's tensors for integral equation modelling, *Geophys. J.R.A.S.*, 42, 1035-1038. (review paper)
- Ramaswamy, V., 1973. Electromagnetic fields of a horizontal dipole situated above and within a two layered earth, Ph.D. Thesis, Univ. of Victoria.
- Ramaswamy, V., Nienaber, W., Dosso, H.W., Jones, F.W., and Lam, L.K., 1975. Numerical and analogue model results for electromagnetic induction for an island situated near a coastline, *Phys. Earth Planet. Int.*, 11, 81-91.
- Rankin, D., 1962. The magneto-telluric effect on a dike, *Geophysics*, 27, 666-676.
- Reddy, I.K., and Rankin, D., 1973. Magnetotelluric response of a two-dimensional sloping contact by the finite element method, *Geophysics*, 38, 193-211.
- Reddy, I.K., and Rankin, D., 1975. Magnetotelluric response of laterally inhomogeneous and anisotropic media, *Geophysics*, 40, 1035-1045.
- Reitzel, J.S., Gough, D.I., Porath, H., and Anderson, C.W., III, 1970. Geomagnetic deep sounding and upper mantle structure in the western United States, 19, 213-235.
- Rikitake, T., 1950. Electromagnetic induction within the earth and its relation to the electrical state of the earth's interior, *Bull. Earthquake Res. Inst., Tokyo Univ.*, 28, 45-100 and 219-283.
- Rikitake, T., 1961. *Sq and Ocean*, J. *Geophys. Res.*, 66, 3245.
- Rikitake, T., 1966. *Electromagnetism and the Earth's Interior*, Elsevier Publishing Company.
- Rikitake, T., 1975. Electromagnetic induction in the earth when an inducing field is modulated by another field of longer period, *J. Geomag. Geoelectr.*, 27, 25-32.

- Roden, R.B., 1964. The effect of an ocean on magnetic diurnal variations, *Geophys. J.R.A.S.*, 8, 375-388.
- Rodi, W.L., 1976. A technique for improving the accuracy of finite element solutions for magnetotelluric data, *Geophys. J.R.A.S.*, 44, 483-506.
- Ryu, J., 1972. Finite element method to electromagnetic induction problems in geophysics, *Trans. A.G.U.* 53, p. 361, Abstract GP58.
- Schmucker, U., 1970. Anomalies of geomagnetic variations in the southwestern United States, *Bull, Scripps Inst. Oceanography, Univ. California, San Diego*, Vol. 13.
- Schmucker, U., 1971a. Interpretation of induction anomalies above nonuniform surface layers, *Geophysics*, 36, 156-165.
- Schmucker, U., 1971b. Electromagnetic induction in a non-uniform layer of finite thickness, XV IUGG General Assembly, Moscow, Abstract III-19, p. 300.
- Schuster, A., 1889. The diurnal variation of terrestrial magnetism, *Phil. Trans. Roy. Soc. London*, A, 208, 163-204.
- Silvester, P., and Haslam, C.R.S., 1972. Magnetotelluric modelling by the finite method, *Geophys. Prospect.*, 20, 872-891.
- Slankis, J.A., 1970. Telluric and magnetotelluric surveys at 8 Hz, Ph.D. Thesis, McGill University.
- Smith, G.D., 1969. Numerical solution of Partial Differential Equations, Oxford Univ. Press.
- Smythe, W.R., 1968. Static and Dynamic Electricity, McGraw-Hill, New York, N.Y.
- Stoyer, C.H., and Greenfield, R.J., 1976. Numerical solutions of the response of a two-dimensional earth to an oscillating magnetic dipole source, *Geophysics*, 41, 519-530.
- Swift, C.M., 1967. A magnetotelluric investigation of an electrical conductivity anomaly in the Southwestern United States, Ph.D. Thesis, Dept. of Geol. and Geophys., M.I.T.

- Swift, C.M., 1971. Theoretical magnetotelluric and terrain response from two-dimensional inhomogeneities, *Geophysics*, 36, 38-52.
- Tammemagi, H.Y., and Lilley, F.E.M., 1973. A magnetotelluric traverse in southern Australia, *Geophys. J.R.A.S.*, 31, 433-445.
- Tatrallyay, M., and Jones, F.W., 1974a. The perturbation of geomagnetic fields by cylindrical structures-I. Numerical method and symmetrical models, *Geophys. J.R.A.S.*, 38, 449-462.
- Tatrallyay, M., and Jones, F.W., 1974b. The perturbation of geomagnetic fields by cylindrical structures-II. Problems of asymmetry and sloping contact models, *Geophys. J.R.A.S.*, 38, 463-477.
- Thomson, D.J., Ramaswamy, V., and Dosso, H.W., 1972. Model measurements of electromagnetic variations near a coastline for localized source fields, *J. Geomag. Geoelectr.*, 24, 317-336.
- Tikhonov, A.N., 1950. *Dokl. Akad. Nauk S.S.S.R.*, 73, 295.
- Tranter, C.J., 1965. *Integral Transforms in Mathematical Physics*, Methuen, London.
- Treumann, R., 1970a. Electromagnetic induction problem in plates with two-dimensional conductivity distribution, I. General theory, *Geomag. Aeron.*, 10, 376-389.
- Treumann, R., 1970b. Electromagnetic induction problem in plates with two-dimensional conductivity distribution, II. Approximate method and solutions, *Geomag. Aeron.*, 10, 464-472.
- Treumann, R., 1970c. Problem of electromagnetic induction in plates with a two-dimensional conductivity distribution, III. Application, *Geomag. Aeron.*, 10, 678-684.
- Treumann, R., 1970d. Three-dimensional analysis of the electromagnetic induction problem of magnetic variation and magnetotelluric sounding, *Geomag. Aeron.*, 10, 849-853.
- Vozoff, K., 1971. The effect of overburden on vertical component anomalies in AFMAG and VLF exploration: A computer model study, *Geophysics*, 36, 53-57.

- Wait, J.R., 1954. On the relation between telluric currents and the earth's magnetic field, *Geophysics*, 19, 281-289.
- Wait, J.R., 1962. *Electromagnetic Waves in Stratified Media*, Pergamon Press.
- Weaver, J.T., 1963. The electromagnetic field within a discontinuous conductor with reference to geomagnetic micropulsations near a coastline, *Can. J. Phys.*, 41, 484-495.
- Weaver, J.T., and Thomson, D.J., 1972. Induction in a non-uniform conducting half-space by an external line current, *Geophys. J.R.A.S.*, 28, 163-185.
- Weidelt, P., 1971. The electromagnetic induction in two thin half-sheets, *Z. Geophysics.*, 37, 649-665.
- Weidelt, P., 1975. Electromagnetic induction in three-dimensional structures, *J. Geophys.*, 41, 85-109.
- Wiese, H., 1962. Geomagnetische tiefentellurik teil II: die streichrichtung der untergrundstrukturen des elektrischen widerstandes, erschlossen aus geomagnetischen variationen, *Geophys. Pura. Appl.*, 52, 83-103.
- Williamson, K., Hewlett, C., and Tammemagi, H.Y., 1974. Computer modelling of electrical conductivity structures, *Geophys. J.R.A.S.*, 37, 533-536.
- Wright, J.A., 1969. The magnetotelluric and geomagnetic response of two-dimensional structures, GAMMA (Inst. Geophysik Meteorologie Tech. Univ. Braunschweig), 1, 102S.
- Wright, J.A., 1970. Anisotropic apparent resistivities arising from non-homogeneous two-dimensional structures, *Can. J. Earth Sci.*, 1, 527-531.
- Yukutake, T., 1967. *Publ. Dom. Obs.*, Ottawa, Ontario, 35(8).

APPENDIX A

THE CALCULATION OF THE ELECTROMAGNETIC FIELDS OF A SHEET CURRENT SOURCE WITH ARBITRARY SPATIAL INTENSITY DISTRIBUTION OVER A LAYERED HALF SPACE - THE COMPUTER PROGRAM AND ITS APPLICATION

A.1 Description of the Program

The general two-dimensional program for a sheet current source with an arbitrary intensity distribution is composed of two programs in which the solution for a general source is constructed from a number of elementary sources by superposition. The first program calculates the field components over a two-dimensional grid with a layered subsurface due to a current source with a Gaussian spatial intensity distribution of small half width (termed an elemental Gaussian). The second program combines the solutions for the field components of a number of spatially shifted elemental Gaussian sources such that a rectangular distribution of current intensity is closely approximated. With an appropriate change in parameters the second program is also used to approximate the arbitrary current intensity distribution in a piecewise continuous manner by weighting a number of spatially shifted rectangular current distributions in accordance with the trapezoidal rule. The solution for the field components due to the arbitrary source and the layered subsurface is thus obtained.

A.2 The Program ELEMENTAL GAUSSIAN

The ELEMENTAL GAUSSIAN program consists of a main program and two subprograms, INTEG and CONST. The main program listing is given in Figures A.1 and A.2. The subprograms INTEG and CONST are given in Figures A.3, A.4 and A.5, A.6 respectively.

The main program calculates the field component values at a specified number of points (NT) along a level at a constant height for positive y values for a Gaussian current distribution at $z_0 = -|h|$.

The integrations for E_x^n , H_y^n and H_z^n are performed through the call to INTEG. The integration subroutine (INTEG) calls the subroutine CONST in which the integrands, excluding the terms $\cos(sy)$ for E_x and H_y and $\sin(sy)$ for H_z (see Chapter 2), are calculated for all values of s at the specified level. For E_x the integrand is:

$$\{A_n e^{-\theta_n z} + B_n e^{\theta_n z}\} C(s) \cdot \cos(sy) \quad . \quad (A.1)$$

For H_y the integrand is:

$$(-i/\omega\mu_0) \{\theta_n [A_n e^{-\theta_n z} - B_n e^{\theta_n z}] C(s)\} \cdot \cos(sy) \quad (A.2)$$

For H_z the integrand is:

$$(i/\omega\mu_0) \{s [A_n e^{-\theta_n z} + B_n e^{\theta_n z}] C(s)\} \cdot \sin(sy) \quad . \quad (A.3)$$


```

C *****ELEMENTAL GAUSSIAN*****
C
C      CAUTION                                CAUTION
C      THE PARAMETERS Z1,D1,D2,P9,ZO,HW ARE EXPRESSED IN METERS
C      THE VALUES IN THE ARRAY Z ARE EXPRESSED IN KILOMETERS.
C
C      Z1---HEIGHT OF UPPER BOUNDARY ABOVE SURFACE (A NEGATIVE VALUE)
C      D1---THICKNESS OF FIRST LAYER---IF HALF SPACE IS DESIRED SET D1
C      GREATER THAN 1.0E+6 METERS.
C      D2---THICKNESS OF SECOND LAYER---IF ONLY ONE LAYER IS USED SET D2
C      GREATER THAN 1.0E+6 METERS---LIKELIKE FOR A HALF HALF SPACE.
C      OI---MAXIMUM INTENSITY OF THE GAUSSIAN CURRNT DISTRIBUTION CENTERED
C      AT THE ORIGIN.
C      ZO---HEIGHT OF CURRENT SOURCE ABOVE SURFACE (A NEGATIVE VALUE)
C      HW---HALF WIDTH OF GAUSSIAN CURRENT DISTRIBUTION
C      N1---NUMBER OF LEVELS TO BE CALCULATED
C      N2,N3,N4,---THE MEANING OF THESE VALUES IS EXPLAINED IN FORMAT
C      STATEMENT 112.
C      N8---NUMBER OF KILOMETERS BETWEEN CALCULATED FIELD VALUES
C      NT---TOTAL NUMBER OF POINTS PER LEVEL
C      N5---ONE HALF THE NUMBER OF INTEGRATION INTERVALS. THIS NUMBER
C      MUST BE AN EVEN NUMBER.
C
C      THE MKS SYSTEM OF UNITS IS USED THROUGHOUT THIS PROGRAM.
C
C      *****
C
C      INTEGER Z(25)
C      DIMENSION CON(4),Y(2001)
C      COMPLEX ODD(2001),EVEN(2001),ORIGIN(2001),EX(2001)
C      COMPLEX ODDHY(2001),ODDHZ(2001),EVENHY(2001),EVENHZ(2001),ORIGHY(2
1001),ORIGHZ(2001),HY(2001),HZ(2001)
C      COMMON/A1/OI,OM,UM,HW,PI,ZO,A,B,D1,D2,NT,N5,N8
C      READ(5,100) Z1,D1,D2,OI,ZO,HW,N1,N2,N3,N4,N8
C      READ(5,101) NT,N5
C
C      Z-----THIS ARRAY CONTAINS THE INTER LEVEL SPACINGS. THE FIRST
C      SPACING IS THE DISTANCE BETWEEN THE FIRST LEVEL AND THE TOP BOUNDARY.
C      THESE VALUES ARE IN KILOMETERS.
C
C      IF(N1.EQ.1) GO TO 103
C      READ(5,102) (Z(K),K=1,N1)
C      GO TO 104
103 READ(5,102) Z(1)
C
C      FREQ---FREQUENCY IN HERTZ.
C      A,B---LIMITS OF INTEGRATION. INTEGRAND IS ASSUMED NEGLIGIBLE AT B. A=0.
C
104 READ(5,105) FREQ,B
C
C      CON---ARRAY CONTAINING THE CONDUCTIVITIES OF THE VARIOUS LAYERS
C      STARTING WITH THE AIR LAYER (CONDUCTIVITY ZERO) AND PROCEEDING DOWNWARD.
C      FOUR CONDUCTIVITIES MUST BE SPECIFIED. IF A HALF SPACE SUBSURFACE
C      IS DESIRED , THE THREE SUBSURFACE CONDUCTIVITIES MUST BE SPECIFIED
C      TO BE THE SAME VALUE.

```

Figure A.1 ELEMENTAL GAUSSIAN main program.


```

C      READ(5,106,END=107) CON
107  A=0.0
      PI=4.0*ATAN(1.0)
      OM=2.0*PI*FREQ
C
C      UM---PERMEABILITY OF FREE SPACE
C
      UM=1.26E-6
      WRITE(6,108)
      WRITE(6,109) Z1,D1,D2,OI,ZO,HW,N1,N8
      WRITE(6,110) FREQ,B
      WRITE(6,111) (CON(I),I=1,4)
      J2=N2-1
      J3=N3-1
      WRITE(6,112) N4,J2,J3
C
C      SELECT LEVELS AND DO INTEGRATION FOR FIELD VALUES BY CALLING INTEG
C
113  I=1
      Z2=Z1+FLOAT(Z(I))*1.0000E+03
      CALL INTEG(ODD,ODDHY,ODDHZ,EVEN,EVENHY,EVENHZ,ORIGIN,ORIGHY,ORIGHZ
1,EX,HY,HZ,Z2,CON,Y)
      WRITE(6,114) I
      WRITE(7) EX
      WRITE(8) HY
      WRITE(9) HZ
      WRITE(6,115)
      WRITE(6,116) (EX(J),J=N2,N3,N4)
      WRITE(6,117)
      WRITE(6,116) (HY(J),J=N2,N3,N4)
      WRITE(6,118)
      WRITE(6,116) (HZ(J),J=N2,N3,N4)
      I=I+1
      IF (I.LE.N1) GO TO 113
      STOP
100  FORMAT(6E10.4,I2,I4,I4,I4,I4)
101  FORMAT(I4,I5)
102  FORMAT(2I3)
105  FORMAT(F7.5,E10.4)
106  FORMAT(E10.4)
108  FORMAT('1','Z1',9X,'D1',9X,'D2',9X,'OI',9X,'ZO',9X,'HW',9X,'N1',4X
1,'N8')
109  FORMAT('-',6(E10.4,1X),I2,2X,I4)
110  FORMAT('-', 'FREQ =',F7.5,'      UPPER LIMIT OF INTEGRATION =',E10.4)
111  FORMAT('-', 'CONDUCTIVITIES= ',4(E10.4,2X))
112  FORMAT('-', 'COMPLEX FIELD VALUES ARE GIVEN AT INTERVALS OF ',I4,1X
1,'KM. OVER A RANGE OF ',I4,' KM. TO ',I4,' KM.')
114  FORMAT('-', 'LEVEL',I4,' COMPLETED')
115  FORMAT('-', 'EX')
116  FORMAT(100('0',5(E10.4,1X,E10.4,3X)/))
117  FORMAT('-', 'HY')
118  FORMAT('-', 'HZ')
      END

```

Figure A.2 ELEMENTAL GAUSSIAN main program (continued).


```

SUBROUTINE INTEG(ODD,ODDHY,ODDHZ,EVEN,EVENHY,EVENHZ,ORIGIN,ORIGHY,
1ORIGHZ,EX,HY,HZ,Z2,CON,Y)
C
C THIS SUBROUTINE DOES THE INTEGRATION THROUGH THE USE OF FILON'S METHOD
C
  DIMENSION CON(4),Y(NT)
  COMPLEX ORIGIN(NT),ODD(NT),EVEN(NT),EX(NT)
  COMPLEX ORIGHY(NT),ORIGHZ(NT),EVENHY(NT),EVENHZ(NT),ODDHY(NT),ODDH
1Z(NT),HY(NT),HZ(NT)
  COMPLEX CONST,CONSHY,CONSHZ,ELIN,HYLIN,HZLIN
  COMMON/A1/CI,OM,UM,HW,PI,ZO,A,B,D1,D2,NT,N5,N8
C
C S---INTERVAL OF INTEGRATION.
C
  S=(B-A)/(FLOAT(N5)*2.)
C
C Y---AFRAY CONTAINING THE DISTANCES FROM THE ORIGIN IN THE POSITIVE Y
C DIRECTION AT WHICH FIELD CALCULATIONS ARE PERFORMED.
C
  DO 200 I=1,NT
    Y(I)=FLOAT(I-1)*1000.
    ORIGHY(I)=(0.0,0.0)
    ORIGHZ(I)=(0.0,0.0)
    EVENHY(I)=(0.0,0.0)
    EVENHZ(I)=(0.0,0.0)
    ODDHY(I)=(0.0,0.0)
    ODDHZ(I)=(0.0,0.0)
    ORIGIN(I)=(0.0,0.0)
    EVEN(I)=(0.0,0.0)
200 ODD(I)=(0.0,0.0)
C
C ARRAYS PREFIXED WITH ODD CONTAIN THE CALCULATIONS OF THE INTEGRAND
C PERFORMED FOR THE ODD NUMBERED INTERVALS OF INTEGRATION, IN ACCORDANCE
C WITH FILON'S METHOD.
C
C ARRAYS PREFIXED WITH EVEN CONTAIN THE CALCULATIONS OF THE INTEGRAND
C PERFORMED FOR THE EVEN NUMBERED INTERVALS OF INTEGRATION, IN ACCORDANCE
C WITH FILON'S METHOD.
C
  T=S
  DO 201 J=1,N5
    CALL CONST(T,Z2,CONSTT,CONSHY,CONSHZ,CON)
    DO 202 I=1,NT,N8
      ODDHY(I)=ODDHY(I)+CONSHY*COS(T*Y(I))
      ODDHZ(I)=ODDHZ(I)+CONSHZ*SIN(T*Y(I))
202 ODD(I)=ODD(I)+CONSTT*COS(T*Y(I))
201 T=T+S+S
    NB=N5-1
    G=S+S
    DO 203 J=1,NB
      CALL CONST(G,Z2,CONSTT,CONSHY,CONSHZ,CON)
      DO 204 I=1,NT,N8
        EVENHY(I)=EVENHY(I)+CONSHY*COS(G*Y(I))
        EVENHZ(I)=EVENHZ(I)+CONSHZ*SIN(G*Y(I))
204 EVEN(I)=EVEN(I)+CONSTT*COS(G*Y(I))

```

Figure A.3 Subroutine INTEG.


```

203 G=G+S+S
    V=1.000E-20
    CALL CONST(V,Z2,CONSTT,CONSHY,CONSHZ,CON)
    DO 205 I=1,NT,N8
    ORIGHY(I)=CONSHY
    ORIGHZ(I)=CONSHZ
    ORIGIN(I)=CONSTT
C
C    FILON'S INTEGRATION METHOD
C
    THE=Y(I)*S
    IF (THE .LE. .1) GO TO 206
    ALP=(THE**2+THE*SIN(THE)*COS(THE)-(2.*(SIN(THE))**2))/THE
    BETA=2.*(THE*(1.+(COS(THE))**2))-2.*SIN(THE)*COS(THE))/THE**3
    GAMMA=4.*(SIN(THE)-THE*COS(THE))/THE**3
    GO TO 207
206 BETA=2./3.+2.*(THE**2)/15.-4.*(THE**4)/105.+2.*(THE**6)/567.
    GAMMA=4./3.-2.*(THE**2)/15.+(THE**4)/210.-(THE**6)/11340.
    ALP=((2.*THE**3)/45.)-((2.*THE**5)/315.)+(2.*THE**7)/4725.)
207 HY(I)=S*(BETA*(EVENHY(I)-.5*ORIGHY(I))+GAMMA*ODDHY(I))
    HZ(I)=S*(ALP*ORIGHZ(I)+BETA*EVENHZ(I)+GAMMA*ODDHZ(I))
205 EX(I)=S*(BETA*(EVEN(I)-.5*ORIGIN(I))+GAMMA*ODD(I))
C
C    LINEAR INTERPOLATION BETWEEN CALCULATED POINTS IN A GIVEN LEVEL.
C
    N9=N8+1
    N10=N8-1
    DO 208 I=N9,NT,N8
    ELIN=(EX(I)-EX(I-N8))/FLOAT(N8)
    HYLIN=(HY(I)-HY(I-N8))/FLOAT(N8)
    HZLIN=(HZ(I)-HZ(I-N8))/FLOAT(N8)
    DO 208 J=1,N10
    EX(I-N8+J)=EX(I-N8)+ELIN*FLOAT(J)
    HY(I-N8+J)=HY(I-N8)+HYLIN*FLOAT(J)
208 HZ(I-N8+J)=HZ(I-N8)+HZLIN*FLOAT(J)
    RETURN
    END

```

Figure A.4 Subroutine INTEG (continued).


```

SUBROUTINE CONST(S,Z2,E1,HY1,HZ1,CON)
  DIMENSION CON(4)
  COMPLEX TH(3),W(3),Q,CEXP,R,B1,CSQRT,A2,A3,A4,B2,B3,Q1,E1
  COMPLEX HY1,HZ1
  COMPLEX CPRIM,CMLX
  COMMON/A1/OI,OM,UM,HW,PI,ZO,A,B,D1,D2,NT,N5,N8

```

```

  THIS SUBROUTINE CALCULATES THE INTEGRAND VALUES.

```

```

  THE SUBSURFACE CAN CONTAIN A MAXIMUM OF TWO LAYERS AND ONE HALF SPACE.

```

```

C
C
C
C
  CPRIM=(0.0,-1.0)*((OI*OM*UM*HW)/(SQRT(2.0*PI)*S))*EXP(S*ZO-S**2*HW
1**2/2.)
  Z=S**2
  DO 300 N=1,3
    Y1=OM*UM*CON(N+1)
    W(N)=CMLX(Z,Y1)
300 TH(N)=CSQRT(W(N))
    IF(D1.GT.1.0E+6) GO TO 301
    IF(D2.GT.1.0E+6) Q1=CMLX(0.0,0.0)
    IF(D2.GT.1.0E+6) GO TO 301
    Q1=((TH(2)-TH(3))/(TH(2)+TH(3)))*CEXP(-2.*TH(2)*D2)
301 IF(D1.GT.1.0E+6) GO TO 302
    Q=((TH(1)+TH(2)+(TH(1)-TH(2))*Q1*CEXP(2.*TH(2)*D1))/(TH(1)-TH(2)+(
1TH(1)+TH(2))*Q1*CEXP(2.*TH(2)*D1)))*CEXP(2.*TH(1)*D1)
    R=(S*(Q+1.))/(TH(1)*(Q-1.))
    B1=(R-1.)/(R+1.)
302 IF(D1.GT.1.0E+6) B1=(S-TH(1))/(S+TH(1))
    IF(Z2.LE.0.0) GO TO 304
    IF(D1.GT.1.0E+6) A4=CMLX(1.0,0.0)+B1
    IF(D1.GT.1.0E+6) GO TO 307
    A2=((1.+B1)*Q)/(Q+1.)
    B2=A2/Q
    IF(Z2.LE.D1) GO TO 305
    A3=((A2+B2*CEXP(2.*TH(1)*D1))/(1.+Q1*CEXP(2.*TH(2)*D1)))*CEXP((TH(
12)-TH(1))*D1)
    B3=A3*Q1
    IF(D2.GT.1.0E+6) GO TO 303
    IF(Z2.LE.D2) GO TO 306
    A4=(A3+B3*CEXP(2*TH(2)*D2))*CEXP((TH(3)-TH(2))*D2)
    GO TO 307
303 A4=A3
    GO TO 307
304 E1=(EXP(-S*Z2)+B1*EXP(S*Z2))*CPRIM
    HY1=((0.0,-1.0)/(OM*UM))*S*(EXP(-S*Z2)-B1*EXP(S*Z2))*CPRIM
    HZ1=((0.0,1.0)*S)/(OM*UM)*E1
    GO TO 308
305 E1=(A2*CEXP(-TH(1)*Z2)+B2*CEXP(TH(1)*Z2))*CPRIM
    HY1=((0.0,-1.0)/(OM*UM))*TH(1)*(A2*CEXP(-TH(1)*Z2)-B2*CEXP(TH(1)*Z
12))*CPRIM
    HZ1=((0.0,1.0)*S)/(OM*UM)*E1
    GO TO 308
306 E1=(A3*CEXP(-TH(2)*Z2)+B3*CEXP(TH(2)*Z2))*CPRIM
    HY1=((0.0,-1.0)/(OM*UM))*TH(2)*(A3*CEXP(-TH(2)*Z2)-B3*CEXP(TH(2)*Z
12))*CPRIM

```

Figure A.5 Subroutine CONST.


```
      HZ1= ( ( (0.0,1.0)*S)/(OM*UM) ) *E1  
      GO TO 308  
307  E1= (A4*CEXP(-TH(3)*Z2)) *CPRIM  
      HY1= ( (0.0,-1.0)/(OM*UM) ) *TH(3) * (A4*CEXP(-TH(3)*Z2)) *CPRIM  
      HZ1= ( ( (0.0,1.0)*S)/(OM*UM) ) *E1  
308  RETURN  
      END
```

Figure A.6 Subroutine CONST (continued).

$C(s)$ is as given in equation (2.94) of Section 2.5. Upon returning to INTEG the integration is performed by the use of Filon's method (Tranter, 1965). The main program then writes the electric and magnetic field values for that level on a file or magnetic tape. This process is then repeated for subsequent levels.

A.3 The Program RECTAZOID

This program sums a finite number of elemental Gaussian solutions to obtain an approximate solution for a rectangular current distribution. The user specifies the number of elemental Gaussians to approximate the rectangular current distribution and assigns their source coefficients the magnitude one. The elemental Gaussian solution for positive values of y calculated by the previous program is read into both positive and negative y regions. In this, the vertical magnetic field quantities must be made negative in the negative y region since the vertical magnetic field is asymmetric about the origin. This solution is then shifted and summed to approximate the rectangular current solution. The result is then stored. This program is again used to give the solution for a piecewise continuous source composed of a summation of rectangular current sources. The general source configuration must be digitized by the user at regular intervals (equal to the width of the rectangles) and these source coefficients are then supplied to the program in the

array SA. The general solution is obtained by superimposing rectangular source solutions which are shifted with respect to one another and multiplied by the appropriate source coefficients in accordance with the trapezoidal rule. The final solution is thus obtained for the layered earth and is that of a piecewise continuous source which approximates a continuous source. The listing of RECTAZOID is given in Figures A.7 and A.8.

A.4 Various Parameters and Their Effects on the Solution

In the programs many parameters can be varied and the values of these can affect the accuracy of the final solution. It is important to consider these parameters and the reasons for choosing their values.

A.4.1 Elemental Gaussian

The final result depends greatly upon the accuracy of the elemental Gaussian solution. The important parameters here are B, N5 and N8.

For half widths of approximately 10 km the source function $C(s)$ is governed by the term e^{sz_0} . Therefore, B should be taken to be at least ten times the damping constant $(1/|z_0|)$ for a source in free space (see Hermance and Peltier (1970)). For a layered-earth model a value of 0.8×10^{-4} or larger will be satisfactory.


```

C *****RECTAZOID*****
C
C NT---NUMBER OF FIELD POINTS USED IN THE ELEMENTAL GAUSSIAN PROGRAM.
C NLEVEL---NUMBER OF LEVELS.
C NSOUR---NUMBER OF SOURCE ELEMENTS. MUST BE ODD NUMBER FOR RECTANGULAR
C SOURCE.
C NSC---NUMBER OF THE SOURCE ELEMENT WHICH IS POSITIONED OVER THE ORIGIN.
C NSHIFT---NUMBER OF ARRAY ELEMENTS THAT FIELD IS TO BE SHIFTED FOR EACH
C CURRENT ELEMENT.
C NHZ---IF HZ MAGNETIC FIELD DATA IS BEING RUN FOR A RECTANGULAR SOURCE
C NHZ=1. AT ALL OTHER TIMES NHZ=0. THIS IS TO ALLOW FOR NON-SYMMETRY OF HZ
C MAGNETIC FIELD VALUES.
C THE DIMENSION OF THE SOURCE ARRAY (SA) MUST EQUAL NSOUR.
C NHW---HALF WIDTH OF ELEMENTAL GAUSSIAN.
C
C *****
C
C COMPLEX ET(4001),EX(2001),EA(4001)
C DIMENSION SA(14)
C READ(5,100) NT,NLEVEL,NSOUR,NSC,NSHIFT,NHZ,NHW
C READ(5,101) N4,N2,N3
C WRITE(6,102)
C WRITE(6,103) NT,NLEVEL,NSOUR,NSC,NSHIFT,NHZ,NHW
C J2=N2+1
C J3=N3-1
C WRITE(6,104) N4,J2,J3
C NT1=NT-1
C NT2=NT+1
C NTOT=2*NT-1
C IF(NSHIFT.GT.NHW) GO TO 106
C
C SOURCE ARRAY FOR RECTANGULAR SOURCE.
C
C DO 105 I=1,NSOUR
105 SA(I)=1.000
C GO TO 107
C
C SOURCE ARRAY FOR LINEARLY APPROXIMATED SOURCE.
C
C 106 READ(7) SA
C 107 I1=1
C 108 IF(NSHIFT.GT.NHW) GO TO 112
C
C ELEMENTAL GAUSSIAN FIELD VALUES
C
C READ(8) EX
C
C FORM SYMMETRIC FIELD ARRAY (EXCEPT IN CASE OF HZ FOR RECTANGULAR SOURCE)
C FROM ELEMENTAL GAUSSIAN DATA.
C
C DO 109 I=1,NT
C EA(NT1+I)=EX(I)
109 EA(I)=EX(NT2-I)
C IF(NHZ.EQ.0) GO TO 111

```

Figure A.7 The program RECTAZOID.


```

DO 110 I=1,NT
110 EA(I)=-EA(I)
111 IF(NSHIFT.EQ.NHW) GO TO 113
C
C      RECTAZOID FIELD VALUES.
C
112 READ(8) EA
C
C      MULTIPLY BY AMPLITUDE OF RECTANGULAR SOURCE CENTERED OVER THE ORIGIN.
C
113 DO 114 I=1,NTOT
114 ET(I)=EA(I)*SA(NSC)
    J=(NSC-1)*NSHIFT
    J1=1
115 IF(J.EQ.0) GO TO 117
C
C      SHIFT AND ADD FOR SOURCE ELEMENTS IN THE NEGATIVE Y REGION.
C
DO 116 I=1,NTOT
IF((I+J).LT.1.OR.(I+J).GT.NTOT) GO TO 116
ET(I)=ET(I)+EA(I+J)*SA(J1)
116 CONTINUE
    J=J-NSHIFT
    J1=J1+1
    GO TO 115
117 K=NSC+1
    J=NSHIFT
118 IF(K.GT.NSOUR) GO TO 120
C
C      SHIFT AND ADD FOR SOURCE ELEMENTS IN THE POSITIVE Y REGION.
C
DO 119 I=1,NTOT
IF((I-J).LT.1.OR.(I-J).GT.NTOT) GO TO 119
ET(I)=ET(I)+EA(I-J)*SA(K)
119 CONTINUE
    J=J+NSHIFT
    K=K+1
    GO TO 118
120 WRITE(9) ET
    WRITE(6,121) I1
    WRITE(6,122) (ET(J),J=1,NTOT,N4)
    I1=I1+1
    IF(I1.GT.NLEVEL) GO TO 123
    GO TO 108
123 STOP
100 FORMAT(I4,6I3)
101 FORMAT(3I5)
102 FORMAT('-', ' NT NLEVEL NSOUR NSC NSHIFT NHZ NHW')
103 FORMAT('-', '1X,I4,5X,I3,4X,I3,2X,I3,5X,I3,1X,I3,1X,I3)
104 FORMAT('-', 'COMPLEX FIELD VALUES ARE GIVEN AT INTERVALS OF ',I5,1X
    1,'KM. OVER A RANGE OF ',I5,' KM. TO ',I5,' KM.')
121 FORMAT('-', 'LEVEL',I4,' COMPLETED')
122 FORMAT(100('0',5(E10.4,1X,E10.4,3X)/))
END

```

Figure A.8 The program RECTAZOID (continued).

A total of 4000 integration intervals ($2*N5$) is sufficient for a half width (HW) of 1-10 km. This value of $N5$ improves the accuracy of the apparent resistivity curves calculated from

$$\rho_a = \frac{1}{\omega \mu_0} \left| \frac{E_x}{H_y} \right|^2$$

(Cagniard, 1953) since when calculating the apparent resistivity any error in the field values produces a greater error in the resistivity values. Satisfactory field values may be obtained by using approximately one-sixth this value of $N5$. These values of B and $N5$ were used in calculating the elemental Gaussian results of Tables 1 and 2 of Chapter 2. In calculating the 240 km half width Gaussian the value of B was taken as 0.1×10^{-4} .

The solution for the field values at any particular level is calculated at a certain number of points and this is indirectly determined by $N8$. The values for intermediate points are determined by a linear interpolation between the calculated points. The quantity $(N8-1)$ represents the number of points between calculated values. In all cases except the sample run $N8$ was set equal to 10. If this value is made too large the solution will be less accurate, especially when the field solutions are shifted and added.

A.4.2 RECTAZOID

The parameters in RECTAZOID which most affect the results are NSOUR and NSHIFT. When synthesizing the rectangular source the best approximation is obtained when the adjacent elemental Gaussians are one half width apart. Because of this, NSHIFT is equal to the half width in kilometres. When arbitrary source currents are approximated NSHIFT is equal to the width of the rectangles. The width of the rectangular source specified by NSOUR can also affect the accuracy of the solution. The normalized values of H_z are most affected by the source geometry and coarse rectangular approximations to the arbitrary source configuration can noticeably affect these profiles.

A.5 Sample Run

Sample calculations have been made and the results of this run are given in Figures A.9, A.10, A.11 and A.12.

The sample run has been designed to provide an easy verification of the program. The total running time to obtain the results given here is approximately 40 s on the IBM 360/67 at the University of Alberta. In the ELEMENTAL GAUSSIAN PROGRAM for this example only three points are calculated and the remaining ones are obtained through linear interpolation. A single value of 50 must be supplied for the Z array since the fields are obtained for


```
Z1      D1      D2      OI      ZO      HW      N1      N8
-.5000E+05 0.5000E+05 0.1100E+07 0.1000E+01 -.1100E+06 0.1000E+05 1 1000

FREQ =1.00000    UPPER LIMIT OF INTEGRATION =0.8000E-04

CONDUCTIVITIES= 0.0      0.1000E-01 0.1000E+00 0.1000E+00

COMPLEX FIELD VALUES ARE GIVEN AT INTERVALS OF 200 KM. OVER A RANGE OF 0 KM. TO 2000 KM.

LEVEL 1 COMPLETED

EX
-.1157E-02 -.1324E-02 -.8798E-03 -.1038E-02 -.6028E-03 -.7521E-03 -.3258E-03 -.4661E-03 -.4885E-04 -.1802E-03
0.2282E-03 0.1058E-03 0.1910E-03 0.8845E-04 0.1538E-03 0.7112E-04 0.1167E-03 0.5380E-04 0.7954E-04 0.3647E-04
0.4238E-04 0.1915E-04

HT
-.5969E-01 -.1477E-02 -.4546E-01 -.1178E-02 -.3122E-01 -.8783E-03 -.1698E-01 -.5789E-03 -.2749E-02 -.2796E-03
0.1149E-01 0.1977E-04 0.9617E-02 0.1673E-04 0.7746E-02 0.1370E-04 0.5876E-02 0.1067E-04 0.4005E-02 0.7634E-05
0.2135E-02 0.4600E-05

HZ
0.0      0.0      0.8815E-06 -.9073E-06 0.1763E-05 -.1815E-05 0.2644E-05 -.2722E-05 0.3526E-05 -.3629E-05
0.4407E-05 -.4536E-05 0.3615E-05 -.3721E-05 0.2822E-05 -.2906E-05 0.2030E-05 -.2091E-05 0.1237E-05 -.1276E-05
0.4448E-06 -.4604E-06
```

Figure A.9 Sample run output for ELEMENTAL GAUSSIAN.

2001 1 3 2 10 1 10

COMPLEX FIELD VALUES ARE GIVEN AT INTERVALS OF 200 KM. OVER A RANGE OF -2000 KM. TO 2000 KM.

LEVEL 1 COMPLETED

-0.9292E-06	0.9616E-06	-0.3712E-05	0.3827E-05	-0.6090E-05	0.6273E-05	-0.8467E-05	0.8718E-05	-0.1084E-04	0.1116E-04
-0.1314E-04	0.1352E-04	-0.1058E-04	0.1089E-04	-0.7933E-05	0.8166E-05	-0.5289E-05	0.5444E-05	-0.2644E-05	0.2722E-05
0.0	0.0	0.2644E-05	-0.2722E-05	0.5289E-05	-0.5444E-05	0.7933E-05	-0.8166E-05	0.1058E-04	-0.1089E-04
0.1314E-04	-0.1352E-04	0.1084E-04	-0.1116E-04	0.8467E-05	-0.8718E-05	0.6090E-05	-0.6273E-05	0.3712E-05	-0.3827E-05
0.9292E-06	-0.9616E-06								

Figure A.10 Sample run output from RECTAZOID for the H_z field values for the rectangular current distribution.

0.200E+02
0.500E+02
0.500E+02
0.500E+02
0.500E+02
0.500E+02
0.300E+03
0.700E+03
0.700E+03
0.700E+03
0.700E+03
0.500E+03
0.300E+03
0.200E+02

Figure A.11 Sample run source coefficients.

NT NLEVEL NSOUR NSC NSHIFT NHZ NHW
2001 1 14 3 30 0 10

COMPLEX FIELD VALUES ARE GIVEN AT INTERVALS OF 200 KM. CVER A RANGE OF -2000 KM. TO 2000 KM.

LEVEL 1 COMPLETED									
-0.1720E-03	0.1778E-03	-0.4064E-02	0.4197E-02	-0.1577E-01	0.1626E-01	-0.2573E-01	0.2650E-01	-0.3569E-01	0.3675E-01
-0.4558E-01	0.4692E-01	-0.5259E-01	0.5413E-01	-0.4408E-01	0.4537E-01	-0.3300E-01	0.3397E-01	-0.2192E-01	0.2256E-01
-0.1084E-01	0.1116E-01	0.2393E-03	-0.2463E-03	0.1132E-01	-0.1165E-01	0.2240E-01	-0.2306E-01	0.3348E-01	-0.3446E-01
0.4449E-01	-0.4579E-01	0.5261E-01	-0.5415E-01	0.4522E-01	-0.4656E-01	0.3526E-01	-0.3631E-01	0.2530E-01	-0.2606E-01
0.1526E-01	-0.1573E-01								

Figure A.12 Sample run output from RECTAZOID for the arbitrary current source. This shows the parameters used in RECTAZOID as well as the vertical magnetic field values.

the surface level. The value of NT was 2001 and N5 was taken to be 20. The other parameters are as specified in Figure A.9. Figure A.10 gives the parameters used in RECTAZOID to construct the 30-km rectangular source. Since only vertical magnetic field data are produced in this run NHZ must be set equal to 1 to ensure the non-symmetry of the H_z field. The value of NHZ must be taken as 1 in construction of the rectangular source, but when synthesizing the arbitrary source from these rectangles NHZ must equal zero. The arbitrary source consists of fourteen rectangular sources weighted as indicated in the source array SA given in Figure A.11. The third rectangular current source is positioned at the origin as indicated by NSC. The parameters of Figure A.12 produce the vertical magnetic field associated with this source and these field values are given as well in Figure A.12. If the electric field or the horizontal magnetic field is desired, the elemental Gaussian data for those fields could be operated upon by RECTAZOID to produce the desired field. In these latter two cases all parameters for RECTAZOID would remain the same as before, except for NHZ which would be set equal to zero.

B30175